Nonlinear and Non-Modal Stability of Structures Evolving in Shear Flows

Conor A. Daly

Queens' College, Cambridge.

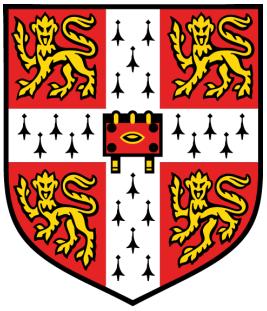

A Dissertation submitted for
the degree of Doctor of Philosophy
at the University of Cambridge
September 2013

Declaration

This thesis describes research carried out in the Department of Applied Mathematics and Theoretical Physics of Cambridge University. The dissertation is the result of my own work and includes nothing which is the outcome of work done in collaboration, except where specifically indicated in the text. The numerical calculations presented were computed using my own MATLAB code, with the exception of the nonlinear simulations of the Navier-Stokes equations and computation of nonlinear solutions in §3. These calculations were made using Navier-Stokes solvers SIMSON and Channelflow with permission from Dr P. Schlatter and Dr T. Schneider respectively. No part of the work contained herein has been submitted to any other university or place of learning for any degree, diploma or other qualification.

Conor A. Daly
Cambridge, September 2013

Acknowledgements

First and foremost I would like to thank my supervisor Prof. Nigel Peake for his perpetual support and limitless patience throughout my time in Cambridge. Nigel's willingness to listen and readiness to provide direction have been invaluable in shaping my thesis, and guiding my entry into the world of research. This, alongside regular discussions on the current state of LFC and the occasional whipping on the squash court, have allowed the past four years to pass very quickly. A great deal of thanks must also go to my office-partner Dr. Ed Brambley, without whose generous insights, my research would not be where it is today. I have been extremely fortunate to share a space with someone whose passions for mathematics, computing and freshly ground Arabica are congruent with my own. I would also like to thank past and present members of the Waves Group: Rosie, Hélène, Justin and Lorna for their feedback on my work and for generously passing on their expertise in LaTeX. I would like to further thank all the friends I have made in DAMTP and the CMS, who have made my time here enjoyable and unforgettable.

It has been a great pleasure to spend three months of my postgraduate study working at KTH in the beautiful city of Stockholm. I would like to thank Prof. Henrik Alfredsson, whose presentation during his visit to DAMTP directly inspired two of the chapters in my thesis; Dr. Philipp Schlatter, who taught me a great deal of computational fluid dynamics and under whose influence I took strides forward in my research; Dr. Alexandre Suryadi, with whom I had many insightful discussions on experimental fluid dynamics; and Prof. Dan Henningson, whose passion for science was simply inspirational and whose garden house provided much more than a roof over my head! I would also like to thank the many friends I made at the Mechanics department in KTH, who made me feel at home during my visit.

I would like to thank Dr. Tobias Schneider for his very generous invitation to the Max Planck Institute, which allowed me to develop my work on nonlinear structures. My short time in the charming town of Göttingen was extremely fruitful, and for this I owe much to the boundless enthusiasm of Dr. Schneider and the computational prowess of Dr. Hecke Schrobsdorff.

I would not be where I am today were it not for the support and encouragement of my parents and family. Mum, who has always pushed me to achieve without pressuring me to succeed, and Dad, who eventually learned not to ask "Is your course finished yet?", but is unrelenting in his ability to administer the occasional whipping on the squash court.

I would like to thank the many friends I have made here in Cambridge and in Queens', all of whom have made my years here very special. There are too many to mention everyone by name, but huge thanks go to my housemates Marion, Brendan, Liz and Stuart, and to Kavita who has given me encouragement and support beyond what I deserve.

Finally I would like to thank the EPSRC, DAMTP and St. Malachy's College for providing the finanical backing which has made my research possible.

Abstract

This thesis explores a range of stability techniques and their application to structures in various constant density fluid flows. In particular, the stability of nonlinear structures which develop in rotating plane Couette flow is analyzed using Floquet theory, which allows the global stability of an important secondary nonlinear structure called a Taylor vortex to be determined. From this the distinct tertiary states which emerge as Taylor vortices break down are characterized and their bifurcation behaviour is studied. Non-modal stability analyses are conducted in rotating plane Couette flow and annular Poiseuille-Couette flow. In each flow the growth mechanisms and the form of the perturbations responsible for the maximum linear energy amplification are discussed. Finally, the non-modal behaviour of the Papkovitch-Fadle operator is treated with reference to spatially developing disturbances in Stokes channel flow. The mechanisms and the rates of convergence of the linear spatial energy amplification are investigated and contrasted with temporal energy amplification.

Contents

Chapter 1

Introduction

Hydrodynamic stability and the transition to turbulence of fluid flow have been under investigation and scientific scrutiny since the late 19^{th} century, when the studies of Rayleigh (1880) and Reynolds (1883) provided early insights into the mathematics and physics involved. With the equations governing the dynamics of a viscous fluid already established by Navier (1822) and Stokes (1845), Rayleigh's contribution, though it is one of many in the field, was to derive an equation governing the evolution of infinitesimal, inviscid waves which perturb a finite mean flow. The ideas underpinning the formulation of this equation, known as the Rayleigh equation, are a major influence on our modern understanding of stability in its mathematical sense. Reynolds' experimental investigations on transition to turbulence in pipe flow heralded the discovery that transition could be characterized in terms of a non-dimensional quantity which takes account of the spatio-temporal scales of the system and the viscosity of the fluid. The Reynolds number, defined $Re = \frac{Uh}{\nu}$ for flow in a channel where U is the mean flow velocity, h is the channel half-width and ν is the kinematic viscosity, has become one of the most important numbers in fluid dynamics. Its discovery has precipitated the identification of a range of non-dimensional numbers which describe various aspects of fluid flow. The inconsistency between experimental observations of the onset of turbulence and theoretical predictions of when transition should occur remains an outstanding problem in 21^{st} century physics, and motivation for current researchers around the world.

The possibility of transiently growing structures in shear flows has long been recognized in fluid mechanics. Among the first to predict the existence of such disturbances was Orr (1907) who, on analyzing the dynamics of a two-dimensional inviscid fluid and underscoring the existence of a transient instability mechanism, wrote, *"It accordingly appears that, in this simple case, although the disturbance, if sufficiently small, must ultimately decrease indefinitely, yet, before doing so, it may be very much increased"*, Orr (1907, p. 32). Transient, non-modal, energy growth of linear perturbations has now become a

cornerstone of hydrodynamic stability analysis, alongside classical eigenvalue, or modal, analysis. Researchers such as Ellingsen & Palm (1974) and Landahl (1980) added to the literature on inviscid, algebraic (as opposed to expontential) growth mechanisms extant in linearly stable fluids. Gustavsson (1991), Butler & Farrell (1992), Reddy & Henningson (1993) and Schmid & Henningson (1994) showed that transient energy growth of linear disturbances over many orders of magnitude is possible in viscous flows, with growth driven by the inviscid, algebraic instabilities and subsequently cut off by viscous dissipation after long times. It was recognized that this transient energy growth is a consequence of the underlying nonnormality of the linearized Navier-Stokes operator (Trefethen *et al.* (1993), Trefethen (1997), Trefethen & Embree (2005)), which renders eigenmodes of the system non-orthogonal with respect to an appropriate norm. Hence we term the study of transient linear energy growth *non-modal* analysis, as a combination of many modes are a necessary requirement for growth. Non-modal growth has been postulated to play a role in the onset of turbulent dynamics in subcritical shear flows, where experimental observations of turbulence are very much at odds with the predicitons of the exponentially growing linear modes of classical linear stability theory. From linear stability theory, we have that plane Poiseuille flow has critical Reynolds number $Re_{cr} = 5772$ (Orszag (1971)) and plane Couette flow is stable for all Reynolds numbers (Romanov (1973)). Numerical calculations suggest that Hagen-Poiseuille flow is linearly stable, though a formal proof of this continues to elude mathematicians. However, in experimental and numerical investigations, transition is found to occur as low as $Re = 1000$ for plane Poiseuille flow, $Re = 360$ in plane Couette flow and $Re = 1020$ in Hagen-Poiseuille flow.

Recent studies have proposed fully nonlinear mechanisms governing subcritical shear flow transition. These include the self-sustaining process proposed by Waleffe (1997, 1998) and its asymptotic analogue of vortex-wave interaction theory featured in the works of Hall & Smith (1991); Hall & Sherwin (2010), Deguchi *et al.* (2013) and Blackman *et al.* (2013). The self-sustaining process and vortex-wave interaction theory are reliant on streak instabilities; a streaky structure forms and loses stability to an inviscid wave; the neutral inviscid wave drives streamwise oriented vortices; and the streamwise vortices in turn drive the streaks. Non-modal growth, in the form of the lift-up mechanism (Landahl (1980)), has been proposed as the cause for the streamwise vortices being driven into streaks. In another approach to the problem of transition, optimization over the fully nonlinear Navier-Stokes equations for the minimal seed required for transition away from laminar flow has been undertaken by Pringle *et al.* (2012), Rabin *et al.* (2012) and Duguet *et al.* (2013); non-modal linear energy amplification plays a role in the nonlinear optimals discovered by these authors. The mechanism proposed by Orr (1907) drives the early growth states of the nonlinear optimal and the lift-up mechanism is once again behind the emergence of streaks. In this light, we consider a non-modal stability analysis

to be an important contribution to the understanding of stability and transition in fluid flows, and this is the motivation for the non-modal stability analyses in §§2, 4 and 5 of this thesis.

In §2 we study the non-modal stability of annular Poiseuille-Couette flow (APCF), a cylindrical flow where the fluid is driven by the combination of an axial pressure-gradient and a sliding inner cylinder. APCF has received attention recently as it incorporates thread-annular flow which is relevant to the medical procedure of thread-injection, a minimally-invasive surgical technique whereby a thread is inserted into a body using a spool and fluid-filled syringe apparatus (see Frei *et al.* (2000) for more details). Walton (2003, 2004, 2005) built upon the earlier linear stability analyses of Sadeghi & Higgins (1991) and Gittler (1993) to study the nonlinear stability and axisymmetric linear stability of APCF. Sadeghi & Higgins (1991) computed non-axisymmetric neutral curves and, following the approach of Cowley & Smith (1985) for planar Poiseuille-Couette flow, derived asymptotic cut-off inner cylinder velocities beyond which no linear instability is supported. Gittler (1993) showed that disconnected axisymmetric neutral curves exist for APCF, a finding later confirmed by Walton (2004) in a comprehensive axisymmetric stability analysis. Walton (2003, 2005) also found non-axisymmetric, large Re nonlinear waves to be supported over a wide parameter range and explored their relevance to thread-annular flow. Experimental studies of APCF are found in papers by Frei *et al.* (2000), who focus on thread-annulus applications, and a short paper by Shands *et al.* (1980), where transition to turbulence and fully turbulent flow are studied. In particular, Shands *et al.* (1980) show that transition occurs far below the linear stability threshold and, furthermore, that an increase of inner cylinder velocity *de-stabilizes* the flow which is at odds with the trend predicted by linear stability theory. Most recently, Wong & Walton (2012) computed finite-amplitude axisymmetric travelling wave solutions and showed that they can be continued below the linear neutral curve to subcritical parameter space. Non-modal growth analysis has been applied to related flows, such as Hagen-Poiseuille flow (Schmid & Henningson (1994)) and sliding Couette flow (Liu & Liu (2012)), but not APCF. Therefore, our aim is to complement the existing works concerning transition in APCF with a non-modal stability analysis.

The seminal work of Taylor (1923) mixed experimental and theoretical methods to describe the emergence of vortex structures in a differentially rotated, concentric-cylinder apparatus. These vortex structures are now called Taylor vortices and are considered key structures in transition of cylindrical and curved fluid flow (see Koschmieder (1993) for a full review). The Taylor vortices were shown to develop due to a linear inviscid instability of the base flow, putting experiment and theory in good agreement with one another

and providing some hope that the phenomena of transition and turbulence may be theoretically understood. Taylor's experiments sparked a flurry of research activity, which included: theoretical studies of Taylor vortex instability such as Davey *et al.* (1968) and Eagles (1971), who used weakly nonlinear analysis to determine the instabilities which affect Taylor vortices; experimental papers such as Coles (1965), Andereck *et al.* (1986) and Hegseth *et al.* (1996), who mapped in parameter space the different flow regimes observed in the experiments; and numerical stability analyses wherein finite-amplitude Taylor vortices are calculated numerically in addition to the higher-order structures they bifurcate towards, such as Nagata (1988), Weisshaar *et al.* (1991) and Antonijoan & Sánchez (2000). Recent experimental attention has been focused on the flow of a differentially rotated fluid through a linear shear layer, known as rotating plane Couette flow (RPCF). Alfredsson & Tillmark (2005), Hiwatashi *et al.* (2007), Tsukahara *et al.* (2010) and Suryadi *et al.* (2013) carried out experimental investigations of transition, with Tsukahara *et al.* (2010) following Andereck *et al.* (1986) by making a map in parameter space demarcating the different flow regimes which exist. Though RPCF is a more challenging flow to model experimentally, it is perhaps more amenable to a theoretical or numerical analysis due to the Cartesian geometry and the ease with which rotation can be added to the governing equations. The equations governing RPCF can be interpreted as a local approximation to Taylor-Couette flow in the co-rotating, narrow-gap limit, and indeed many of the aforementioned theoretical and numerical studies are based in the Cartesian framework.

In §3 we attempt to further the theoretical understanding of transition in supercritical RPCF. We begin with a characterization of the linear instabilities which de-stabilize the basic, primary flow and the finite-amplitude structures, often called secondary states in this context, which emerge from each unstable mode. The most important secondary structures are the Taylor vortices discussed in the preceeding paragraph, as the least stable perturbations of the primary flow bifurcate towards them. We perform a thorough investigation of the stability properties of Taylor vortices using Floquet theory to solve for perturbation growth rates. We study the stability of Taylor vortices with a range of spanwise wavenumbers β, to extend previous works such as Nagata (1998) who focused on Taylor vortices in RPCF with the critical primary wavenumber $\beta = 1.558$. Our stability analysis is then used to investigate tertiary bifurcations in RPCF, with a study of the structures that Taylor vortices develop into as they lose stability. Many of these structures have an analogue in the cylindrical Taylor-Couette flow, such as wavy vortex flow (Davey *et al.* (1968), Nagata (1988)) and twist vortices (Weisshaar *et al.* (1991), Antonijoan & Sánchez (2000)), but our approach uncovers a new streamwise-independent structure and a basic oscillatory state. Our analysis of the bifurcation sequence in RPCF is subsequently used to study the flow regimes observed in the experiments of Tsukahara

et al. (2010) and Suryadi *et al.* (2013). We propose a simplified transition model, the aim of which is to provide insight into the complex dynamics of transition, which we use in a comparison between experimental observation and theoretical and numerical modelling.

§4 continues our study of RPCF with a non-modal stability analysis on its subcritical parameter subspace. RPCF has two rotational regimes: cyclonic rotation, for which the mean vorticity is aligned with the system rotation and anti-cyclonic rotation, for which the mean vorticity and the system rotation counteract one another. The anti-cyclonic rotation regime has been of particular interest in the astrophysics community, where it is used as a local model for large-scale astrophysical accretion disks. The possibility of hydrodynamic turbulence in accretion disks is a subject of lively debate amongst astrophysicists. It is postulated that hydrodynamic turbulence could be the driving force behind an inward transport of angular momentum, which is necessary for the disks to accrete matter (Narayan *et al.* (1987), Longaretti (2002), Tevzadze *et al.* (2003), Yecko (2004), Shartman *et al.* (2012)). In this vein, Yecko (2004) made calculations of the non-modal growth for anti-cyclonic rotation. Using the rotation number $Ro = \frac{2\Omega h}{U}$ as a non-dimensional measure of rotation, where Ω is the rotation rate of the system, h is the channel half-width and U is the speed of each opposingly moving plate, Yecko found strong growth in the case $Ro = 1$, with this rotation rate related to a constant angular momentum rotating disk. This growth is driven by the anti lift-up effect (Antkowiak & Brancher (2007)), a mechanism with opposing characteristics to the lift-up mechanism of non-rotating flow. Yecko reported weaker two-dimensional growth for $Ro = \frac{4}{3}$, which is a local model for a Keplerian accretion disk, with this growth attributed to the mechanism originally proposed by Orr. Yecko subsequently concluded that anti-cyclonic hydrodynamic transition would be possible for high Reynolds numbers. We do not address the specific route in which a disturbance reaches turbulence in our work, rather, we identify the dominant linear energy growth mechanisms which we suspect will be relevant to the transition process.

Finally, in §5 we study the nonnormality of the Papkovitch-Fadle operator. The Papkovitch-Fadle operator is derived from the mathematical system which independently describes physical problems in both fluid mechanics and solid mechanics. In fluid mechanics, the problem corresponds to the Stokes flow of a viscous fluid within a semi-infinite two-dimensional strip. In solid mechanics, modelling the elastic deformation of a clamped semi-infinite plate requires the solution of the Papkovitch-Fadle operator. The operator is named after Papkovitch (1940) and Fadle (1941) who independently worked on the problem of elastic deformation in a finite strip, or rectangle, and in so doing gave expressions for the eigenfunctions relating to the semi-infinite domain. Much

of the previous literature on the problem is concerned with the suitability of expressing arbitrary edge data as a sum of these eigenfunctions. Smith (1952) examined the solid mechanics problem and developed an algorithm to determine the bending displacement of a semi-infinite elastic strip, under arbitrary displacements and stresses at the free edge. Smith's solution takes the form of a series of Papkovitch-Fadle eigenfunctions and conditions are established to guarantee convergence of that series. Noting that these conditions are too restrictive for most applications, Joseph (1977); Joseph & Sturges (1978), Gregory (1979, 1980*a*,*b*) and Spence (1982) showed that convergence could be guaranteed beyond Smith's conditions, and used their results to solve a wider range of Stokes flow and plate elasticity problems than previously possible.

Trefethen (1997); Trefethen & Embree (2005) highlighted the nonnormality of the Papkovitch-Fadle operator and computed its pseudospectra and plots of the optimal amplification of arbitrary edge conditions, along the semi-infinite dimension. The optimal disturbances were recognized to be Moffatt eddies (Moffatt (1963)), which are known to develop in a wall bounded corner of a viscous fluid. Optimal growth of spatially developing disturbances has also been treated in the context of boundary layers by Andersson *et al.* (1999), Luchini (2000) and Tempelmann *et al.* (2010) where it has been used as a key component in prediction models for transition to turbulence. A spatial optimal growth framework was also developed by Reshotko & Tumin (2001) in Hagen-Poiseuille flow, and for planar, wall-bounded parallel flows by Schmid & Henningson (2001). These works on spatial non-modal growth complement the much larger literature on non-modal growth in temporal flows, and together they form the basis of our understanding of the spatio-temporal development of structures within a fluid. In §5 we return to the question of the maximum spatial amplification that can be achieved by an arbitrary edge condition expressed as a finite series of Papkovitch-Fadle eigenfunctions. Framing the problem in a Stokes flow context, we investigate the convergence of the optimal edge condition with modal truncation. We then assess the extent to which our findings for Stokes flow are relevant to flows with spatial convection by studying two-dimensional spatial plane Poiseuille flow. To conclude, we compare our findings for spatial flows with an asymptotic analysis of the convergence of optimals in temporal plane Couette flow.

Chapter 2

Non-modal growth in annular Poiseuille-Couette flow

In this chapter we consider the temporal transient energy amplification of non-modal disturbances in annular Poiseuille-Couette flow (APCF); the flow between concentric cylinders with an axially translating inner cylinder and a pressure gradient driving the fluid across the annular gap. The outline of the chapter is as follows: in §2.1 we introduce the governing equations and derive the axially and azimuthally independent laminar base profile. In §2.2 we recap previous authors' linear stability results and in so doing verify our own calculations. We further maximize over wavenumbers to produce neutral curves in (Re, V) parameter space, with Re the Reynolds number based on the pressure gradient and V the inner cylinder velocity. In §2.3 we formulate the optimal energy growth problem and define the maxima by which we analyse the transient energy growth. In §2.4 we present the results of our non-modal growth calculations and assess the growth mechanisms driving the linear energy amplification. Finally, in §2.5 we compare our findings with the experimental study of Shands *et al.* (1980).

2.1 Governing equations

We consider annular Poiseuille-Couette flow (APCF); the flow of an incompressible, Newtonian fluid bounded between two rigid, co-axial cylinders with impermeable walls. A constant axial pressure gradient drives the fluid in the gap between the cylinders and, in addition, the inner cylinder is free to move with a prescribed velocity, in the axial direction. We work in cylindrical polar coordinates $(\tilde{x}, \tilde{r}, \tilde{\theta})$, aligned along the common axis of the cylinders. The fluid velocity $\tilde{\boldsymbol{u}}$ and pressure $\tilde{p}$ are governed by the cylindrical

Navier-Stokes equations

$$\frac{\partial \tilde{\boldsymbol{u}}}{\partial \tilde{t}} + \tilde{\boldsymbol{u}} \cdot \widetilde{\nabla} \tilde{\boldsymbol{u}} = -\frac{1}{\rho} \widetilde{\nabla} \tilde{p} + \nu \widetilde{\nabla}^2 \tilde{\boldsymbol{u}}, \tag{2.1a}$$

$$\widetilde{\nabla} \cdot \tilde{\boldsymbol{u}} = 0, \tag{2.1b}$$

where ρ and ν are the constant fluid density and kinematic viscosity, respectively. Given an inner cylinder radius A and outer cylinder radius B, the no-slip boundary condition is applied on the cylinder walls $r = A, B$. For axial pressure drop Δp over pipe length L and an inner cylinder velocity of $\widetilde{V}$, we have the following axisymmetric and axially independent exact solution of (2.1), which serves as a laminar flow profile

$$\widetilde{U}(\tilde{r}) = \widetilde{U}_p(\tilde{r}) + \widetilde{U}_c(\tilde{r}), \tag{2.2a}$$

with

$$\widetilde{U}_p(\tilde{r}) = \frac{\Delta p}{4\mu L \log \frac{B}{A}} \left(\tilde{r}^2 \log \frac{B}{A} - (B^2 - A^2) \log \tilde{r} + B^2 \log A - A^2 \log B \right), \tag{2.2b}$$

$$\widetilde{U}_c(\tilde{r}) = \widetilde{V} \frac{\log \frac{B}{\tilde{r}}}{\log \frac{B}{A}}, \tag{2.2c}$$

where $\mu = \rho\nu$ is the dynamic viscosity and $A < \tilde{r} < B$. $\widetilde{U}_p(\tilde{r})$ and $\widetilde{U}_c(\tilde{r})$ denote the Poiseuille and Couette components, respectively. The geometry is depicted in Figure 2.1.

To non-dimensionalize the flow we use the radial gap length scale $B - A$, the fluid density ρ and the mean Poiseuille velocity $\overline{U}$. For cross-sectional area A_c, $\overline{U}$ is defined as

$$\overline{U} = \frac{1}{A_c} \int_{A_c} \widetilde{U}_p \, dS = \frac{2}{B^2 - A^2} \int_A^B \widetilde{U}_p(r) \, r dr, \tag{2.3a}$$

$$= \frac{\Delta p}{8\mu L \log \frac{B}{A}} \left(B^2 - A^2 - (B^2 + A^2) \log \frac{B}{A} \right). \tag{2.3b}$$

The flow can then be described in terms of non-dimensional quantities; the radius ratio η of the cylinders, the Reynolds number Re based on the pressure gradient and the non-dimensionalized velocity V of the translating inner cylinder

$$\eta = \frac{A}{B}, \quad Re = \frac{\overline{U}(B - A)}{\nu}, \quad V = \frac{\widetilde{V}}{\overline{U}}. \tag{2.4}$$

The non-dimensionalized laminar profile is

$$U(r) = 2 \frac{(1 - r^2(1 - \eta)^2) \log \eta - (1 - \eta^2) \log(r(1 - \eta))}{1 - \eta^2 + (1 + \eta^2) \log \eta} + V \frac{\log(r(1 - \eta))}{\log \eta}, \tag{2.5}$$

for $\frac{\eta}{1-\eta} < r < \frac{1}{1-\eta}$ and with $0 < \eta < 1$. In Figure 2.2 we plot the laminar profile at various values of η and V. Assuming an infinitesimal perturbation of the form

$$[\bar{u}, \bar{v}, \bar{w}, \bar{p}] = [u, v, w, p](r)\mathrm{e}^{\mathrm{i}(kx+m\theta)+\omega t}, \tag{2.6}$$

with $k \in \mathbb{R}$, $m \in \mathbb{Z}$ and $\omega \in \mathbb{C}$, we linearize the Navier-Stokes equations about the laminar profile $U(r)$ to get

$$\omega u + \mathrm{i}kUu + vU' = -\mathrm{i}kp + \frac{1}{Re}\left\{u'' + \frac{u'}{r} - \left(\frac{m^2}{r^2} + k^2\right)u\right\}, \tag{2.7a}$$

$$\omega v + \mathrm{i}kUv = -p' + \frac{1}{Re}\left\{v'' + \frac{v'}{r} - \left(\frac{1+m^2}{r^2} + k^2\right)v + \frac{2\mathrm{i}mw}{r^2}\right\}, \tag{2.7b}$$

$$\omega w + \mathrm{i}kUw = -\frac{\mathrm{i}mp}{r} + \frac{1}{Re}\left\{w'' + \frac{w'}{r} - \left(\frac{1+m^2}{r^2} + k^2\right)w + \frac{2\mathrm{i}mv}{r^2}\right\}, \tag{2.7c}$$

$$\mathrm{i}ku + v' + \frac{v}{r} + \frac{\mathrm{i}mw}{r} = 0, \tag{2.7d}$$

where $' = \frac{d}{dr}$. The no-slip boundary condition holds on each cylinder surface, giving

$$u = v = w = 0 \qquad \text{at} \quad r = \frac{\eta}{1-\eta}, \frac{1}{1-\eta}. \tag{2.8}$$

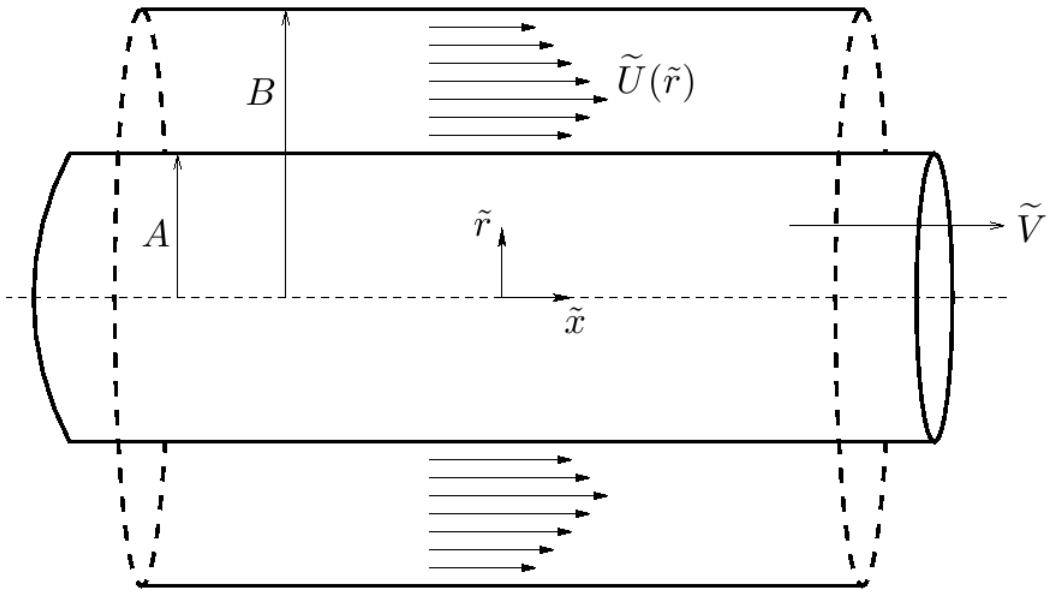

Figure 2.1: Flow geometry with dimensional quantities labelled.

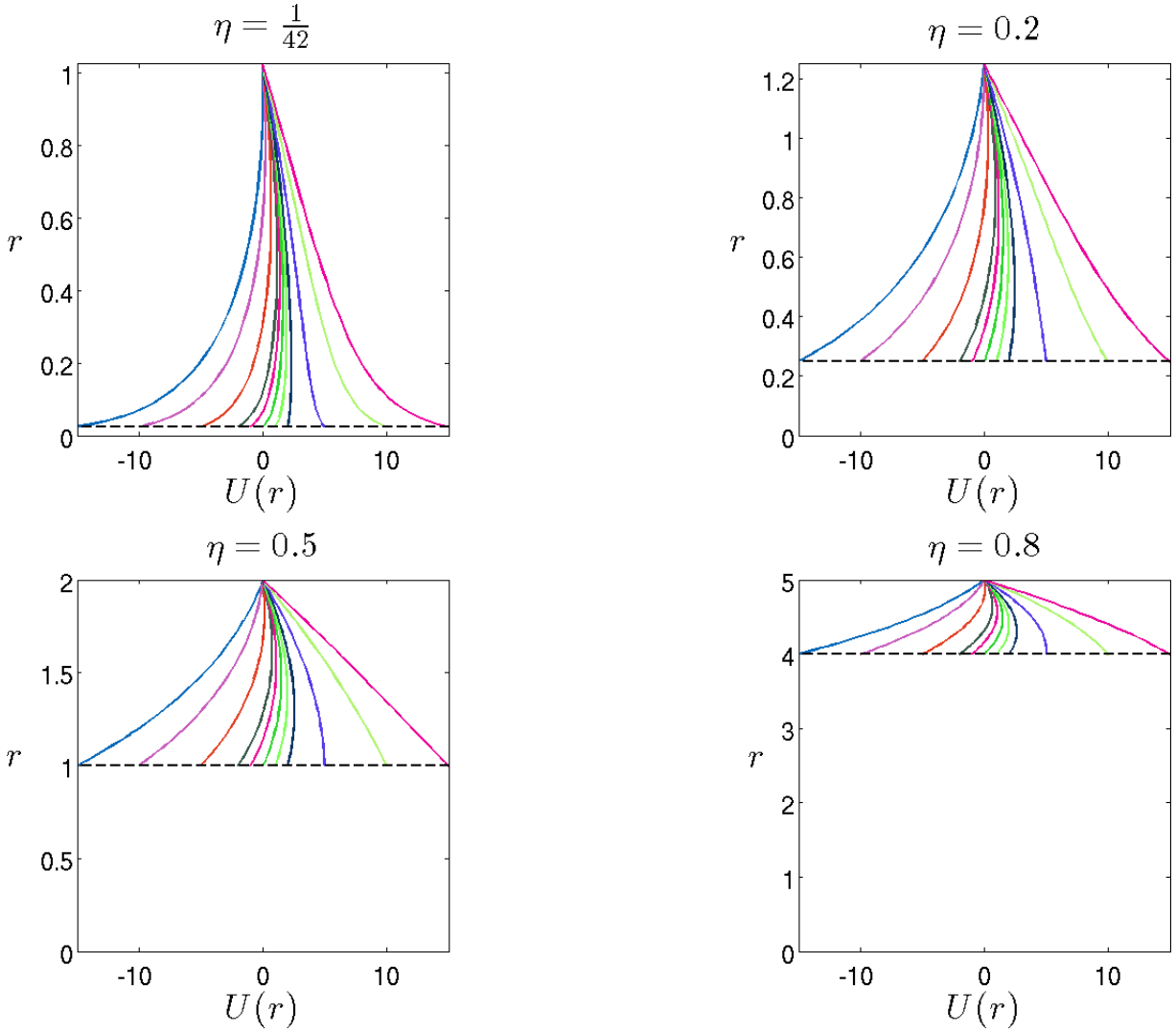

Figure 2.2: Base flow profiles in r for the radius ratios $\eta = \frac{1}{42}, 0.2, 0.5, 0.8$. $U(r)$ with $V = -15, -10, -5, -2, -1, 0, 1, 2, 5, 10, 15$ is plotted for each radius ratio. The black dashed line in each Figure marks the inner cylinder boundary $r = \frac{\eta}{1-\eta}$.

2.1.1 Alternative non-dimensionalizations

Our choice of non-dimensionalization is not unique; various alternative characteristic length scales and velocities have been used by previous authors studying APCF. In the experiments of Shands *et al.* (1980) and Frei *et al.* (2000), lengths and velocities are non-dimensionalized by the hydraulic diameter, $D = 2(B - A)$, and the total mean flow velocity

$$\widehat{U} = \frac{1}{A_c} \int_{A_c} \widetilde{U}_p + \widetilde{U}_c \, dS = \overline{U} + \overline{V}, \tag{2.9a}$$

$$= \frac{\Delta p}{8\mu L \log \frac{B}{A}} \left(B^2 - A^2 - (B^2 + A^2) \log \frac{B}{A} \right) + \widetilde{V} \left(\frac{B^2 - A^2 - 2A^2 \log \frac{B}{A}}{2(B^2 - A^2) \log \frac{B}{A}} \right). \tag{2.9b}$$

The Reynolds number $\widehat{Re}$ and non-dimensional inner cylinder velocity $\widehat{V}$, defined in terms of D and $\widehat{U}$, are

$$\widehat{Re} = \frac{\widehat{U}D}{\nu}, \qquad \widehat{V} = \frac{\widetilde{V}}{\widehat{U}}, \tag{2.10}$$

where ν is the kinematic viscosity of the fluid as before. In order to convert from the experimental quantities to ours, we first note that,

$$\overline{V} = \widetilde{V}\left(\frac{\eta^2 - 1 - 2\eta^2 \log \eta}{2(1-\eta^2)\log \eta}\right). \tag{2.11}$$

After some straightforward manipulations we derive the following relations for Re and V in terms of $\widehat{Re}$ and $\widehat{V}$

$$Re = \frac{\widehat{Re}}{2}\left\{1 - \widehat{V}\left(\frac{\eta^2 - 1 - 2\eta^2 \log \eta}{2(1-\eta^2)\log \eta}\right)\right\}, \tag{2.12a}$$

$$V = \frac{2\widehat{V}(1-\eta^2)\log \eta}{2(1-\eta^2)\log \eta - (\eta^2 - 1 - 2\eta^2 \log \eta)\widehat{V}}. \tag{2.12b}$$

In the theoretical works of Walton (2003, 2004, 2005) the outer cylinder radius, B, is used as the length scale and velocities are non-dimensionalized using the pressure driven velocity $U_w = \frac{\Delta p B^2}{4\mu L}$. Hence Walton's parameters, Re_w V_w and k_w are related to ours through

$$Re = \frac{1-\eta}{f(\eta)} Re_w, \tag{2.13a}$$

$$V = f(\eta) V_w, \tag{2.13b}$$

$$k = (1-\eta) k_w, \tag{2.13c}$$

where we define

$$f(\eta) = \frac{2\log \eta}{1 - \eta^2 + (1+\eta^2)\log \eta}. \tag{2.13d}$$

Further conversion is needed for comparison with the results of Sadeghi & Higgins (1991), who chose the maximum pressure driven velocity, $\max_{\tilde{r}} \widetilde{U}_p$, and cylinder half-gap, $\frac{B-A}{2}$, as their characteristic quantities

$$Re = \frac{2}{f(\eta)g(\eta)} Re_{sh}, \tag{2.14a}$$

$$V = f(\eta)g(\eta) V_{sh}, \tag{2.14b}$$

$$k = 2k_{sh}, \tag{2.14c}$$

where $f(\eta)$ is defined as before, and

$$g(\eta) = \eta^2 + \frac{1-\eta^2}{2\log\eta}\left(1 - \log\left(\frac{\eta^2-1}{2\eta^2\log\eta}\right)\right). \tag{2.14d}$$

2.1.2 Thread-annular flow

A pertinent physical application of APCF is in thread-annular flow, which is a model for a medical injection procedure involving insertion of an implant into a body in a minimally invasive manner. In the procedure, a thread is surrounded by a fluid and stored on a spool within a container with a long cylindrical outlet. It is then inserted into the desired location by pressurizing the fluid such that the thread travels along the cylindrical section of the container before entering the body. More details on the technique can be found in Frei *et al.* (2000). A crude mathematical model for the dynamics of the procedure is a system of pressure-driven fluid constrained to move in the gap between concentric cylinders with a sliding inner cylinder. Thread-annular flow can be considered a specific case of APCF, where the inner cylinder is not independently driven, but free to slide. A maximum inner cylinder velocity can be derived for the thread-annulus problem, by balacing the pressure-driven forces on the inner cylinder with the resistive action of the shear. Assuming the fluid to be in the laminar solution (2.5), the non-dimensionalized resistive shear force F_τ acting on the inner cylinder over a length ℓ is

$$F_\tau = \frac{2\pi\eta\ell\, Re}{1-\eta}\left(\frac{dU}{dr}\right)\bigg|_{r=\frac{\eta}{1-\eta}} = 2\pi\ell Re\left\{\frac{V}{\log\eta} - \left(\frac{4\eta^2\log\eta + 2(1-\eta^2)}{1-\eta^2+(1+\eta^2)\log\eta}\right)\right\}. \tag{2.15}$$

The non-dimensionalized force on the inner cylinder due to the pressure gradient across the annular gap is

$$F_p = -\pi\ell\left(\frac{\eta}{1-\eta}\right)^2\frac{dP}{dx} = \pi\ell Re\left(\frac{8\eta^2\log\eta}{1-\eta^2+(1+\eta^2)\log\eta}\right) \tag{2.16}$$

The total resistive force on the inner cylinder is then $F_r = F_p + F_\tau$. When F_r is zero, the thread reaches its maximum velocity

$$V_{max} = \frac{2(1-\eta^2)\log\eta}{1-\eta^2+(1+\eta^2)\log\eta}. \tag{2.17}$$

2.2 Linear stability

By modification of the Rayleigh inflection point criterion to account for cylindrical geometry, we investigate whether APCF is linearly stable to inviscid perturbations. We begin with the Rayleigh equation in cylindrical coordinates

$$(U-c)\left(\frac{\phi}{r}-\left(\frac{\phi'}{\kappa r}\right)'\right)-\left(\frac{U'}{\kappa r}\right)'\phi=0, \tag{2.18}$$

where $\phi = rv$, $\kappa = k^2 + \frac{m^2}{r^2}$ and $c = \frac{-\mathrm{i}\omega}{k}$ in our notation. Multiplication of (2.18) by the factor $(\frac{\phi^*}{U-c})$, where ϕ^* is the complex conjugate of the potential ϕ, and integrating over the annular gap gives

$$\int_{\frac{\eta}{1-\eta}}^{\frac{1}{1-\eta}}\frac{\phi\phi^*}{r}-\left(\frac{\phi'}{\kappa r}\right)'\phi^* dr-\int_{\frac{\eta}{1-\eta}}^{\frac{1}{1-\eta}}\left(\frac{U'}{\kappa r}\right)'\frac{\phi\phi^*}{U-c}\,dr=0. \tag{2.19}$$

Integration by parts of the integral on the left gives

$$\int_{\frac{\eta}{1-\eta}}^{\frac{1}{1-\eta}}\frac{|\phi|^2}{r}+\frac{|\phi'|^2}{\kappa r}dr-\int_{\frac{\eta}{1-\eta}}^{\frac{1}{1-\eta}}\left(\frac{U'}{\kappa r}\right)'\frac{|\phi|^2}{U-c}\,dr=0. \tag{2.20}$$

The integral on the left is strictly positive and real. The second integral is complex valued, and with c_i denoting the imaginary part of the complex wavespeed c, we express the imaginary part of the second integral as

$$c_i\int_{\frac{\eta}{1-\eta}}^{\frac{1}{1-\eta}}\left(\frac{U'}{\kappa r}\right)'\frac{|\phi|^2}{|U-c|^2}dr=0. \tag{2.21}$$

Since $\frac{|\phi|^2}{|U-c|^2}$ is strictly positive, in order for the integral to be satisfied for $c_i > 0$ the factor $(\frac{U'}{\kappa r})'$ must change sign somewhere in the interval $\frac{\eta}{1-\eta} \le r \le \frac{1}{1-\eta}$. However, for the base flow (2.5), we have

$$\left(\frac{U'}{\kappa r}\right)'=\frac{2(2Pm^2-Qk^2)r}{(k^2r^2+m^2)^2}, \tag{2.22}$$

with the constants P and Q given by

$$P=-\frac{2(1-\eta)^2\log\eta}{1-\eta^2+(1+\eta^2)\log\eta} \tag{2.23}$$

$$Q=\frac{V}{\log\eta}-\frac{2(1-\eta^2)}{1-\eta^2+(1+\eta^2)\log\eta}. \tag{2.24}$$

Provided $2Pm^2 - Qk^2 \neq 0$, $(\frac{U'}{\kappa r})'$ cannot change sign in the interval $\frac{\eta}{1-\eta} \le r \le \frac{1}{1-\eta}$, implying $c_i = 0$ in order for expression (2.21) to be satisfied. Therefore, the Rayleigh stability criterion only tells us that the base flow is linearly stable to inviscid waves

whenever $2Pm^2 - Qk^2 \neq 0$. However, since the Rayleigh argument is only a necessary condition for instability, we cannot deduce that the flow is unstable if $2Pm^2 - Qk^2 = 0$. In order for $2Pm^2 - Qk^2 = 0$ to be satisfied, P and Q must have opposite sign. Since $0 < \eta < 1$, P is strictly positive. Therefore we require $Q < 0$, which implies

$$V > V^* = \frac{2(1-\eta^2)\log\eta}{1-\eta^2+(1+\eta^2)\log\eta}. \tag{2.25}$$

Here V^* is precisely the maximum inner cylinder velocity V_{max} achieveable in thread-annular flow, meaning that thread-annular flow is always stable to inviscid waves.

Viscous waves can de-stabilize APCF and we numerically determine these instabilities by solving the linear system (2.7) for $\omega \in \mathbb{C}$, using the Chebyshev collocation technique outlined in Schmid & Henningson (2001). Typically, the collocation technique uses Chebyshev polynomials of the first kind, T_n, to approximate functions of the non-periodic coordinate ξ, say, at discrete locations ξ_j called Gauss-Lobatto grid points

$$\xi_j = \cos\left(\frac{(j-1)\pi}{N-1}\right), \qquad f(\xi_j) = \sum_{n=1}^{N-1} a_n T_{n-1}(\xi_j), \qquad j = 1, 2, \ldots, N. \tag{2.26}$$

Since the Gauss-Lobatto points lie between $-1 \leq \xi_j \leq 1$, we map from the annular gap $r \in [\frac{\eta}{1-\eta}, \frac{1}{1-\eta}]$ to $\xi \in [-1, 1]$ using

$$r_j = \frac{1}{2}\left(\frac{1+\eta}{1-\eta} - \xi_j\right), \qquad \frac{\eta}{1-\eta} \leq r_j \leq \frac{1}{1-\eta}. \tag{2.27}$$

With derivatives of the dependent variables represented by Chebyshev differentiation matrices, this discretization allows us to solve the generalized $4N \times 4N$ eigenvalue problem

$$\mathcal{L}\hat{\boldsymbol{q}}_\ell = \omega_\ell \mathcal{M}\hat{\boldsymbol{q}}_{\boldsymbol{\ell}}, \tag{2.28}$$

for ω_ℓ and $\hat{\boldsymbol{q}}_\ell = (u_\ell, v_\ell, w_\ell, p_\ell)$, where the operators A and B are given by

$$\mathcal{L} = \begin{pmatrix} \chi + \frac{1}{Re}\frac{1}{r^2} & -\frac{dU}{dr} & 0 & -\mathrm{i}k \\ 0 & \chi & -\frac{1}{Re}\frac{2\mathrm{i}m}{r^2} & -\frac{d}{dr} \\ 0 & \frac{1}{Re}\frac{2\mathrm{i}m}{r^2} & \chi & -\frac{\mathrm{i}m}{r} \\ \mathrm{i}k & \frac{d}{dr} + \frac{1}{r} & \frac{\mathrm{i}m}{r} & 0 \end{pmatrix}, \tag{2.29}$$

$$\mathcal{M} = \begin{pmatrix} 1 & 0 & 0 & 0 \\ 0 & 1 & 0 & 0 \\ 0 & 0 & 1 & 0 \\ 0 & 0 & 0 & 0 \end{pmatrix}, \tag{2.30}$$

and we have defined

$$\chi = \frac{1}{Re}\left(\frac{d^2}{dr^2} + \frac{1}{r}\frac{d}{dr} - \left(\frac{1+m^2}{r^2} + k^2\right)\right) - \mathrm{i}kU. \tag{2.31}$$

Our solutions to the linear stability equations are found by numerical computation of the full spectrum using the eigenproblem routines in MATLAB. A number of spurious modes are found by solving the system in this way. We guard against spurious modes entering our calculations in the following way: the rows of $\mathcal{L}$ which are modified to enforce the no-slip boundary condition on the cylinder walls are multiplied by an arbitrary constant A. Therefore the equation for u at the inner wall, for example, becomes

$$Au_\ell|_{r=\frac{\eta}{1-\eta}} = \omega_\ell u_\ell|_{r=\frac{\eta}{1-\eta}}. \tag{2.32}$$

This forces spurious eigenvalues to take the value $\omega_s = A$, and by choosing an appropriate A we can ensure spurious modes are kept out of our calculations. Having arrived at a set of modes, we list the eigenvalues in terms of decreasing real part, $\omega_1, \omega_2, \ldots, \omega_\ell, \ldots$, such that the primary mode corresponds to the least stable. In Figure 2.3 we plot the eigenvalue spectra for the case $(k, m, \eta, Re) = (1, 1, 0.5, 2000)$, at various inner cylinder velocities V.

We use the computations of Walton (2005) to validate our numerical routines, as their paper includes calculations of neutral curves for radius ratio $\eta = 0.4$, over various azimuthal wavenumbers and inner cylinder velocities. Using a bisection technique, we calculate the corrsponding neutral curves using our non-dimensionalization, and compare them with Walton's results. In Figure 2.4 we compare our calculations with those of Walton (2005) by re-printing Figure 4(a) from Walton's paper alongside our own computations re-scaled to the variables used by Walton. We find good agreement between our results and those of Walton, with little noticeable difference between the curves.

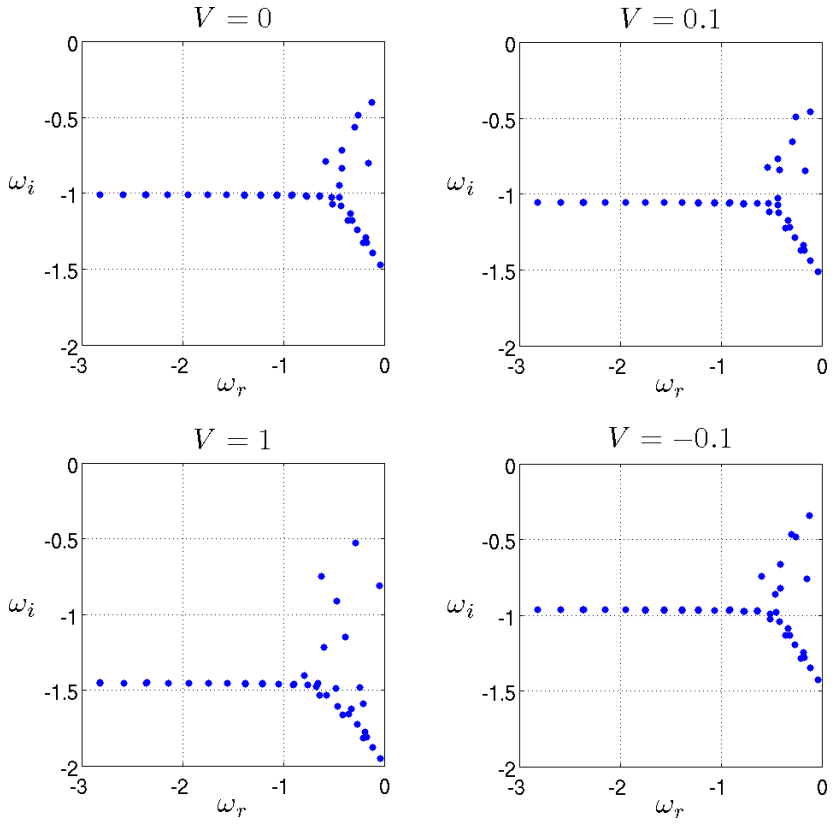

Figure 2.3: Complex eigenvalues ω_ℓ of the linear stability equations for $(k, m, \eta, Re) = (1, 1, 0.5, 2000)$ at the inner cylinder velocities $V = 0, 0.1, 1, -0.1$ as indicated.

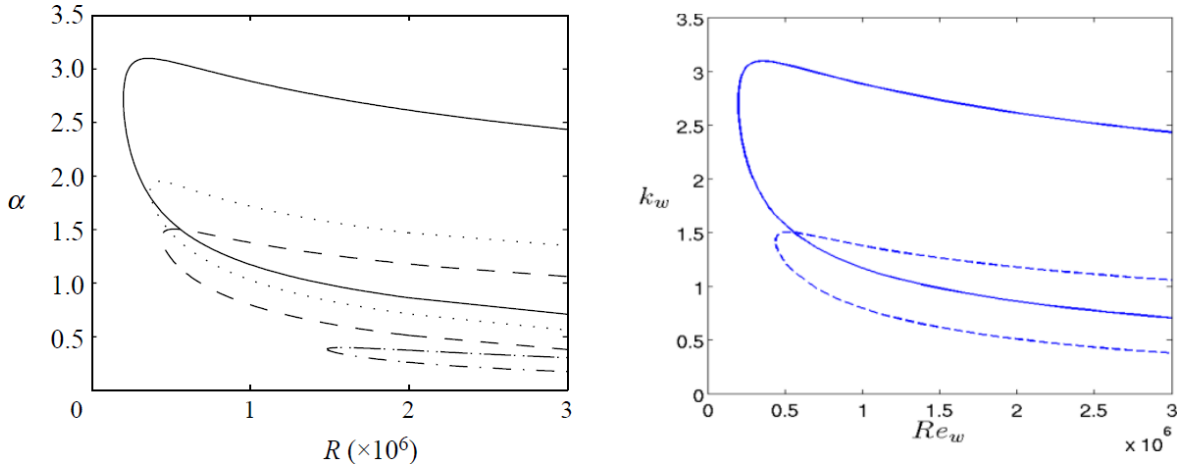

Figure 2.4: On the left we re-print Walton's neutral curves for $\eta = 0.4$, $m = 1$ and $V = 0$ (solid), $V = 0.015$ (dotted), $V = 0.03$ (dashed) and $V = 0.1$ (dot-dashed). The axial wavenumber in Walton's paper is denoted α. On the right we plot our calculations re-scaled to Walton's quantities, with $V_w = 0$ (solid) and $V_w = 0.03$ (dashed).

Further to the (Re, k) curves, we compute neutral curves in the (Re, V)-parameter space by maximizing unstable growth rates over axial wavenumber k for fixed azimuthal wavenumber m. In particular we plot neutral curves for the radius ratios considered in §2.4: $\eta = 0.2, 0.5, 0.8$. We could not find any linearly unstable modes for $Re \leq 10^5$ when $\eta = \frac{1}{42}$. Our results are shown in Figures 2.5, 2.6 and 2.7. In each Figure, we plot neutral curves at the least stable azimuthal orders for $Re < 10^5$. Across all radius ratios, $|V| \gtrsim 1$ is stablizing, as the critical Re is pushed higher than its $V = 0$ value. V small and negative is de-stabilizing in the cases $\eta = 0.2$ and $\eta = 0.5$, as shown in Figures 2.5 and 2.6. From Figure 2.7 we see that small positive V is de-stabilizing for $\eta = 0.8$. We find the lowest critical (Re, V) combination when $\eta = 0.2$ for $(Re, V) = (6441, -0.15)$. Walton (2005) reports disconnected neutral axisymmetric neutral curves; our calculations are in agreement with this, though our results do not include Re large enough to support disconnected axisymmetric neutral curves. Walton additionally mentions that they do not find disconnected non-axisymmetric neutral curves. Our calculations support this conclusion, however, we find that the $m = 1$ neutral curve for $\eta = 0.5$, and all neutral curves for $\eta = 0.8$ are scalloped, with three local turning points in (Re, V), for $V < 0$, $V \approx 0$ and $V > 0$. Sadeghi & Higgins (1991) found asymptotic cutoff velocities for $0.5 < \eta < 1$ for axisymmetric and non-axisymmetric modes and positive inner cylinder velocities, adapting the methods used by Cowley & Smith (1985) for planar Poiseuille-Couette flow. In Figure 2.6 we plot the cutoff velocities for $\eta = 0.5$, as listed in their paper, alongside our neutral curves. Our computations are consisent with their asymptotic findings.

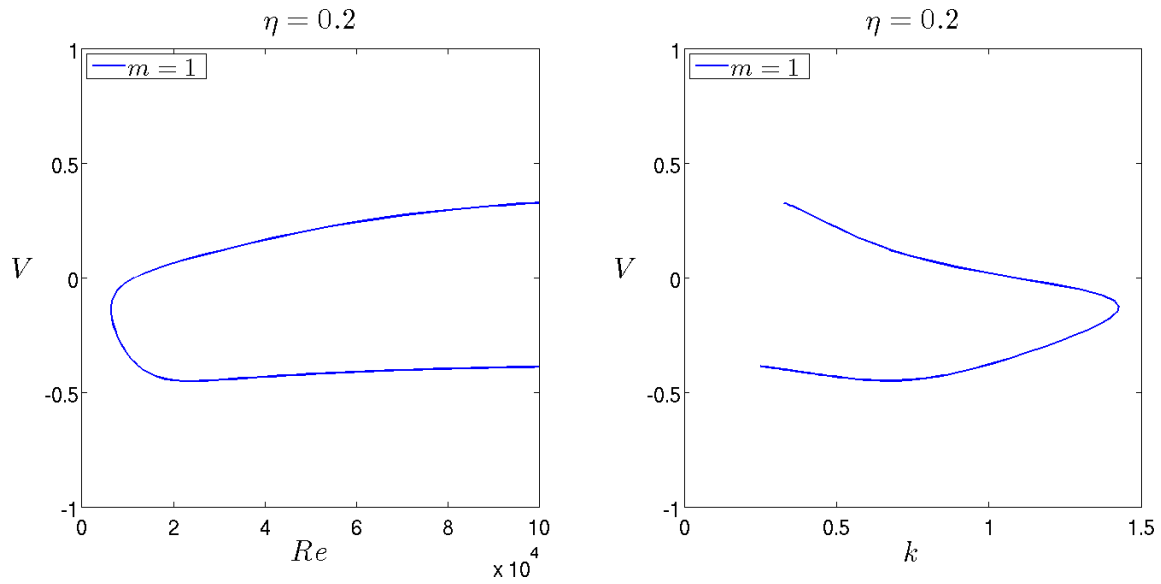

Figure 2.5: Left: Neutral curves in (Re, V) at azimuthal order $m = 1$ and radius ratio $\eta = 0.2$. Right: Critical axial wavenumbers k corresponding to the neutral modes in the left panel.

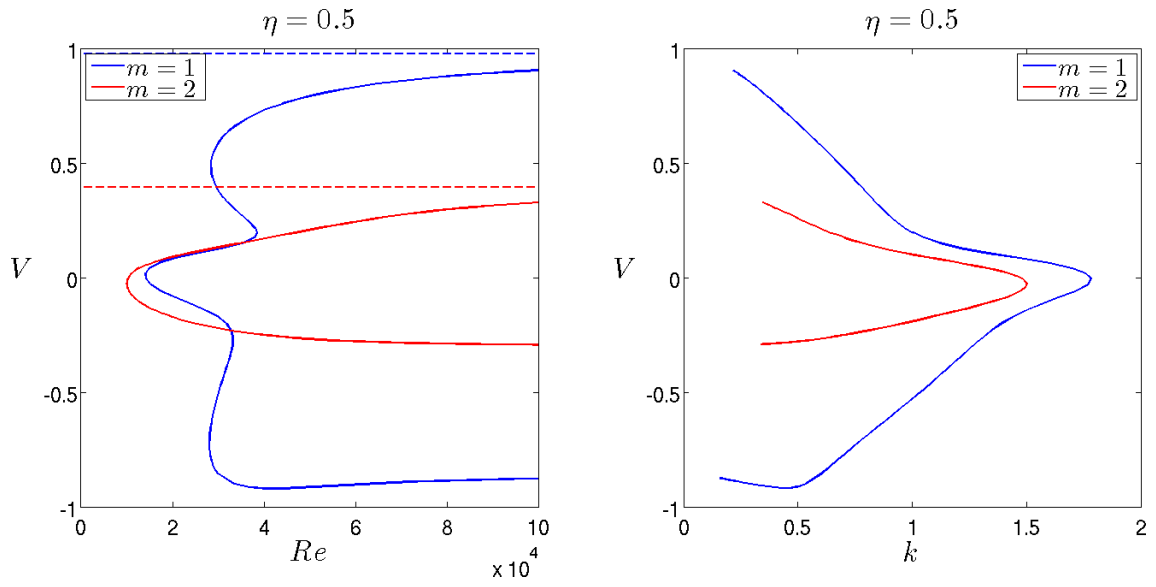

Figure 2.6: Left: Neutral curves in (Re, V) at azimuthal orders $m = 1, 2$ and radius ratio $\eta = 0.5$. The dashed lines indicate the cutoff velocities derived by Sadeghi & Higgins (1991). Right: Critical axial wavenumbers k corresponding to the neutral modes in the left panel.

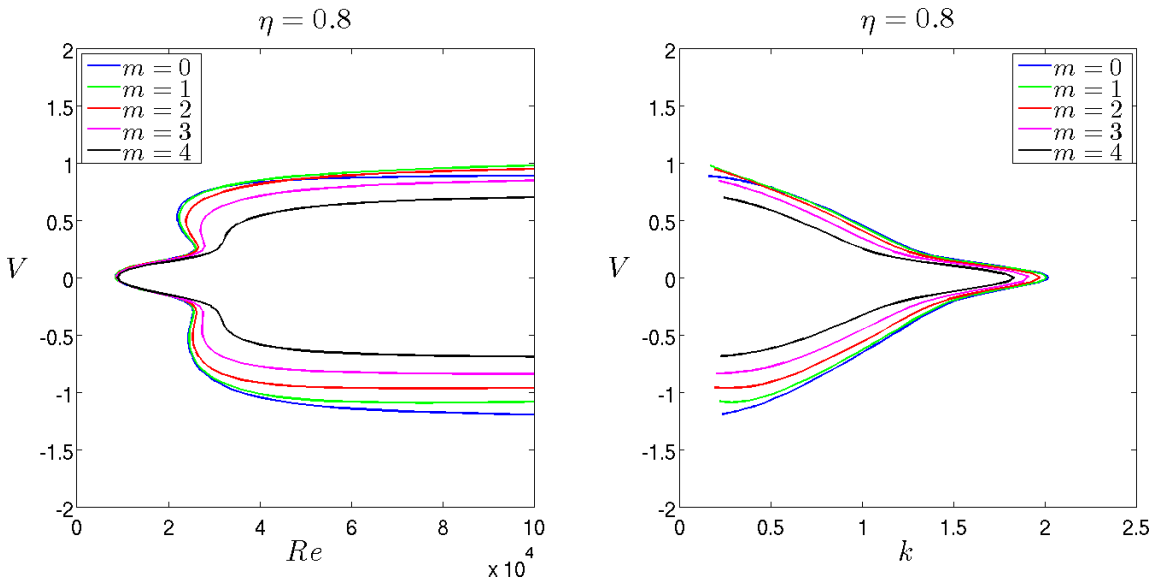

Figure 2.7: Left: Neutral curves in (Re, V) at azimuthal orders $m = 0, 1, 2, 3, 4$ and radius ratio $\eta = 0.8$. Right: Critical axial wavenumbers k corresponding to the neutral modes in the left panel.

2.3 Non-modal growth

Our solutions to the linear stability equations are used to compute the non-modal energy growth in APCF. We solve for $\omega_\ell \in \mathbb{C}$ and vector $\hat{\boldsymbol{q}}_\ell = (\hat{\boldsymbol{u}}_\ell, \hat{p}_\ell)$ satisfying the linear system (2.28)

$$\mathcal{L}\hat{\boldsymbol{q}}_\ell = \omega_\ell \mathcal{M}\hat{\boldsymbol{q}}_\ell. \tag{2.33}$$

An arbitrary velocity disturbance can be expanded in terms of the first L modes of the stability equations

$$\boldsymbol{u}(x, r, \theta, t) = \mathrm{e}^{\mathrm{i}(kx+m\theta)} \sum_{\ell=1}^{L} a_\ell \hat{\boldsymbol{u}}_\ell(r) \mathrm{e}^{\omega_\ell t}, \tag{2.34}$$

for $a_\ell \in \mathbb{C}$. We then introduce the norm

$$E(t) = \|\boldsymbol{u}(t)\|^2 = \int_{\frac{\eta}{1-\eta}}^{\frac{1}{1-\eta}} \boldsymbol{u}^H \boldsymbol{u}\, r dr, \tag{2.35}$$

which is related to the physical kinetic energy of the fluid, $\widetilde{E}$, in the periodic domain $[0, \frac{2\pi}{k}] \times [\frac{\eta}{1-\eta}, \frac{1}{1-\eta}] \times [0, \frac{2\pi}{m}]$ by the relation

$$E = \frac{mk\widetilde{E}}{2\rho\pi^2}, \tag{2.36}$$

where ρ is the constant fluid density. For $\hat{a} = (a_1, a_2, \ldots, a_L)$ and $\Lambda = \mathrm{diag}(\omega_1, \omega_2, \ldots, \omega_L)$, $E(t)$ can be written

$$E(t) = \hat{a}^H \mathrm{e}^{\Lambda^H t} M \mathrm{e}^{\Lambda t} \hat{a}, \tag{2.37}$$

where $\mathrm{e}^{\Lambda t}$ is the matrix exponential of Λt, and M is the $L \times L$ matrix

$$M_{jk} = \int_{\frac{\eta}{1-\eta}}^{\frac{1}{1-\eta}} \hat{\boldsymbol{u}}_k^H \hat{\boldsymbol{u}}_j\, r dr. \tag{2.38}$$

M is both Hermitian ($M = M^H$) and positive definite. Since M is Hermitian, its singular value decomposition can be written

$$M = U_M \Sigma_M U_M^H, \tag{2.39}$$

where $\Sigma_M = \mathrm{diag}(\sigma_1, \sigma_2, \ldots, \sigma_L)$ is a diagonal matrix of the singular values of M in descending order $\sigma_1 > \sigma_2 > \ldots > \sigma_L$, and U_M is a unitary matrix. For $\sqrt{\Sigma_M} = \mathrm{diag}(\sqrt{\sigma_1}, \sqrt{\sigma_2}, \ldots, \sqrt{\sigma_L})$ we have

$$F = U_M \sqrt{\Sigma_M}, \tag{2.40}$$

which allows us to factor M into $M = F^H F$. Hence, we have

$$\|\boldsymbol{u}(t)\|^2 = \hat{a}^H \mathrm{e}^{\Lambda^H t} F^H F \mathrm{e}^{\Lambda t} \hat{a} = \|F\mathrm{e}^{\Lambda t}\hat{a}\|_2^2, \tag{2.41}$$

where $\|.\|_2$ is the Euclidean 2-norm. The maximum energy amplification G is simply

$$G(t) = \max_{\boldsymbol{u}_0 \neq 0} \frac{E(t)}{E(0)} = \max_{\boldsymbol{u}_0 \neq 0} \frac{\|\boldsymbol{u}(t)\|^2}{\|\boldsymbol{u}_0\|^2}, \tag{2.42}$$

$$= \max_{\hat{a} \neq 0} \frac{\|F\mathrm{e}^{\Lambda t}\hat{a}\|_2^2}{\|F\hat{a}\|_2^2}, \tag{2.43}$$

$$= \max_{\hat{a} \neq 0} \frac{\|F\mathrm{e}^{\Lambda t}F^{-1}F\hat{a}\|_2^2}{\|F\hat{a}\|_2^2}, \tag{2.44}$$

$$= \|F\mathrm{e}^{\Lambda t}F^{-1}\|_2^2. \tag{2.45}$$

$G(0) = 1$ by definition. Linear non-modal energy growth is supported in a flow if $G(t) > 1$ for any non-zero t. $G(t)$ represents the maximum possible energy amplification at time t of an initial perturbation, though different initial perturbations will be responsible for maximum growth at distinct times. Suppose, having found the maximum energy amplification achieveable at time t_m, we wish to find the form of the optimal initial perturbation and also its form at t_m. Let $\boldsymbol{u}_0$ denote the optimal perturbation, with

$$\boldsymbol{u}_0 = \mathrm{e}^{\mathrm{i}(kx+m\theta)} \sum_{\ell=1}^{L} a_\ell \hat{\boldsymbol{u}}_\ell, \quad \text{and} \quad \|\boldsymbol{u}_0\| = 1. \tag{2.46}$$

Then, since $\boldsymbol{u}_0$ will have energy $\|F\mathrm{e}^{\Lambda t_m}F^{-1}\|_2^2$ at t_m, we have

$$B\hat{a} = \|F\mathrm{e}^{\Lambda t_m}F^{-1}\|_2 \hat{a}\mathrm{e}^{\Lambda t_m} = \mu\hat{a}\mathrm{e}^{\Lambda t_m}, \tag{2.47}$$

where $B = F\mathrm{e}^{\Lambda t_m}F^{-1}$. The constant $\mu = \|F\mathrm{e}^{\Lambda t_m}F^{-1}\|_2$ is simply the principal singular value of B. The singular value decomposition of B allows us to write

$$BV_B = U_B\Sigma_B, \tag{2.48}$$

for unitary matrices V_B and U_B, and the matrix of singular values of B, $\Sigma_B = \mathrm{diag}(\sigma_1, \sigma_2, \ldots, \sigma_L)$. If we denote the principal eigenvectors of V_B and U_B as v_1 and u_1, respectively, then since $\mu = \sigma_1$ we have

$$Bv_1 = \sigma_1 u_1, \tag{2.49}$$

from which we can identify $\hat{a} = v_1$. The linear optimal $\boldsymbol{u}_0$ can then be found by expanding $\hat{a}$ over the basis vectors $\hat{\boldsymbol{u}}_1 \ldots \hat{\boldsymbol{u}}_L$. The optimal at time t_m is found by simply expanding $\hat{a}$ over the vectors $\hat{\boldsymbol{u}}_1\mathrm{e}^{\omega_1 t_m} \ldots \hat{\boldsymbol{u}}_L\mathrm{e}^{\omega_L t_m}$

Given that the gain $G = G(t, k, m, \eta, Re, V)$ is a six parameter function, we introduce two maxima which allow us to represent the level of non-modal growth possible for a perturbation at a fixed Reynolds number, inner cylinder velocity and radius ratio. First, we maximize G over time

$$G_{max}(k, m, \eta, Re, V) = \max_t G(t, k, m, \eta, Re, V) = G(t_{max}, k, m, \eta, Re, V). \tag{2.50}$$

G_{max} represents the greatest linear energy amplification that a perturbation with prescribed wavenumbers can experience. We further maximize over the wavenumbers k and m to define

$$\mathbb{G}(\eta, Re, V) = \max_{k,m} G_{max}(k, m, \eta, Re, V) = G(T_{max}, k_{max}, m_{max}, \eta, Re, V), \tag{2.51}$$

such that $\mathbb{G}$ denotes the maximum linear energy growth possible for a given Re, V and η combination. k_{max}, m_{max} and T_{max} correspond to the axial wavenumber, azimuthal wavenumber and the amplification time of the perturbation responsible for the amplification $\mathbb{G}$. If $\mathbb{G} = 1$, then all perturbations are non-modally stable. We shall refer to the perturbation which achieves the maximum, *optimal*, growth $\mathbb{G}$ as the *linear optimal*. We use $\mathbb{G}$ as a measure of the non-modal stability of the flow, with large values of $\mathbb{G}$ interpreted as being de-stabilizing.

The MATLAB golden mean search `fminbnd` is used to find G_{max} and $\mathbb{G}$. Finding G_{max} requires a straightforward optimization over time; however, G may have local maxima, so we vary the time horizon at each step to increase the likelihood of finding G_{max}. Since the azimuthal wavenumber m is integer valued, we consider a range of m in turn, and use the golden mean search to maximize over axial wavenumber k to find $\mathbb{G}$. This is computationally more expensive than finding G_{max}, as a new spectrum of modes must be computed for each wavenumber combination (m, k). In order to reduce the number of wavenumber searches required to find $\mathbb{G}$, we assume that the optimal wavenumber m_{max} varies smoothly with Re, V and η. To check against this assumption, we perform random spotchecks of G_{max} over a wider range of wavenumbers than typically considered with Re, V and η fixed.

2.4 Optimal growth in APCF

We begin our analysis of non-modal growth by plotting curves of G_{max} in the (Re, k)-plane, to investigate how transients interact with linearly unstable modes. The results in Figure 2.8 show that, while changes in V have a significant effect on the linearly unstable region, there is little qualitative effect on the transient behaviour. The curves of G_{max} approach the unstable boundary smoothly, as illustrated in Figure 2.9.

Isolines of $\mathbb{G}$ in (Re, V)-space are presented in Figure 2.10 at the radius ratios $\eta = \frac{1}{42}, 0.2, 0.5, 0.8$. Each plot is generated from a grid of 31×115 grid-points in (Re, V). The radius ratio $\eta = \frac{1}{42} \approx 0.0238$ was chosen to coincide with the ratio considered by Shands *et al.* (1980), for which there is experimental data on the transitional values of Re and V. We will make a comparison to this data in §2.5. The isolines are asymmetrical with respect to postive or negative inner cylinder velocity, with a turning point at slightly negative V. However, the asymmetry in V becomes less pronounced as η increases. The qualitative trend is that non-zero inner cylinder velocity has a *de-stabilizing* influence on the base flow as, aside from the small stabilizing region of $V < 0$, $\mathbb{G}$ is found to increase with $|V|$. This is in contrast to the modal linear stability results from §2.2, where a non-zero inner cylinder velocity has a stabilizing effect. The de-stabilizing trend is robust across all the radius ratios considered, with little change in the maximum energy growth achieved by each optimal. The thick red curves in Figure 2.10 are the energy stability boundaries, defined for V fixed to be the maximum Re for which $\mathbb{G} = 1$. We compute the energy stability boundary using a bisection method, for fixed V, to calculate the energy-critical Re to an accuracy of $\epsilon = 10^{-6}$. To the left of the energy stability curve, the energy of all disturbances is strictly monotically decaying. In parallel with results from the canonical shear flows, the Reynolds numbers on the energy stability boundary, Re_E are many orders of magnitude smaller than the critical Re from linear stability theory.

In Figure 2.11 we plot the optimal azimuthal wavenumbers m_{max} at each point in the (Re, V)-plane. These plots invariably look less well resolved than the contours of $\mathbb{G}$, but this is a consequence of the integer nature of m_{max}. The same grid is used in the calculation of both Figures. Typically m_{max} varies in unit steps, however for $\eta = \frac{1}{42}$ when $Re > 10^{3.5}$, m_{max} jumps from one to three as V increases from below to $V \approx -0.63$. m_{max} then falls back to two as V is increased further. This sequence is depicted for $Re = 10^4$ in Figure 2.12. We find that the values of m_{max} increase as the radius ratio η approaches unity. For $\eta = \frac{1}{42}$ we have $1 \leq m_{max} \leq 3$, whereas for $\eta = 0.8$ we find $13 \leq m_{max} \leq 19$. Lower azimuthal orders are selected when $|V|$ becomes large. The behaviour of k_{max} also changes for $|V|$ large: the optimals are axially independent for

small inner cylinder velocities, but weakly oblique disturbances are optimal for large $|V|$, as is shown in Figure 2.13. The scenario is reminiscient of planar flows, in that streamwise independent disturbances maximize growth for plane Poiseuille flow, whereas slightly oblique disturbances maximize the transient growth in plane Couette flow (Butler & Farrell (1992), Reddy & Henningson (1993)). We find that when k_{max} is non-zero, $k_{max} \propto Re^{-1}$ at fixed V. Examples of this relationship are displayed in Figure 2.14.

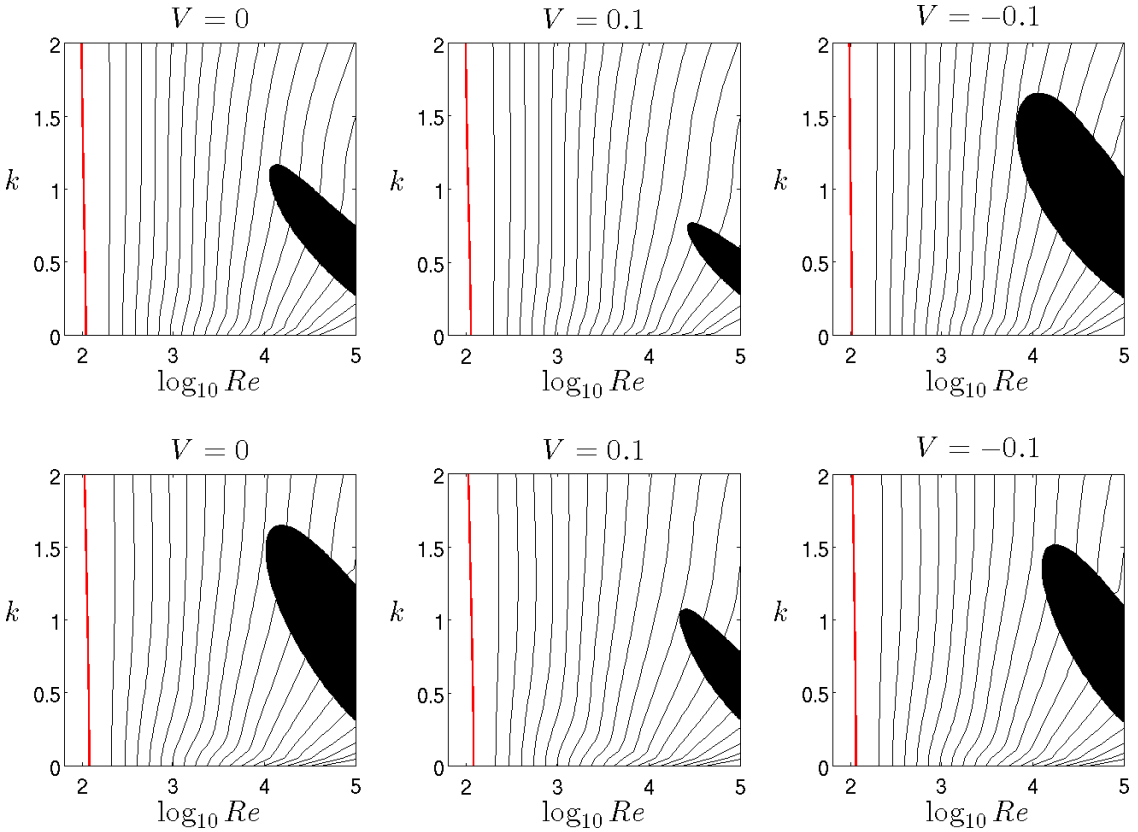

Figure 2.8: Contours of G_{max}. Top row: $\eta = 0.2$, $m = 1$. Bottom row: $\eta = 0.5$, $m = 2$. The red curves in each panel mark the energy stability boundary. The black curves are contours of G_{max}, from $\log_{10} G_{max} = 0.25, 0.5, \ldots, 4.5$. The black shaded region is linearly unstable.

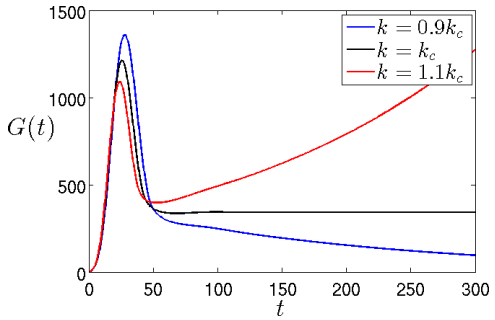

Figure 2.9: Gain curves showing the approach to the neutral curve. For $k > k_c$ G is unbounded in the limit $t \to \infty$. $(Re, V, \eta, m) = (10^{4.5}, 0, 0.5, 2)$, $k_c = 0.688$.

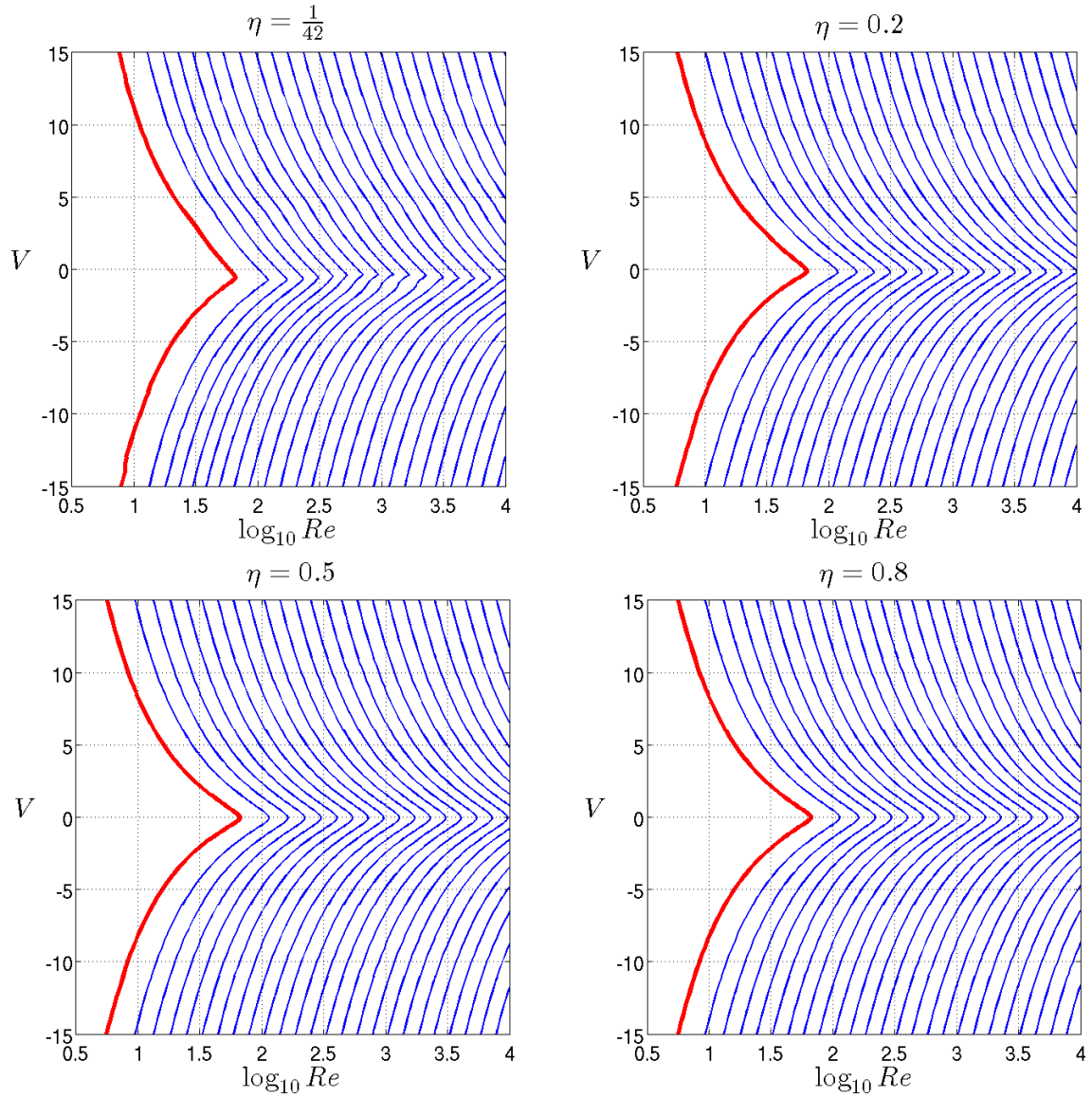

Figure 2.10: Contours of maximum linear optimal growth $\mathbb{G}$ in the (Re, V)-plane for radius ratios $\eta = \frac{1}{42}, 0.2, 0.5, 0.8$. The thick red curve demarcates the energy stability boundary. The blue curves are contours of $\log_{10} \mathbb{G} = 0.25, 0.5, 0.75, \ldots, 6$.

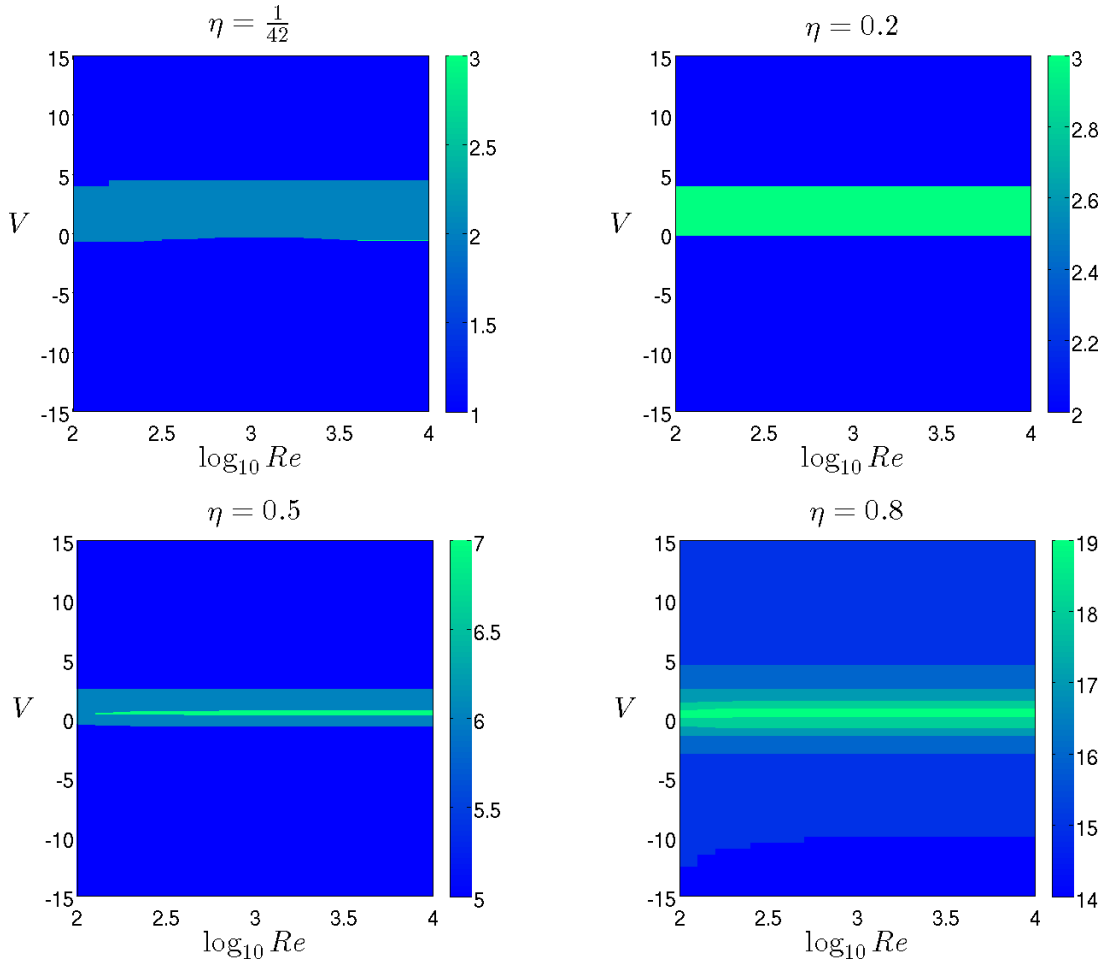

Figure 2.11: Colour-plots of azimuthal wavenumbers m_{max} corresponding to $\mathbb{G}$ in the (Re, V)-plane for radius ratios $\eta = \frac{1}{42}, 0.2, 0.5, 0.8$. For each η, m_{max} increases for $|V|$ small.

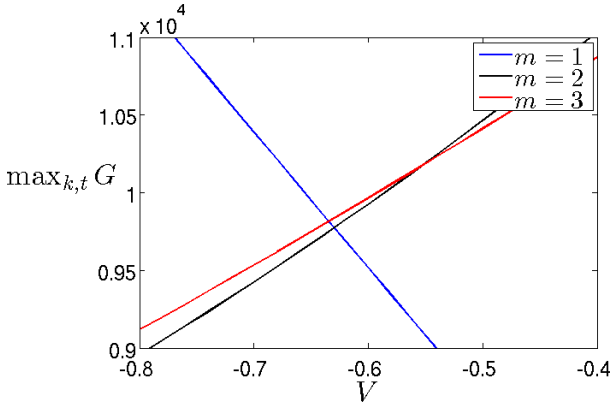

Figure 2.12: $\mathbb{G}$ for $(Re, \eta) = (10^4, \frac{1}{42})$ is the supremum of the intersection of the depicted curves. A non-unit change in m_{max} from one to three can be seen for $V \approx -0.63$.

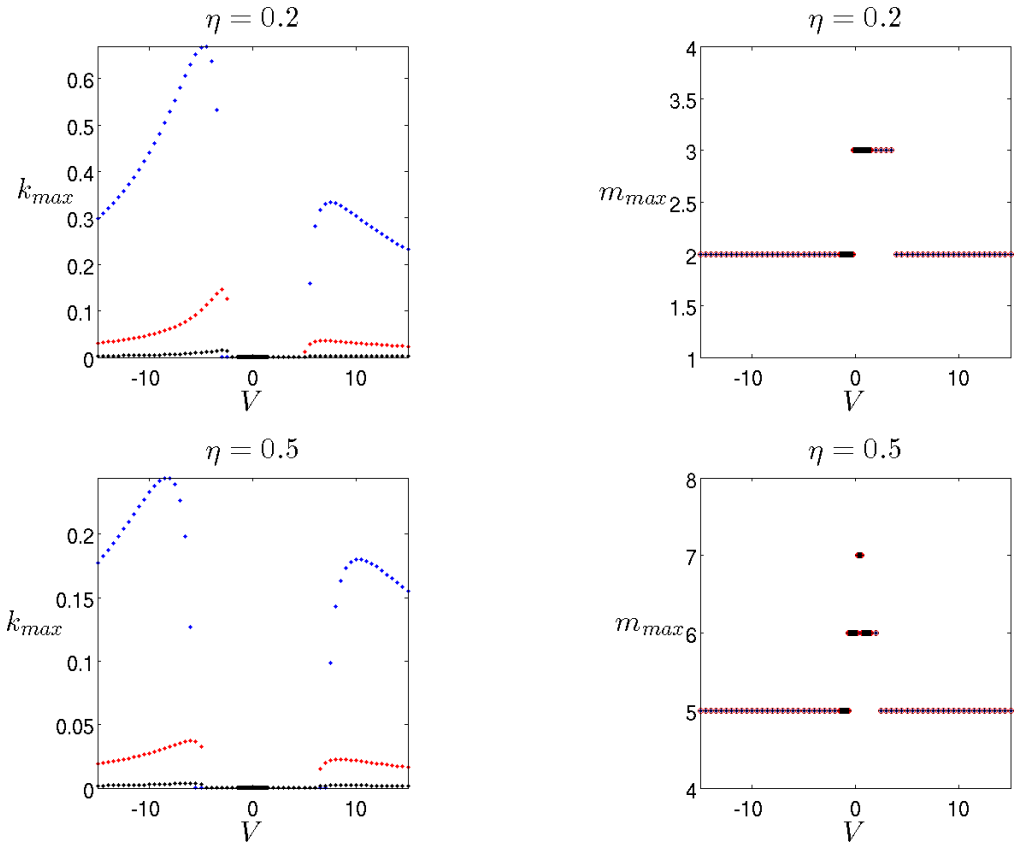

Figure 2.13: Optimal wavenumbers k_{max} and m_{max} against V, for $Re = 10^2$ (blue), $Re = 10^3$ (red) and $Re = 10^4$ (black), at the radius ratios $\eta = 0.2$ and $\eta = 0.5$. Non-zero axial wavenumbers are preferred for $|V|$ large, and m_{max} increases for $|V|$ small.

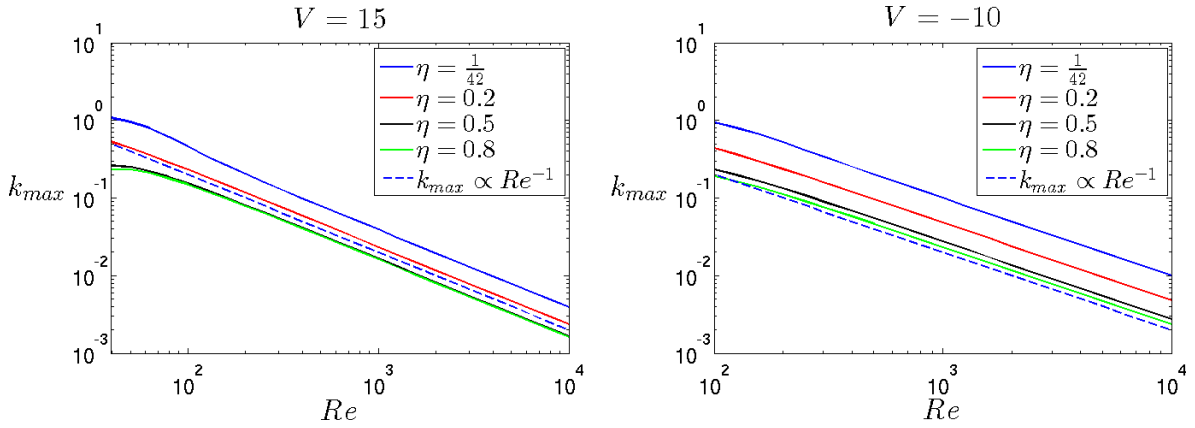

Figure 2.14: Where k_{max} is non-zero, it follows $k_{max} \propto Re^{-1}$ with V fixed.

2.4.1 Optimal perturbations and growth mechanism

We find that both the axially independent ($k_{max} = 0$) and the weakly oblique ($k_{max} \propto Re^{-1}$) optimals have energy gains that scale with the square of the Reynolds number $\mathbb{G} \propto Re^2$. In addition, we find that the time taken to reach the optimal, T_{max}, scales with the Reynolds number as $T_{max} \propto Re$. A typical example is plotted in Figure 2.15. These scalings are suggestive of energy amplification via the lift-up effect, a well-documented inviscid, algebraic growth mechanism (Landahl (1980)), that has been found to drive optimal growth in viscous planar flows (Gustavsson (1991), Butler & Farrell (1992), Reddy & Henningson (1993), Schmid & Henningson (2001), Chapman (2002)) and in Hagen-Poiseuille flow (Bergström (1993), Schmid & Henningson (1994)). Physically, the lift-up mechanism refers to extraction of energy from the mean flow as low-energy vortices are 'lifted-up' into high-energy streaks in the direction of the mean flow. Perturbations must be three-dimensional to experience this growth, as the mechanism involves wall-normal velocity interacting with the base flow in such a way that wall-normal vorticity is amplified.

To confirm that the lift-up mechanism is responsible for the energy growth of the optimals in APCF, we analyse the evolution of the energy fraction of an arbitrary optimal disturbance. The energy fractions are defined

$$E_u = \frac{\int_{\frac{\eta}{1-\eta}}^{\frac{1}{1-\eta}} u^* u \, r dr}{\int_{\frac{\eta}{1-\eta}}^{\frac{1}{1-\eta}} \boldsymbol{u}^H \boldsymbol{u} \, r dr}, \qquad E_v = \frac{\int_{\frac{\eta}{1-\eta}}^{\frac{1}{1-\eta}} v^* v \, r dr}{\int_{\frac{\eta}{1-\eta}}^{\frac{1}{1-\eta}} \boldsymbol{u}^H \boldsymbol{u} \, r dr}, \qquad E_w = \frac{\int_{\frac{\eta}{1-\eta}}^{\frac{1}{1-\eta}} w^* w \, r dr}{\int_{\frac{\eta}{1-\eta}}^{\frac{1}{1-\eta}} \boldsymbol{u}^H \boldsymbol{u} \, r dr}, \tag{2.52}$$

and can be calculated at an arbitrary time for a given velocity perturbation. We plot the evolution of the energy fractions for two optimals in Figure 2.16: one axially independent and one weakly oblique. We find that in each case energy is transferred to the axial velocity. We take this as confirmation of the lift-up effect being the amplification mechanism driving the transient growth. Combined with the results of Figure 2.10, a non-zero inner cylinder velocity can be interpreted as enhancing the lift-up mechanism by causing greater linear energy growth. In Figures 2.17, 2.18, 2.19 and 2.20 we plot cross-sectional velocity fields of a selection of optimal perturbations at $t = 0$ and $t = T_{max}$. Each Figure consists of a vector plot of the (v, w) velocity field and a colour-plot of the axial velocity u, with positive and negative velocities coloured red and blue respectively. In Figure 2.17 we observe a localization feature of the optimals whereby the streaks at T_{max} have moved towards the inner cylinder. We find this feature only to be present for small radius radio and in cases with large positive or negative inner cylinder velocity, The optimal in Figure 2.18 has an inner and outer streak layered structure, with the inner ring of streaks

strengthening between $t = 0$ and T_{max}. Our calculations suggest this structure is typical of the optimals with fixed or low velocity inner cylinder. As the radius ratio increases in Figures 2.19 and 2.20, the increase in azimuthal order is evident in the greater number of vortices and streaks in the optimal.

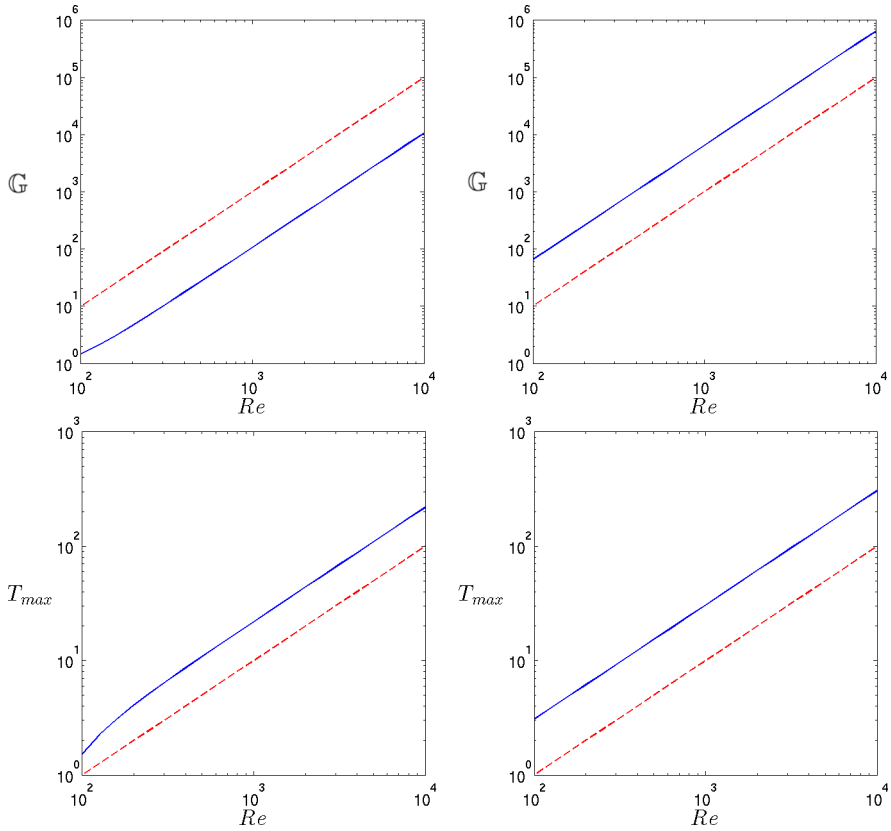

Figure 2.15: $\mathbb{G}$ and T_{max} against Re for radius ratio $\eta = 0.2$ and $V = 0$ (left) and $V = 10$ (right). The red dashed lines represent the asymptotic scalings $\mathbb{G} \propto Re^2$ and $T_{max} \propto Re$.

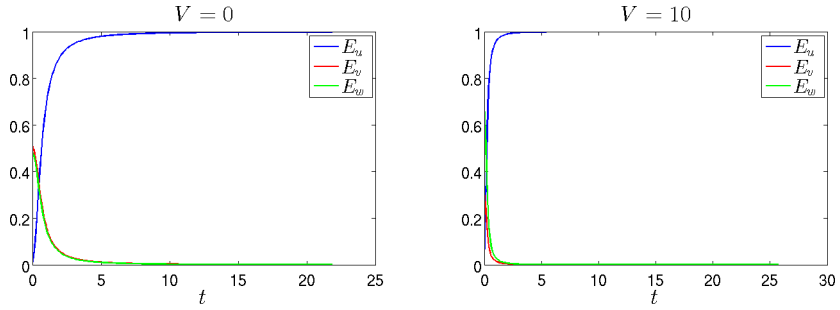

Figure 2.16: Energy fractions showing the emergence of streaks in the optimals for both $V = 0$ and $V = 10$. The optimal for $V = 0$ is axially independent with $(k_{max}, m_{max}, T_{max}) = (0, 3, 21.84)$, and the optimal for $V = 10$ is weakly oblique with $(k_{max}, m_{max}, T_{max}) = (0.0312, 2, 25.69)$. $(Re, \eta) = (10^3, 0.2)$ in both cases.

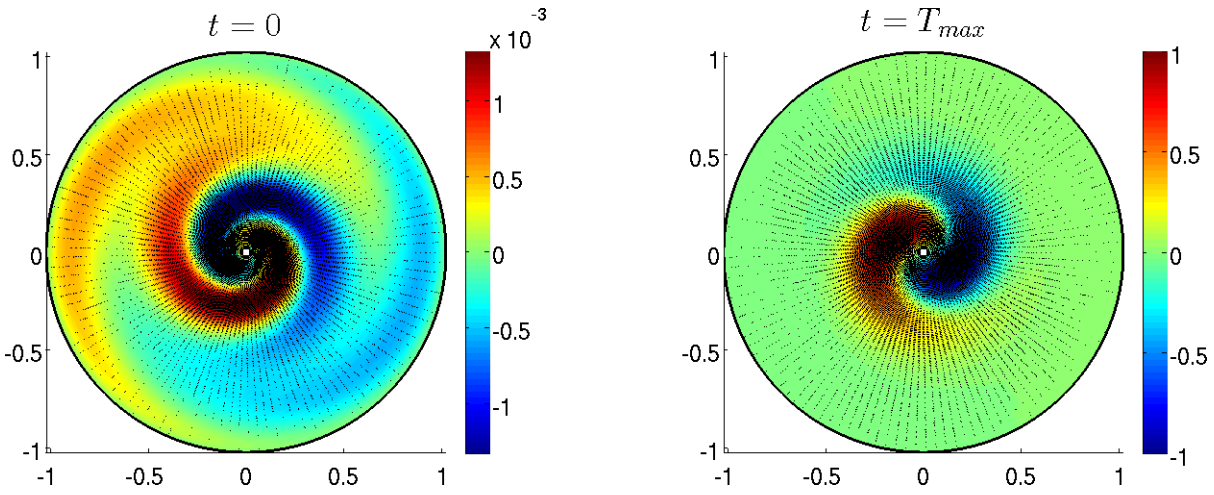

Figure 2.17: Optimal perturbations at $t = 0$ and $t = T_{max} = 19.15$ for $(Re, V, \eta, k_{max}, m_{max}) = (10^3, -5, \frac{1}{42}, 0.2666, 1)$.

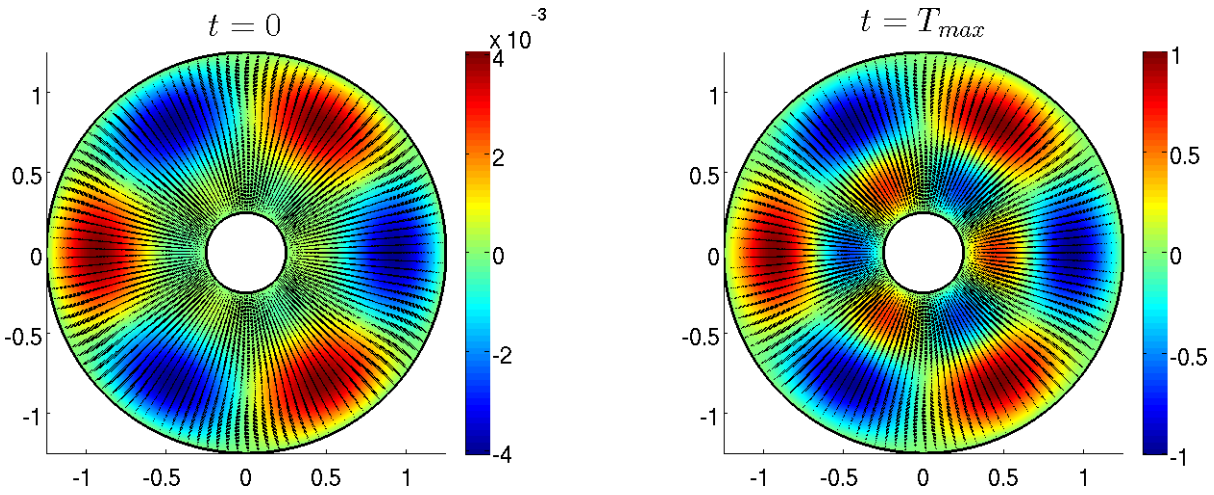

Figure 2.18: Optimal perturbations at $t = 0$ and $t = T_{max} = 21.84$ for $(Re, V, \eta, k_{max}, m_{max}) = (10^3, 0, 0.2, 0, 3)$.

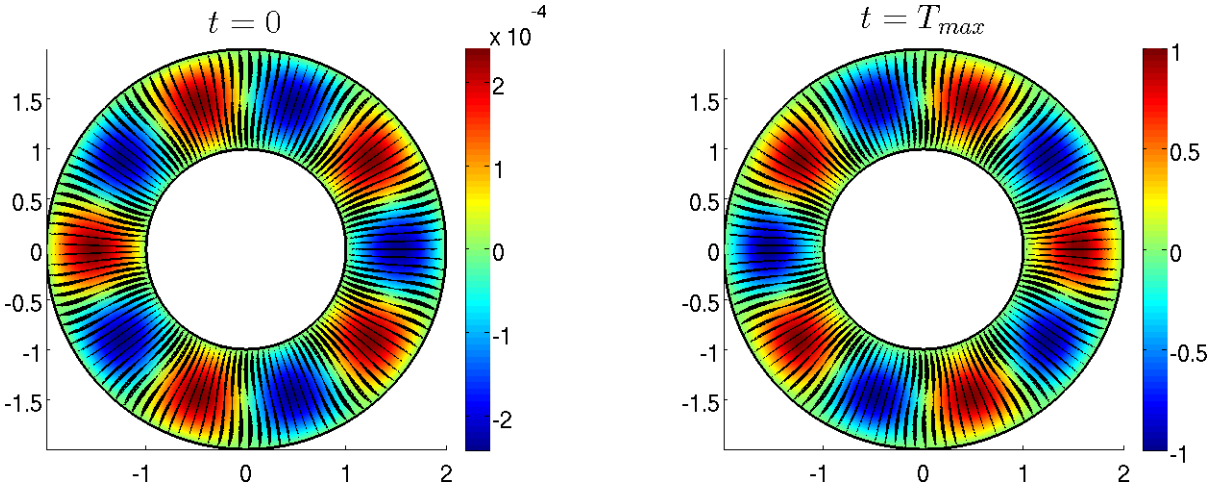

Figure 2.19: Optimal perturbations at $t = 0$ and $t = T_{max} = 34.22$ for $(Re, V, \eta, k_{max}, m_{max}) = (10^3, 5, 0.5, 0, 5)$.

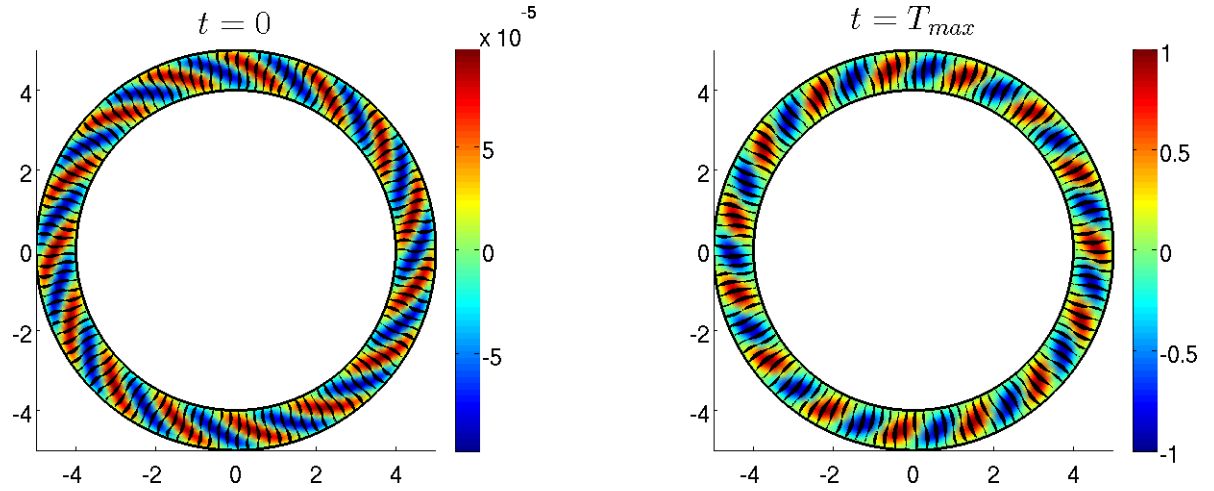

Figure 2.20: Optimal perturbations at $t = 0$ and $t = T_{max} = 30.26$ for $(Re, V, \eta, k_{max}, m_{max}) = (10^3, 10, 0.8, 0.0214, 15)$.

2.4.2 Axisymmetric growth

The azimuthal velocity in the linear system (2.7) decouples from the axial and radial velocities for axisymmetric perturbations ($m = 0$). Therefore, axisymmetric perturbations cannot be amplified by the three-dimensional lift-up mechanism since momentum can only be exchanged between the axial and radial velocities. We find instead that optimals grow via the Orr mechanism (Orr (1907)), typified by perturbations which are initially inclined against the mean flow and gain energy by evolving to align themselves with the mean shear. The Orr mechanism is a much weaker effect than the lift-up mechanism, with characteristic Re scalings $\mathbb{G} \propto Re^{\frac{2}{3}}$ and $T_{max} \propto Re^{\frac{1}{3}}$. Optimal growth of oblique modes in plane Couette and plane Poiseuille flows was shown to have this scaling by Chapman (2002) and Heaton & Peake (2007), who additionally showed that the same scalings are recovered in a cylindrical geometry.

Axisymmetric modes in APCF recover the aforementioned Re scalings; we demonstrate this in Figure 2.22. Since the axisymmetric modes grow on a different scale to non-axisymmetric optimals, we repeat the contour plots of Figure 2.10 to explore how axisymmetric transients behave in (Re, V)-space. $\mathbb{G}_{m=0}$ is calculated as described in §2.3 but with wavenumber optimization over k only, and m fixed at zero. Contours of $\mathbb{G}_{m=0}$ are plotted in Figure 2.21. The effect of inner cylinder velocity on $\mathbb{G}_{m=0}$ is generally the same as for $\mathbb{G}$, in that large $|V|$ creates an increase in the energy amplification. However, each contour has a maximum Re for V_m with $V_m < 0$. V_m decreases as contour size increases, and the effect is more pronounced at smaller radius ratios. This means that there is a region of negative V which has a stabilizing influence on the transient behaviour. In particular, for $\eta = \frac{1}{42}$ and $\mathbb{G}_{m=0} > 10$, the region $0 < V < -15$ is stabilizing with respect to the stationary inner cylinder since the contours of $\mathbb{G}_{m=0} > 10$ do not bend back to their value at $V = 0$, as can be seen in Figure 2.21. In all cases, $V > 0$ has a de-stablizing effect on the transients.

The axial wavenumbers k_{max} from our calculations of $\mathbb{G}_{m=0}$ are always O(1). The wavenumbers experience a sharp turning point when plotted against V, at $V \approx 0$ for fixed Re, and we display some examples of this in Figure 2.23. Additionally, the curves in Figure 2.23 appear to flatten out for $|V|$ large, which is perhaps an indication of Couette shear dominating over pressure-driven forces.

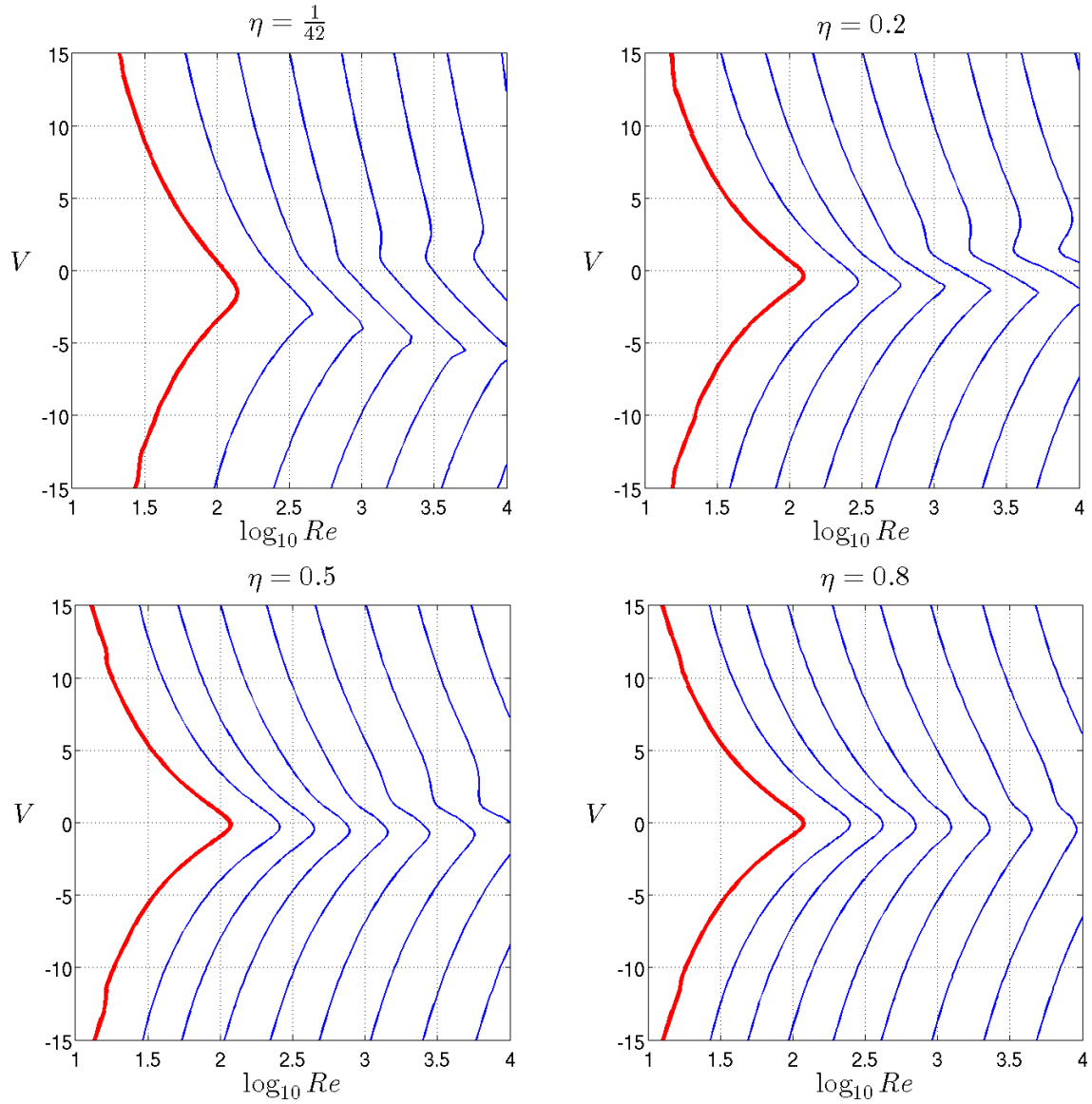

Figure 2.21: Contours of maximum axisymmetric growth $\mathbb{G}_{m=0}$ in the (Re, V)-plane for radius ratios $\eta = \frac{1}{42}, 0.2, 0.5, 0.8$. The thick red curve demarcates the axisymmetric energy stability boundary. The blue curves are contours of $\log_{10} \mathbb{G}_{m=0} = 0.25, 0.5, 0.75, \ldots, 2$.

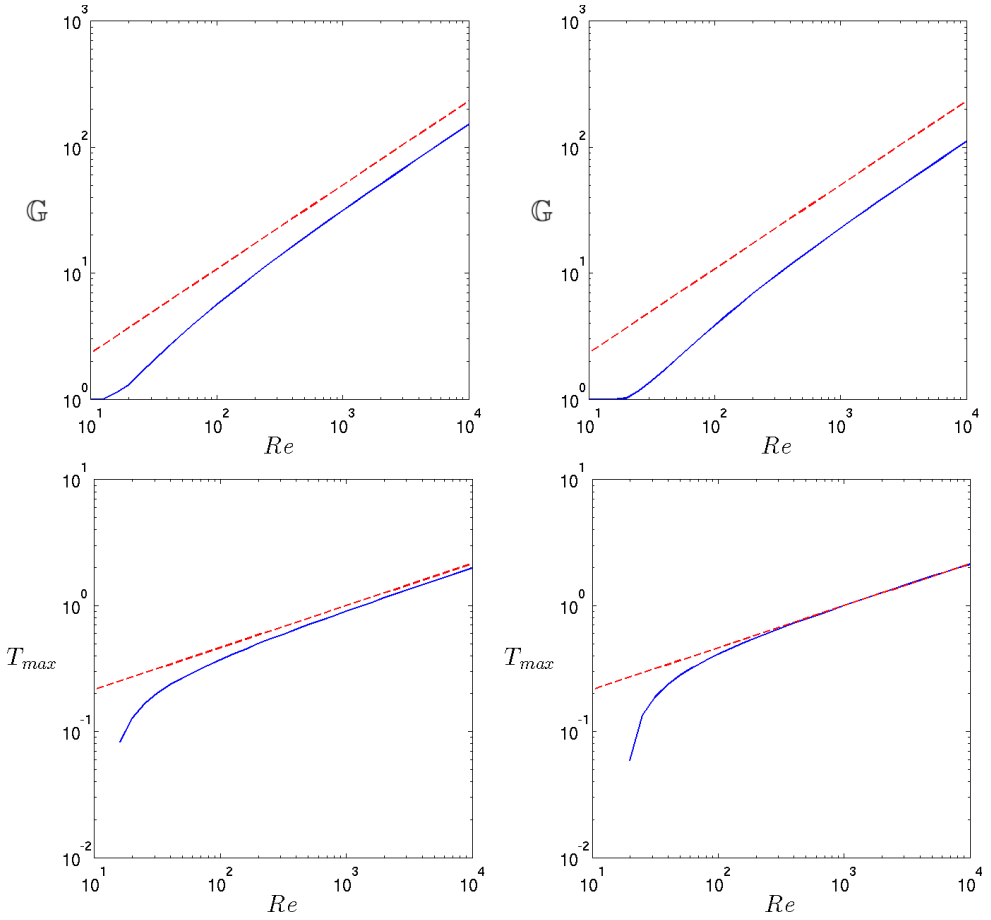

Figure 2.22: $\mathbb{G}$ and T_{max} against Re for radius ratio $\eta = 0.5$ and $V = -10$ (left) and $V = 15$ (right). The red dashed lines represent the asymptotic scalings $\mathbb{G} \propto Re^{\frac{2}{3}}$ and $T_{max} \propto Re^{\frac{1}{3}}$.

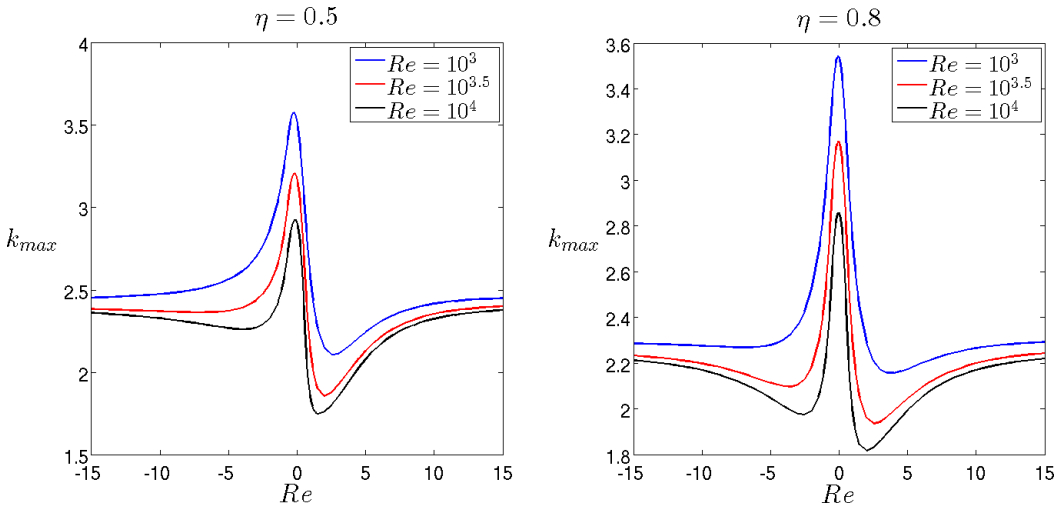

Figure 2.23: Wavenumbers k_{max} for the axisymmetric optimals $\mathbb{G}_{m=0}$.

2.4.3 Radius ratio dependence of $\mathbb{G}$

We now investigate how $\mathbb{G}$ changes as the radius ratio is varied over the range $0 < \eta < 1$. From Figures 2.10 and 2.21, we saw that the contours of $\mathbb{G}$ and $\mathbb{G}_{m=0}$ were relatively unchanged over the radius ratios considered in the Figures, though the wavenumbers responsible for the maximum growth changed. This is confirmed in Figure 2.24, where $\mathbb{G}$ is plotted against η at various inner cylinder velocities. The curves have a scalloped appearance, owing to a succession of azimuthal orders contributing to the optimal. In each plot, in spite of quantitative changes in $\mathbb{G}$ as η varies, the order of magnitude of $\mathbb{G}$ is unchanged, meaning that the maximum linear energy amplification possible is not strongly dependent on the specific geometry of the annulus considered.

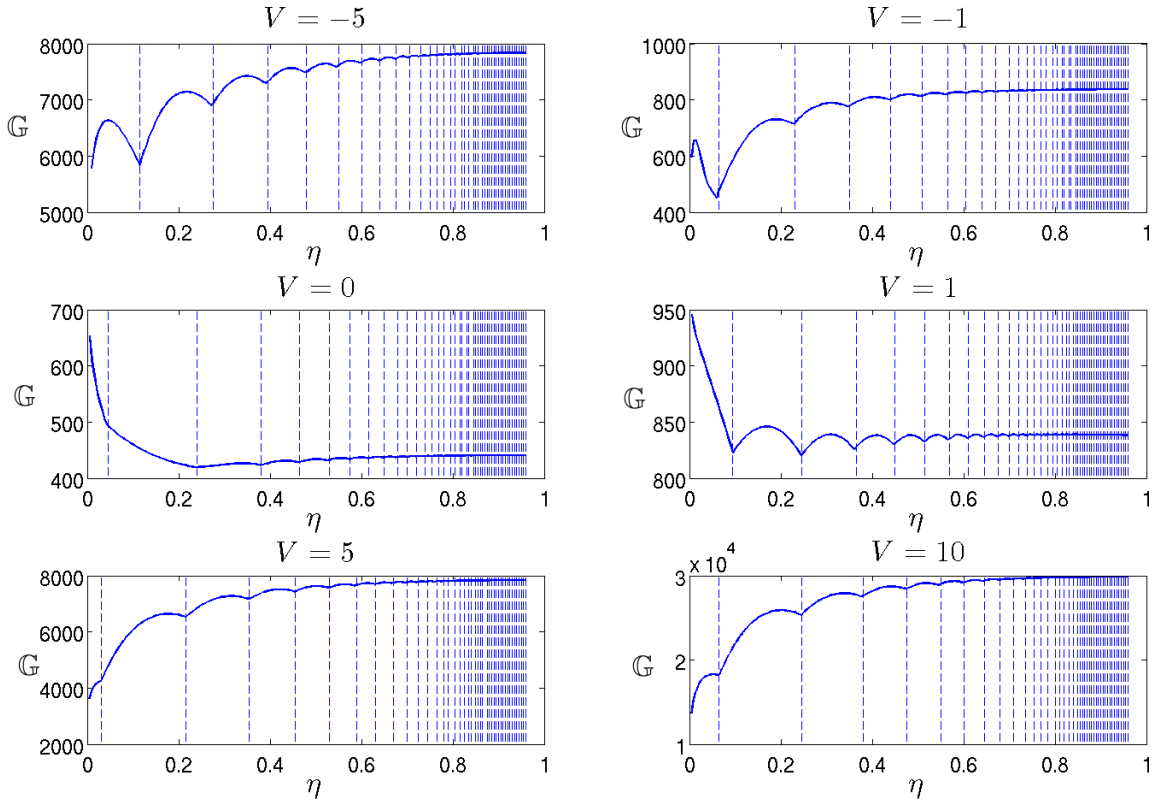

Figure 2.24: $\mathbb{G}$ against η at various inner-cylinder velocities. $Re = 2000$. Dashed lines indicate the locations where m_{max} changes value.

Furthermore, we can determine the optimal radial-azimuthal aspect ratio $a_{r\theta}$ from our computational data. We define $a_{r\theta}$ to be the ratio of the wall-normal gap and the average azimuthal periodic length of the optimal disturbance

$$a_{r\theta} = \frac{B-A}{\frac{2\pi}{m_{max}}\left(\frac{B+A}{2}\right)} = \frac{m_{max}}{\pi}\left(\frac{B-A}{B+A}\right) = \frac{m_{max}}{\pi}\left(\frac{1-\eta}{1+\eta}\right). \tag{2.53}$$

Generally $a_{r\theta}$ converges on a constant value as $\eta \to 1$, indicating that the optimals prefer a certain parameter dependent aspect ratio as they approach the narrow gap limit. A particularly interesting case is when $V = 0$, where we find that as the radius ratio approaches unity, $a_{r\theta}$ approaches the wall-normal-spanwise aspect ratio a_{yz} of the optimal perturbation in plane Poiseuille flow. This is in keeping with the notion that annular Poiseuille flow approaches plane Poiseuille flow in the narrow-gap limit. We plot our findings in Figure 2.25, where we have calculated a_{yz} for plane Poiseuille disturbances based on an optimal spanwise wavenumber $\beta \approx 2$, which gives

$$a_{yz} = \frac{2}{\left(\frac{2\pi}{\beta}\right)} = \frac{2}{\left(\frac{2\pi}{2}\right)} = \frac{2}{\pi} \approx 0.6366. \tag{2.54}$$

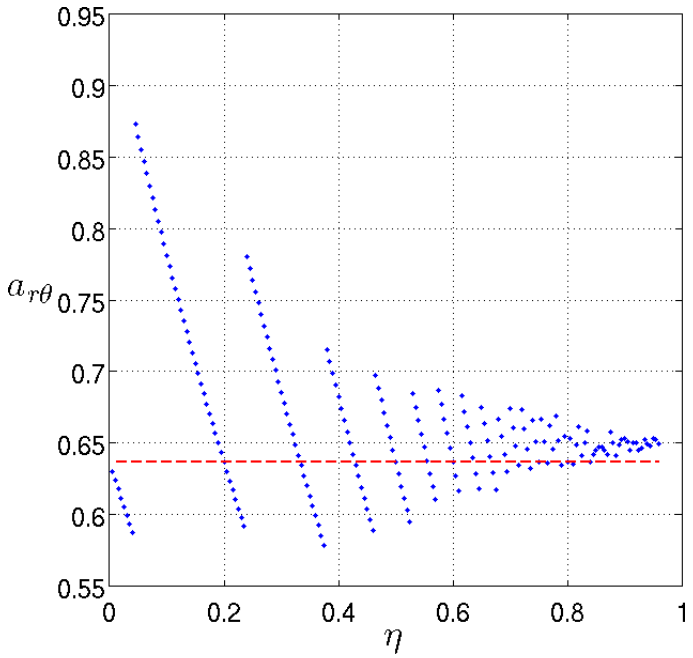

Figure 2.25: The optimal radial-azimuthal aspect ratio $a_{r\theta}$ is plotted against the radius ratio η (blue dots), for $(Re, V) = (2000, 0)$. It can be seen that $a_{r\theta}$ converges towards a constant as $\eta \to 1$. The red dashed line denotes the value of the wall-normal-spanwise aspect ratio $a_{yz} = \frac{2}{\pi}$ for optimal disturbances in plane Poiseuille flow. We infer that in the narrow gap limit the optimal disturbances of annular Poiseuille share the characteristics of optimal disturbances in plane Poiseuille flow.

2.5 Comparison to experimental data

Experimental data relating to APCF is relatively scarce, with Shands *et al.* (1980) and Frei *et al.* (2000) being the only authors conducting experiments in APCF that we are aware of. Frei *et al.* (2000) are primarily concerned with thread-annular flow, and explicit data on the parameters at which the flow transitions is not given in their work. In the Shands *et al.* (1980) experiments they do report specific (Re, V) values at which the laminar flow was observed to break down; we therefore focus on data from their experiments.

Shands *et al.* (1980) gauge the transition to turbulence of the fluid in their experiments by measuring the friction factor $\lambda = \frac{2\Delta p D}{\rho L \widehat{U}^2}$. The quantities Δp, D, ρ, L and $\widehat{U}$ are defined in §2.1. From equation (2.9b) we have that under laminar flow, the total mean velocity, $\widehat{U}$, must satisfy

$$\widehat{U} = \frac{\Delta p}{8\mu L \log\frac{B}{A}}\left(B^2 - A^2 - (B^2+A^2)\log\frac{B}{A}\right) + \widetilde{V}\left(\frac{B^2 - A^2 - 2A^2\log\frac{B}{A}}{2(B^2-A^2)\log\frac{B}{A}}\right). \tag{2.55}$$

Dividing through by $\widehat{U}$ gives

$$1 = \frac{\Delta p B^2}{8\rho\nu L\widehat{U}}\left(\frac{1-\eta^2+(1+\eta^2)\log\eta}{\log\eta}\right) + \frac{\widetilde{V}}{\widehat{U}}\left(\frac{\eta^2-1-2\eta^2\log\eta}{2(1-\eta^2)\log\eta}\right) \tag{2.56}$$

$$1 = \frac{1}{32}\left(\frac{\Delta p D}{\rho L\widehat{U}^2}\right)\left(\frac{\widehat{U}D}{\nu}\right)\left(\frac{1-\eta^2+(1+\eta^2)\log\eta}{(1-\eta)^2\log\eta}\right) + \frac{\widetilde{V}}{\widehat{U}}\left(\frac{\eta^2-1-2\eta^2\log\eta}{2(1-\eta^2)\log\eta}\right). \tag{2.57}$$

Hence for laminar flow λ, $\widehat{Re}$ and $\widehat{V}$ have the following relationship

$$1 = \frac{\lambda\widehat{Re}}{64}\left(\frac{1-\eta^2+(1+\eta^2)\log\eta}{(1-\eta)^2\log\eta}\right) + \widehat{V}\left(\frac{\eta^2-1-2\eta^2\log\eta}{2(1-\eta^2)\log\eta}\right). \tag{2.58}$$

At fixed $\widehat{Re}$, Shands *et al.* (1980) measure the $\widehat{V} > 0$ for which (2.58) first breaks down, thereby determining the point at which flow transitions away from laminar flow. In Figure 2.26 we re-print Fig. 3 from Shands *et al.* (1980), which shows the friction factor λ plotted against $\widehat{V}$ for $\widehat{Re} = 1100, 1900$ and gap ratio $\eta = \frac{1}{42}$. In the Figure, measurements of the friction factor fall along equation (2.58) until transition occurs when $\widehat{V} = 3.3, 2$ for $\widehat{Re} = 1100, 1900$, respectively. Additionally, Shands *et al.* (1980) report transition when $\widehat{V} = 2.7$ and $\widehat{Re} = 1300$, and transition in the fixed inner cylinder case for $\widehat{Re} = 2000$. In our non-dimensionalization, these values correspond to $Re = 308, 416, 697$ and $V = 5.89, 4.22, 2.73$.

Without any explicit comment on how linear optimal perturbations may contribute to

transition away from the laminar base flow, we plot the values at which Shands *et al.* (1980) report transition for $\eta = \frac{1}{42}$, alongside our curves of $\mathbb{G}$ in Figure 2.27. The transition values lie within $10^2 < \mathbb{G} < 10^{2.5}$ and, suggestively, greater inner cylinder velocity is *de-stabilizing* in both the experiments and in the sense that it increases $\mathbb{G}$. Since linearly unstable modes appear to be, in general, stabilized by inner-cylinder velocity, we draw the tentative conclusion that the energy amplification mechanisms driving the linear optimal growth play a greater role in the break down of the laminar flow than the linearly unstable modes. Furthermore, Shands *et al.* (1980) remark that, having repeated their experiments for different radius ratios, transition is found to occur at similar parameter values. This is in keeping with our finding in §2.4.3 that the maximum energy amplification $\mathbb{G}$ is not strongly sensitive to changes in the radius ratio.

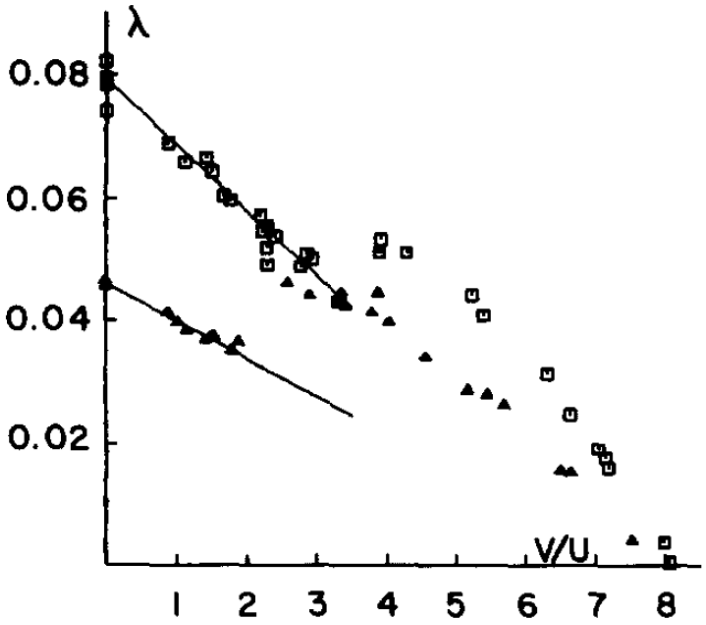

Figure 2.26: Re-print of Fig. 3 from Shands *et al.* (1980). The friction factor λ is plotted against inner cylinder velocity $\widehat{V} = \frac{\tilde{V}}{\tilde{U}}$ for $\widehat{Re} = 1100$ (squares) and $\widehat{Re} = 1900$ (triangles). The two straight lines indicate the laminar relationship (2.58), which breaks down when $\widehat{V} = 3.3, 2$ and $\widehat{Re} = 1100, 1900$ respectively.

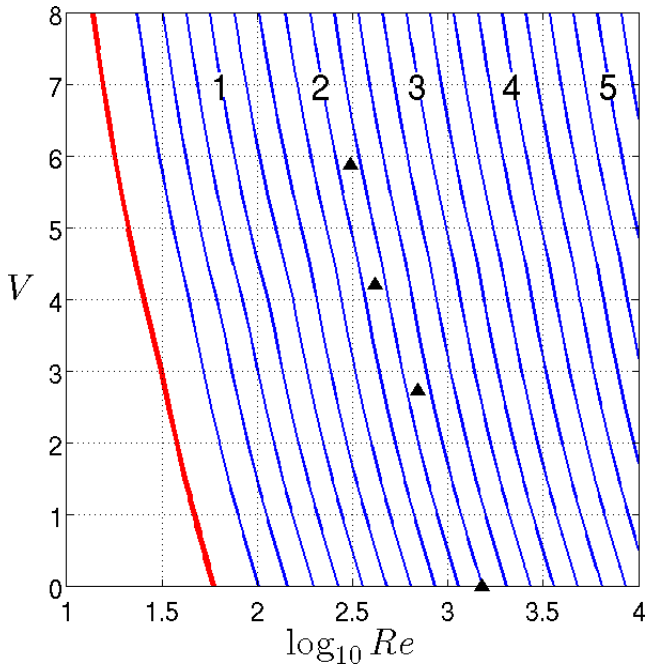

Figure 2.27: Contours of $\mathbb{G}$ in (Re, V)-space for $\eta = \frac{1}{42}$ are plotted alongside transition values observed in Shands *et al.* (1980). The contour values are $\log_{10}\mathbb{G} = 0.25, 0.5, \ldots, 5.25$ with contours $\log_{10}\mathbb{G} = 1, 2, 3, 4, 5$ labelled. The black triangles mark the points of transition. The red curve demarcates the energy stability boundary.

2.6 Conclusion

This chapter began with a re-cap of the linear stability properties of APCF, which we augmented by calculating neutral curves in (Re, V)-space. We find that non-zero inner cylinder velocity V tends to have a stabilizing influence on the modal stability of perturbations to the base flow.

We then conducted a non-modal stability analysis, using the maximum energy amplification over all wavenumber combinations as a measure of the non-modal instability for an arbitrary (Re, V) pair. We found transient energy amplification driven by the lift-up mechanism is possible for non-axisymmetric waves. The order of magnitude of the maximum growth is not found to be strongly correlated to the radius ratio of the cylinders. Axisymmetric waves experience energy amplification via the Orr mechanism, though this amplification is not as strong as the lift-up mechanism. However, the maximum energy amplification associated with both axisymmetric and non-axisymmetric modes is found to *increase* with increasing inner cylinder velocity magnitude, which implies that non-zero inner cylinder velocity has a *de-stabilizing* influence on perturbations to the mean flow, in contrast with the modal stability results.

Finally we compare our results with the study of Shands *et al.* (1980), who studied APCF in an experimental set up, and indicated the (Re, V) parameters at which they observed transition to turbulence. The transitional values lie within a few contours of maximum growth, suggesting a relationship between the linear energy growth mechanisms and a break down in the laminar flow.

Chapter 3

Stability and bifurcations in rotating plane Couette flow

In this chapter we focus on the stability and bifurcation behaviour of structures in supercritical rotating plane Couette flow (RPCF). The governing equations and the geometry of the problem are introduced in §3.1. In §3.2 we review the linear stability properties of the basic flow. In §3.3 an account is given of the methods we use to find nonlinear numerical secondary and tertiary solutions to the governing equations. In §3.4 we describe the Floquet theory techniques which we use to determine the stability of spatially and temporally periodic states. §3.5 is a discussion of the secondary states which bifurcate from the base flow. In §3.6 we perform a Floquet stability analysis of Taylor vortex flow, an important secondary structure in RPCF. Bifurcations of tertiary solutions, which emerge following the break-down of Taylor vortices, are presented in §3.7. Finally, in §3.8 we investigate the relevance of the secondary and tertiary states to the transition phenomena observed in physical experiments of RPCF, and propose a simple model with which the transition process can be analyzed.

3.1 Governing equations

Rotating plane Couette flow (RPCF) is the flow of an incompressible, Newtonian fluid under linear shear and Coriolis rotation. The fluid is constrained between moving impermeable walls; with velocity difference $2\tilde{U}$ between the upper and lower walls and channel width $2\tilde{h}$. We define unit vectors $\boldsymbol{i}$, $\boldsymbol{j}$ and $\boldsymbol{k}$ pointing in the streamwise, wall-normal and spanwise directions respectively, as shown in Figure 3.1. Working towards a non-dimensionalized system of equations, we first consider the dimensional momentum balance in a rotating frame of reference

$$\frac{\partial \tilde{\boldsymbol{u}}}{\partial \tilde{t}} + \tilde{\boldsymbol{u}} \cdot \tilde{\nabla} \tilde{\boldsymbol{u}} = -\frac{1}{\tilde{\rho}} \tilde{\nabla} \tilde{p} + \tilde{\nu} \tilde{\nabla}^2 \tilde{\boldsymbol{u}} + 2\big(\tilde{\boldsymbol{u}} \times \tilde{\boldsymbol{\Omega}}\big) - \tilde{\boldsymbol{\Omega}} \times \tilde{\boldsymbol{\Omega}} \times \tilde{\boldsymbol{x}} - \frac{d\tilde{\boldsymbol{\Omega}}}{d\tilde{t}} \times \tilde{\boldsymbol{x}}, \qquad (3.1)$$

where $\tilde{\rho}$ is the fluid density, $\tilde{\nu}$ is the kinematic viscosity and $\tilde{\boldsymbol{x}}$ is a position vector pointing from the axis of rotation. For steady rotation about the z-axis we have $\tilde{\boldsymbol{\Omega}} = \tilde{\Omega}\boldsymbol{k}$, which allows us to drop the time-dependent Euler force term $\frac{d\tilde{\boldsymbol{\Omega}}}{d\tilde{t}} \times \tilde{\boldsymbol{x}}$. Since the centrifugal force term, $\tilde{\boldsymbol{\Omega}} \times \tilde{\boldsymbol{\Omega}} \times \tilde{\boldsymbol{x}}$, contains no dynamic variables, we introduce the pressure $\bar{p}$

$$\bar{p} = \tilde{p} - \frac{\tilde{\rho}\tilde{\Omega}^2}{2}\tilde{\boldsymbol{x}}^2, \tag{3.2}$$

where $\tilde{\boldsymbol{x}}^2 = \tilde{\boldsymbol{x}} \cdot \tilde{\boldsymbol{x}}$. This allows the momentum equations to be expressed as

$$\frac{\partial \tilde{\boldsymbol{u}}}{\partial \tilde{t}} + \tilde{\boldsymbol{u}} \cdot \tilde{\nabla}\tilde{\boldsymbol{u}} = -\frac{1}{\tilde{\rho}}\tilde{\nabla}\bar{p} + \tilde{\nu}\tilde{\nabla}^2\tilde{\boldsymbol{u}} + 2\big(\tilde{\boldsymbol{u}} \times \tilde{\boldsymbol{\Omega}}\big). \tag{3.3}$$

We now introduce three non-dimensional parameters: the Reynolds number Re, the rotation number Ro and a second rotation number Ω

$$Re = \frac{\tilde{U}\tilde{h}}{\tilde{\nu}}, \qquad Ro = \frac{2\tilde{\Omega}\tilde{h}}{\tilde{U}}, \qquad \Omega = \frac{2\tilde{\Omega}\tilde{h}^2}{\tilde{\nu}} = Re\, Ro. \tag{3.4}$$

Hence, after non-dimensionalization and inclusion of the continuity equation, the velocity and pressure $(\boldsymbol{u}, p)$ satisfy

$$\frac{\partial \boldsymbol{u}}{\partial t} + \boldsymbol{u} \cdot \nabla\boldsymbol{u} = -\nabla p + \frac{1}{Re}\nabla^2\boldsymbol{u} + Ro\big(\boldsymbol{u} \times \boldsymbol{k}\big), \tag{3.5a}$$

$$\nabla \cdot \boldsymbol{u} = 0, \tag{3.5b}$$

with the no-slip boundary condition imposed on the each of the walls. The linear shear profile $\boldsymbol{U} = y\boldsymbol{i}$, is a solution to this system with pressure distribution $P = P_0 - \frac{1}{2}Ro\, y^2$, where P_0 is the ambient pressure. Of the two rotation numbers Ro and Ω, Ro is useful since it appears as a single coefficient controlling the Coriolis force in (3.5), whereas Ω is independent of the wall velocity in terms of its non-dimensionalization meaning that it describes the effects of rotation independent of Re. For the majority of this chapter we describe rotation in terms of Ro, however, in §3.8 we use Ω, in accordance with experimental preference.

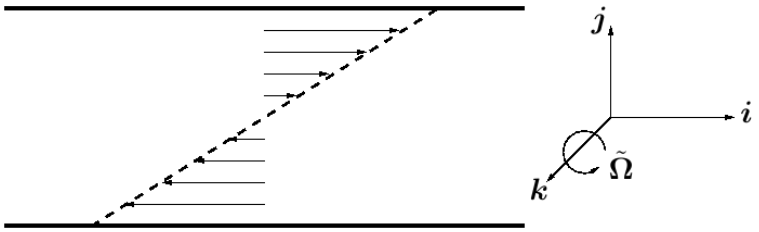

Figure 3.1: Sketch of the flow geometry.

3.2 Linear stability

It has been shown that RPCF is linearly unstable by Lezius & Johnston (1976), who drew on the equivalence of the linearized system (3.5) to two-dimensional Rayleigh-Bénard convection. The flow loses stability in the rotation parameter range $0 < Ro < 1$, to spanwise periodic disturbances with wavenumber $\beta \approx 1.55$. The neutral curve takes the form

$$Re^2 = \frac{107}{Ro(1 - Ro)}. \tag{3.6}$$

More generally we can solve directly for the eigenfrequencies and eigenmodes of the linearized system using a pseudo-spectral technique. We Fourier transform the velocity vectors in the directions x and z and assume exponential dependence in time, with Fourier coefficients α, β and ω respectively. The fluid vectors become

$$[u, v, w, p](x, y, z, t) = [u, v, w, p](y)\mathrm{e}^{\mathrm{i}(\alpha x + \beta z) + \omega t}. \tag{3.7}$$

With base flow, or primary state, $\boldsymbol{U} = U(y)\boldsymbol{i} = y\boldsymbol{i}$, the linear stability equations are

$$\omega u + U\mathrm{i}\alpha u + vU' = -\mathrm{i}\alpha p + \frac{1}{Re}\left(u'' - (\alpha^2 + \beta^2)u\right) + Rov \tag{3.8a}$$

$$\omega v + U\mathrm{i}\alpha v = -p' + \frac{1}{Re}\left(v'' - (\alpha^2 + \beta^2)v\right) - Rou \tag{3.8b}$$

$$\omega w + U\mathrm{i}\alpha w = -\mathrm{i}\beta p + \frac{1}{Re}\left(w'' - (\alpha^2 + \beta^2)w\right) \tag{3.8c}$$

$$\mathrm{i}\alpha u + v' + \mathrm{i}\beta w = 0. \tag{3.8d}$$

The system can be cast into a generalized eigenvalue problem

$$A\boldsymbol{q} = \omega B\boldsymbol{q}, \tag{3.9}$$

for $\boldsymbol{q} = (u, v, w, p)$ and matrix operators A and B given by

$$A = \begin{pmatrix} \mathcal{A} & Ro - \frac{dU}{dy} & 0 & -\mathrm{i}\alpha \\ -Ro & \mathcal{A} & 0 & -\frac{d}{dy} \\ 0 & 0 & \mathcal{A} & -\mathrm{i}\beta \\ \mathrm{i}\alpha & \frac{d}{dy} & \mathrm{i}\beta & 0 \end{pmatrix}, \tag{3.10}$$

$$B = \begin{pmatrix} 1 & 0 & 0 & 0 \\ 0 & 1 & 0 & 0 \\ 0 & 0 & 1 & 0 \\ 0 & 0 & 0 & 0 \end{pmatrix}. \tag{3.11}$$

where we have defined

$$\mathcal{A} = \frac{1}{Re}\left(\frac{d^2}{dy^2} - (\alpha^2 + \beta^2)\right) - \mathrm{i}\alpha U. \tag{3.12}$$

We solve for ω by expressing $\boldsymbol{q}$ as a truncated series of Chebyshev polynomials and discretizing the system accordingly. The technique is outlined in greater detail in Schmid & Henningson (2001).

Above the critical Reynolds number $Re_{cr} \approx 20.7$ there is a finite range of Ro or, equivalently, Ω for which the flow is linearly unstable.

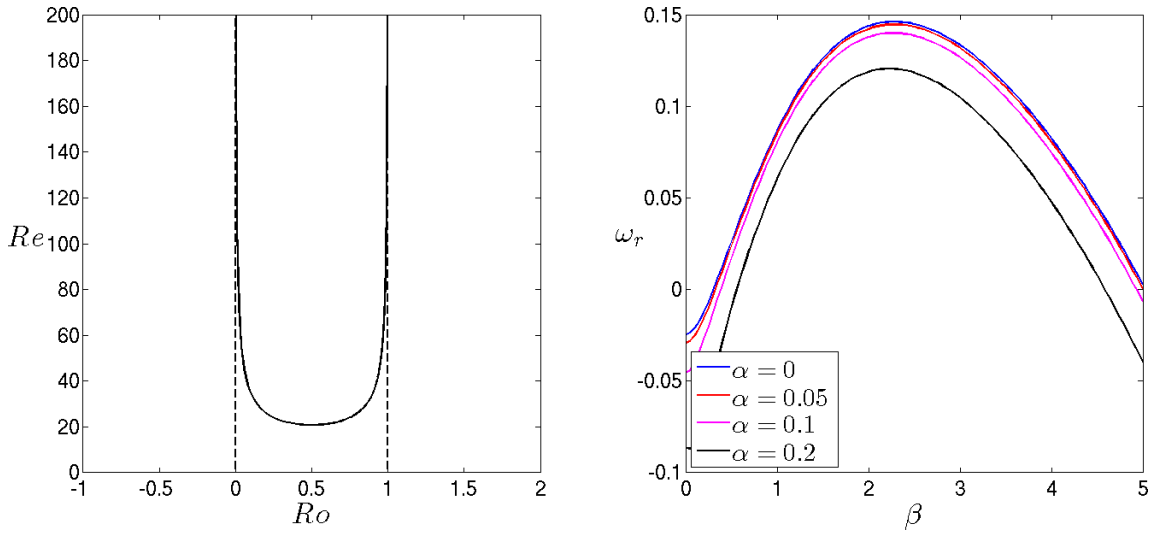

Figure 3.2: Left: Neutral curve. Right: ω_r denotes the real part of the leading eigenvalue for $Re = 100$, $Ro = 0.1$. Perturbations with $\alpha = 0$ are least stable.

Our calculations show that linearly unstable perturbations take the form of streamwise oriented vortices, with wavenumbers $\alpha = 0$ and β non-zero or obliquely oriented vortices with both α and β non-zero. We find that, for fixed β, Re and Ro, the leading streamwise vortex (SV) eigenmode is generically more unstable than the leading oblique vortex (OV) eigenmode:

$$\omega_r(0, \beta) > \omega_r(\alpha, \beta). \tag{3.13}$$

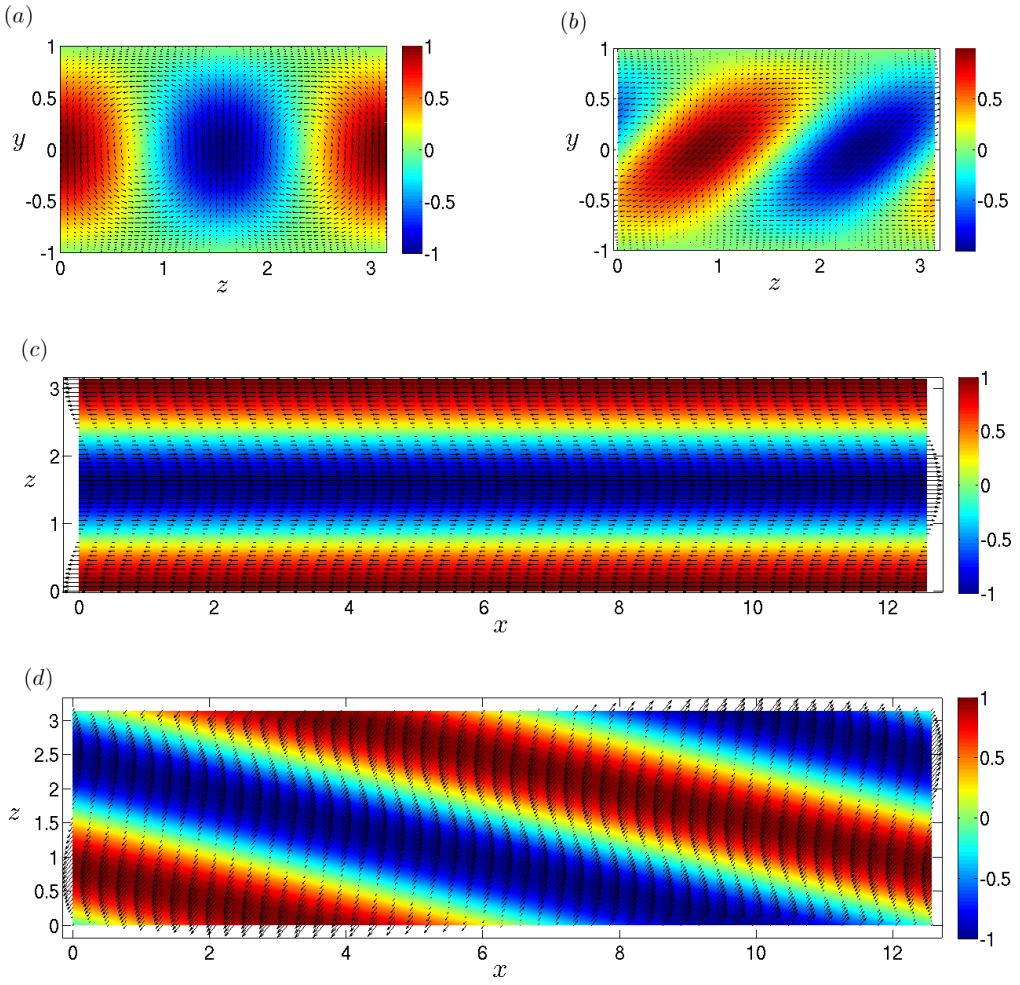

Figure 3.3: Velocity fields $\boldsymbol{u}$ of (a) SV and (b) OV perturbations in the (y, z)-plane (top) with $x = 0$ and ((c) and (d)) the (x, z)-plane (bottom) with $y = 0$ for $(Re, Ro) = (50, 0.1)$ and $(\alpha, \beta) = (0.5, 2)$.

3.2.1 Flowfield visualization

It is often useful to visualize a fluid structure, whether it is a stability eigenmode or nonlinear solution to the Navier-Stokes equations. However, it is not straightforward to display a fully three-dimensional flowfield in such a way that none of its features are lost. Throughout this work we use two-dimensional projections of flowfields to concisely give a visual sense of their character. In each Figure we have a colour-plot of the streamwise velocity u, and a vector plot of the wall-normal and spanwise velocities (v, w). To display the streamwise variation of a flowfield we fix $y = 0$ and plot the (x, z)-plane. To view the vortical structure of a flowfield we fix $x = 0$ and plot the (y, z)-plane. Each Figure has a true aspect ratio.

3.3 Nonlinear states

We refer to numerical solutions of the nonlinear Navier-Stokes equations as nonlinear states. For a given initial guess, a Newton-Krylov-hookstep algorithm is used to find a steady or time-periodic state. Typically, our initial guesses come from predictions given by linear stability theory. Calculations are made using two direct numerical simulators. SIMSON (Chevalier *et al.* (2007)) is used for numerical integration of the Navier-Stokes equations, and Channelflow (Gibson (2008)) is used to integrate the Navier-Stokes equations, find equilibrium and time-periodic solutions, and to continue the solutions in parameter space. Both codes use spectral discretization in the periodic directions, and discretization of the wall-normal direction in Chebyshev polynomials. Time integration is performed using a finite-differencing technique. Both codes have been widely validated by other authors, and we find excellent agreement between the two in our simulations.

The Newton-Krylov-hookstep algorithm outlined in Viswanath (2007), and implemented within Channelflow, is used to determine equilibrium and time-periodic solutions to the Navier-Stokes equations. Let

$$\frac{\partial \boldsymbol{u}}{\partial t} = L_{NS}\boldsymbol{u}, \qquad F^t_{NS}(\boldsymbol{u}) = \boldsymbol{u} + \int_0^t L_{NS}\boldsymbol{u}(\tau)\, d\tau \tag{3.14}$$

be the Navier-Stokes equations and their time-t forward map. The equations are solved in perturbation formulation about the primary flow $\boldsymbol{U} = y\boldsymbol{i}$, so the operator L_{NS} is defined as

$$L_{NS} = \frac{1}{Re}\nabla^2\boldsymbol{u} - \nabla p + Ro\big(\boldsymbol{u}\times\boldsymbol{k}\big) - \boldsymbol{U}\cdot\nabla\boldsymbol{u} - \boldsymbol{u}\cdot\nabla\boldsymbol{U} - \boldsymbol{u}\cdot\nabla\boldsymbol{u}. \tag{3.15}$$

The Newton-Krylov-hookstep algorithm finds solutions by minimizing the residual $G(\boldsymbol{u})$

$$G(\boldsymbol{u}) = F^T_{NS}(\boldsymbol{u}) - \boldsymbol{u}. \tag{3.16}$$

The algorithm was used by other authors to find solutions in plane Couette flow, where the absence of linear instabilities makes finding an initial condition which converges towards a solution difficult (Viswanath (2007), Gibson *et al.* (2009)). Though the basins of attraction of solutions in our case will generally be greater than in non-rotating plane Couette flow due to supercriticality, the algorithm is still useful for its computational efficiency. We will give a brief outline of how the algorithm works. Writing the solution vector as $\boldsymbol{x} = (\boldsymbol{u}, \alpha_s, \beta_s, \omega_s)$, where α_s and β_s are the wavenumbers in the periodic directions and ω_s is the frequency of a time-periodic state, the Newton step requires

solution of

$$DG(\boldsymbol{x}_n)(\boldsymbol{x}_{n+1} - \boldsymbol{x}_n) = -G(\boldsymbol{x}_n), \tag{3.17}$$

where $G(\boldsymbol{u})$ has been appended to account for the invariance of the solution under translations in its periodic directions x, z or t and guard against solution updates which are simply translations, and $DG(\boldsymbol{x})$ is the Jacobian of the system. Equation (3.17) is solved for the updated solution guess $\boldsymbol{x}_{n+1}$ using the GMRES Krylov subspace method (Saad & Schultz (1986), Sánchez *et al.* (2004)). If the Newton step fails to decrease the residual below a prescribed tolerance, a hookstep algorithm is employed to find a solution update which does decrease the residual sufficiently. The hookstep algorithm uses the Lagrange multipliers technique to minimize

$$\|DG(\boldsymbol{x}_n)(\boldsymbol{x}_{n+1} - \boldsymbol{x}_n) + G(\boldsymbol{x}_n)\|^2, \tag{3.18}$$

subject to

$$\|\boldsymbol{x}_{n+1} - \boldsymbol{x}_n\|^2 < \delta^2, \tag{3.19}$$

so that, in effect, we are taking a reduced Newton step. In summary, in the Newton-Krylov-hookstep algorithm the classic Newton iteration scheme is augmented by a Krylov subspace technique to enhance computational efficiency and a hookstep algorithm to increase the accuracy of each solution update. More detail on the full algorithm can be found in Viswanath (2007) and the references cited above. All solutions found in this thesis have an accuracy of $\|G(\boldsymbol{u})\| < 10^{-14}$.

Having found a state with velocity field $\boldsymbol{u} = (u, v, w)$ we use the cross-flow energy E_{cf} as a measure of the nonlinear solution,

$$E_{cf}(\alpha_s, \beta_s, Re, Ro) = \frac{1}{2\mathcal{D}_V} \int_{\mathcal{D}} v^2 + w^2 dV. \tag{3.20}$$

where $\mathcal{D}$ is the x and z periodic domain $[0, L_x] \times [-1, 1] \times [0, L_z] = [0, \frac{2\pi}{\alpha_s}] \times [-1, 1] \times [0, \frac{2\pi}{\beta_s}]$, and $\mathcal{D}_V$ is its volume. E_{cf} is defined in this way so that it is independent of the domain. For example, no distinction is made between a given solution and the same solution on a doubled domain. The four parameter dependence of E_{cf} invites us to fix three parameters and investigate trajectories of solutions on a low-dimensional subspace. As such we typically fix the geometric parameters (α_s, β_s) and investigate bifurcations in Ro, with the remaining dynamic parameter Re fixed.

3.4 Floquet stability analysis

Suppose we have found a nonlinear Navier-Stokes solution, that is periodic in any of the directions x and z or time t. Its stability properties can be determined through Floquet analysis.

3.4.1 Steady states

First considering steady solutions, we utilize the spatial periodicity of the state by expressing it as a Fourier series in the periodic variables. Given wavenumbers α_s in x, β_s in z; we have

$$\boldsymbol{U}_s(x,y,z) = \sum_{j=-\infty}^{\infty}\sum_{k=-\infty}^{\infty} \boldsymbol{U}_{jk}(y)\mathrm{e}^{\mathrm{i}(j\alpha_s x + k\beta_s z)}, \tag{3.21}$$

where

$$\boldsymbol{U}_{jk}(y) = \frac{\alpha_s\beta_s}{4\pi^2}\int_0^{\frac{2\pi}{\alpha_s}}\int_0^{\frac{2\pi}{\beta_s}} \boldsymbol{U}_s(x,y,z)\mathrm{e}^{-\mathrm{i}(j\alpha_s x + k\beta_s z)}\,dxdz. \tag{3.22}$$

We insert the Fourier series expansion of $\boldsymbol{U}_s$ into the linearized Navier-Stokes equations in the form

$$\frac{\partial \boldsymbol{u}}{\partial t} + \boldsymbol{U}_s\cdot\nabla\boldsymbol{u} + \boldsymbol{u}\cdot\nabla\boldsymbol{U}_s = -\nabla p + \frac{1}{Re}\nabla^2\boldsymbol{u} + Ro\big(\boldsymbol{u}\times\boldsymbol{k}\big), \tag{3.23a}$$

$$\nabla\cdot\boldsymbol{u} = 0. \tag{3.23b}$$

Following Floquet's theorem, we write the perturbation vector $\boldsymbol{q} = (u,v,w,p)$ as

$$\boldsymbol{q}(x,y,z,t) = \mathrm{e}^{\mathrm{i}(\alpha x+\beta z)+\sigma t}\sum_{m=-\infty}^{\infty}\sum_{n=-\infty}^{\infty} \hat{\boldsymbol{q}}_{mn}(y)\mathrm{e}^{\mathrm{i}(m\alpha_s x + n\beta_s z)}, \tag{3.24}$$

with the parameters α, β and σ free to be tuned away from the fundamental wavenumbers and frequencies. Using the expressions for $\boldsymbol{q}$ and $\boldsymbol{U}_s$ we can match exponents in the perturbation equations and derive an infinite system of coupled equations of the form

$$A_{mn}\hat{\boldsymbol{q}}_{mn} + \sum_{j,k} F^{jk}_{mn}\hat{\boldsymbol{q}}_{m-j,n-k} = \sigma B\hat{\boldsymbol{q}}_{mn}, \quad \forall m,n\in\mathbb{Z}. \tag{3.25}$$

The operators A, B and F are defined as

$$A_{mn} = \begin{pmatrix} \mathcal{A} & \frac{dU_0}{dy} - Ro & 0 & \mathrm{i}(\alpha+m\alpha_s) \\ Ro & \mathcal{A}+\frac{dV_0}{dy} & 0 & \frac{d}{dy} \\ 0 & \frac{dW_0}{dy} & \mathcal{A} & \mathrm{i}(\beta+n\beta_s) \\ \mathrm{i}(\alpha+m\alpha_s) & \frac{d}{dy} & \mathrm{i}(\beta+n\beta_s) & 0 \end{pmatrix}, \tag{3.26}$$

$$F^{jk}_{mn} = \begin{pmatrix} \mathrm{i}j\alpha_s U_{jk} + \mathcal{F} & \frac{dU_{jk}}{dy} & \mathrm{i}k\beta_s U_{jk} & 0 \\ \mathrm{i}j\alpha_s V_{jk} & \frac{dV_{jk}}{dy} + \mathcal{F} & \mathrm{i}k\beta_s V_{jk} & 0 \\ \mathrm{i}j\alpha_s W_{jk} & \frac{dW_{jk}}{dy} & \mathrm{i}k\beta_s W_{jk} + \mathcal{F} & 0 \\ 0 & 0 & 0 & 0 \end{pmatrix}, \tag{3.27}$$

$$B = -\begin{pmatrix} 1 & 0 & 0 & 0 \\ 0 & 1 & 0 & 0 \\ 0 & 0 & 1 & 0 \\ 0 & 0 & 0 & 0 \end{pmatrix}, \tag{3.28}$$

where we have used

$$\mathcal{A} = \mathrm{i}(\alpha + m\alpha_s)U_0 + V_0\frac{d}{dy} + \mathrm{i}(\beta + n\beta_s)W_0 - \frac{1}{Re}\left(\frac{d^2}{dy^2} - (\alpha + m\alpha_s)^2 - (\beta + n\beta_s)^2\right), \tag{3.29}$$

$$\mathcal{F} = \mathrm{i}(\alpha + (m-j)\alpha_s)U_{jk} + V_{jk}\frac{d}{dy} + \mathrm{i}(\beta + (n-k)\beta_s)W_{jk}, \tag{3.30}$$

and

$$\boldsymbol{U}_{jk} = (U_{jk}, V_{jk}, W_{jk}), \quad \boldsymbol{U}_0 = \boldsymbol{U}_{00}. \tag{3.31}$$

We can then prescribe wavenumbers α and β and, provided $|\boldsymbol{U}_{jk}| < 1$ to guarantee convergence, solve by truncation and discretization for σ. We truncate the system in the periodic directions with

$$-T_m < m < T_m, \qquad -T_n < n < T_n. \tag{3.32}$$

The wall-normal direction, y, is discretized using the standard pseudo-spectral technique with N Chebyshev polynomials. This procedure reduces the system to an $M \times M$ eigenvalue problem with

$$M = 4N(2T_m + 1)(2T_n + 1). \tag{3.33}$$

All eigenvalue computations are carried out using the Arnoldi routine as implemented in MATLAB, since only the first few eigenvalues and eigenmodes are relevant in linear stability analyses.

3.4.2 Time-periodic states

We now consider the stability of a state which is periodic in time with period T

$$\boldsymbol{U}_s(x, y, z, t) = \boldsymbol{U}_s(x, y, z, t + T). \tag{3.34}$$

The equations governing an infinitesimal perturbation to the state are, as before, equations (3.23). However, with a view to transforming (3.23) into a closed evolution system

and reducing computational memory requirements, we switch from velocity and pressure variables to poloidal-toroidal potentials. Since the velocity is divergence free, we express the velocity as the sum of the poloidal potential ϕ and the toroidal potential ψ

$$\boldsymbol{u} = \nabla \times \nabla \times \phi \boldsymbol{j} + \nabla \times \psi \boldsymbol{j}, \tag{3.35}$$

where $\nabla\times$ denotes the curl operator. The no-slip boundary conditions impose

$$\phi = \phi' = \psi = 0, \tag{3.36}$$

on the walls $y = \pm 1$. We apply the operators $\boldsymbol{j} \cdot \nabla \times \nabla\times$ and $\boldsymbol{j} \cdot \nabla\times$ to the linearized Navier-Stokes equation to form two independent equations for ϕ and ψ

$$\partial_t \nabla^2 \Delta_2 \phi = \left(\frac{1}{Re}\nabla^2 - U\partial_x\right)\nabla^2\Delta_2\phi + U''\partial_x\Delta_2\phi - Ro\,\partial_z\Delta_2\psi - \boldsymbol{j}\cdot\left(\nabla\times\nabla\times\left(\boldsymbol{u}\cdot\nabla\boldsymbol{U}_s + \boldsymbol{U}_s\cdot\nabla\boldsymbol{u}\right)\right), \tag{3.37a}$$

$$\partial_t \Delta_2 \psi = \left(\frac{1}{Re}\nabla^2 - U\partial_x\right)\Delta_2\psi - U'\partial_z\Delta_2\phi + Ro\,\partial_z\Delta_2\phi - \boldsymbol{j}\cdot\left(\nabla\times\left(\boldsymbol{u}\cdot\nabla\boldsymbol{U}_s + \boldsymbol{U}_s\cdot\nabla\boldsymbol{u}\right)\right), \tag{3.37b}$$

where $\Delta_2 = \partial_x^2 + \partial_z^2$ is the two-dimensional Laplacian, and we have assumed that the mean flow is purely streamwise

$$\boldsymbol{U}_0 = U(y,t)\boldsymbol{i}. \tag{3.38}$$

The velocity perturbation $\boldsymbol{u}$ in system (3.37) is mapped to the poloidal-toroidal potentials, $\boldsymbol{\xi} = (\phi, \psi)$, using (3.35)

$$\boldsymbol{u} = \begin{pmatrix} \partial_{xy}^2 & -\partial_z \\ -\Delta_2 & 0 \\ \partial_{yz}^2 & \partial_x \end{pmatrix}\boldsymbol{\xi}. \tag{3.39}$$

It is convenient to write the system (3.37) more succinctly using operator notation

$$\partial_t M\boldsymbol{\xi} = L(\boldsymbol{U}_s)\boldsymbol{\xi} \tag{3.40}$$

$$\implies \partial_t\boldsymbol{\xi} = \mathcal{L}(\boldsymbol{U}_s)\boldsymbol{\xi}, \quad \mathcal{L}(\boldsymbol{U}_s) = M^{-1}L(\boldsymbol{U}_s). \tag{3.41}$$

Since $\boldsymbol{U}_s$ is periodic in time so too is the operator $\mathcal{L}(\boldsymbol{U}_s)$. We now construct the Poincaré map, $P(\boldsymbol{U}_s)$, which is formally given by

$$P(\boldsymbol{U}_s) = \exp\left(\int_0^T \mathcal{L}(\boldsymbol{U_s})dt\right). \tag{3.42}$$

The Poincaré map gives the action of system (3.41) on an arbitrary potential vector $\boldsymbol{\xi}$ over one period. i.e.

$$\boldsymbol{\xi}(\boldsymbol{x}, t+T) = P(\boldsymbol{U}_s)\boldsymbol{\xi}(\boldsymbol{x}, t). \tag{3.43}$$

The eigenvalues μ of $P(\boldsymbol{U}_s)$ are the Floquet multipliers over the period

$$\mu = \mathrm{e}^{\sigma T}, \tag{3.44}$$

from which we determine the exponent σ

$$\sigma = \frac{1}{T}\log\mu. \tag{3.45}$$

En route to computing $P(\boldsymbol{U}_s)$, by Floquet's theorem we have that $\boldsymbol{\xi}$ need not have the same periodicity as $\boldsymbol{U}_s$, so we write

$$\boldsymbol{\xi}(x, y, z, t) = \mathrm{e}^{\mathrm{i}(\alpha x+\beta z)+\sigma t}\sum_{m=-\infty}^{\infty}\sum_{n=-\infty}^{\infty}\hat{\boldsymbol{\xi}}_{mn}(y, t)\mathrm{e}^{\mathrm{i}(m\alpha_s x+n\beta_s z)} \tag{3.46}$$

as we had for $\boldsymbol{q} = (\boldsymbol{u}, p)$ in equation (3.24). The modes $\hat{\boldsymbol{\xi}}_{mn}(y, t)$ are assumed to be periodic in time with the same period as $\boldsymbol{U}_s$. Therefore we can frame (3.41) as a system of infinitely many coupled equations

$$\partial_t\hat{\boldsymbol{\xi}}_{mn} = A_{mn}\hat{\boldsymbol{\xi}}_{mn} + \sum_{j,k}F^{jk}_{mn}\hat{\boldsymbol{\xi}}_{m-j,n-k}, \quad \forall m, n \in \mathbb{Z}. \tag{3.47}$$

As in the case for steady states, we truncate the system in the periodic directions with

$$-T_m < m < T_m, \qquad -T_n < n < T_n. \tag{3.48}$$

and discretize in the wall-normal direction with N Chebyshev polynomials. With the system suitably discretized and truncated, we use the second-order implicit trapezium rule method to advance the equations in time. For

$$y' = f(y, t), \tag{3.49}$$

the trapezium rule gives

$$y_{s+1} = y_s + \frac{h}{2}\big(f(y_s, t_s) + f(y_{s+1}, t_{s+1})\big), \tag{3.50}$$

where $h = t_{s+1} - t_s$. Thus we have

$$\boldsymbol{\xi}_{s+1} = \boldsymbol{\xi}_s + \frac{h}{2}\big(\mathcal{L}_s\boldsymbol{\xi}_s + \mathcal{L}_{s+1}\boldsymbol{\xi}_{s+1}\big), \tag{3.51}$$

$$\big(I - \frac{h}{2}\mathcal{L}_{s+1}\big)\boldsymbol{\xi}_{s+1} = \big(I + \frac{h}{2}\mathcal{L}_s\big)\boldsymbol{\xi}_s, \tag{3.52}$$

$$\boldsymbol{\xi}_{s+1} = \big(I - \frac{h}{2}\mathcal{L}_{s+1}\big)^{-1}\big(I + \frac{h}{2}\mathcal{L}_s\big)\boldsymbol{\xi}_s, \tag{3.53}$$

where I is the identity operator. The trapezium rule is chosen because we found that explicit methods were generally unstable and higher-order methods have greater computational memory requirements at each time step. The action of the Poincaré map is found by time-stepping the equations over one period T. At each time step the base flow $\boldsymbol{U}_s$ must be updated. We do this by Fourier series approximation of the base flow at the desired time point. From DNS of $\boldsymbol{U}_s$ over one period we save the flowfield at 100 time points, and from these we numerically approximate the temporal Fourier transform

$$\tilde{\boldsymbol{U}}_\ell = \int_0^T \boldsymbol{U}_s(t)\mathrm{e}^{\frac{\mathrm{i}2\pi\ell t}{T}}\,dt, \tag{3.54}$$

so that the flowfield at an arbitrary time t can be expressed by the Fourier series

$$\boldsymbol{U}_s(t) = \sum_{\ell=-\infty}^{\infty} \tilde{\boldsymbol{U}}_\ell \mathrm{e}^{-\frac{\mathrm{i}2\pi\ell t}{T}}. \tag{3.55}$$

A summation truncation of $-30 \leq \ell \leq 30$ is used. Comparison of the Fourier series approximation of the flowfield with a previously saved field has an error $O(10^{-11})$. The advantages of using the poloidal-toroidal potentials rather than primitive variables are that we do not need an extra calculation to update the pressure at each time step, and the problem size is now reduced by half such that the operators are approximated by square matrices of order $M = 2N(2T_m + 1)(2T_n + 1)$. This eases the memory requirements for each stability calculation and allows for higher truncations to be reached. Time-stepping of the linear perturbation equations and the final eigenvalue calculations are performed in MATLAB, while DNS of $\boldsymbol{U}_s$ required for the temporal Fourier transform is carried out by Channelflow (Gibson (2008)).

3.4.3 Global stability

Having now outlined how to find the stability of a spatially-periodic state $\boldsymbol{U}_s(\alpha_s, \beta_s, Re, Ro)$ to an infinitesimal perturbation, we can thus produce a stability map by finding the exponents $\sigma(\alpha, \beta, \alpha_s, \beta_s, Re, Ro)$ over all de-tuning parameters α and β. In this way, we can determine whether a state is globally stable. Owing to the periodicity of $\boldsymbol{U}_s$ there is some saving in the range of α and β at which σ must be computed to find the global stability properties. In what follows, we discuss the relevant (α, β) stability domain for

a steady base flow, however the argument for unsteady states is analogous. Recall (3.25)

$$A_{mn}\hat{\boldsymbol{q}}_{mn} + \sum_{j,k} F^{jk}_{mn}\hat{\boldsymbol{q}}_{m-j,n-k} = \sigma B\hat{\boldsymbol{q}}_{mn}, \quad \forall m,n \in \mathbb{Z}. \tag{3.56}$$

We can consider the operators A_{mn} and F^{jk}_{mn} as functions of α and β with α_s, β_s, Re and Ro fixed. Clearly

$$A_{mn}(\alpha+\alpha_s,\beta+\beta_s) = A_{m+1,n+1}(\alpha,\beta), \tag{3.57}$$

and

$$F^{jk}_{mn}(\alpha+\alpha_s,\beta+\beta_s) = F^{jk}_{m+1,n+1}(\alpha,\beta). \tag{3.58}$$

Since the system (3.25) is completed by summation over $m,n \in \mathbb{Z}$, we have that

$$\sigma(\alpha+\alpha_s,\beta+\beta_s) = \sigma(\alpha,\beta). \tag{3.59}$$

By induction we can generalize this to

$$\sigma(\alpha+p\alpha_s,\beta+q\beta_s) = \sigma(\alpha,\beta), \quad p,q \in \mathbb{Z}. \tag{3.60}$$

Furthermore, we have that

$$A_{mn}(-\alpha,-\beta) = A_{-m,-n}(\alpha,\beta)^*, \tag{3.61}$$

and

$$F^{jk}_{mn}(-\alpha,-\beta) = F^{-j,-k}_{-m,-n}(\alpha,\beta)^*, \tag{3.62}$$

where $.^*$ denotes the (element-wise) complex conjugate, and we have used

$$\boldsymbol{U}_{jk}(y)^* = \int_0^{\frac{2\pi}{\alpha}}\int_0^{\frac{2\pi}{\beta}} \boldsymbol{U}_s(x,y,z)\mathrm{e}^{\mathrm{i}(j\alpha_s x + k\beta_s z)}\,dxdz = \boldsymbol{U}_{-j,-k}. \tag{3.63}$$

Suppose we have found $\sigma = \sigma(\alpha,\beta)$ which satisfies

$$A_{mn}(\alpha,\beta)\hat{\boldsymbol{q}}_{mn} + \sum_{j,k} F^{jk}_{mn}(\alpha,\beta)\hat{\boldsymbol{q}}_{m-j,n-k} = \sigma B\hat{\boldsymbol{q}}_{mn}, \quad \forall m,n \in \mathbb{Z} \tag{3.64}$$

and we wish to find $\tilde{\sigma} = \sigma(-\alpha,-\beta)$

$$A_{mn}(-\alpha,-\beta)\tilde{\boldsymbol{q}}_{mn} + \sum_{j,k} F^{jk}_{mn}(-\alpha,-\beta)\tilde{\boldsymbol{q}}_{m-j,n-k} = \tilde{\sigma} B\tilde{\boldsymbol{q}}_{mn}, \quad \forall m,n \in \mathbb{Z}. \tag{3.65}$$

Then using (3.61) and (3.62) we have

$$A_{-m,-n}(\alpha,\beta)^*\tilde{\boldsymbol{q}}_{mn} + \sum_{j,k} F^{-j,-k}_{-m,-n}(\alpha,\beta)^*\tilde{\boldsymbol{q}}_{m-j,n-k} = \tilde{\sigma} B\tilde{\boldsymbol{q}}_{mn}, \quad \forall m,n \in \mathbb{Z}. \tag{3.66}$$

Taking the conjugate of (3.64) gives

$$A_{mn}(\alpha,\beta)^*\hat{\boldsymbol{q}}^*_{mn} + \sum_{j,k} F^{jk}_{mn}(\alpha,\beta)^*\hat{\boldsymbol{q}}^*_{m-j,n-k} = \sigma^* B\hat{\boldsymbol{q}}^*_{mn}, \quad \forall m,n\in\mathbb{Z} \tag{3.67}$$

and since these equations must be satisfied for $m,n,j,k\in\mathbb{Z}$ we conclude that

$$\tilde{\sigma}=\sigma^* \quad \Longrightarrow \quad \sigma(-\alpha,-\beta)=\sigma(\alpha,\beta)^*. \tag{3.68}$$

Now, suppose we wish to find

$$\sigma=\sigma(r\alpha_s, s\beta_s), \quad \text{with } \frac{1}{2}<r,s<1. \tag{3.69}$$

Then

$$\sigma=\sigma(-r\alpha_s,-s\beta_s)^*=\sigma(-r\alpha_s+\alpha_s,-s\beta_s+\beta_s)^* \tag{3.70}$$

$$=\sigma((1-r)\alpha_s,(1-s)\beta_s)^*. \tag{3.71}$$

Hence the global stability properties of $\boldsymbol{U}_s$ can be determined for de-tuning wavenumbers in the domain

$$0\le\alpha\le\frac{\alpha_s}{2}, \quad 0\le\beta\le\frac{\beta_s}{2}. \tag{3.72}$$

If $\boldsymbol{U}_s$ is periodic in only one direction and independent of the other, such as the Taylor vortex solution in §3.5.1, then the stability domain becomes the semi-infinite strip

$$0\le\alpha<\infty, \quad 0\le\beta\le\frac{\beta_s}{2}. \tag{3.73}$$

3.4.4 Convergence

By variation of the truncation parameters T_m and T_n and the Chebyshev discretization N we can assess the convergence of the eigenvalues σ for a given solution $\boldsymbol{U}_s$. Our computational capability puts an upper limit on the truncation and discretization we can use. Running on a machine with 24GB RAM, we find that a matrix size $M\le 17000$ can be handled. For a Taylor vortex solution we can truncate to a high degree of accuracy, since the state is streamwise independent and truncation is required in the spanwise direction only. For fully three-dimensional flows we cannot truncate to the same degree, though we still find good convergence of the leading eigenmode. In Tables 3.1, 3.2, 3.3 and 3.4 we list the leading eigenvalues from stability calculations on a Taylor vortex, a wavy vortex (see WVF §3.7.1) and an oscillatory wavy vortex (see oWVF §3.7.3) at various truncations.

		N		
		17	25	49
T_n	6	0.025574	0.025573	0.025573
	7	0.025726	0.025725	0.025725
	8	0.025687	0.025686	0.025686
	9	0.025692	0.025691	0.025691
	10	0.025691	0.025690	0.025690
	11	0.025691	0.025690	0.025690
	12	0.025691	0.025690	0.025690
	13	0.025691	0.025690	0.025690
	14	0.025691	0.025690	0.025690
	15	0.025691	0.025690	0.025690
	16	0.025691	0.025690	0.025690
	17	0.025691	0.025690	0.025690
	18	0.025691	0.025690	0.025690
	19	0.025691	0.025690	0.025690
	20	0.025691	0.025690	0.025690

Table 3.1: Values of the leading eigenvalue σ for a Taylor vortex solution with $(\alpha, \beta, \beta_s, Re, Ro) = (0.5, 0, 0.5236, 2.513, 100, 0.1)$.

		T_n					
		4	5	6	7	8	9
T_m	4	0.023226	0.021836	0.021661	0.021647	0.021648	0.021648
	5	0.022822	0.021309	0.021169	0.021164	0.021164	0.021164
	6	0.022805	0.021334	0.021163	0.021163	0.021163	0.021163
	7	0.022830	0.021351	0.021187	0.021184	0.021185	-
	8	0.022836	0.021356	0.021191	0.021189	-	-
	9	0.022834	0.021356	0.021191	-	-	-

Table 3.2: Values of the leading eigenvalue σ for a wavy vortex solution with $N = 17$ and $(\alpha, \beta, \alpha_s, \beta_s, Re, Ro) = (0, 1.2565, 0.5236, 2.513, 100, 0.1)$.

		T_n				
		4	5	6	7	8
T_m	4	0.023229	0.021838	0.021663	0.021649	0.021650
	5	0.022830	0.021317	0.021178	0.021172	-
	6	0.022817	0.021345	0.021174	-	-
	7	0.022844	0.021364	-	-	-
	8	0.022851	-	-	-	-

Table 3.3: Values of the leading eigenvalue σ for a wavy vortex solution with $N = 25$ and $(\alpha, \beta, \alpha_s, \beta_s, Re, Ro) = (0, 1.2565, 0.5236, 2.513, 100, 0.1)$.

		T_n			
		3	4	5	6
T_m	3	0.002903	0.006839	0.006993	0.006992
	4	0.002937	0.006840	0.007024	0.007016
	5	0.002933	0.006837	0.007021	0.007014
	6	0.002933	0.006838	0.007021	0.007014

Table 3.4: Values of the leading exponent σ for oscillatory wavy vortex flow $(\alpha, \beta, \alpha_s, \beta_s, Re, Ro) = (0.1, 0.375, 0.8, 3, 100, 0.55)$, $N = 17$, $h = \frac{T}{500} = 0.03844$.

3.4.5 Validation

Predictions from the stability calculations are validated against the Navier-Stokes solver SIMSON (Chevalier *et al.* (2007)). We compare the growth rates predicted by the stability analysis with growth rates of a divergence-free, random disturbance comprised of Stokes modes which is added to the solution and integrated forwards. A domain-doubling technique is used to test growth rates of a subharmonic perturbation; the solution is repeated in the periodic direction such that subharmonic disturbances can be superimposed on to the original solution. In Figure 3.4 we plot the evolution of the perturbation energy-density

$$E = \frac{\tilde{E}}{\rho} = \frac{1}{2}\int_{\mathcal{D}} u^2 + v^2 + w^2 dV, \tag{3.74}$$

of a given mode, where ρ is the fluid density, $\mathcal{D}$ is the periodic domain and $\tilde{E}$ is the physical kinetic energy. We can then compare the growth rate of the perturbation as observed from simulations with the prediction made by the stability analysis. As can be seen in Figure 3.4, excellent agreement is obtained in each case.

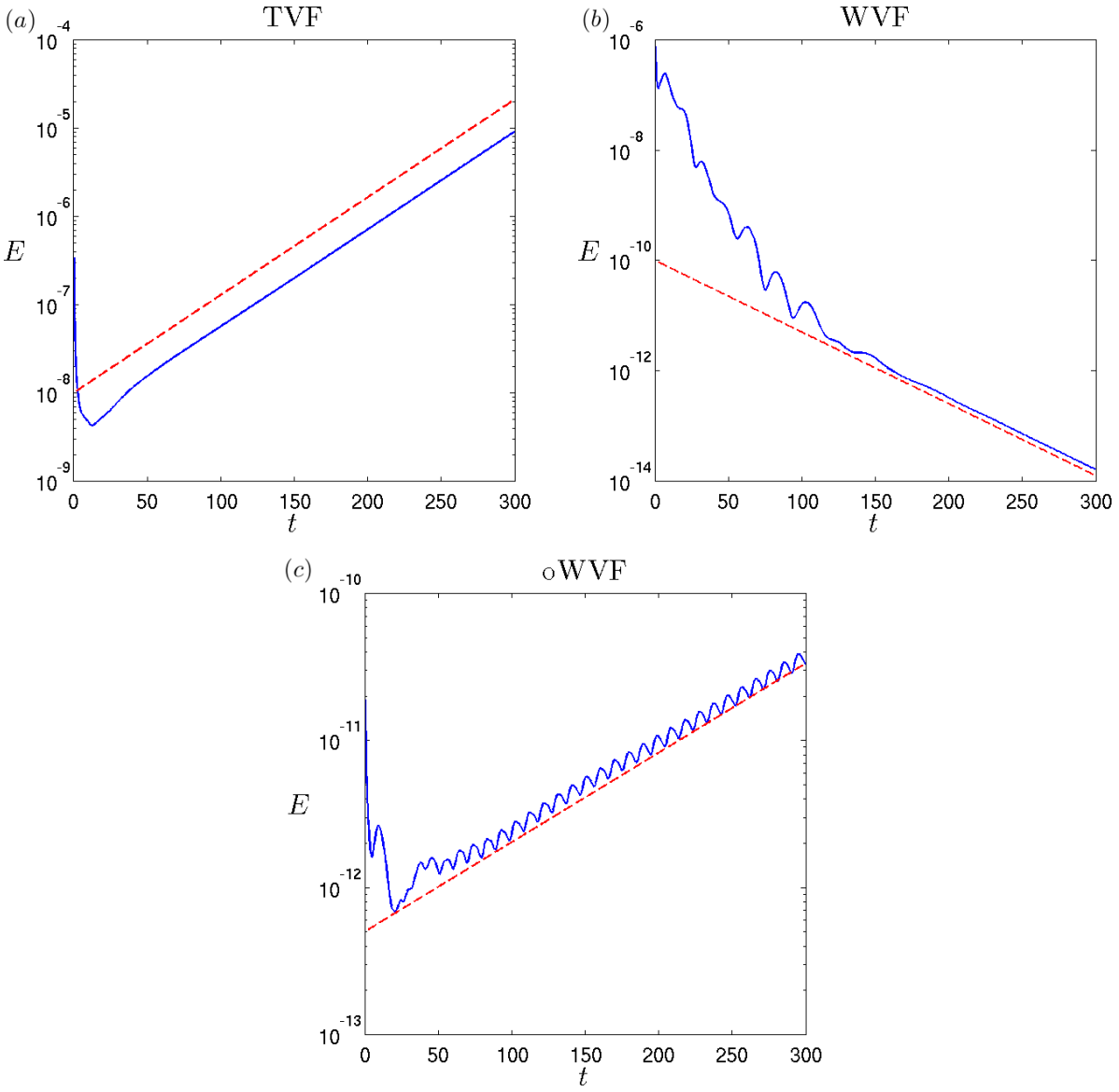

Figure 3.4: (a) TVF with $(\alpha, \beta, \beta_s, Re, Ro) = (0.5, 0, 2, 100, 0.11)$, (b) WVF with $(\alpha, \beta, \alpha_s, \beta_s, Re, Ro) = (0, 1, 0.5, 2, 100, 0.11)$ and (c) oWVF with $(\alpha, \beta, \alpha_s, \beta_s, Re, Ro) = (0.1, 0.375, 0.8, 3, 100, 0.55)$. In each panel, the blue curve is the perturbation evolution from DNS of the Navier-Stokes equations and the red dashed line is the Floquet theory prediction based on the leading growth rate σ_r.

3.5 Secondary states

In §§3.5.1 to 3.5.3 we characterize the secondary states in supercritical RPCF. We investigate the effect of rotation on the solutions by making bifurcation diagrams in (Ro, E_{cf})-sapce for $Re = 100$. In each bifurcation diagram we include information on the harmonic stability of the state i.e. the stability of the solution to a perturbation with $\alpha = \alpha_s$ and $\beta = \beta_s$ as defined in (3.24). Unstable states are represented by a dashed line while stable states are indicated with an unbroken line.

3.5.1 Taylor vortex flow

A bifurcation initiated by the leading streamwise vortex instability eigenmode results in Taylor vortex flow (TVF). TVF consists of a pair of streamwise independent counter-rotating vortices and counter-propagating streaks. The streamwise streak component of the velocity field changes appearance as the geometry of the vortices varies from long to short spanwise wavelength, with the streaks become more rounded as the wavelength is decreased. The ellipticity and orientation of the vortical part of the flowfield also changes as the wavenumber increases. These changes in the flowfields can be seen in Figure 3.5. We plot bifurcations of TVF from the primary state ($E_{cf} = 0$) in Figure 3.7. The Figure includes curves of the growth rate of the linear mode responsible for each bifurcation from which we can see that each bifurcation is transcritical, with TVF appearing only when the linear mode has a positive growth rate. TVF only becomes harmonically unstable for $\beta = 4$, in the range $0.084 < Ro < 0.91$. The Taylor vortices possess mirror symmetry $\mathbf{Z}$, where

$$\mathbf{Z}[u, v, w](x, y, z) = [u, v, -w](x, y, -z). \tag{3.75}$$

This symmetry feature is apparent from the flowfields in Figures 3.5, with the axis of reflection being the mid-point of the spanwise domain.

3.5.2 Second Taylor vortex flow

As noted by Nagata (2013) the primary flow loses stability to a second streamwise vortex eigenmode, prompting a bifurcation to a second Taylor vortex flow (TVF_2). TVF_2 has a double layered vortical structure, with a pair of counter-rotating vortices aligned in the wall-normal direction, alongside another pair of counter-rotating vortices in the spanwise direction, as can be seen in Figure 3.6. The mirror symmetry $\mathbf{Z}$ holds in TVF_2, with the axis of reflection the mid-point of the spanwise domain in our Figures. Bifurcations of TVF_2 in Ro are plotted in Figure 3.8. The trajectories of the solutions are reminiscient of those of the first TVF in the (Ro, E_{cf}) parameter space, and each bifurcation is similarly transcritial. TVF_2 is unstable at each point in our bifurcation diagrams.

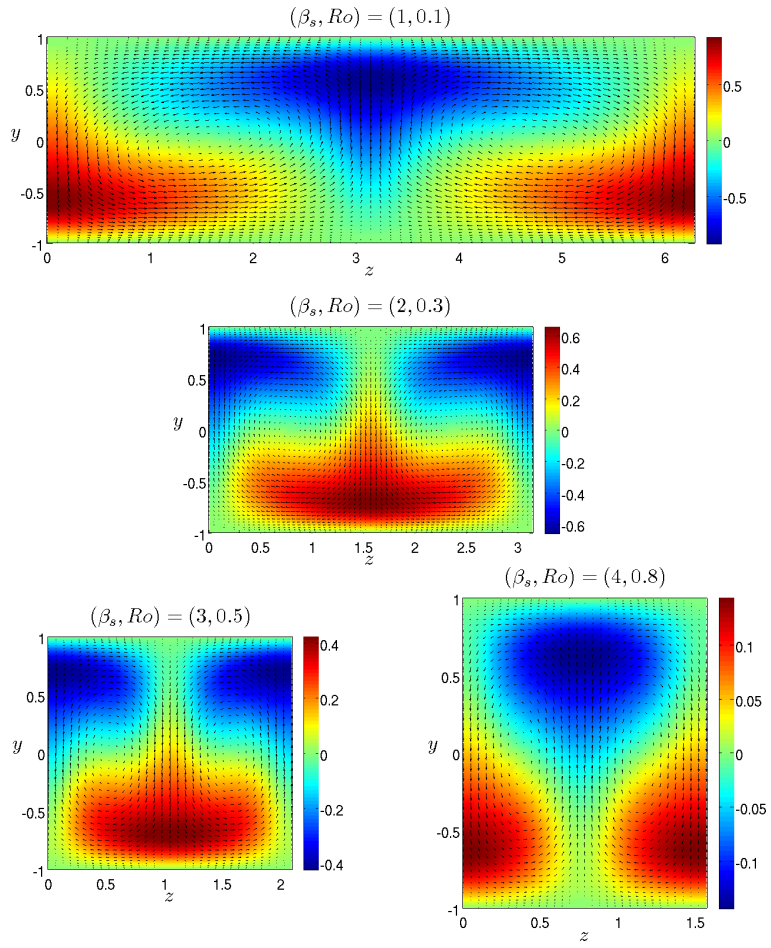

Figure 3.5: Taylor vortex flowfields at various spanwise wavelengths and rotation numbers. $Re = 100$ in all cases. The orientation of the vortices and the structure of the streamwise streaks are subject to change as β_s and Ro are varied.

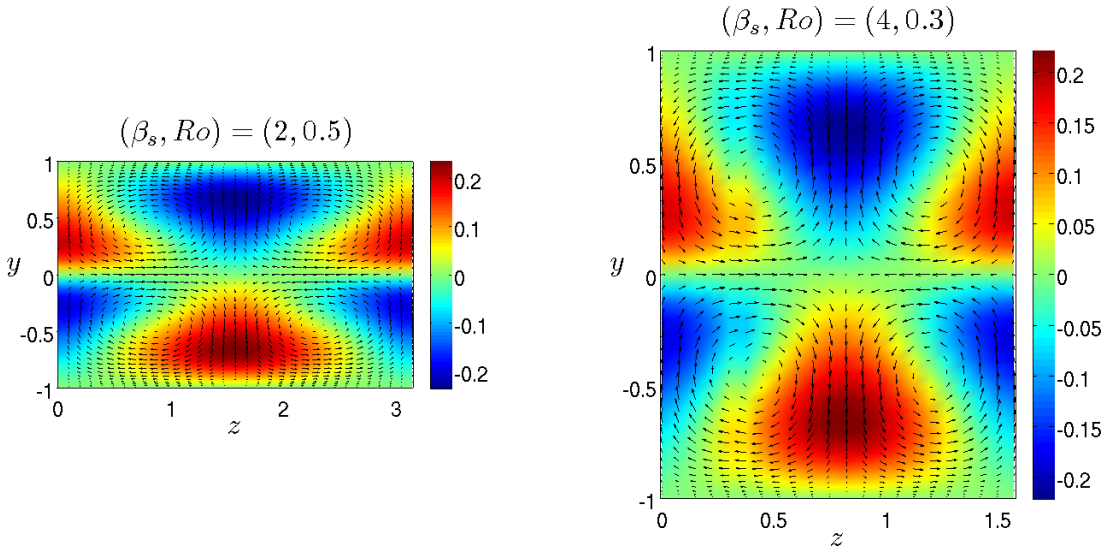

Figure 3.6: Flowfields of TVF_2 at $Re = 100$ for $\beta_s = 2$, $Ro = 0.5$ and $\beta = 4$, $Ro = 0.3$.

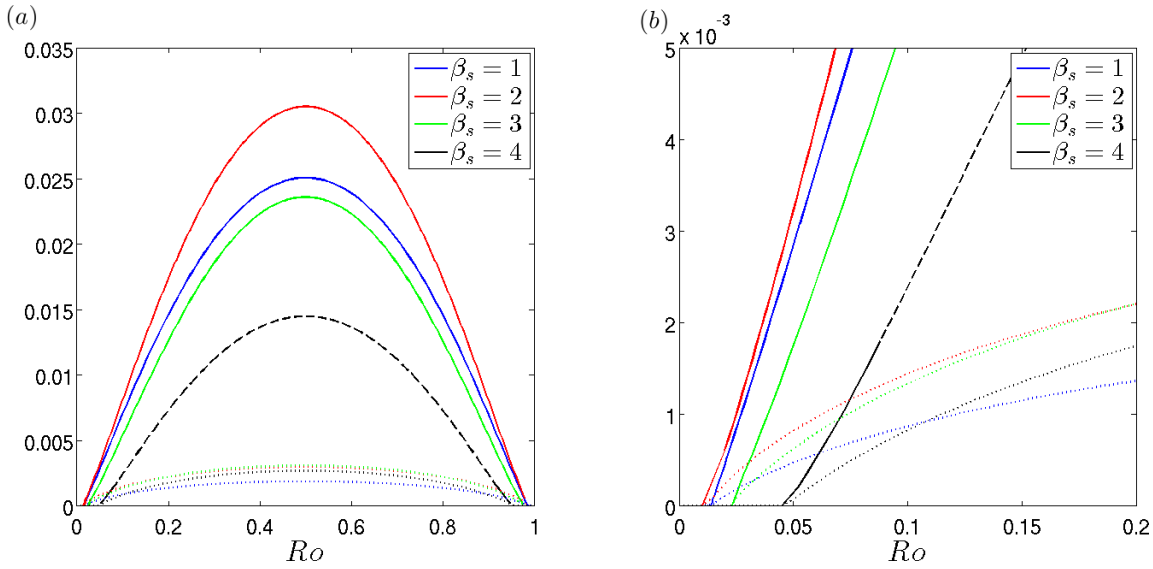

Figure 3.7: (a) Taylor vortex bifurcations for various spanwise wavenumbers. $Re = 100$ in each case. In each case the growth rate of the linear mode responsible for the bifurcation is plotted as a dashed line of the colour corresponding to the TVF trajectory. The linear growth rates are scaled $\frac{\omega_r}{Re}$. (b) Blow-up of the low Ro region where the loss of stability of TVF with $\beta_s = 4$, and the emergence of each TVF with the linear mode, can be clearly seen.

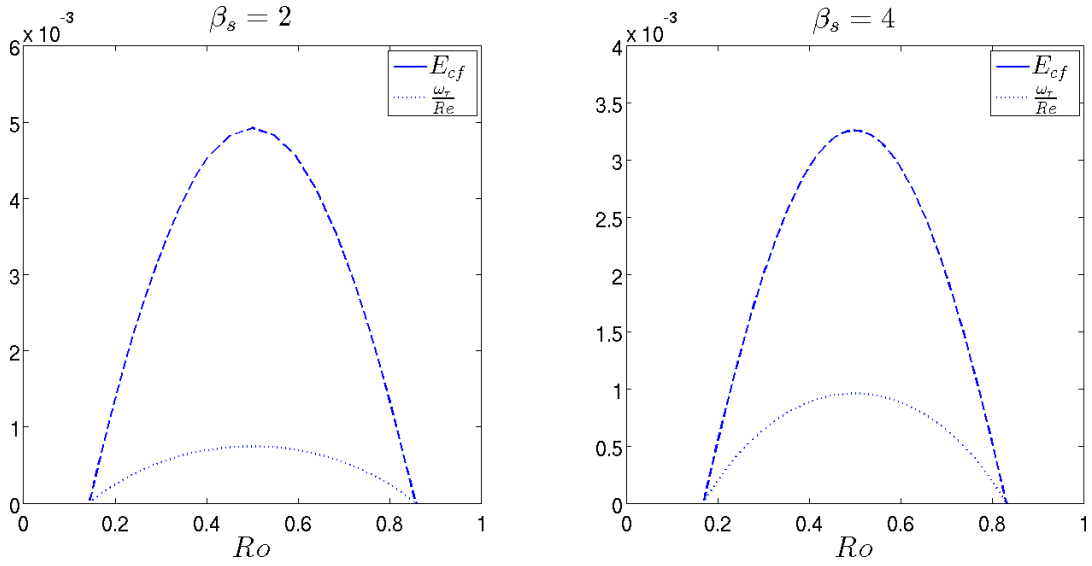

Figure 3.8: Bifurcations of TVF_2 at $\beta_s = 2$ and $\beta = 4$, with $Re = 100$ in both cases. The linear mode responsible for the bifurcation is included in each panel. Both solutions are unstable along their entire trajectories.

3.5.3 Oblique vortex flow

In addition to losing stability to streamwise independent perturbations, linear stability theory tells us that the primary state can also be de-stabilized by oblique waves. As α is increased from zero, we generically find that the two unstable oblique modes move closer together until they merge to become a pair of modes with non-zero frequency, i.e. with $\omega_i \neq 0$. An example of this is shown in Figure 3.9. The two zero frequency unstable modes develop into steady, nonlinear oblique vortex flow (OVF). OVF, like TVF, takes the form of pairs of counter-rotating vortices, but unlike TVF the counter-propagating streaks are oblique; inclined at an angle $\theta = \tan\frac{\alpha}{\beta}$ away from the streamwise direction. We investigate the trajectories of OVF in the (Ro, E_{cf}) subspace as it bifurcates from the linear shear profile, for the case $(\beta, Re) = (2, 100)$. We find that for $\alpha \lesssim 0.225$ there are upper and lower solutions which bifurcate from each unstable eigenmode. We name these OVF_1 and OVF_2 respectively. In Figure 3.10 we see that each solution forms two distinct curves in (Ro, E_{cf}). OVF_1 is harmonically stable for a large portion of its bifurcation, whereas the OVF_2 is always unstable. We note that OVF_1 is unstable for $Ro \lesssim 0.1$, though we do not pursue tertiary bifurcations here. As α is increased the two solutions merge to form a closed trajectory in (Ro, E_{cf}) and a separate, disjointed set of high and low rotation solutions. This is shown in Figure 3.11. A depiction of the flowfields of two OVF solutions is given in Figure 3.12. OVF has a Taylor-Couette flow analogue in spiral vortex flow (SPI), which has recently been studied by Hoffmann *et al.* (2009), Altmeyer *et al.* (2010) and Deguchi & Altmeyer (2013), though in these cases the spiral vortices are travelling waves, rather than steady flows as considered here.

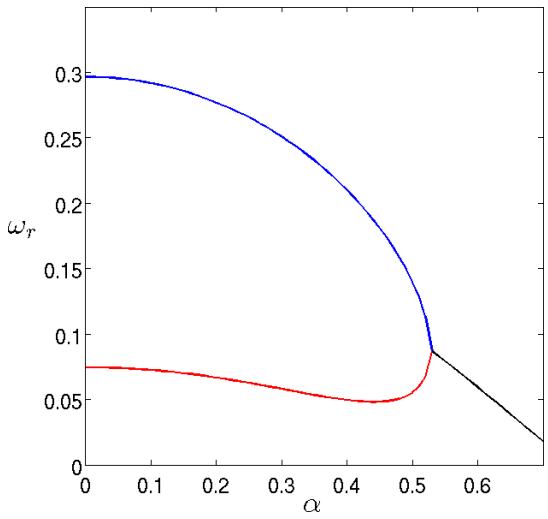

Figure 3.9: Linear stability modes $(\beta, Re, Ro) = (2, 100, 0.5)$. The blue corresponds to the first unstable mode, red is the second mode and black is the merged mode with $\omega_i \neq 0$.

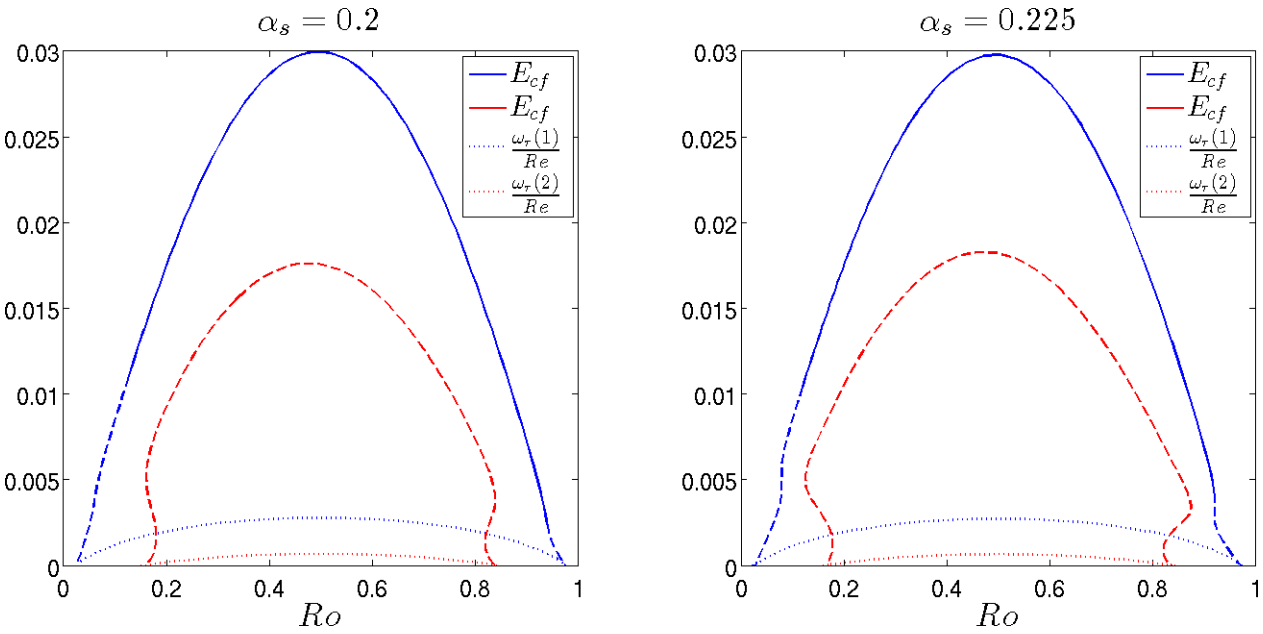

Figure 3.10: OVF_1 and OVF_2 for $(\alpha_s, \beta_s, Re) = (0.2, 2, 100)$ and $(\alpha_s, \beta_s, Re) = (0.225, 2, 100)$. The growth rates of the linear modes which initiate bifurcation from the primary state are indicated by dotted lines.

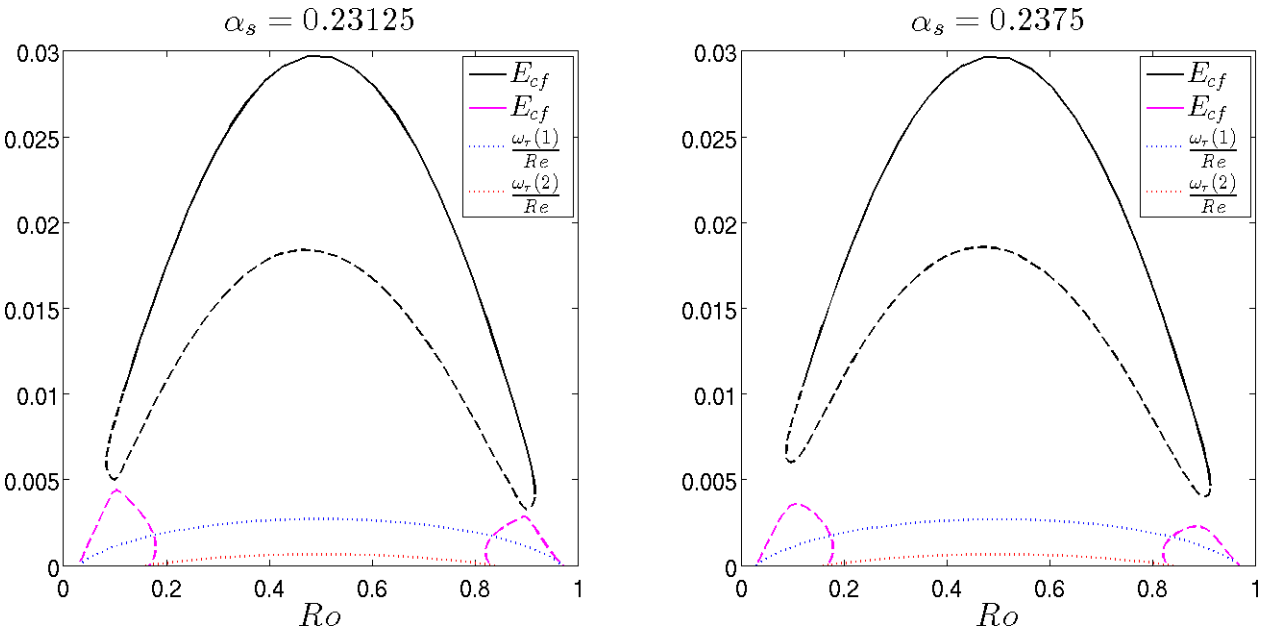

Figure 3.11: Merged OVF solutions for $(\alpha_s, \beta_s, Re) = (0.23125, 2, 100)$ and $(\alpha_s, \beta_s, Re) = (0.2375, 2, 100)$. The curves are coloured differently to Figure 3.10 to indicate that merging has taken place. The outer and inner solutions of each curve can still be considered OVF_1 and OVF_2, respectively. The growth rates of the linear modes which initiate bifurcation from the primary state are indicated by dotted lines.

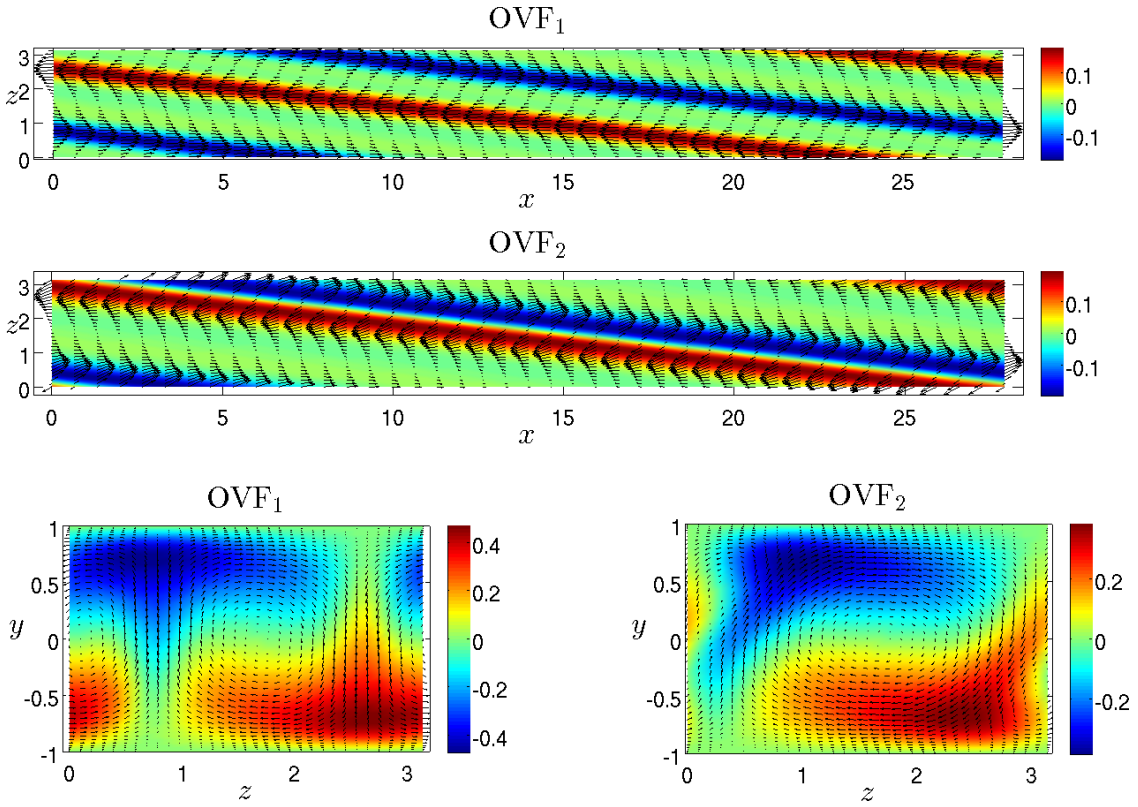

Figure 3.12: Flowfields of the oblique vortex flows OVF_1 and OVF_2 for $(\alpha_s, \beta_s, Re, Ro) = (0.225, 2, 100, 0.5)$.

3.5.4 Summary of secondary states

The secondary states which we have discussed fall into two categories: streamwise independent and streamwise periodic states. Two streamwise independent states, TVF and TVF_2 have been introduced and their bifurcations in Ro have been calculated. Streamwise periodic states OVF_1 and OVF_2 bifurcate as distinct solutions at low streamwise wavenumber α_s before merging as α_s is increased. It is to be expected that any transition from the primary Couette flow will pass through one of these secondary states.

3.6 Stability of Taylor vortex flow

In this section we determine the global stability of Taylor vortex flow. In particular we focus on the stability of the first Taylor vortex solution, labelled TVF, since the most unstable primary instability typically develops into this solution. Therefore it is useful to characterize the secondary instabilities that emerge when TVF loses stability. Let β_s denote the spanwise wavenumber of a Taylor vortex pair. By varying the detuning parameters α and β from equation (3.24), we can determine the global stability of a Taylor vortex solution. It is typically found that the least stable perturbations are either streamwise periodic and tuned to the fundamental, i.e. $(\alpha, \beta) = (\alpha, 0)$, or of Eckhaus type with $(\alpha, \beta) = (0, \beta)$ (Eckhaus (1965)). From §3.4.3 we have that the wavenumber domain which spans the full stability properties is the semi-infinite strip

$$0 \leq \alpha < \infty, \quad 0 \leq \beta \leq \frac{\beta_s}{2}. \tag{3.76}$$

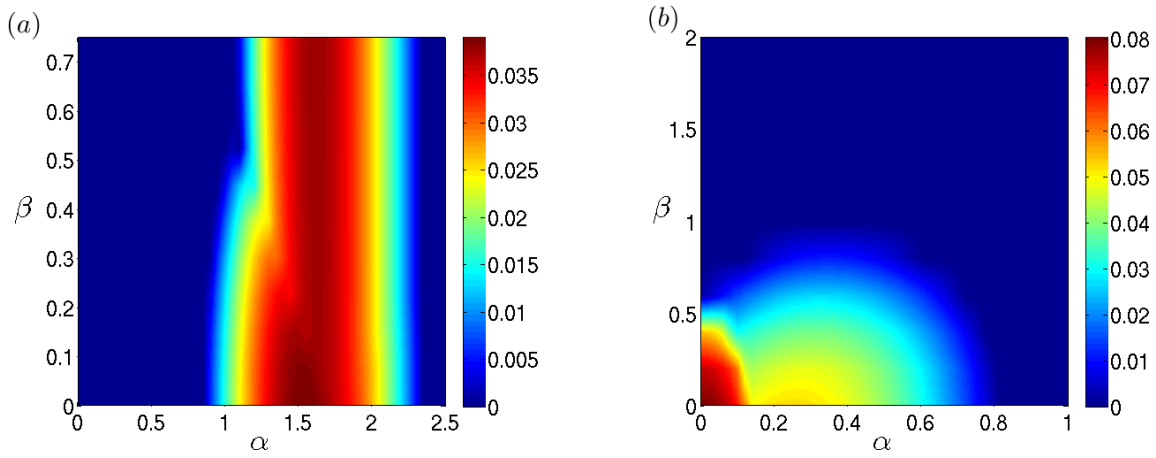

Figure 3.13: Global stability of TVF with (a) $(\beta_s, Re, Ro) = (1.5, 100, 0.7)$ and (b) $(\beta_s, Re, Ro) = (4, 100, 0.3)$, with perturbation growth rates $\sigma_r \geq 0$ coloured. In (a) the least stable perturbation is streamwise periodic and tuned to the fundamental spanwise wavenumber. In (b) the least stable perturbation is harmonic, with $\alpha = \beta = 0$.

In Figure 3.13 we plot the global stability properties of two typical TVF profiles. To clearly highlight the unstable parameter regions, we plot the intersection of the growth rate σ_r with the neutral plane $\sigma_r = 0$, such that all stable regions are coloured dark blue regardless of the value of the decay rate. In each of the cases considered we find that the least stable perturbation is tuned to the fundamental, i.e. has spanwise detuning wavenumber $\beta = 0$. As such, we choose three Reynolds numbers $Re = 50, 100$ and 250, and calculate the streamwise secondary instabilities at various β_s. The chosen Reynolds numbers roughly correspond to the start, the middle and the end of the transition region,

as observed experimentally in Tsukahara *et al.* (2010). The spanwise wavenumbers of the Taylor vortices, β_s, are chosen such that they are spread across the linearly unstable region of the primary flow, as shown in Figure 3.14.

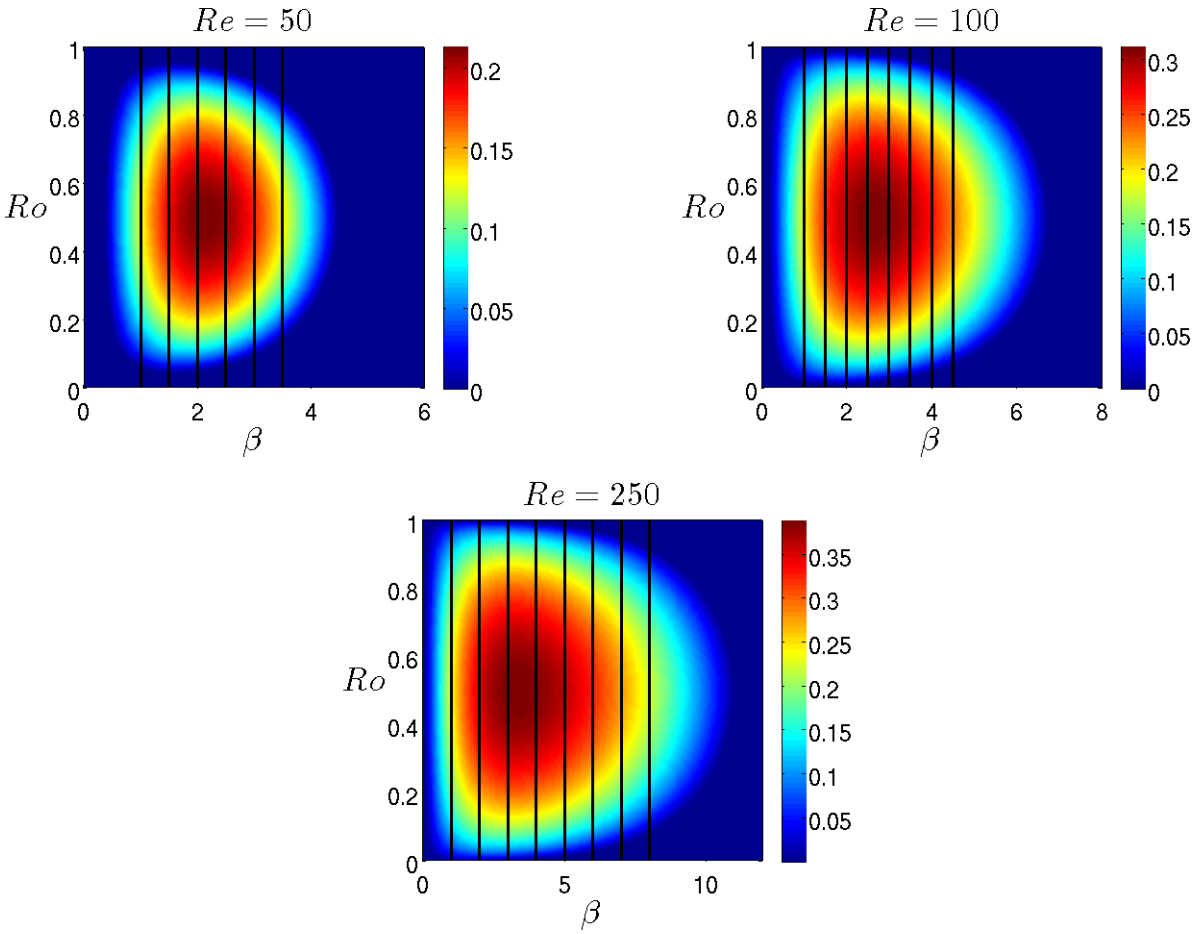

Figure 3.14: Colour-plots of the primary instability growth rate ω_r at $Re = 50, 100, 250$. The thick black lines mark the locations of β_s for the Taylor vortices considered at each Re.

To create each stability map in this section, minimum grids of 100×200 points in (α, Ro) or (β, Ro) are used. The number of points used in each map varies, as we refine in the grid to better resolve cases with complicated instability regions. The colouring of the map is then interpolated to give a smooth visual effect. An example is given in Figure 3.15.

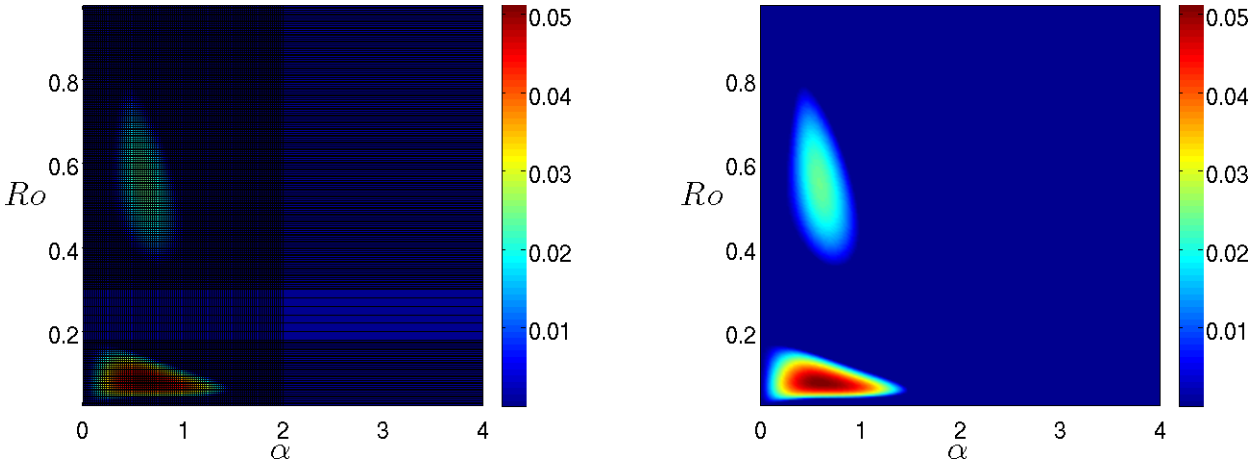

Figure 3.15: The colouring of the plot on the left is interpolated to give the plot on the right.

3.6.1 Streamwise instability maps

In Figures 3.16, 3.21 and 3.26 we plot the streamwise instabilities which affect Taylor vortices of various spanwise wavelengths for $Re = 50$, $Re = 100$ and $Re = 250$. In Figure 3.16 where we have $Re = 50$, for $\beta_s = 1, 1.5, 2$ and 2.5 we see a wedge shaped region of instability for $0 \lesssim Ro \lesssim 0.2$ and $0 \lesssim \alpha \lesssim 0.6$. This is known as wavy vortex instability (Davey *et al.* (1968), Nagata (1986, 1998)), and we plot examples of its mode structure and eigenvalues of the stability operator in a case with wavy instability, in Figures 3.17 and 3.18. The wavy instability causes Taylor vortices to lose stability to structures elongated in the streamwise direction, with modulated high-velocity/low-velocity streaks. Throughout the wedge regions in Figure 3.16, the stability operator has one unstable eigenmode with $\sigma_i = 0$. As the spanwise wavenumber of the Taylor vortices increases to $\beta_s = 3$ the wavy instability is no longer present, and the vortices become stable to all streamwise perturbations. For $\beta_s = 1$ a region of instability occurs at high rotation parameters, $0.6 \lesssim Ro \lesssim 1$ and $0.5 \lesssim \alpha \lesssim 1.5$. This is known as twist vortex instability (Weisshaar *et al.* (1991)). There are two unstable modes, the wavy twist and twist vortex modes, which compete to de-stabilize the Taylor vortices. We show examples of each mode and the stability eigenvalues in Figures 3.19 and 3.20. We find that the wavy twist mode has a larger growth rate compared to the twist mode for $Re = 50$. The twist instabilities are more sensitive to the spanwise wavelength of the TVF than the wavy instability, as they are not observed for $\beta_s \geq 1.5$.

An increase in Re has the generic effect of increasing the range and strength of instabilities across the range of TVF, as can be seen for $Re = 100$ Figure 3.21. The wavy vortex instability maintains the wedge shape observed for $Re = 50$, though the region

stretches to $\alpha > 1$ for $\beta_s = 2.6, 3$, and is confined to a smaller Ro range in comparison to $Re = 50$. For $0.4 \lesssim Ro \lesssim 1$ and $\beta_s = 1, 1.5$ we see a region of twist instabilities. Whichever mode is least stable is dependent on α and Ro, as it switches between the wavy twist and twist mode in (α, Ro)-space. Figure 3.22 gives an example of this. A mid-Ro instability emerges for $\beta_s = 2.5$ and strengthens as β_s increases to 3.5. The stability operator has a pair of complex conjugate modes in this case so we term this the oscillatory wavy instability, since we expect unstable perturbations to oscillate in time as their amplitude grows. The instability first occurs in the range $0.5 \lesssim \alpha \lesssim 1$, giving the modes a streamwise elongated appearance similar to the low-Ro wavy instability modes. This instability was noted by Nagata (1988), whose attention was restricted to Taylor vortices with spanwise wavelength $\beta_s = 1.5585$, in which case the instability first emerges for $Re \approx 137.5$. We plot examples of the mode and the eigenvalues of the stability operator in Figures 3.23 and 3.25. As β_s increases the range of α over which the oscillatory instability is present decreases until the region merges with a harmonic instability region in $\beta_s = 4$. The harmonic instability persists for $\beta_s = 4.5$. We find that the unstable mode in this case leans against the Taylor vortex streaks causing them to be tilted in the spanwise direction, therefore we call this the skew instability. The mode is depicted in Figure 3.24, and its stability operator eigenvalues are shown in Figure 3.25. Note in Figure 3.25 for the operators with skew instability, there is an eigenvalue close to zero, which we will call σ^0. When calculating the stability of a periodic solution to harmonic perturbations, we expect zero eigenvalues to appear as an indication that the state is indeed a solution to the governing equations. For our calculations, we compute $\sigma_r^0 < 10^{-6}$, which we interpret as an indication of the accuracy of our code.

The stability maps for $Re = 250$ in Figure 3.26 show instabilities covering greater proportions of the (α, Ro) domain than was covered for $Re = 50, 100$. The instabilities themselves, however, are the same as those which appeared for lower Re. For $\beta_s = 1$ a region of wavy twist instability dominates (α, Ro)-space, with a small region of wavy instability at low Ro. The wedge shaped region of wavy instability from $Re = 50, 100$ is present again for $\beta_s = 2$, at low Ro, and a thin strip of oscillatory instability appears for $Ro \approx 0.02$ and $1 \lesssim \alpha \lesssim 3$. For $\beta_s = 2$ at higher Ro, there are three distinct regions of instability. Two oscillatory instabilities account for the two lower α regions, while a combination of steady wavy twist and twist instabilities dominate for the higher α region. For $\beta_s = 3$ and 4 the oscillatory instability dominates over $0.1 \lesssim Ro \lesssim 0.9$, with a wedge region of steady wavy instability persisting for $Ro \lesssim 0.1$. For $\beta_s \geq 5$ the harmonic skew instability dominates, and instabilities have increasingly longer streamwise wavelengths. Unlike the cases for $Re = 50, 100$, there are no regions other than close to the linear stability boundary where the Taylor vortices for $Re = 250$ are stable to streamwise perturbations.

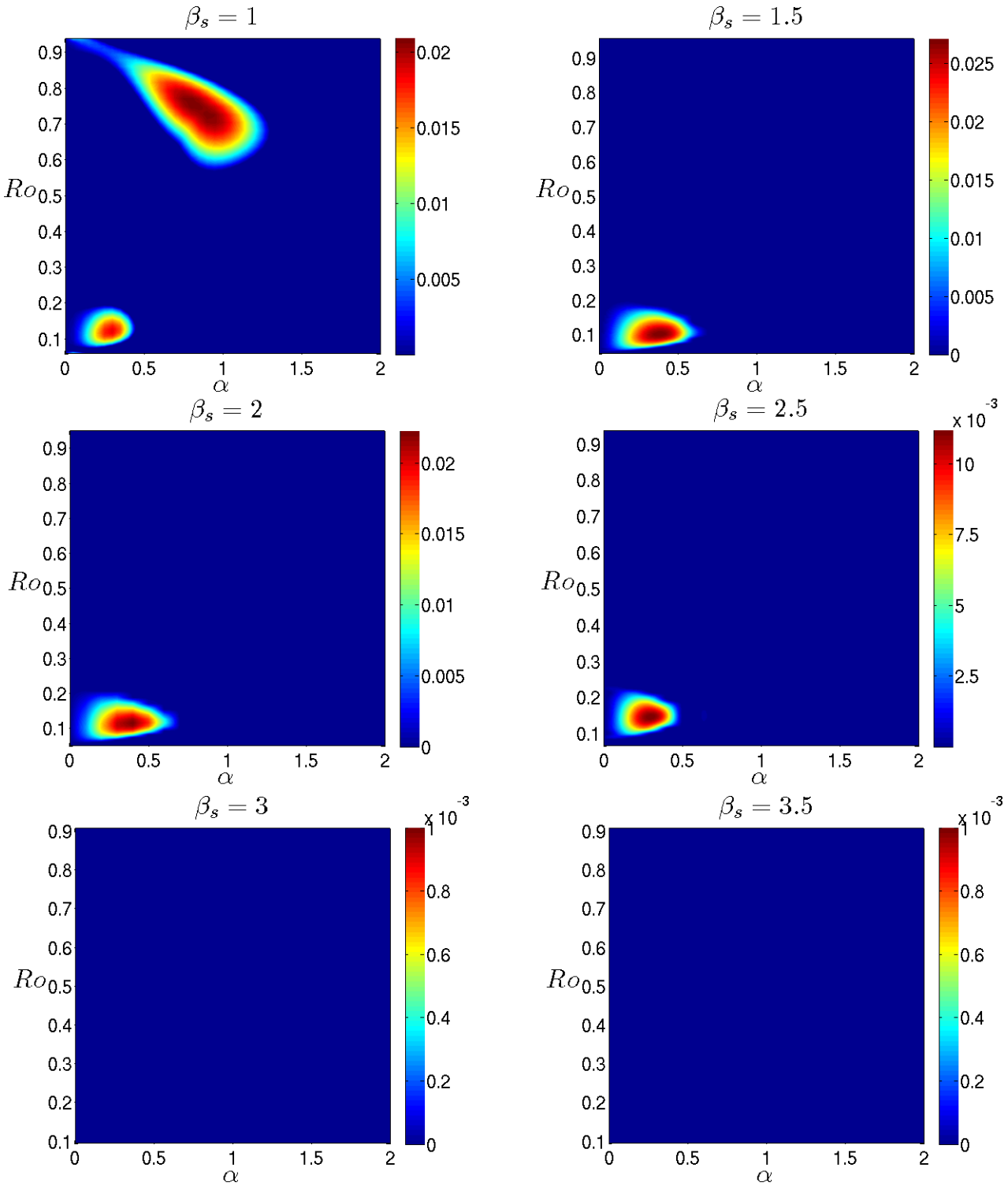

Figure 3.16: Streamwise instability for $Re = 50$. $\sigma_r \geq 0$ is coloured in (α, Ro)-space.

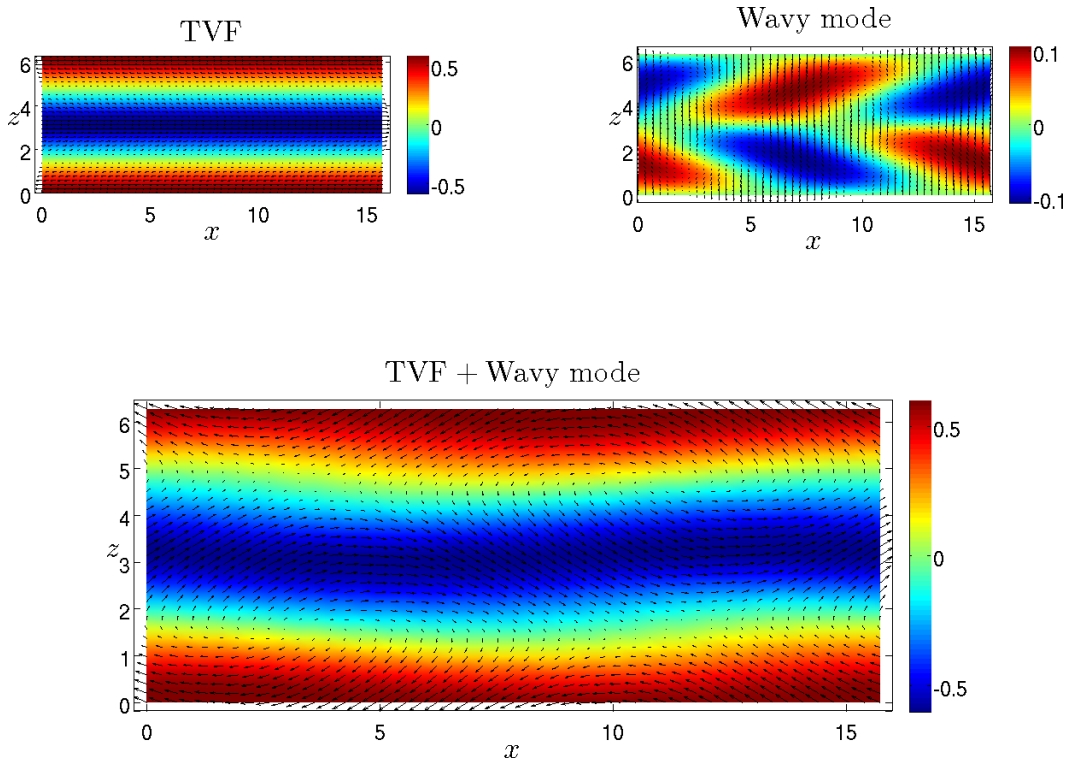

Figure 3.17: Wavy instability mode for $(\alpha, \beta_s, Re, Ro) = (0.4, 1, 50, 0.1)$. On the top left we have TVF and on the right is the wavy mode which de-stabilizes it. Beneath we plot a combination of the two modes.

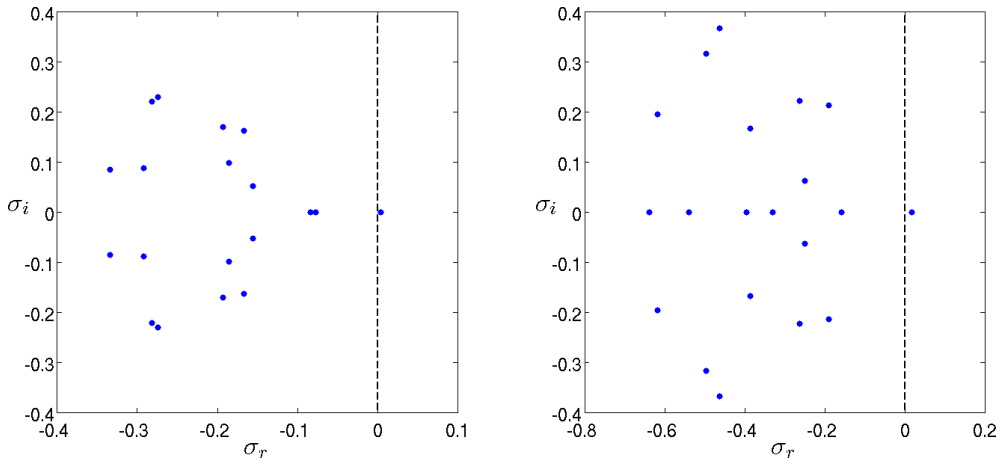

Figure 3.18: Eigenvalues of the stability operator with a wavy instability for $(\alpha, \beta_s, Re, Ro) = (0.4, 1, 50, 0.1021)$ (left) and $(\alpha, \beta_s, Re, Ro) = (0.5, 2, 50, 0.1261)$ (right).

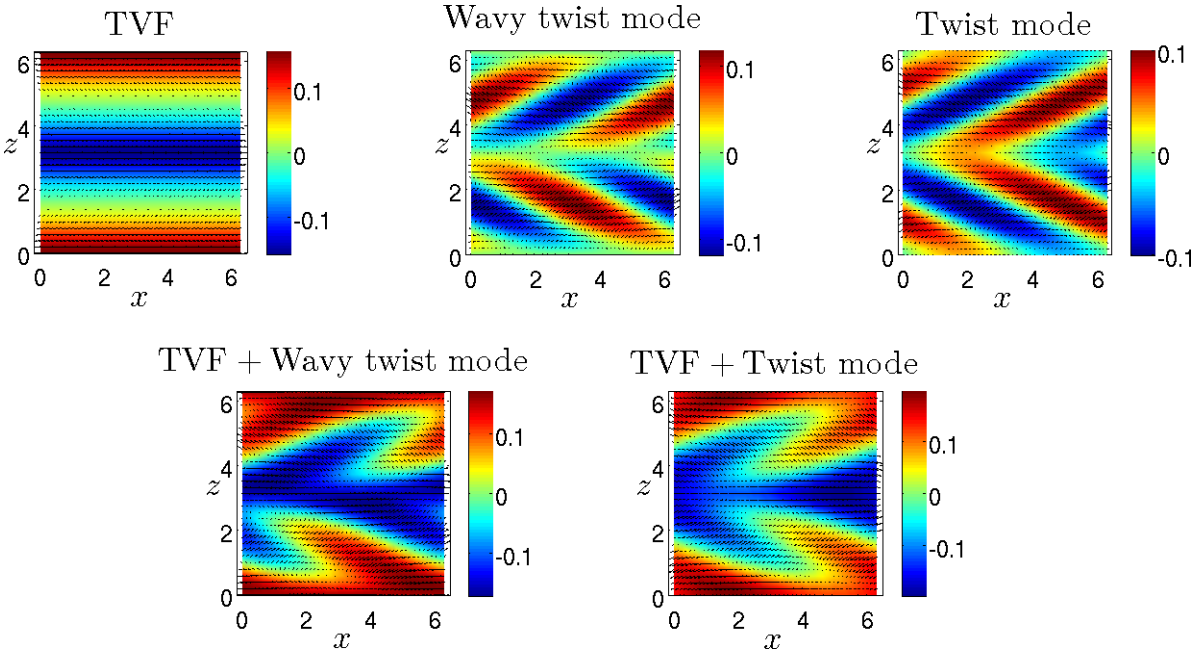

Figure 3.19: Wavy twist and twist instability modes for $(\alpha, \beta_s, Re, Ro) = (1, 1, 50, 0.7606)$. The top row have an unstable TVF and the twist perturbations which de-stablize the vortex. The bottom row depicts the composition of the TVF and each instability mode.

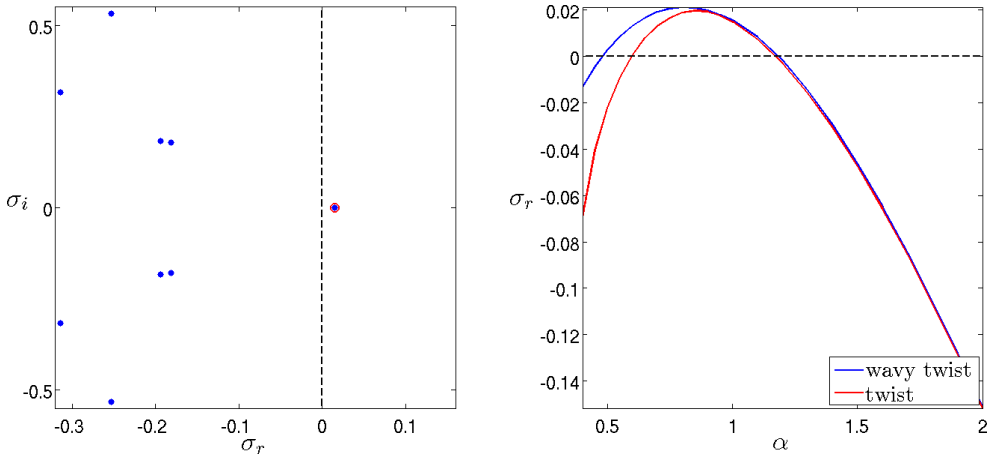

Figure 3.20: Eigenvalues of the stability operator with a wavy instability for $(\alpha, \beta_s, Re, Ro) = (1, 1, 50, 0.7606)$. The twist eigenvalue is circled in red so as to distinguish it from the wavy twist eigenvalue, since the two are very close. On the right we plot the growth rates σ_r of the wavy twist (blue) and the twist (red) modes against α, for $Ro = 0.7606$. In this instance, the wavy twist mode dominates for all streamwise wavenumbers.

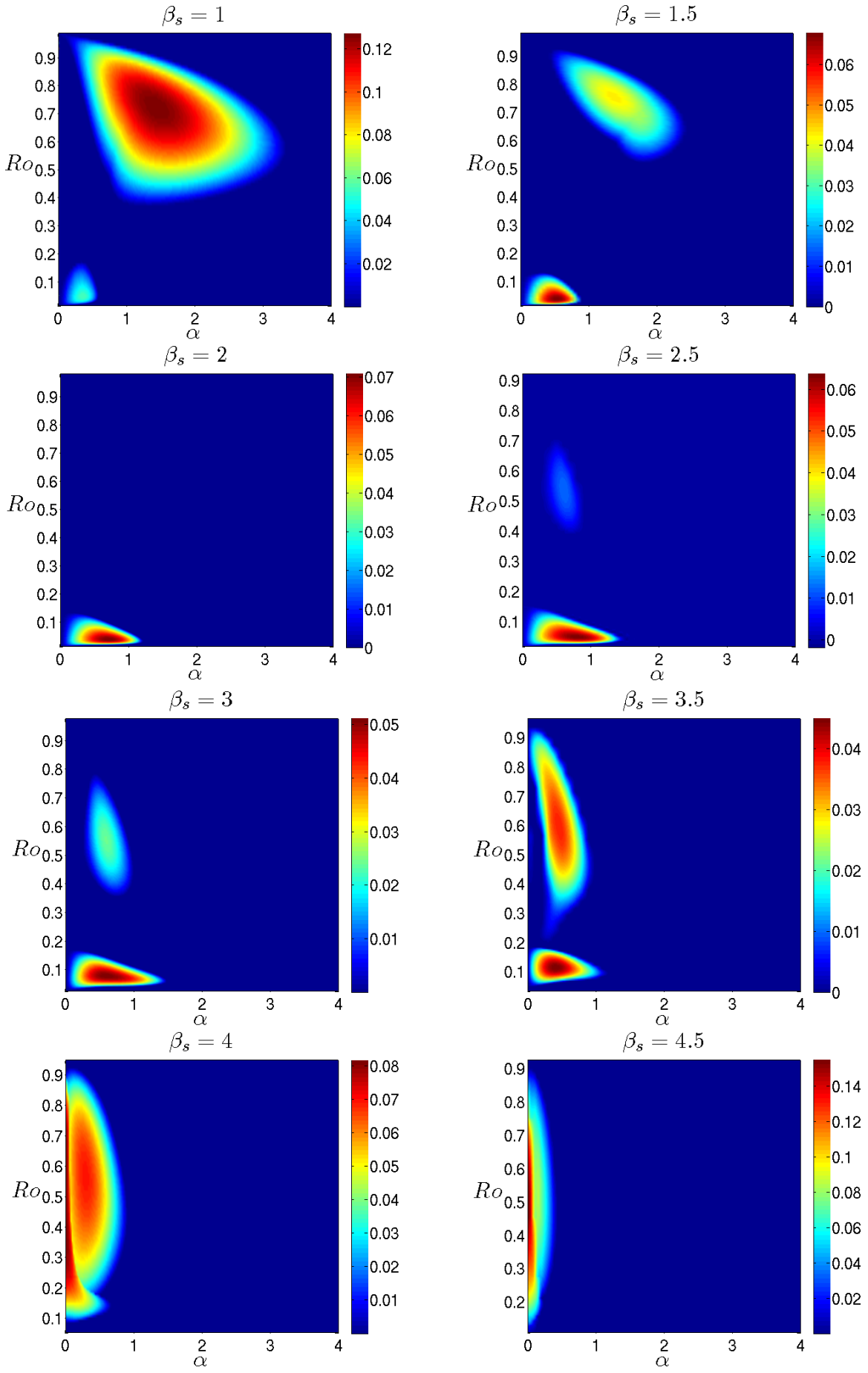

Figure 3.21: Streamwise instability for $Re = 100$. $\sigma_r \geq 0$ is coloured in (α, Ro)-space.

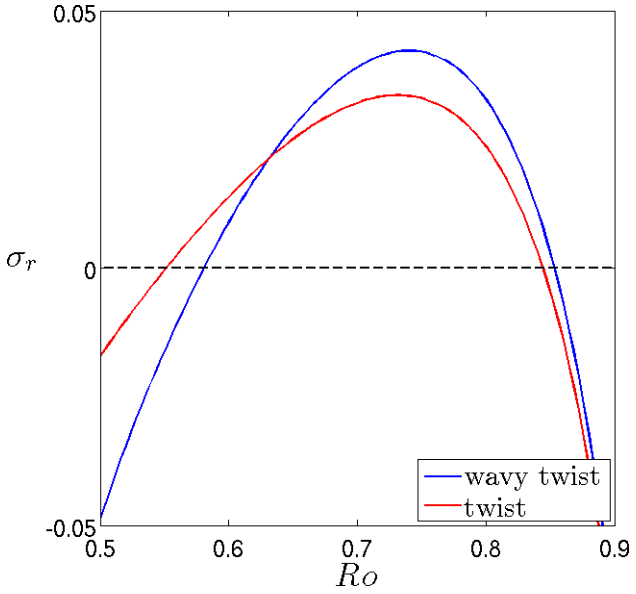

Figure 3.22: Wavy twist (blue) and twist (red) instability modes competing in Ro. $(\alpha, \beta_s, Re) = (1.5, 1.5, 100)$. Unlike the case for $Re = 50$ in Figure 3.20, the least stable modes changes from twist to wavy twist as Ro increases.

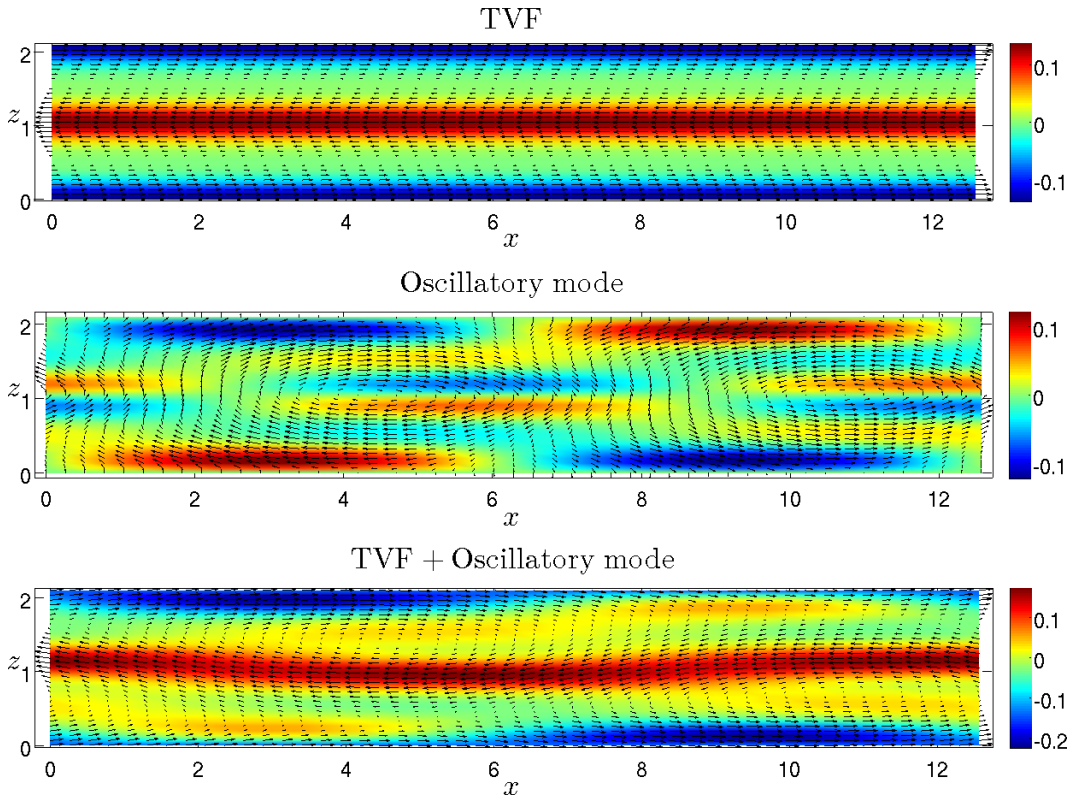

Figure 3.23: From top to bottom we plot TVF; the oscillatory wavy perturbation mode; and the combination of the two flowfields. The parameters here are $(\alpha, \beta_s, Re, Ro) = (0.5, 3, 100, 0.5)$.

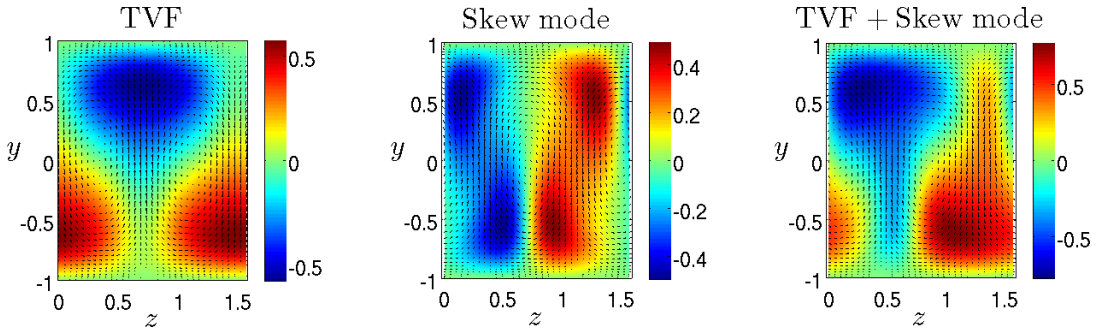

Figure 3.24: From left to right we have TVF; the skew mode; and the combination of TVF and the skew mode. We have chosen the name "skew" instability as the combination flowfield resembles a Taylor vortex pair which is skewed in the (y, z)-plane. The parameter values are $(\beta_s, Ro, Re) = (4, 0.2, 100)$.

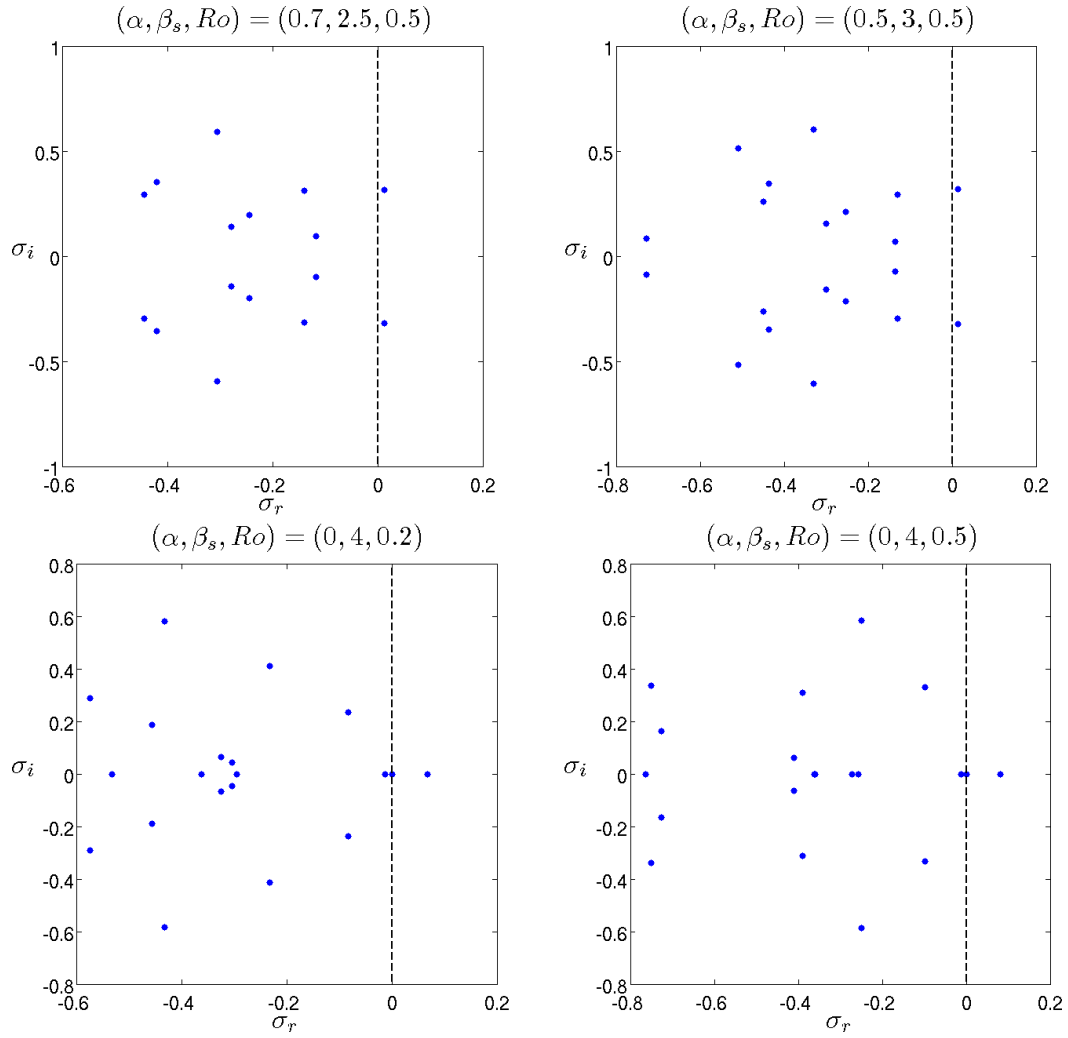

Figure 3.25: Stability operators with unstable oscillatory wavy modes (top) and skew modes (bottom). $Re = 100$ in all cases.

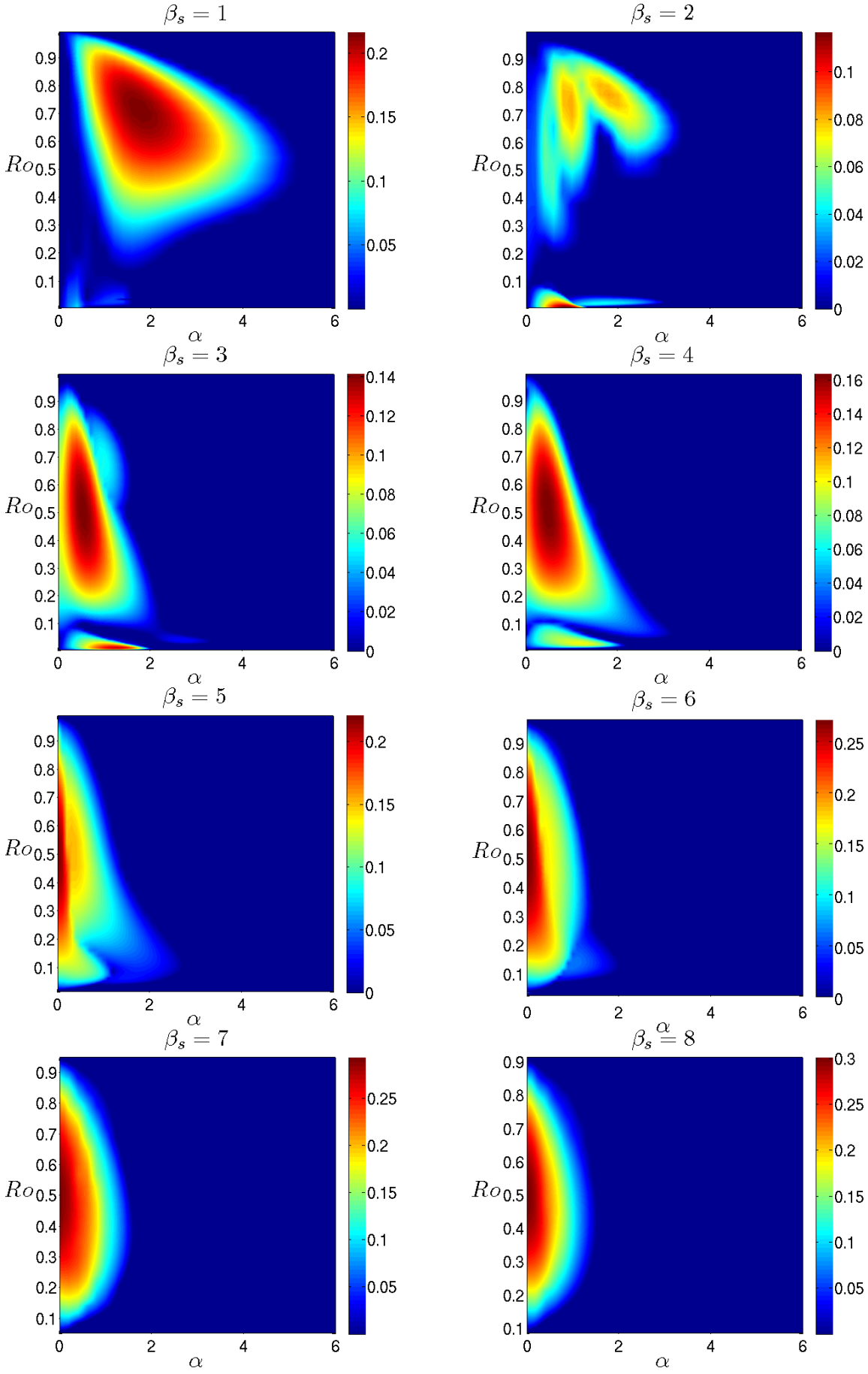

Figure 3.26: Streamwise instability for $Re = 250$. $\sigma_r \geq 0$ is coloured in (α, Ro)-space.

3.6.2 Eckhaus instability maps

In Figures 3.27, 3.28 and 3.30 we plot the streamwise independent instabilities that affect Taylor vortices for $Re = 50, 100$ and 250. An instability caused by a perturbation which is periodic in the same direction as the base state is called Eckhaus instability (Eckhaus (1965)). For $Re = 50, 100$, Eckhaus instability is limited to TVF with higher β_s wavenumber so in Figures 3.27 and 3.28 we include maps for the two largest β_s considered. In each Figure, low Ro and high Ro tongues of subharmonic instability appear for the Taylor vortices. These modes have $\sigma_i = 0$, and initiate a bifurcation towards TVF with lower β_s as is outlined in Figure 3.29 for a case with $Re = 50$. In Figure 3.28, for $Re = 100$, these tongues are restricted to a smaller region of the parameter space, and the skew instability emerges between $0.1 \lesssim Ro \lesssim 0.9$. As was the case with streamwise instabilities, for $Re = 250$ the Taylor vortices are in general much less stable than was the case for lower Reynolds numbers. Only $\beta_s = 1$ is Eckhaus stable, all other vortices being de-stabilized by streamwise independent perturbations. We find that in most cases the maximum Eckhaus instability is in fact harmonic, being either the skew instability or an oscillatory version of it. Vortices with higher spanwise wavenumber have stronger Eckhaus instability than those with lower wavenumber, as evidenced by increase in maximum growth rate as β_s is increased in Figure 3.30. The low and high Ro tongues of instability present in the $Re = 50, 100$ Eckhaus instability maps appear only at $\beta_s = 7, 8$ for $Re = 250$, with the tongues confined to Ro very close to the upper and lower linear stability boundaries.

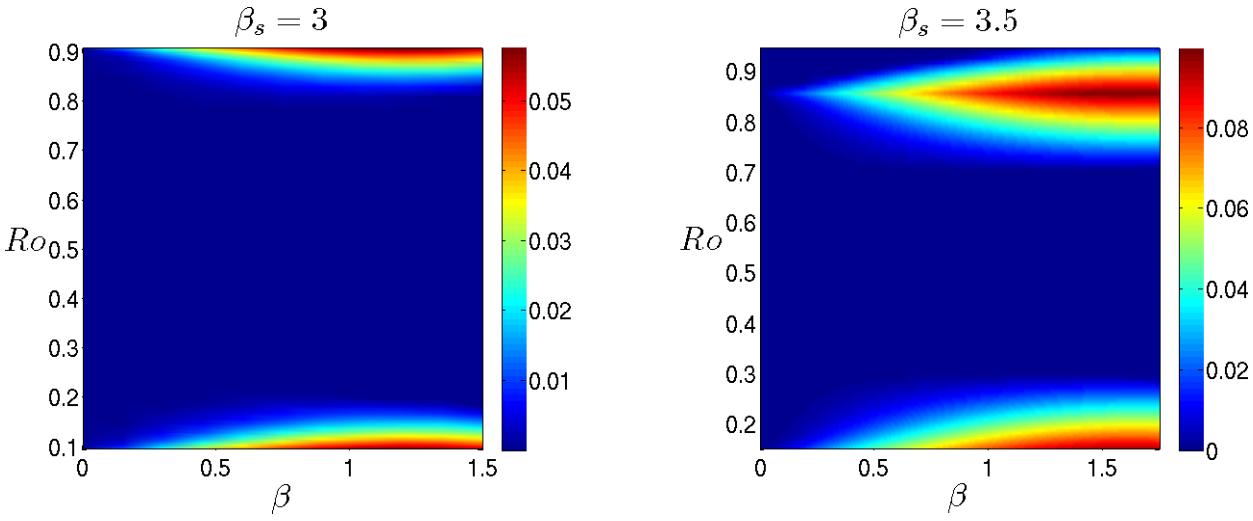

Figure 3.27: Eckhaus instability for $Re = 50$ $\sigma_r \geq 0$ is coloured in (β, Ro)-space.

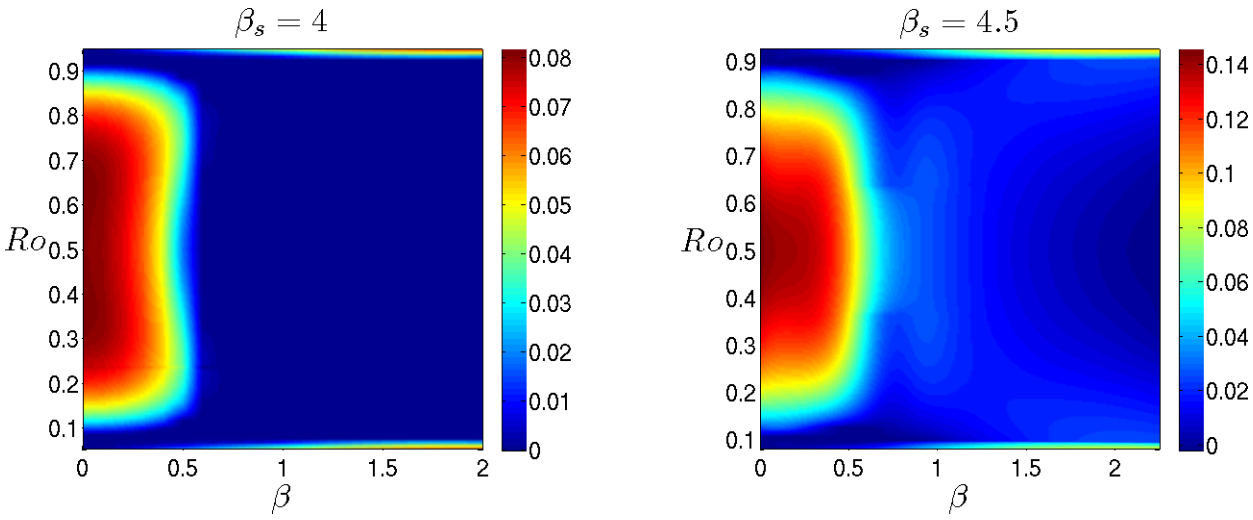

Figure 3.28: Eckhaus instability for $Re = 100$ $\sigma_r \geq 0$ is coloured in (β, Ro)-space.

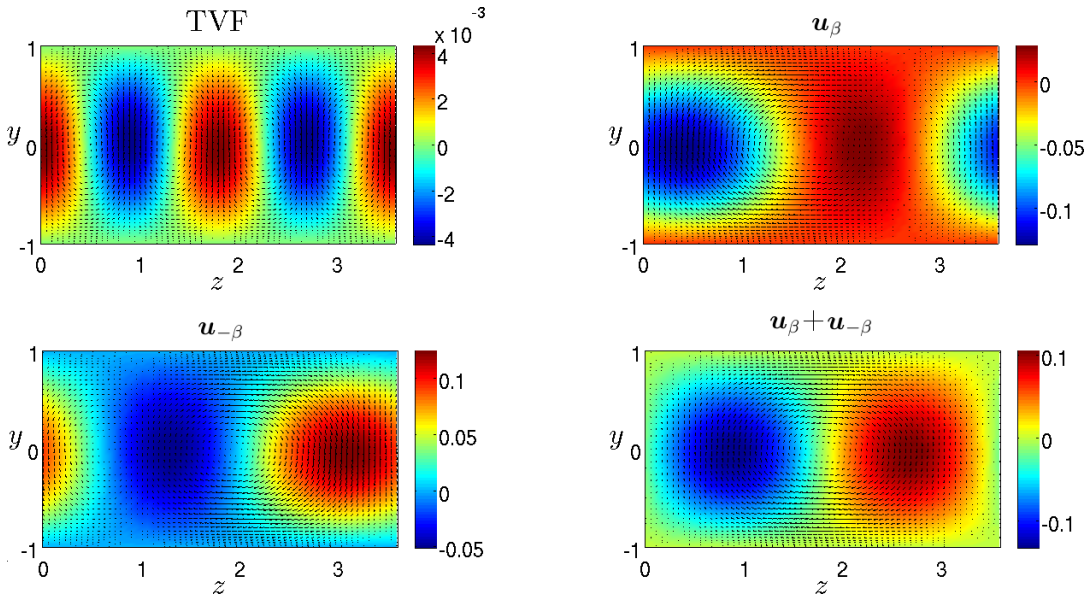

Figure 3.29: Subharmonic Eckhaus modes at $(\beta, \beta_s, Re, Ro) = (1.75, 3.5, 50, 0.859)$. At the top we plot TVF with $\beta_s = 3$ over the doubled wavelength $\frac{4\pi}{3}$. On the top right we plot $\boldsymbol{u}_\beta$, the velocity perturbation about the Taylor vortex, corresponding to Eckhaus mode $\beta = 1.75$. $\boldsymbol{u}_{-\beta}$ corresponds to the conjugate mode, plotted in the bottom left panel. In the final panel we plot the superposition of the two perturbations, which resemble a Taylor vortex flowfield with $\beta_s = 1.75$.

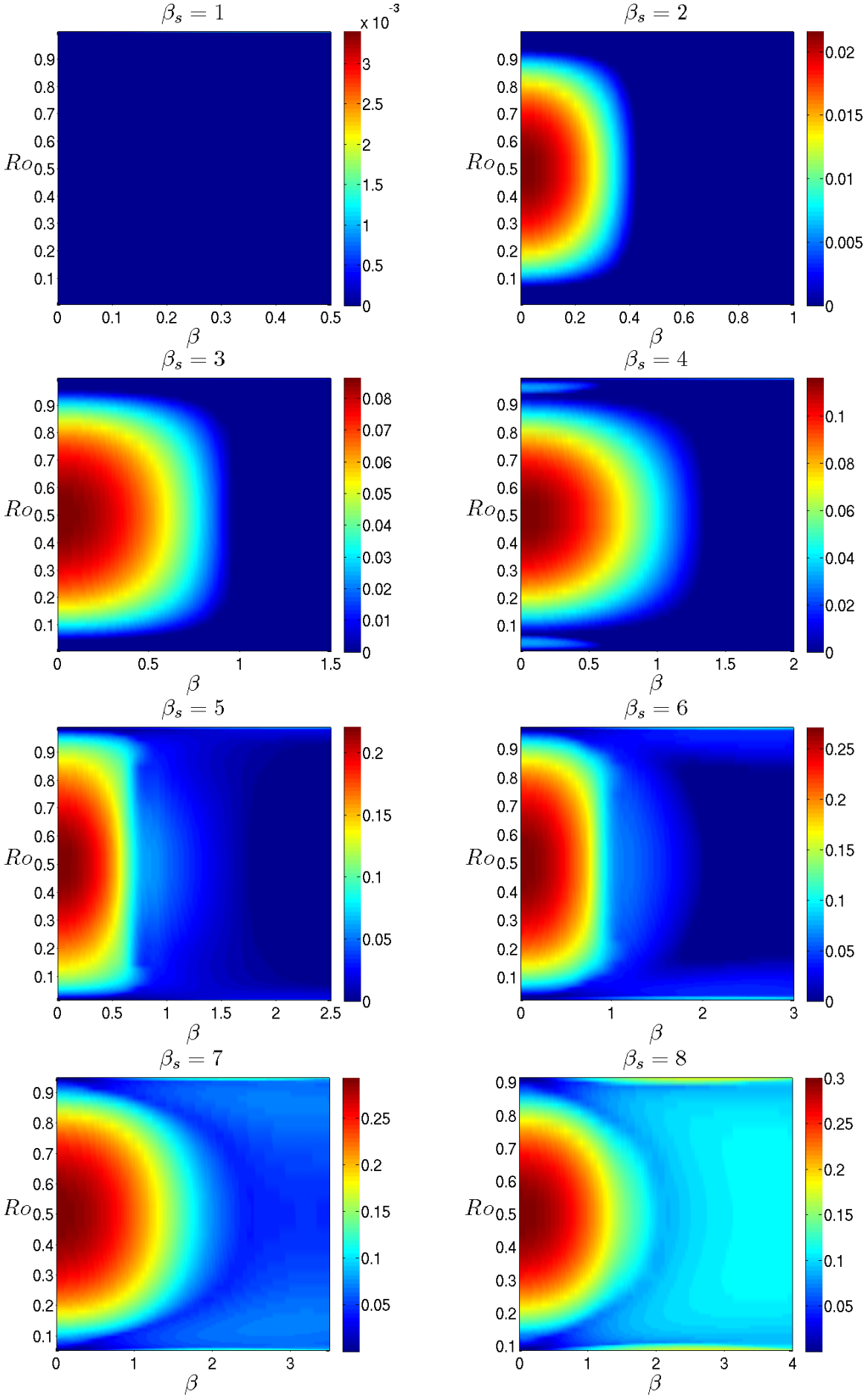

Figure 3.30: Eckhaus instability for $Re = 250$. $\sigma_r \geq 0$ is coloured in (β, Ro)-space.

3.6.3 Summary of TVF stability properties

The stability of TVF has been shown to be strongly dependent on the spanwise wavenumber β_s of the Taylor vortices, the rotation number Ro and the Reynolds number Re. We have mapped the streamwise instabilities across all Ro for $Re = 50, 100, 250$ and across a set of β_s for which there exist Taylor vortices, in Figures 3.16, 3.21 and 3.26, and the Eckhaus instabilities across the same parameters in Figures 3.27, 3.28 and 3.30. Care has been taken to analyze each stability mode, to give a characterization to the instabilities which cause TVF to break down at given points in parameter space. The instabilities cover a larger region of (α, Ro) space as Re is increased, offering some promise that experimentally observed transition phenomena can be explained via bifurcation of structures from TVF. Our analysis has focused on purely streamwise and purely spanwise instabilities, so it is of course possible that there exist oblique instabilities which de-stabilize the Taylor vortices. However, as shown in Figure 3.13, where we find oblique instabilities in our calculations, they are often not as strong as purely streamwise or spanwise modes. We take this as justification in studying the reduced range of instabilities, in order to give a clearer view of the parameter dependence of the stability properties of TVF.

By giving an indication of where in the $(\alpha, \beta, \beta_s, Re, Ro)$ parameter space Taylor vortices will break down, our stability maps provide an ideal starting point for investigating the tertiary bifurcations which branch from secondary TVF.

3.7 Bifurcations of tertiary states

We define a tertiary state to be a structure which bifurcates directly from a secondary state, but not the primary state. In this analysis we identify a range of the tertiary states which bifurcate from Taylor vortex flow at transitional Reynolds numbers. To this end, we restrict our attention to $Re = 100$, since §3.6 indicates a range of instabilities present for this Re. To assess the effects of rotation on the tertiary states we track their trajectories in (Ro, E_{cf})-space and create bifurcation diagrams in §§3.7.5, 3.7.6 and 3.7.7 We use the Newton-Krylov-hookstep algorithm outlined in §3.3 to find the tertiary states and an adaptive quadratic continuation technique to continue them in solution space. In each bifurcation diagram, the harmonic stability or instability of each structure is indicated by a solid or dashed curve respectively, as was our convention in §3.5.

In addition we perform a global stability analysis on a representative set of the tertiary solutions which appear in our bifurcation diagrams. An extensive tertiary stability analysis would require examination of each solution at all the wavenumbers at which it exists, as was done for TVF in §3.6, which would be computationally expensive. Therefore we simply select cases of each tertiary flow to analyze. The tertiary states on which we perform global stability analyses are marked by dots where they appear in the bifurcation diagrams. Well converged eigenfunctions require a greater truncation than is needed to compute well converged eigenvalues, so we do not include plots of the eigenfunctions in this thesis.

In order to produce coherent maps of the instabilities affecting each solution an extra layer of interpolation is added to the procedure for the maps in §3.6. For a steady solution, stability values are calculated at 100 data points in the (α, β) domain. These data points are then interpolated, using a cubic spline algorithm, onto a grid of over 1000 points before we create the colour-plot. For time-periodic states, since stability values are more computationally expensive to compute, cubic spline interpolation is used over a grid of 20 data points. As in §3.6, we plot the growth rates σ_r with the intersection of the neutral plane, $\sigma_r = 0$, such that the regions of instability can be clearly seen.

We begin with an introduction to each of the tertiary states in §§3.7.1, 3.7.2, 3.7.3 and 3.7.4.

3.7.1 Wavy vortex flow

Wavy vortex flow (WVF) is a steady structure which develops when Taylor vortices lose stability to wavy vortex modes. Wavy vortices are a well-known feature of Taylor-Couette flow (see for example Davey *et al.* (1968), Andereck *et al.* (1986), Nagata (1986), Koschmieder (1993)), and were discussed by Nagata (1998) in the context of rotating plane Couette flow. Wavy vortices lose the mirror symmetry **Z** of Taylor vortices, but they hold shift-reflect and shift-rotation symmetries **S** and **Ω**. An example of the streamwise and spanwise variation of the flowfield is given in Figure 3.31. The flowfields closely resemble the superposition of the linear wavy mode and TVF from Figure 3.17.

$$\mathbf{S}[u,v,w](x,y,z) = [u,v,-w](x+\frac{\pi}{\alpha},y,-z+\frac{\pi}{\beta}) \tag{3.77a}$$

$$\mathbf{\Omega}[u,v,w](x,y,z) = [-u,-v,w](-x,-y,z+\frac{\pi}{\beta}) \tag{3.77b}$$

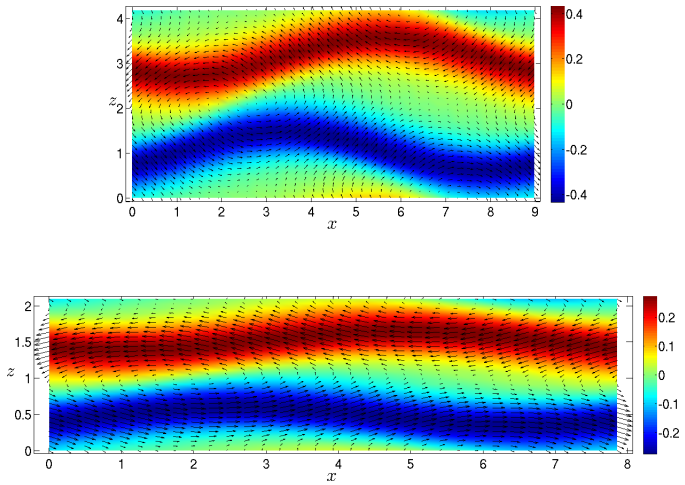

Figure 3.31: Wavy vortex flows $(\alpha_s, \beta_s, Re, Ro) = (0.7, 1.5, 100, 0.05)$ and $(\alpha_s, \beta_s, Re, Ro) = (0.8, 3, 100, 0.12)$.

3.7.2 Twist and wavy twist vortex flow

Twist (TWI) and wavy twist (wTWI) vortex flows emerge from the twist and wavy twist instabilities of Taylor vortex flow (Weisshaar *et al.* (1991), Antonijoan & Sánchez (2000)). Examples of the flowfields are given in Figure 3.32 where, like WVF, the mid-plane flowfields of the twist flows closely resemble their linear counterparts from Figure 3.19. wTWI has the symmetries **S** and **Ω** loses mirror symmetry **Z**, whereas TWI retains the mirror symmetry of TVF.

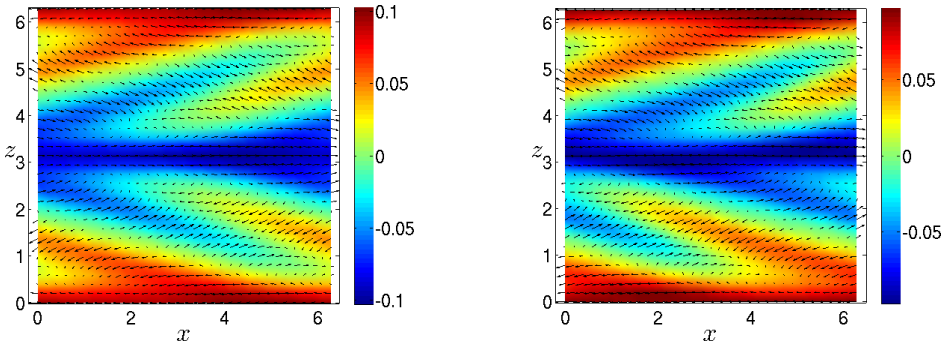

Figure 3.32: Twist (left) and wavy twist (right) vortices for $(\alpha_s, \beta_s, Re, Ro) = (1, 1, 100, 0.8)$.

3.7.3 Oscillatory wavy vortex flow

The complex conjugate eigenvalues of the oscillatory wavy instability instigate a Hopf bifurcation from Taylor vortex flow towards a periodic orbit of the Navier-Stokes equations. To our knowledge, calculations of the oscillatory flow bifurcating directly from TVF has not been previously reported in the literature for Taylor-Couette flow, circular Couette flow or rotating plane Couette flow, though the oscillatory instability has been known since Nagata (1988). However, Hopf bifurcations from tertiary states have been reported, such as those discussed in Nagata & Kawahara (2004), and oscillatory flows in plane Couette flow have also been found (Kawahara & Kida (2001), Viswanath (2007), Kreilos & Eckhardt (2012)). The structure has a remarkably simple sinusoidal oscillatory amplitude, which is manifest in its E_{cf} evolution in Figure 3.33. We have named it the oscillatory wavy vortex flow (oWVF) as its flowfield resembles that of a steady wavy vortex which oscillates in time, as can be seen in Figure 3.34. Its structure is much simpler than the periodic orbits found in non-rotating plane Couette flow by, for example, Kawahara & Kida (2001) and Viswanath (2007), though its E_{cf} evolution is reminiscent of the $\overline{1}$ orbit found by Kreilos & Eckhardt (2012). oWVF holds the same symmetries as WVF and wTWI: shift-reflection $\mathbf{S}$ and shift-rotation $\mathbf{\Omega}$.

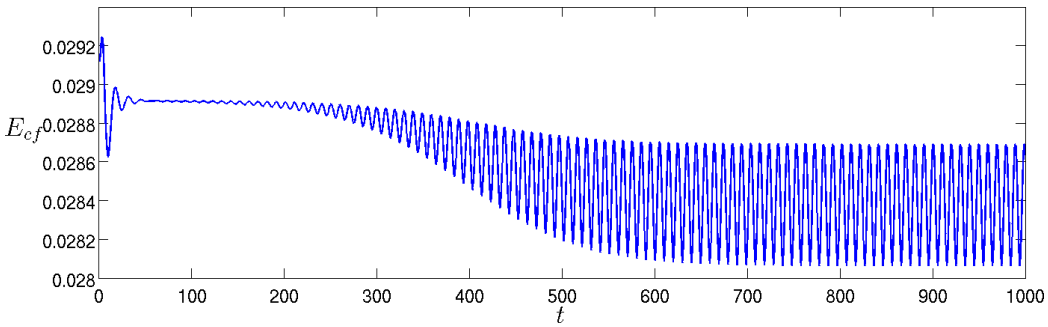

Figure 3.33: Perturbed TVF evolving towards oWVF for $(\alpha_s, \beta_s, Re, Ro) = (0.6, 2.4, 100, 0.5)$.

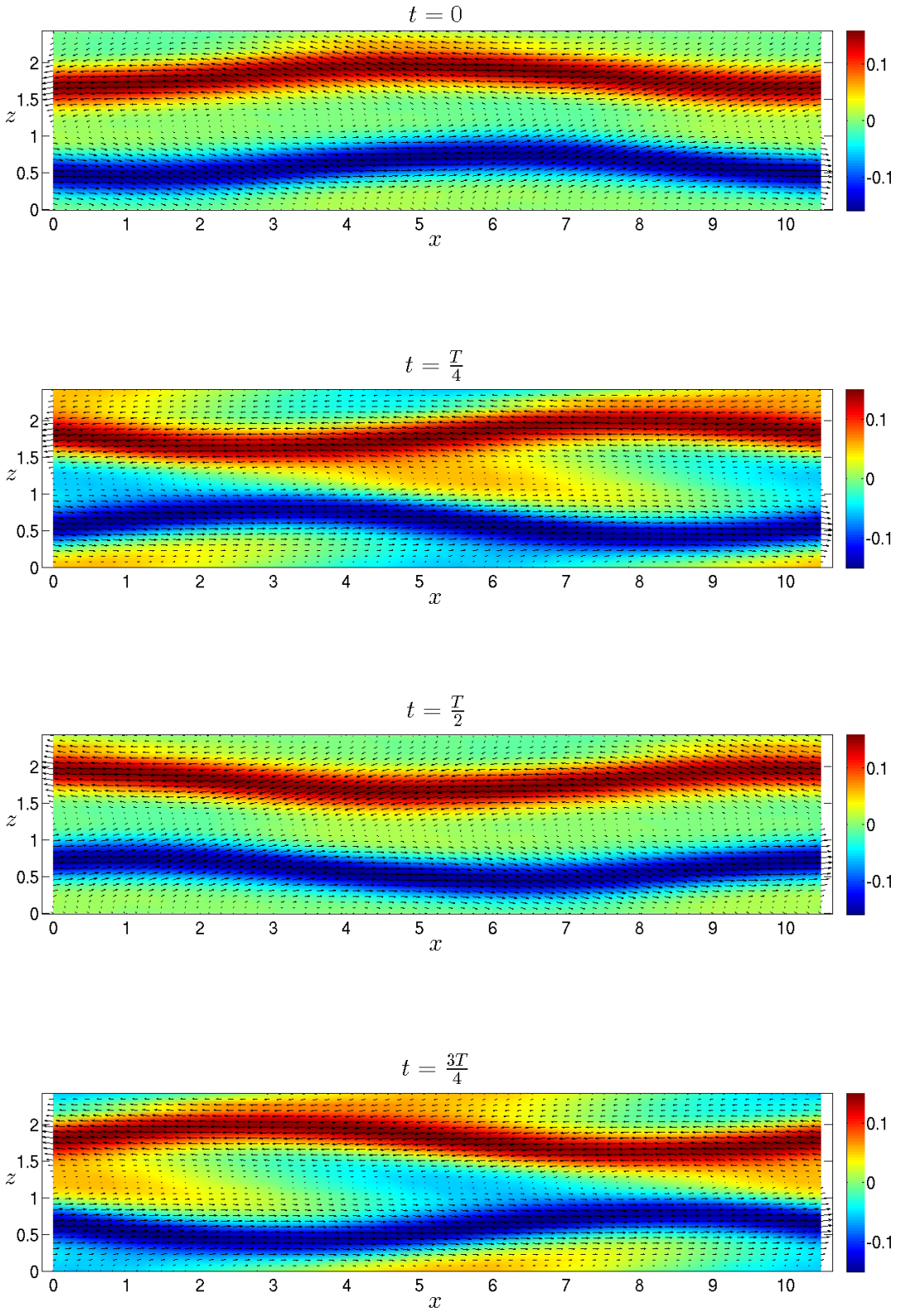

Figure 3.34: Oscillatory wavy vortex flow for $(\alpha_s, \beta_s, Re, Ro) = (0.6, 2.6, 100, 0.5)$, pictured at four time points throughout one period of its oscillation. The flowfield has a wavy structure and the symmetries $\mathbf{S}$ and $\mathbf{\Omega}$ are satisfied throughout its orbit.

3.7.4 Skewed vortex flow

Skewed vortex flow (SVF) is the steady, streamwise independent flow which bifurcates from Taylor vortices via the skew instability. SVF loses mirror symmetry **Z**, like the previous tertiary states excluding TWI. The spanwise skewness of the vortices is readily apparent in velocity field pictured in Figure 3.35. The flowfield is quite different from the linear mode and TVF combination of Figure 3.24, suggesting that a greater number of spanwise harmonics are excited during nonlinear saturation of the linear mode. We are unaware of SVF being reported by other authors.

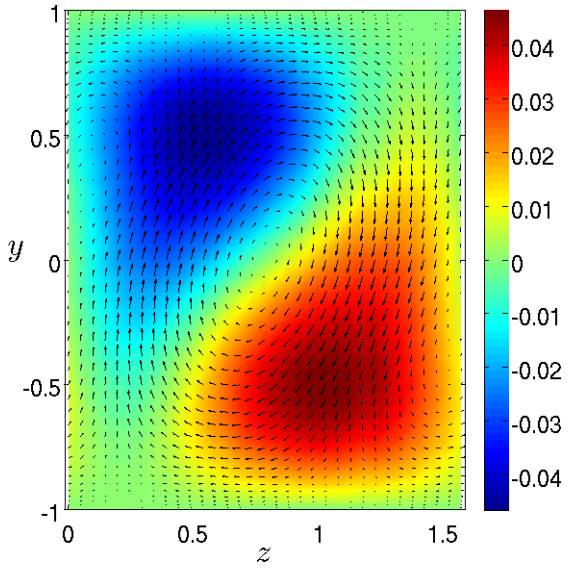

Figure 3.35: Skewed vortex flow for $(\beta_s, Re, Ro) = (4, 100, 0.9)$.

3.7.5 Bifurcation of twist, wavy twist and wavy vortex flows

Having classified the instabilities that cause Taylor vortices to break down and the tertiary states that they develop into, we can trace their trajectories in the (Ro, E_{cf}) subspace, with α_s, β_s and Re fixed. In Figure 3.36 we show how WVF and wTWI bifurcate from TVF with $\beta_s = 1.5$. WVF is born when TVF loses stability to the wavy vortex mode and when TVF regains stability WVF dies, thus bifurcation to WVF is considered transcritical in this case. The stability of this WVF solution changes twice, with instability to oscillatory perturbations in the regions $0.0154 < Ro < 0.02$ and $0.0246 < Ro < 0.041$. Global stability analysis on a harmonically stable and unstable WVF solution, shown in Figure 3.40, indicate that both states de-stabilize to a subharmonic instability with maximum growth rate at approximately $(\alpha, \beta) = (0.35, 0.135)$.

wTWI emerges, in Figure 3.36, in a saddle-node bifurcation at $Ro = 0.604$ with an upper and lower branch of solutions in the range $0.604 < Ro < 0.756$, and both solutions are harmonically unstable to complex conjugate modes. The lower branch becomes harmonically stable at $Ro = 0.635$ meaning that there are two stable attractors over $0.635 < Ro < 0.756$ since TVF is also stable, while the upper branch solution is unstable throughout the bifurcation. At $Ro = 0.756$, TVF loses stability and the lower branch wTWI becomes the only attractor, while the upper branch merges with TVF. The structure of upper branch wTWI differs from the structure of its lower counterpart, as highlighted in the (x, z)-projections of two example flowfields in Figure 3.38. The lower branch solution has a sinusoidal arrangement of vortex pairs embedded between streamwise streaks, whereas the upper branch solution consists of three pairs of vortices embedded between each streak, along one streamwise wavelength. Each group of three, in the upper branch solution, contains two strong and one weak vortex pairs, with the weak and strong pairings aligning either side of the streak. In Figure 3.39 we plot the global stability properties of the harmonically stable lower branch solution and the harmonically unstable upper branch solution indicated by dots in Figure 3.36. The lower branch solution is globally stable, whilst the upper branch solution is unstable to a perturbation of any (α, β) wavenumber pairing. However, the upper branch solution is maximally unstable to harmonic perturbations.

In Figure 3.37 we plot bifurcations for $\alpha_s = 1.5$. TVF remains stable for $Ro < 0.55$, above which stability is lost to a twist mode. We then see TWI and wTWI bifurcate transcritically from TVF. TWI is harmonically stable in the range $0.55 < Ro < 0.618$, beyond which it loses stability to a stationary mode. We investigate the global stability of the two solutions indicated in the bifurcation diagram in Figure 3.41. Harmonically stable TWI

loses stability to a subharmonic stationary mode with maximum $(\alpha, \beta) = (0.37, 0.23)$, while the harmonically unstable TWI is globally unstable with maximum to an oscillatory subharmonic mode at $(\alpha, \beta) = (0.72, 0.48)$. TVF becomes stable once more for $Ro > 0.852$ and the tertiary states collapse.

In Figures 3.42 and 3.43 we investigate bifurcations in the geometric parameter α_s at $Ro = 0.7$ and $Ro = 0.8$, to explore the relationship between the tertiary solutions at $\alpha_s = 0.7$ and $\alpha_s = 1.5$. For both rotation numbers, TWI bifurcates transcritically in α_s. wTWI merges with TVF for large α_s for both rotation numbers, but its behaviour at low α_s is different in each case. For $Ro = 0.7$ in Figure 3.42, the upper and lower branch wTWI from Figure 3.36 appear, with an exchange of harmonic stability as wTWI increases in E_{cf} to re-join with TVF at the point where it de-stabilizes. For $Ro = 0.8$ in Figure 3.43 however, no upper and lower branches are found, and the solution decreases in E_{cf} as $\alpha_s \to 0$, tending towards TVF with $\beta_s = 3$. This suggests wTWI energes in a subcritical, subharmonic bifurcation from TVF with $\beta_s = 3$. A long wavelength wTWI flowfield is shown in Figure 3.44, where it can be seen that the twists become increasingly localized as the state moves towards TVF.

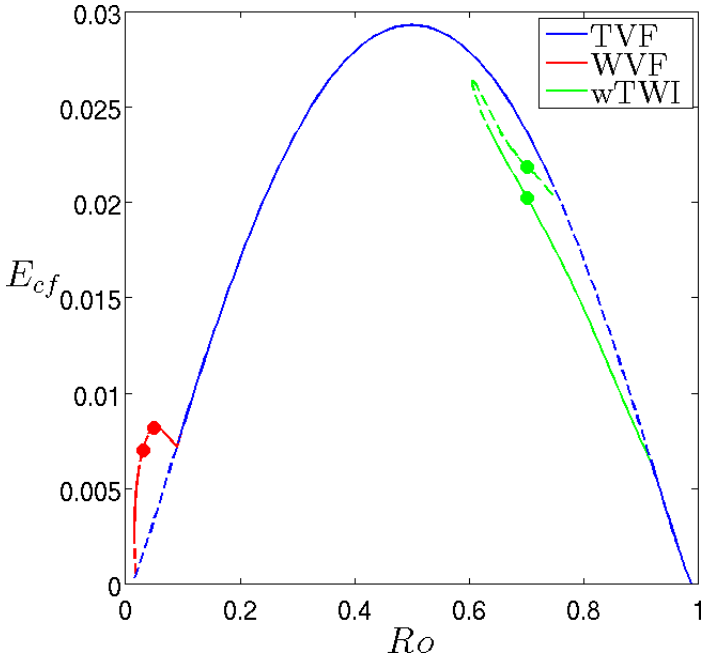

Figure 3.36: Tertiary bifurcations for $(\alpha_s, \beta_s, Re) = (0.7, 1.5, 100)$. The global stability of the WVF solutions marked by red dots is calculated in Figure 3.40. The green dots correspond to the wTWI solutions plotted in Figure 3.38 and used in global stability calculations in Figure 3.39.

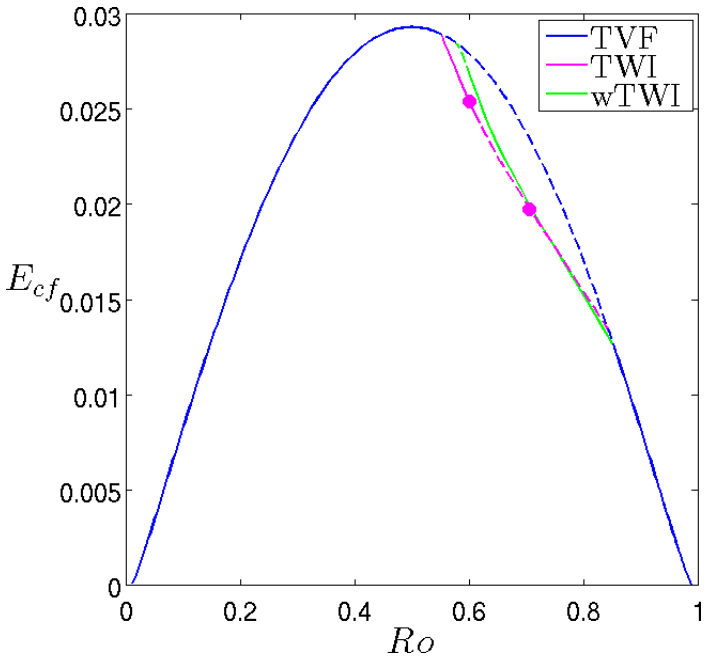

Figure 3.37: Tertiary bifurcations for $(\alpha_s, \beta_s, Re) = (1.5, 1.5, 100)$. The purple dots correspond to the TWI solutions for global stability computations in Figure 3.41.

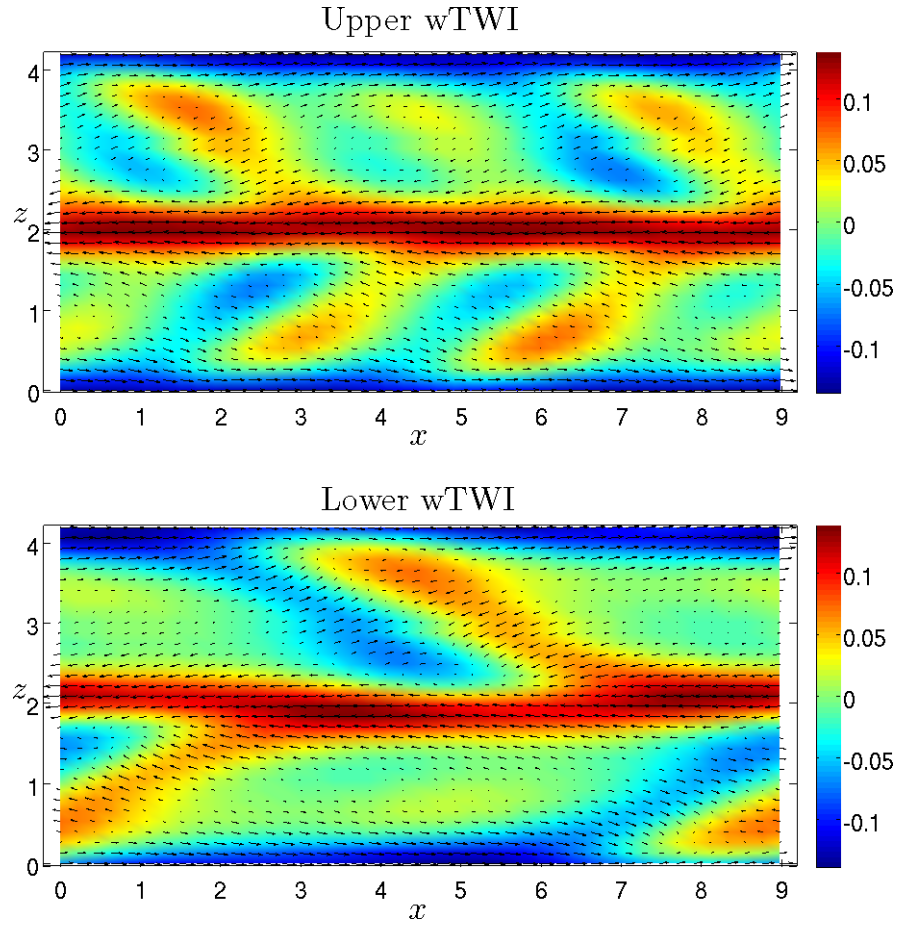

Figure 3.38: Stable and unstable wTWI solutions at $(\alpha_s, \beta_s, Re, Ro) = (0.7, 1.5, 100, 0.7)$.

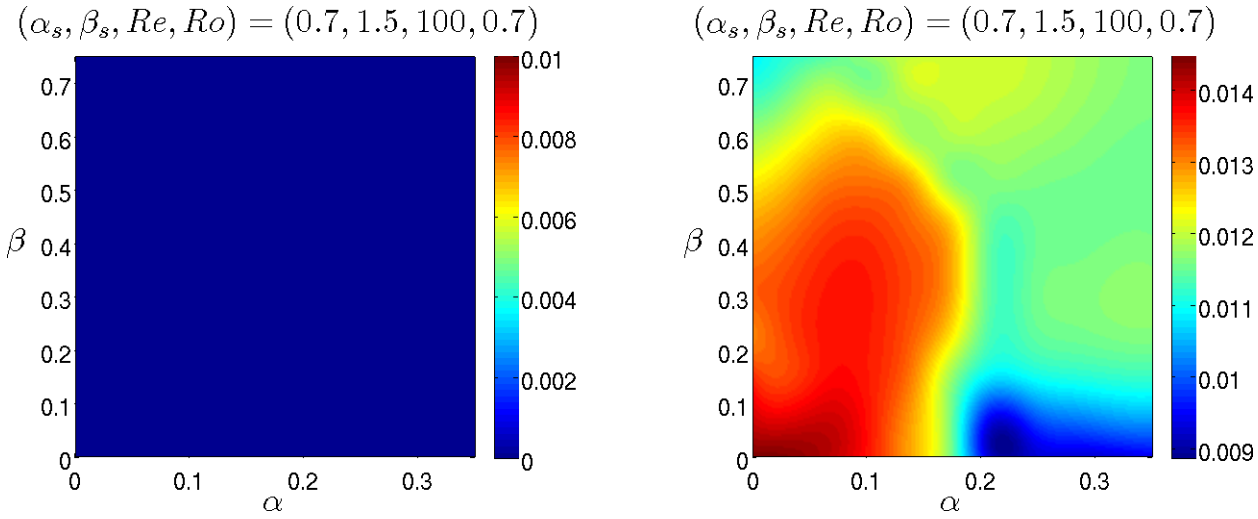

Figure 3.39: Stability of harmonically stable and unstable wTWI solutions at $(\alpha_s, \beta_s, Re, Ro) = (0.7, 1.5, 100, 0.7)$. $\sigma_r \geq 0$ is coloured. The harmonically stable solution is in fact globally stable, whilst the harmonically unstable solution is unstable to all perturbations. The least stable mode is the oscillatory harmonic mode.

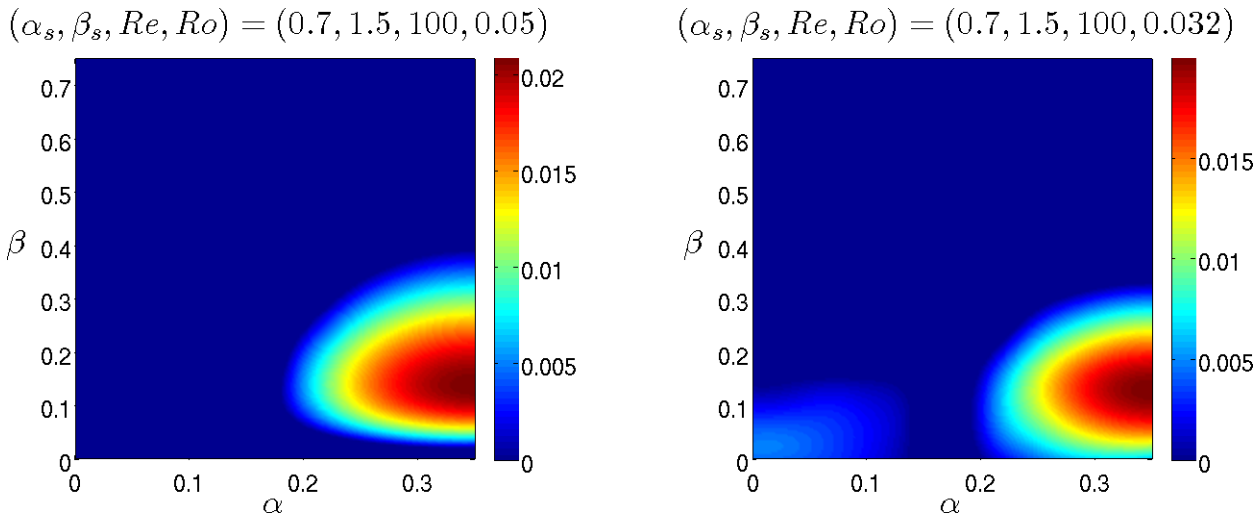

Figure 3.40: Stability of harmonically stable and unstable WVF solutions at $Ro = 0.05$ and $Ro = 0.032$ for $(\alpha_s, \beta_s, Re) = (0.7, 1.5, 100)$. $\sigma_r \geq 0$ is coloured. Both solutions lose stability to oscillatory subharmonic perturbations with the least stable mode at approximately $(\alpha, \beta) = (0.35, 0.135)$ for each state. The harmonic instability at $Ro = 0.032$ is also oscillatory.

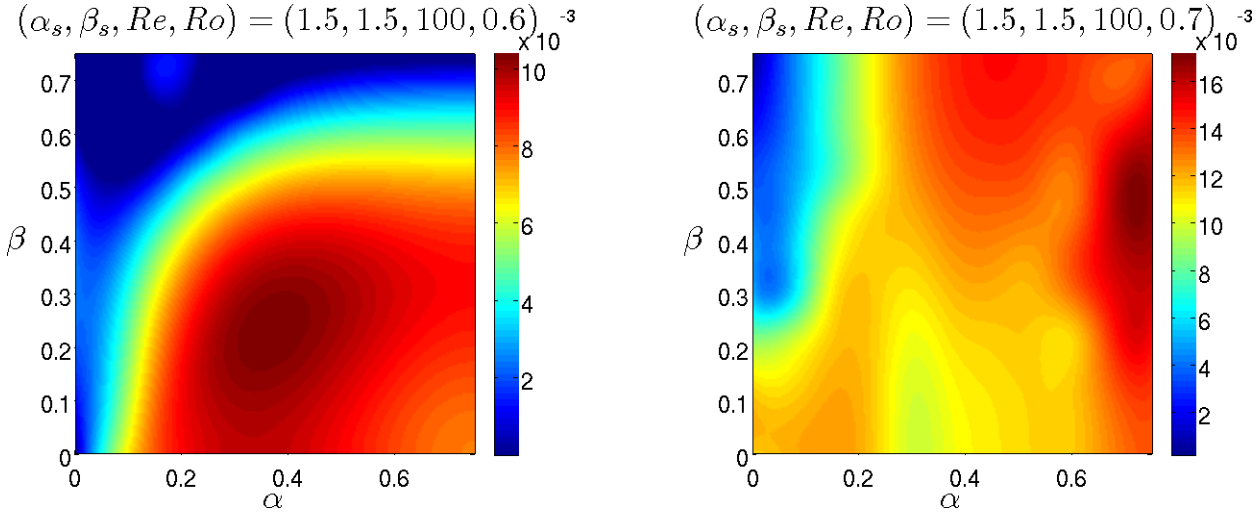

Figure 3.41: Stability of harmonically stable and unstable TWI solutions at $Ro = 0.6$ and $Ro = 0.7$ for $(\alpha_s, \beta_s, Re) = (1.5, 1.5, 100)$. $\sigma_r \geq 0$ is coloured. Both solutions de-stabilize to stationary, subharmonic perturbations. The harmonic instability for the $Ro = 0.7$ state is also a stationary mode.

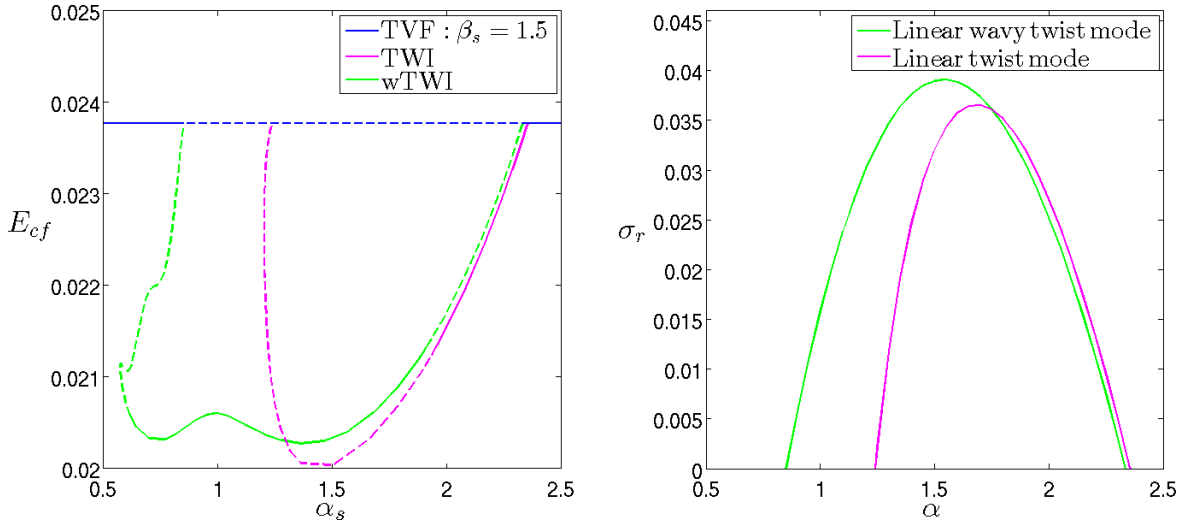

Figure 3.42: Left: continuation in (α_s, E_{cf})-subspace for $(\beta_s, Re, Ro) = (1.5, 100, 0.7)$. Right: secondary stability of TVF $(\beta_s, Re, Ro) = (1.5, 100, 0.7)$.

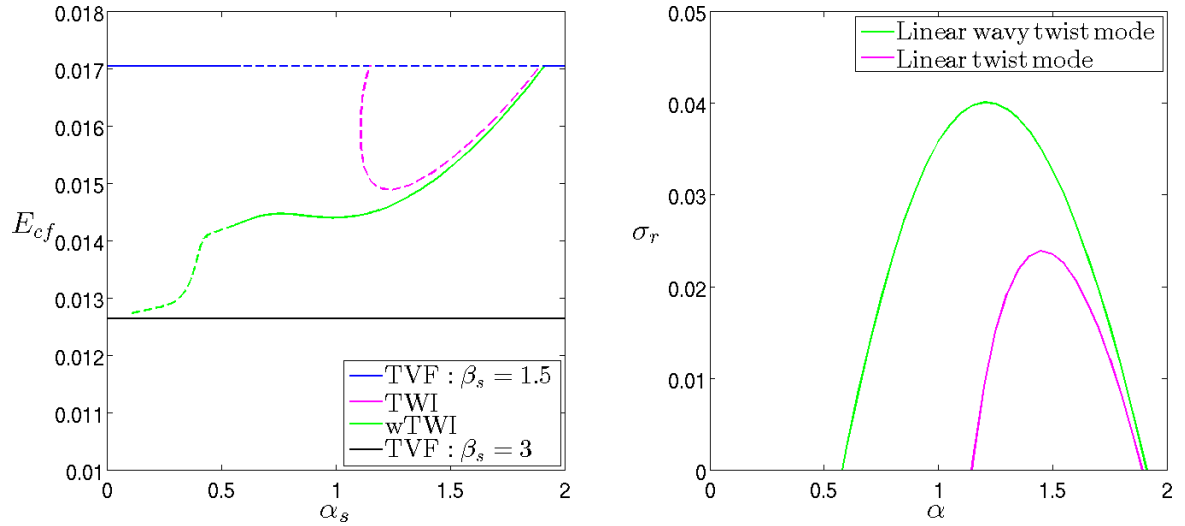

Figure 3.43: Left: continuation in (α_s, E_{cf})-subspace for $(\beta_s, Re, Ro) = (1.5, 100, 0.8)$. Right: secondary stability of TVF $(\beta_s, Re, Ro) = (1.5, 100, 0.8)$.

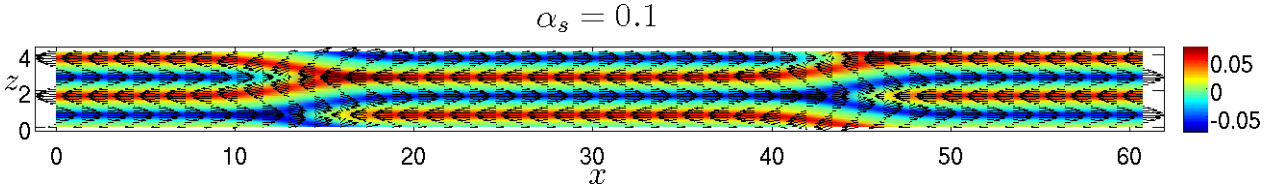

Figure 3.44: wTWI solution with $\alpha_s = 0.1$ and $(\beta_s, Re, Ro) = (1.5, 100, 0.8)$. The twists become increasingly localized as $\alpha_s \to 0$ and the solution approaches TVF with $\beta_s = 3$.

3.7.6 Bifurcation of wavy and oscillatory wavy vortex flows

We trace the trajectories of WVF and oWVF for $(\alpha_s, \beta_s) = (0.6, 2.6)$ and $(\alpha_s, \beta_s) = (0.8, 3)$ in Figures 3.45 and 3.46. In Figure 3.45, for $(\alpha_s, \beta_s) = (0.6, 2.6)$ we find a transcritical bifurcation from TVF towards WVF in the range $0.026 < Ro < 0.128$ and a Hopf bifurcation towards oWVF over $0.384 < Ro < 0.7$. The black curve which represents oWVF is the arithmetic mean of maximum and minium cross-flow energy that the solution oscillates between during its temporal evolution, for each Ro. The oWVF solution branch is a stable attractor in this case, as it is always harmonically stable. The WVF solution branch is harmonically unstable to complex conjugate eigenmodes, prompting the existence of time-periodic quaternary states which we do not pursue here.

For $(\alpha_s, \beta_s) = (0.8, 3)$ in Figure 3.46, the transcritical bifurcation towards WVF is similar to the previous case. The oWVF trajectory becomes more complex. Beginning with a Hopf bifurcation at $Ro = 0.355$, the solution reaches a turning point in (Ro, E_{cf})-space at $Ro = 0.438$, where it loses stability and subsequently loops over parameter space, reaching a minimum rotation number $Ro = 0.189$. The state re-gains harmonic stability at $Ro = 0.485$ and re-joins TVF at $Ro = 0.646$. The periods of both oWVF states from our two bifurcation diagrams are plotted in Figure 3.47, alongside the period of the unstable linear mode which de-stabilizes TVF. Figure 3.47 suggests that in the $(\alpha_s, \beta_s) = (0.8, 3)$ geometry there should exist a set of states for $0.43 < Ro < 0.48$ with period $T \approx 21.5$, though we are unable to find any such periodic orbits to satisfactory accuracy.

A situation arises at $Ro = 0.45$ where there do not exist any stable attractors in the domain $(\alpha_s, \beta_s) = (0.8, 3)$. oWVF, TVF and the base flow are all unstable. Thus, a random perturbation settles into a quasi-chaotic motion, moving between the unstable TVF and oWVF, though not visiting the base flow. In Figure 3.48 we plot the cross-flow energy evolution for a random initial condition (a random distribution of Stokes modes) with initial energy $E_{cf}(t = 0) = 10^{-6}$. Linear instability causes the perturbation to grow until nonlinear saturation when the fluid settles on TVF at $t = 105$. At $t = 340$ TVF breaks down resulting in a transient structure. The lower boundary of the E_{cf} oscillations of the transient state decreases steadily until $t = 1331$ when oWVF emerges. At $t = 1615$ oWVF breaks down and TVF re-appears, however, there is now enough background noise to cause TVF to de-stabilize on a much shorter timescale. By $t = 1738$ the flow has returned to the transient structure, and the cycle repeats again. The symmetries $\mathbf{S}$ and $\mathbf{\Omega}$ are satisfied throughout the process. The dynamics are reminiscent of the regeneration cycle described by Kawahara & Kida (2001) for plane Couette flow.

The stability properties of a harmonically stable and unstable oWVF solution, indicated by dots in Figures 3.45 and 3.46, are shown in Figure 3.49. We find that neither solution is globally stable. The harmonically stable solution is unstable to subharmonic modes with maximum at $(\alpha, \beta) = (0.45, 0.16)$. The frequency of the modes is tuned to the fundamental, suggesting they will oscillate with the same period as the oWVF solution. The instability of the harmonically unstable solution is strongest at the harmonic point. There is a region of spanwise subharmonic instability from $0.5 < \beta < 1$, but it is a much weaker instability than the harmonic modes.

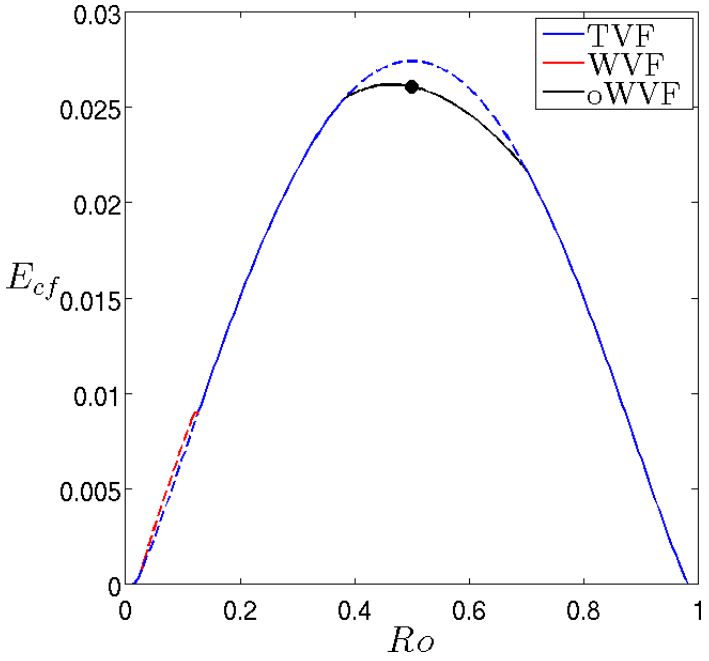

Figure 3.45: Tertiary bifurcations for $(\alpha_s, \beta_s, Re) = (0.6, 2.6, 100)$. The global stability of the solution indicated by the dot is calculated in Figure 3.49.

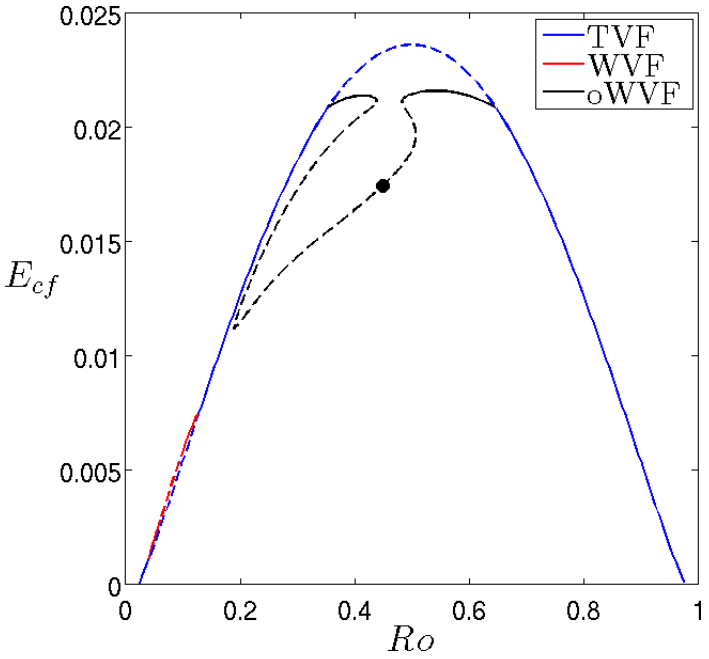

Figure 3.46: Tertiary bifurcations for $(\alpha_s, \beta_s, Re) = (0.8, 3, 100)$. The global stability of the solution indicated by the dot is calculated in Figure 3.49.

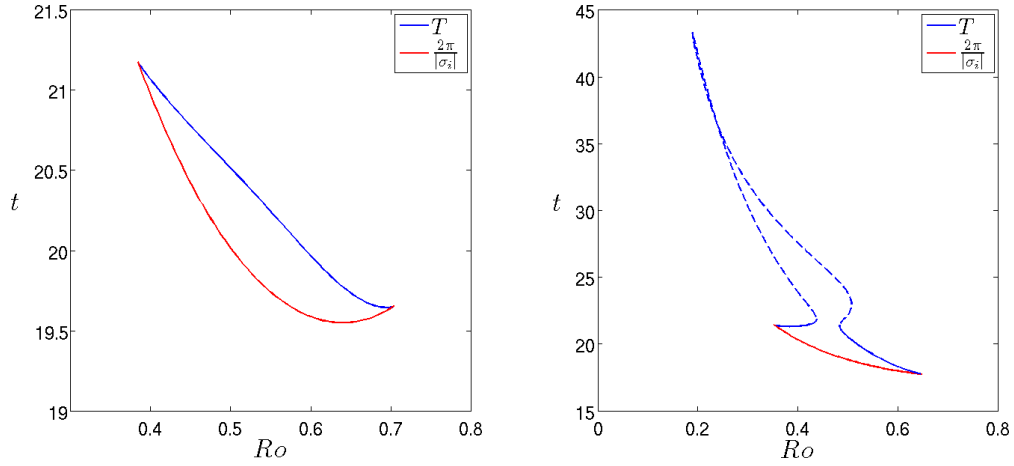

Figure 3.47: Period T of oWVF for $(\alpha_s, \beta_s, Re) = (0.6, 2.6, 100)$ and $(\alpha_s, \beta_s, Re) = (0.8, 3, 100)$. The solid line is the period of the orbit and the dashed line is the period of the secondary instability, $\frac{2\pi}{|\sigma_i|}$.

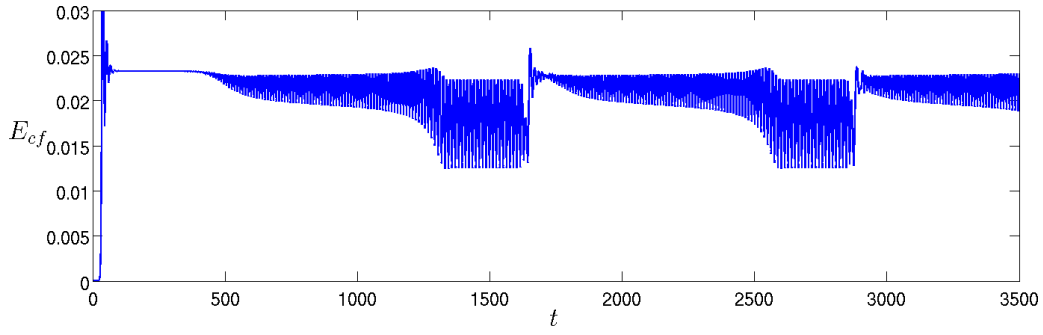

Figure 3.48: Cross-flow energy evolution of random initial condition for $(\alpha_s, \beta_s, Re, Ro) = (0.8, 3, 100, 0.45)$.

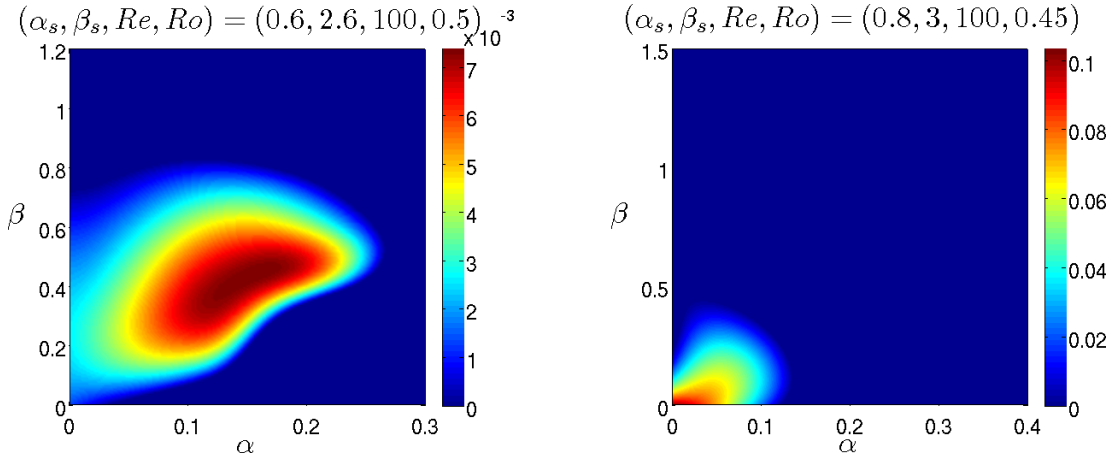

Figure 3.49: Stability of harmonically stable (left) and unstable (right) oWVF solutions. $\sigma_r \geq 0$ is coloured. Both states lose stability to subharmonic perturbations tuned to the fundamental frequency.

3.7.7 Bifurcation of skewed vortex flow

In Figure 3.50 we plot bifucations of streamwise-independent structures which bifurcate from TVF with $\beta_s = 4$. We find that SVF exists for a short range of high and low Ro. At $Ro = 0.085$ SVF bifurcates from TVF in a transcritical bifurcation. At $Ro = 0.235$ SVF joins with the second Taylor vortex solution, TVF_2. TVF_2 is itself unstable to complex conjugate eigenmodes, prompting a Hopf bifurcation to time-periodic solutions. We do not include the unsteady solutions in Figure 3.50, as tracing the solutions became difficult due to a rapidly increasing period of oscillations. The second branch of SVF connects TVF and TVF_2 at high Ro. Both the harmonically stable and unstable SVF solutions considered in Figure 3.51 lose stability to streamwise and spanwise subharmonic modes. The $Ro = 0.1$ solution is maximally unstable at $(\alpha, \beta) = (0.6, 0.2)$, losing stability to a complex conjugate pair of eigenmodes. An Eckhaus instability region with zero-phase modes arises close to $\beta = 2$, with local maximum $(\alpha, \beta) = (0, 0.2)$. The $Ro = 0.85$ solution is harmonically unstable to a complex-conjugate pair of modes. However, this instability is overtaken by zero-phase Eckhaus modes with maximum growth rate at half the spanwise wavenumber, $(\alpha, \beta) = (0, 2)$.

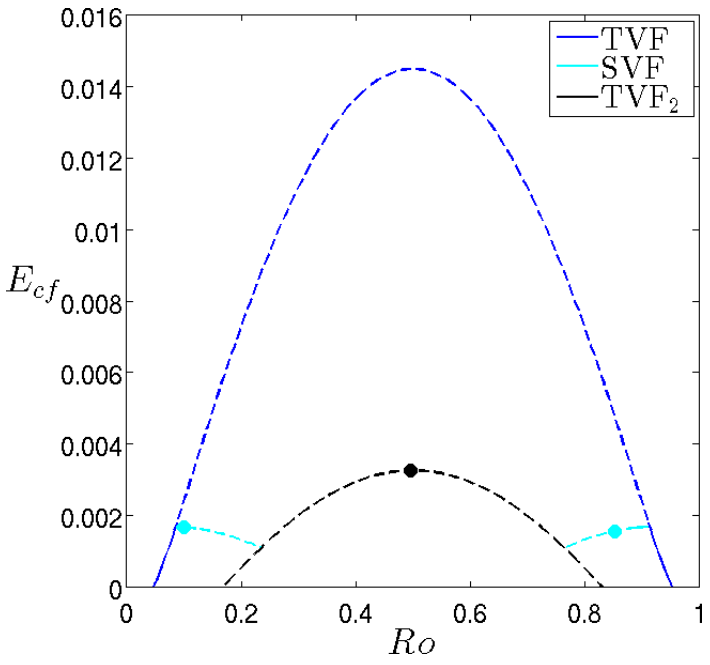

Figure 3.50: Tertiary bifurcations for $(\alpha_s, \beta_s, Re) = (0, 4, 100)$

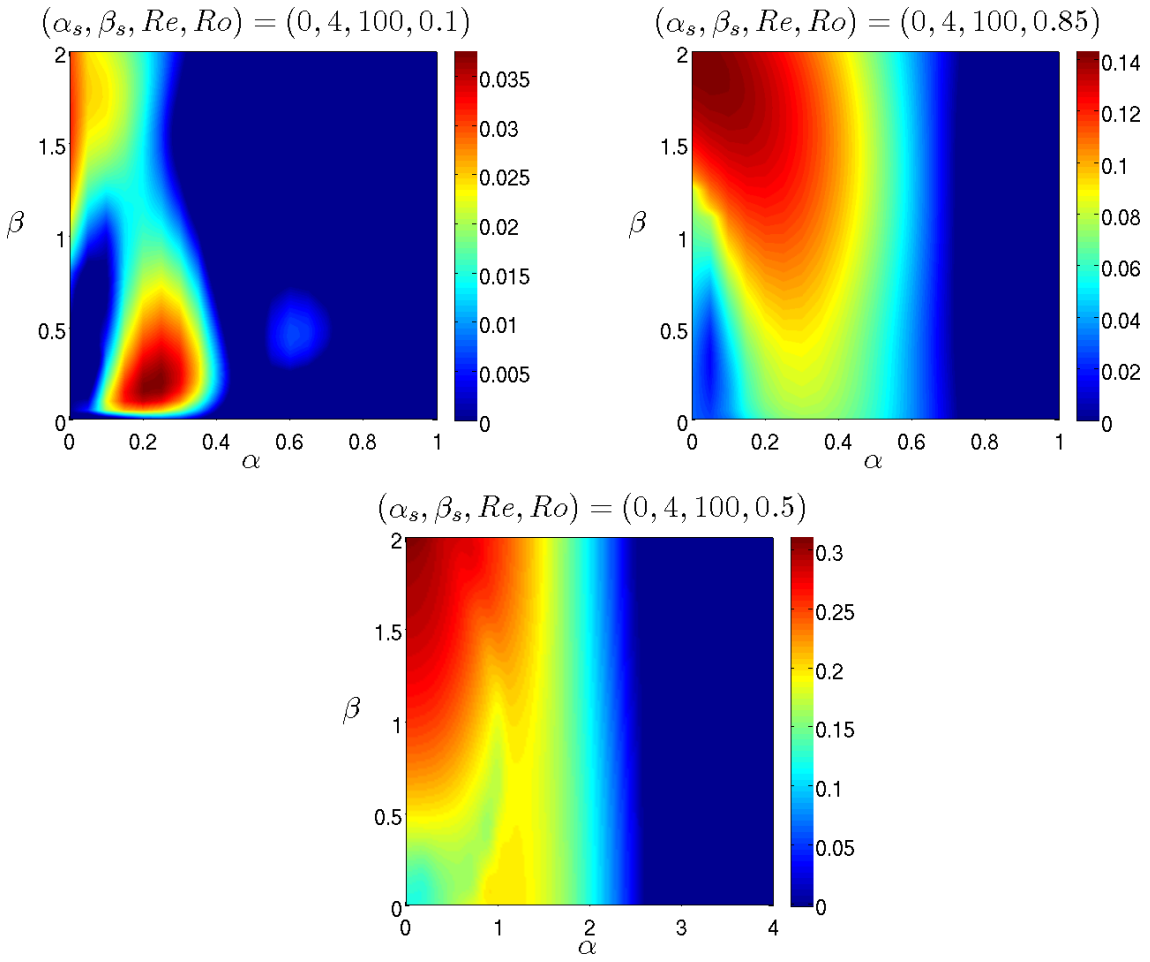

Figure 3.51: Stability of harmonically stable (top-left) and unstable (top-right) SVF solutions and TVF_2 (bottom). $\sigma_r \geq 0$ is coloured in (α, β).

3.8 Transition modelling

In this section we investigate the extent to which our stability analysis of secondary and tertiary states provide insight into the supercritical transitions observed in the experiments of Tsukahara *et al.* (2010) and Suryadi *et al.* (2013), who have mapped flow states in the (Ω, Re)-plane. The experimenters guarded against hysteresis effects by arriving at parameter combinations in two ways; case-Re where Re is fixed while Ω is increased to its target value; and case-Ω where the rotation number is fixed and Re is slowly decreased from 1000 towards the desired value. Having settled the flow on a point in (Ω, Re)-space the experimenters wait for some time to allow the fluid to settle before making observations and characterizations of the flowfield.

We analyze transition in two ways. Firstly, we perform a numerical analogue to the experiments: a long-time large periodic box simulation of a random initial flowfield. Secondly, we introduce a simple model in §3.8.2 which makes a prediction of the final flow state without resorting to a large scale simulation of the Navier-Stokes equations, or incorporating vortex splitting and merging, such as is discussed by Guo & Finlay (1991). Our first approach serves as an assessment of how well the Navier-Stokes equations with streamwise and spanwise periodic boundary conditions capture the dynamics of the experiments. As noted in Tsukahara *et al.* (2010), Ekman layers are likely to form at the lower boundary of their apparatus, causing a change in wavelengths between structures near the lower wall and those away from it. An Ekman layer is formed at a solid wall in a rotating fluid, and their effects have been discussed in Taylor-Couette experiments (Czarny *et al.* (2003), Hollerbach & Fournier (2004), Altmeyer *et al.* (2010), Heise *et al.* (2013)), however, we do not include the effects of Ekman layers in this analysis.

The focus of this study is the transition between laminar flow states, prior to transitions to quasi or fully turbulent dynamics. As such, we fix $Re = 100$ and investigate changes in the flow structures with respect to the rotation parameter. Tsukahara *et al.* (2010) found four flow states in the region $0 < \Omega < 30$, which corresponds to $0 < Ro < 0.3$ (see Figure 3.52 for a re-print of their state-space map). In increasing Ω, the flow states are labelled COU3Ds (spatio-temporally intermittent three-dimensional roll-cells) from $2 < \Omega < 7$, COU3D (three-dimensional roll-cells) from $7 < \Omega < 12$, COU2Dm (two-dimensional meandering roll-cells) from $12 < \Omega < 15$ and COU2Dh (two-dimensional roll-cells at high rotation number) from $15 < \Omega < 30$. Photographs of the flow states COU3Ds, COU3D and COU2Dh are re-printed from Tsukahara *et al.* (2010) in Figures, 3.53, 3.54 and 3.55. Suryadi *et al.* (2013) have extended the rotation parameters and found that for $Re = 100$: two-dimensional roll-cells persist over $30 < \Omega < 70$, and for

$\Omega = 90$ two distinct patterns are observed at different times. Photographs of the two flow states as observed in the latter experiments, which we will label (A) and (B), are printed in Figure 3.56. The photographs were kindly sent by private communication with the authors. Of the two flowfields, (A) has a much greater degree of streamwise structure in comparison with (B), which contains localized folds between streaky structures.

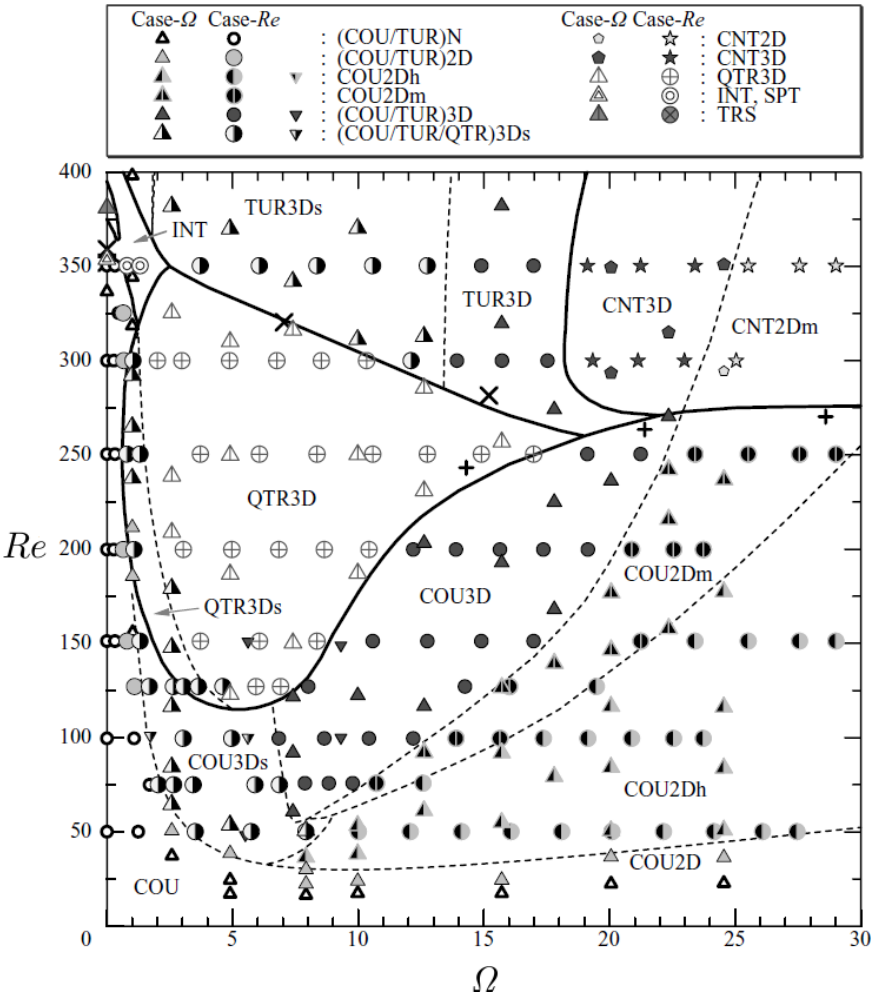

Figure 3.52: Re-print of Figure 3 from Tsukahara *et al.* (2010), showing the flow states observed at different locations in the (Re, Ω) parameter space. We focus on the transition between states with fixed Reynolds number, $Re = 100$.

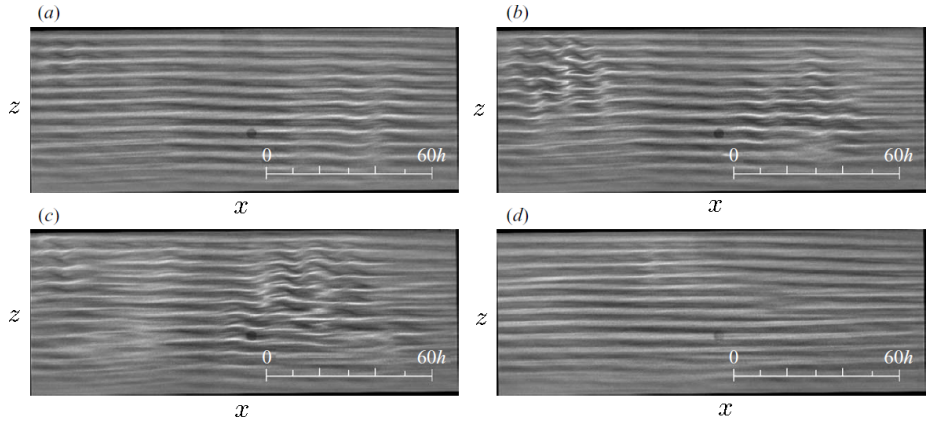

Figure 3.53: Re-print of Figure 10 from Tsukahara *et al.* (2010), showing the flow state COU3Ds for $(Re, \Omega) = (151,1.32)$. (a), (b), (c) and (d) correspond to images recorded at time intervals of 0, 12, 24 and 50 seconds.

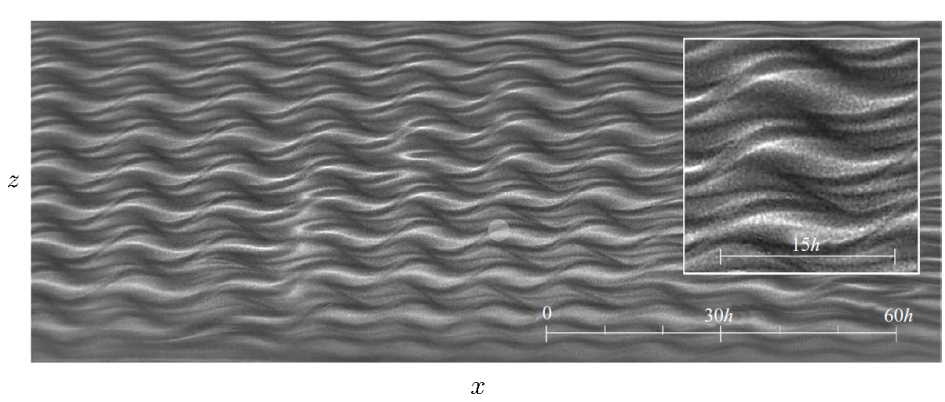

Figure 3.54: Re-print of Figure 9(a) from Tsukahara *et al.* (2010), showing the flow state COU3D for $(Re, \Omega) = (99.6,8.65)$.

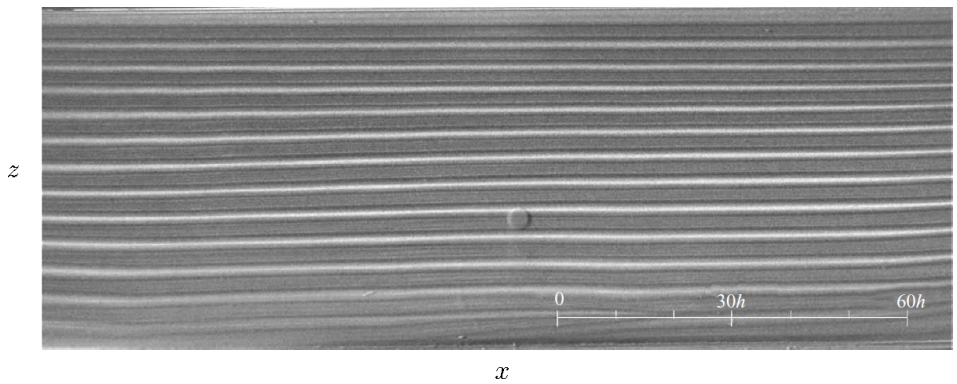

Figure 3.55: Re-print of Figure 14 from Tsukahara *et al.* (2010), showing the flow state COU2Dh for $(Re, \Omega) = (178,24.6)$.

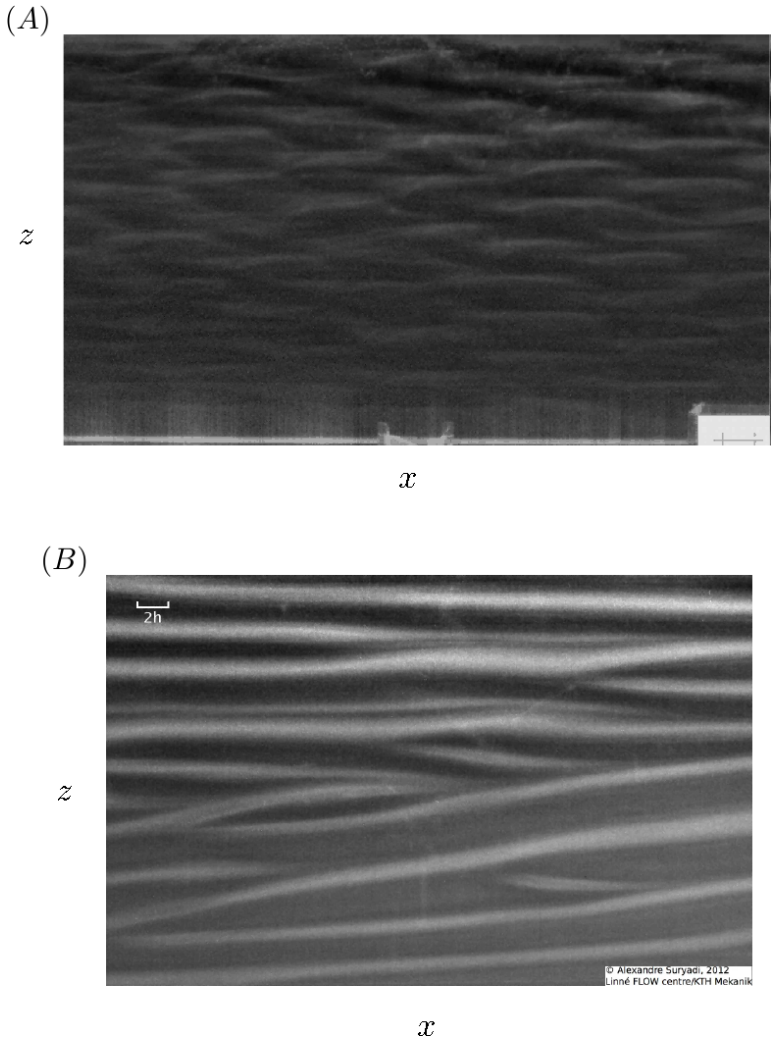

Figure 3.56: Photographs of the two distinct flow states observed experimentally by Suryadi *et al.* (2013) for $(Re, \Omega) = (100, 90)$. (Private communication).

3.8.1 Numerical procedure

For each numerical simulation we have used a domain $\mathbf{D}$, with fundamental wavenumbers $\alpha_f = 0.2$ and $\beta_f = 0.4$

$$\mathbf{D} = [0, 10\pi] \times [-1, 1] \times [0, 5\pi], \tag{3.78}$$

which is discretized as $N_x \times N_y \times N_z = 256 \times 49 \times 128$. This discretization is chosen such that the number of points per unit length is in keeping with other large domain simulations, for example Duguet *et al.* (2010) who used $N_x \times N_y \times N_z = 2048 \times 33 \times 1024$ in the very large domain $[0, 800] \times [-1, 1] \times [0, 356]$. The precise geometry of the experimental apparatus is not reported for each case in Tsukahara *et al.* (2010), since the wall-normal gap is modified for each Re. However, the streamwise and spanwise lengths are reported as 1500mm and 360mm respectively, so a wall-normal width of 10mm, for example, would imply a domain of $300h \times 2h \times 72h$. Thus $\mathbf{D}$ is much smaller than the

experimental domain, which can of course introduce a reason of discrepancy between our simulations and the experiments.

A random initial perturbation of the base flow, $\boldsymbol{u}_0$, is generated using

$$\boldsymbol{u}_0 = \sum_{j=-N_x/2+1}^{N_x/2} \sum_{k=-N_z/2+1}^{N_z/2} \sum_{\ell=0}^{N_y-1} \mu_{j,k,s} T_\ell(y) \mathrm{e}^{\mathrm{i}(j\alpha_f x + k\beta_f)}, \tag{3.79}$$

where $T_\ell(y)$ is the ℓ^{th} Chebyshev polynomial of the first kind, and

$$\mu_{j,k,s} = \lambda(1-s)^{|j|+|k|+|\ell|}, \tag{3.80}$$

where λ is a random number with $\lambda \in [-1, 1]$. s is a parameter controlling the smoothness of the field. We set $s = 0.2$ and initial energy $E_0 = 5 \times 10^{-2}$ for the initial perturbation. The same field is used as the initial condition for each simulation.

3.8.2 Model prediction

We now introduce a simplified model of the transition scenario which we use to make a predicition of the final flow state at each Ω. We begin by calculating the spectral energy $E^0_{\alpha\beta}$ of the initial disturbance, $\boldsymbol{u_0}(x, y, z)$. For

$$\boldsymbol{v}_{\alpha\beta}(y) = \int_0^{\frac{2\pi}{\alpha}} \int_0^{\frac{2\pi}{\beta}} \boldsymbol{u}_0(x, y, z) \mathrm{e}^{\mathrm{i}(\alpha x + \beta z)} \, dz dx, \tag{3.81}$$

we have

$$E^0_{\alpha\beta} = \frac{1}{2} \int_{-1}^{1} \boldsymbol{v}_{\alpha\beta} \boldsymbol{v}^*_{\alpha\beta} \, dy. \tag{3.82}$$

From linear theory, the growth rate $\omega_{\alpha\beta}$ at which disturbances are linearly amplified about the linear base profiled is calculated. During the primary linear growth phase we expect the energy of each mode to grow as

$$E(t) = E^0_{\alpha\beta} \mathrm{e}^{2\omega_{\alpha\beta} t}. \tag{3.83}$$

We then define a saturation energy, E_s, being the energy at which we expect nonlinear effects to dominate the dynamics. Since disturbances with $\alpha = 0$ have the largest linear growth rates (cf §3.2), we assume that a spanwise wavenumber, β^{II}, will emerge from the linear growth phase to dominate the secondary dynamics. To determine β^{II}, we solve for the saturation time t_s

$$t_s(\beta) = \frac{1}{2\omega_\beta} \log\left(\frac{E_s}{E^0_{0\beta}}\right). \tag{3.84}$$

Then β^{II} is defined to be the wavenumber which minimizes the saturation time

$$t_s(\beta^{\mathrm{II}}) = \min_{\beta} t_s(\beta). \tag{3.85}$$

We then assume a secondary Taylor vortex solution with spanwise wavenumber β^{II} to emerge, which we will denote, $\boldsymbol{U}^{\mathrm{II}}(\alpha, \beta) = \boldsymbol{U}^{\mathrm{II}}(0, \beta^{\mathrm{II}})$. If the vortex is unstable to streamwise disturbances, a streamwise wavenumber α^{III} will appear which maximizes the growth rate σ of a linear perturbation to the Taylor vortex

$$\sigma(\alpha^{\mathrm{III}}) = \max_{\alpha} \sigma(\alpha). \tag{3.86}$$

A third solution, $\boldsymbol{U}^{\mathrm{III}}(\alpha^{\mathrm{III}}, \beta^{\mathrm{II}})$, can then be computed. From a further Floquet analysis on this third state we determine wavenumbers α^{IV} and β^{IV} which satisfy

$$\sigma(\alpha^{\mathrm{IV}}, \beta^{\mathrm{IV}}) = \max_{\alpha,\beta} \sigma(\alpha, \beta), \tag{3.87}$$

$$\alpha^{\mathrm{IV}} \leq \alpha^{\mathrm{III}}, \quad \beta^{\mathrm{IV}} \leq \beta^{\mathrm{II}}, \tag{3.88}$$

where σ is again the growth rate of a linear perturbation to the third state. A new state, $\boldsymbol{U}^{\mathrm{IV}}(\alpha^{\mathrm{IV}}, \beta^{\mathrm{IV}})$ is found by repeating $\boldsymbol{U}^{\mathrm{III}}$ over the wavenumber domain $(\alpha^{\mathrm{IV}}, \beta^{\mathrm{IV}})$, adding a random perturbation to the flowfield, and then evolving towards a steady state or periodic orbit. The random perturbation selects the natural bifurcation away from $\boldsymbol{U}^{\mathrm{III}}$ towards $\boldsymbol{U}^{\mathrm{IV}}$, without the need to perturb the system with specified eigenmodes from the Floquet analysis. This process is continued until a globally stable solution is found, or until finding a solution becomes too computationally expensive. We expect this solution to feature flowfields of the simulations and experiments. We have refrained from defining the progression of solutions as tertiary and quaternary in favour of III, IV, ..., since we have defined tertiary solutions in §3.7 to be structures which originate in a bifurcation from secondary states, meaning IV and higher states could be classified as *tertiary* solutions in keeping with this convention.

In the analysis which follows we choose saturation energy $E_s = 0.00125$, on the assumption that velocities with amplitude $A_s = \sqrt{2E_s} = 0.05$ give a reasonable estimate for the onset of nonlinear interactions. For the stability calculations we need only compute growth rates for wavenumbers that are harmonics of the fundamentals, since they are the only ones supported by the domain

$$\alpha = 0, 0.2, 0.4, 0.6, \ldots \tag{3.89}$$

$$\beta = 0, 0.4, 0.8, 1.2, \ldots. \tag{3.90}$$

3.8.3 Time-periodic flow: $\Omega = 2.5$

For $\Omega = 2.5$ our simulation gives an unsteady, quasi-periodic flowfield, with E_{cf} evolution reaching a local maximum approximately every $200-300$ time units, shown in Figure 3.57 along with snapshots of the flowfield at certain times. The fluid is arranged into vortices with spanwise wavenumber $\beta = 1.2$ which oscillate in time, switching between wavy vortices and streamwise independent vortices during the oscillation. The streamwise variation of the vortices does not appear to be periodic on a smaller scale than the domain length, suggesting that the structure has streamwise wavenumber $\alpha = 0.2$. The dynamics could be crudely interpreted as a small-domain version of the COU3Ds observed by Tsukahara *et al.* (2010) for $2 < \Omega < 7$, who describe an intermittent process of three-dimensional (wavy) vortices changing to two-dimensional (streamwise independent) vortices and so on. In the transition model we find that the wavenumber minimizing the saturation time is $\beta^{\mathrm{II}} = 1.2$, so we set the secondary solution, $\boldsymbol{U}^{\mathrm{II}}(0, 1.2)$, to be TVF. $\boldsymbol{U}^{\mathrm{II}}$ is unstable to streamwise periodic perturbations, and its least stable mode is stationary, with wavenumber $\alpha^{\mathrm{III}} = 0.4$. Thus $\boldsymbol{U}^{\mathrm{III}}(0.4, 1.2)$ is a steady WVF, and we find that $\boldsymbol{U}^{\mathrm{III}}(0.4, 1.2)$ loses stability in a harmonic Hopf bifurcation, which generates an oscillatory wavy vortex flow (oWVF) $\boldsymbol{U}^{\mathrm{IV}}(0.4, 1.2)$ with period $T_p = 148.71$. $\boldsymbol{U}^{\mathrm{IV}}(0.4, 1.2)$ has a subharmonic instability to complex conjugate modes with half the natural frequency of $\boldsymbol{U}^{\mathrm{IV}}$, implying a structure will emerge which is periodic in time with the wavenumber combination $(\alpha^{\mathrm{V}}, \beta^{\mathrm{II}}) = (0.2, 1.2)$., though the period of the solution is too high to analyzed here. However, the results of the transition model would appear to be in good agreement with the simulation which, as described above, contained oscillating vortices with wavenumber $(\alpha, \beta) = (0.2, 1.2)$. The model results are contained in Figure 3.58, where we plot the saturation time against spanwise wavenumber and the growth rates from the stability calculations about the solutions $\boldsymbol{U}^{\mathrm{II}}$, $\boldsymbol{U}^{\mathrm{III}}$ and $\boldsymbol{U}^{\mathrm{IV}}$, respectively.

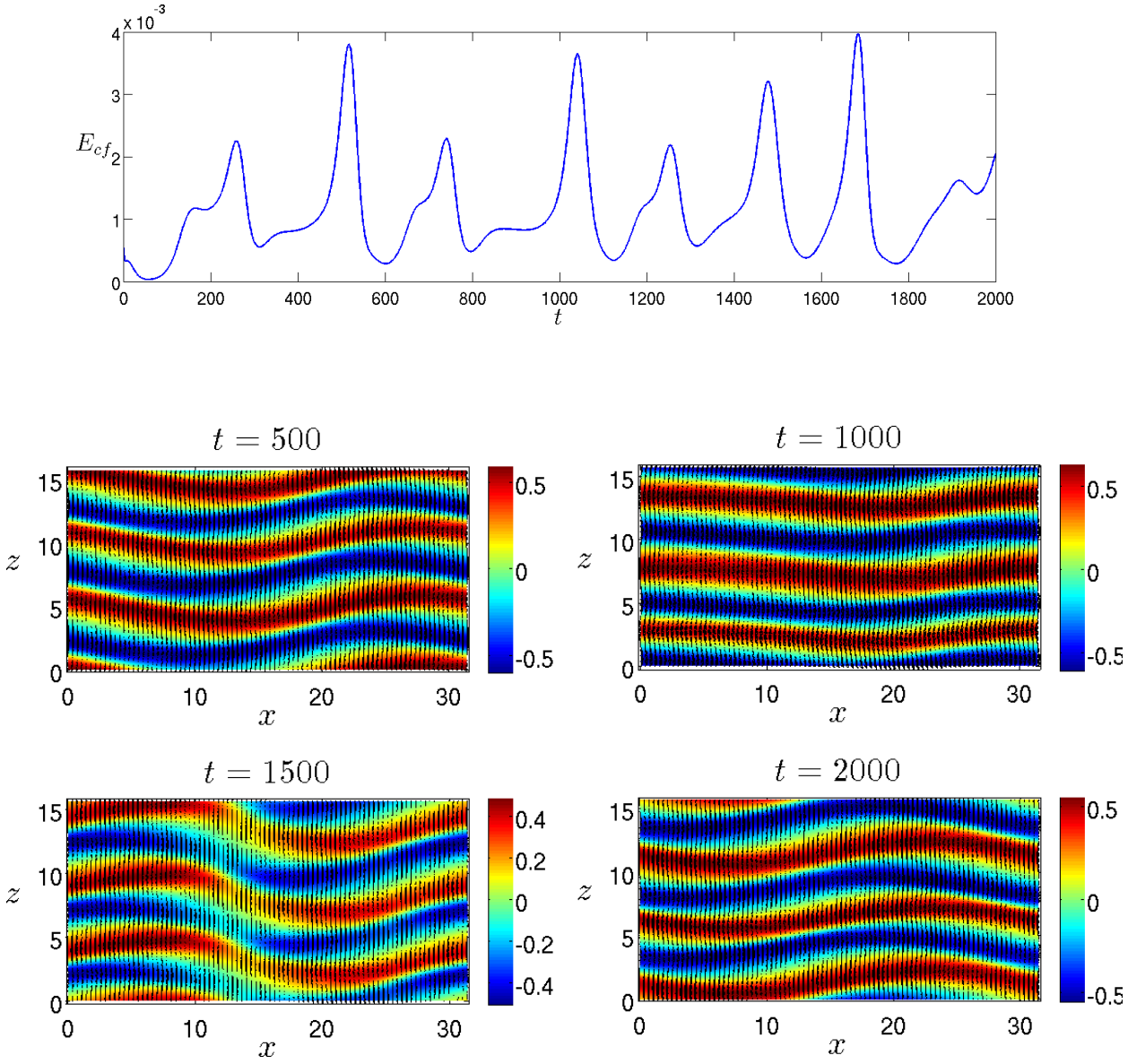

Figure 3.57: Simulation results for $\Omega = 2.5$. The E_{cf} evolution, plotted at the top, clearly displays the unsteadiness of the flowfield, sustained over 2000 time units. From the snapshots of the flowfield in the four bottom panels, we can see that the wavy pattern of the vortices oscillates in time. cf with the oscillatory parts of COU3Ds in Figure 3.53.

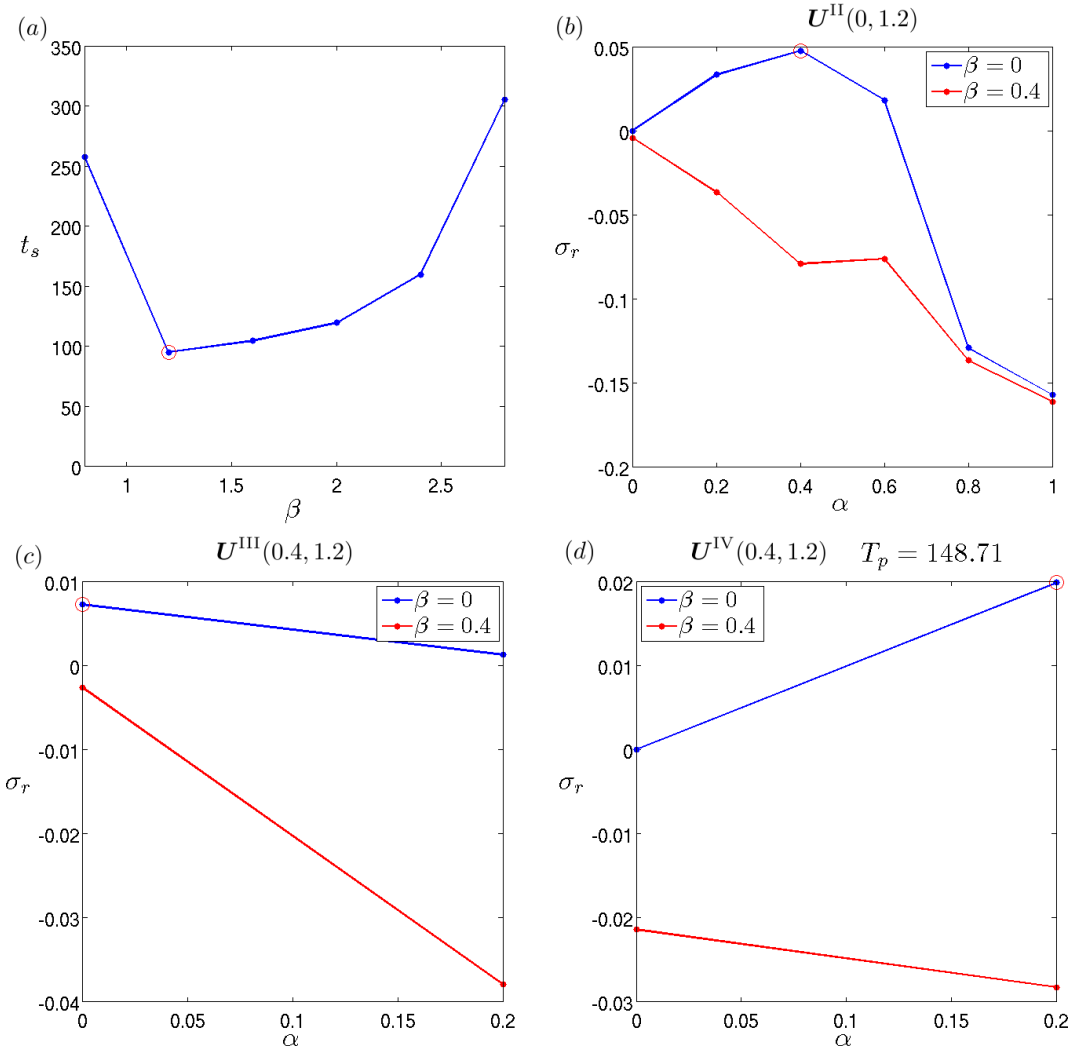

Figure 3.58: Results of the transition model for $\Omega = 2.5$. (a) Saturation time t_s against spanwise wavenumber β. $\beta^{\mathrm{II}} = 1.2$ minimizes t_s. In (b), (c) and (d) we plot the growth rates σ_r of the least stable perturbations of the solutions $\boldsymbol{U}^{\mathrm{II}}$ (TVF), $\boldsymbol{U}^{\mathrm{III}}$ (WVF) and $\boldsymbol{U}^{\mathrm{IV}}$ (oWVF) for all the subharmonic wavenumbers supported in $\mathbf{D}$. The least stable mode throughout $\mathbf{D}$ is circled in each panel.

3.8.4 Wavy vortex flow: $\Omega = 10$

For $\Omega = 10$, the simulation finishes in a stable WVF state with wavenumbers $(\alpha, \beta) = (0.4, 1.2)$. The cross-flow energy evolution and the final flowfield are shown in Figure 3.59, with the assembly of wavy vortex structures clearly visible in the velocity field. The stable WVF arrangement is in strong agreement with Tsukahara *et al.* (2010), who found stable wavy vortex flow, labelled COU3D in the range $7 < \Omega < 12$. The transition model additionally predicts a WVF final state. In the model, $\beta^{\mathrm{II}} = 1.2$ is selected by minimization of t_s, and the TVF $\boldsymbol{U}^{\mathrm{II}}(0, 1.2)$ de-stabilizes to a streamwise periodic wave with $\alpha^{\mathrm{III}} = 0.4$. $\boldsymbol{U}^{\mathrm{II}}(0, 1.2)$ subsequently transitions to the WVF $\boldsymbol{U}^{\mathrm{III}}(0.4, 1.2)$ which is stable in $\mathbf{D}$, as shown in Figure 3.60. We note that the streamwise wavenumber $\alpha^{\mathrm{III}} = 0.4$ produces a wavelength $x_L = \frac{2\pi}{\alpha^{\mathrm{III}}} \approx 15.71$, which is in good agreement with the wavelength of the wavy vortices of COU3D in Figure 3.54.

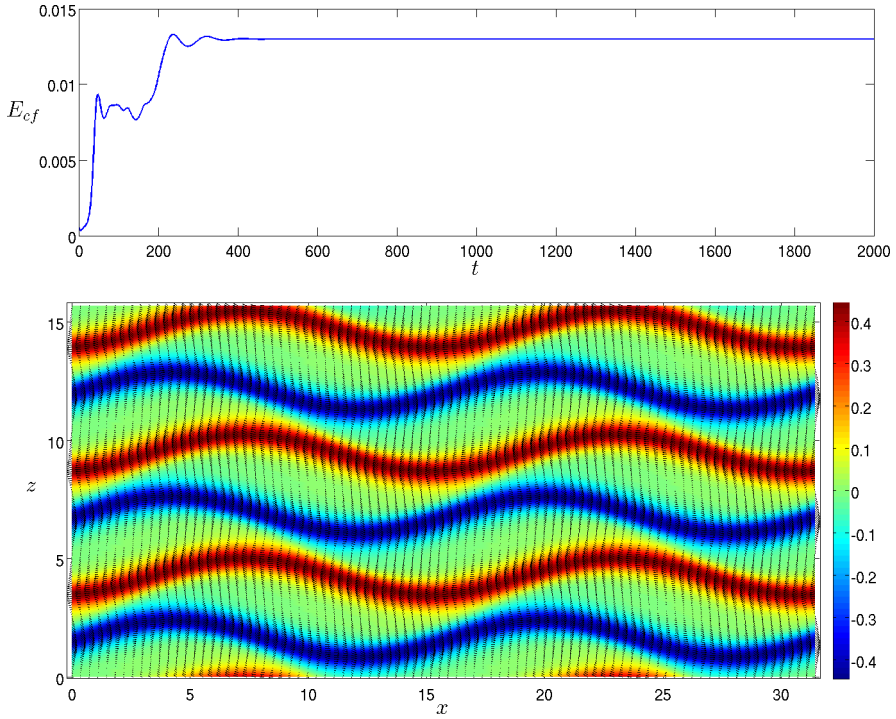

Figure 3.59: Simulation results for $\Omega = 10$. At the top is the E_{cf} evolution. On the bottom is the final flowfield in $\mathbf{D}$, which consists of a stable configuration of wavy vortices. cf with the COU3D flowfield in Figure 3.54.

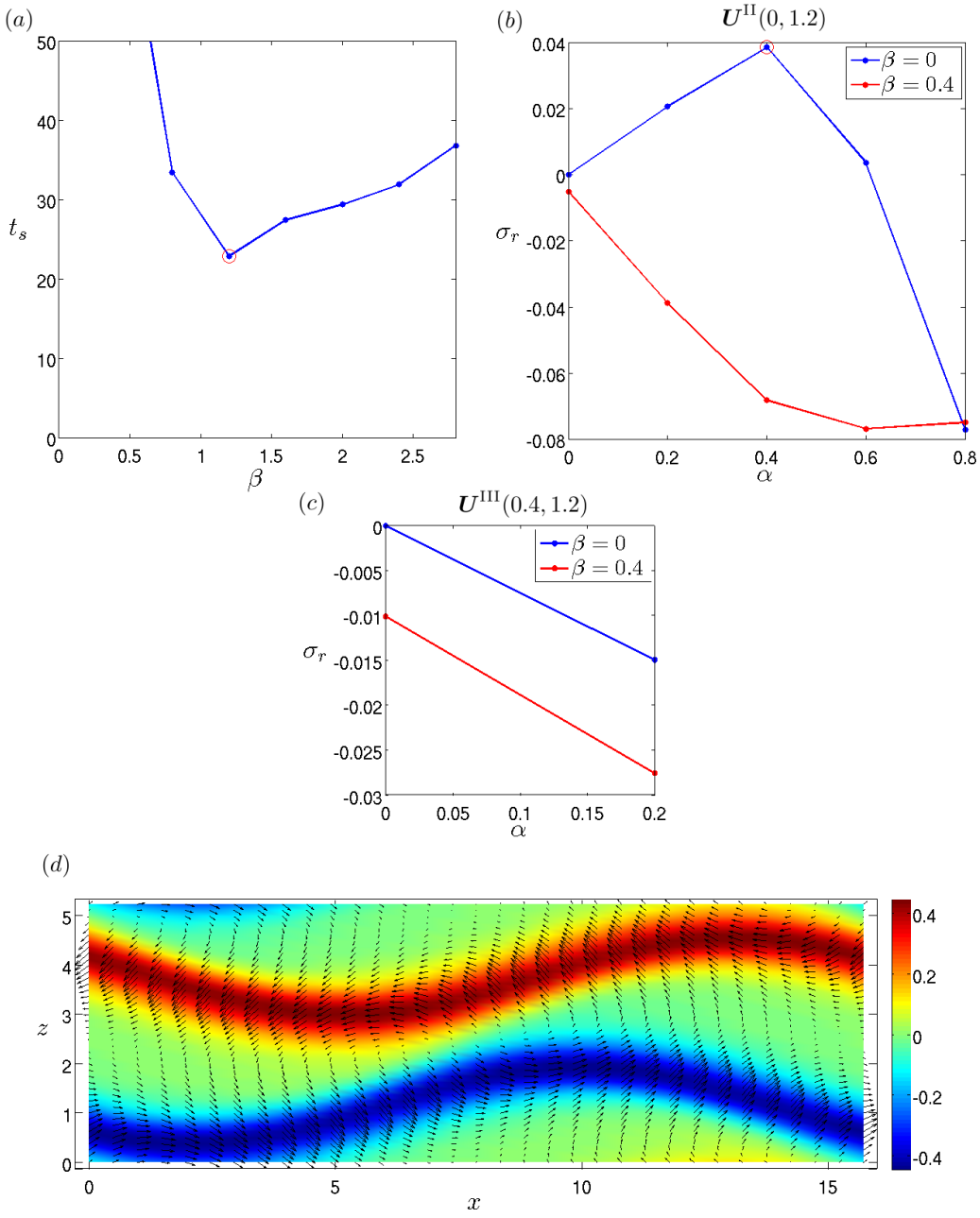

Figure 3.60: Transition model results for $\Omega = 10$. In (a), (b), (c) and (d) we plot the saturation time t_s against spanwise wavenumber β; the stability of $\boldsymbol{U}^{\mathrm{II}}(0, 1.2)$ in $\mathbf{D}$; the stability of $\boldsymbol{U}^{\mathrm{III}}(0.4, 1.2)$; and the stable wavy vortex flowfield corresponding to $\boldsymbol{U}^{\mathrm{III}}(0.4, 1.2)$. The red circles in (a) and (b) indicate the wavenumbers selected in each step.

3.8.5 Taylor vortex flow: $\Omega = 20$

As the system rotation is increased to $\Omega = 20$, the simulation in **D** finishes with a stable TVF with $\beta_s = 1.2$. We interpret this as an example of the COU2Dh Tsukahara *et al.* (2010) observed for $15 < \Omega < 30$. The cross-flow energy evolution and the flowfield consisting of an array of Taylor vortices are plotted in Figure 3.61. The transition model once again selects the spanwise wavenumber β^{II}, and we find that there are no secondary instabilities about the Taylor vortex at this spanwise wavelength and rotation parameter. The model results are shown in Figure 3.62. Thus the experiment, simulation and model all produce stable Taylor vortices in this case.

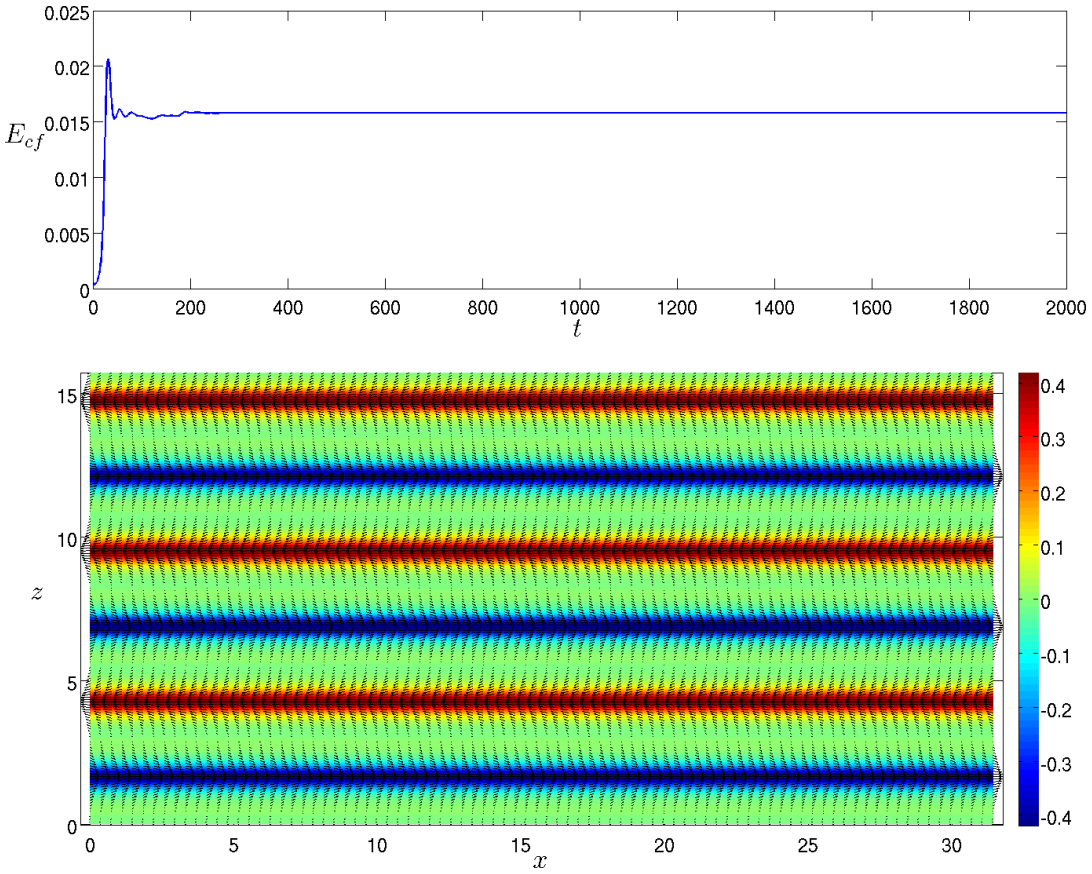

Figure 3.61: Simulation results for $\Omega = 20$. At the top is the E_{cf} evolution. On the bottom is the final flowfield: a stable arrangement of Taylor vortices. cf with the COU2Dh flowfield in Figure 3.55.

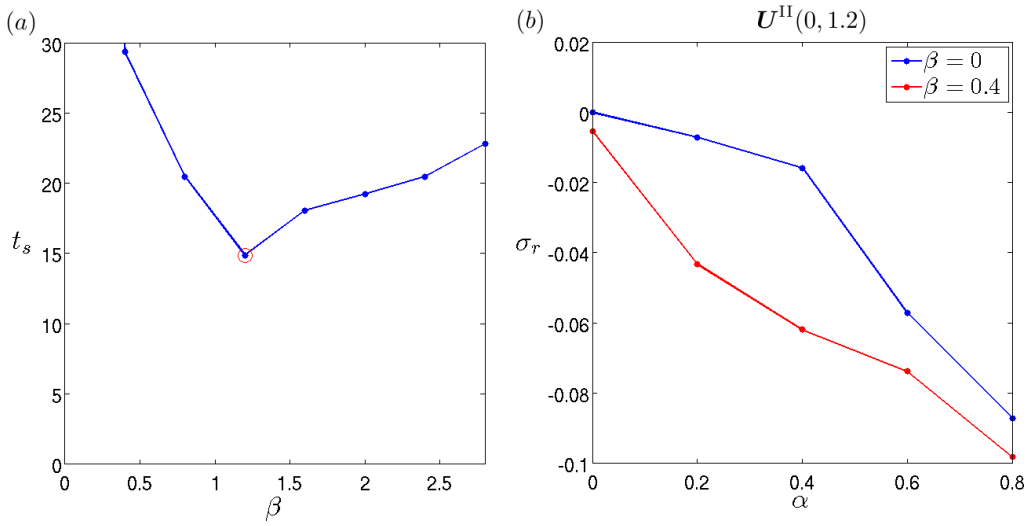

Figure 3.62: Transition model results for $\Omega = 20$. (a) Saturation time t_s against spanwise wavenumber β. (b) Secondary stability of the TVF $\boldsymbol{U}^{\mathrm{II}}(0, 1.2)$.

3.8.6 Taylor vortex flow: $\Omega = 50$

From the energy evolution of the simulation in Figure 3.63 we see that for $\Omega = 50$, the fluid has a lengthy unsteady phase over the first 3000 time units, after which there is an abrupt transition to a stable steady state. The unsteady flowfield contains a mixture of streaks and twist vortices, with a localized street of twist vortices settling in the region $0 < x < 10$, $5 < z < 12$ by $t = 2000$, and the steady flowfield is an arrangement of Taylor vortices with spanwise wavenumber $\beta = 1.6$, as is shown in Figure 3.63. The final flow structure agrees with the experimental observations of Suryadi *et al.* (2013), who report stable two-dimensional streamwise vortices persisting in the range $40 < \Omega < 70$, though structures similar to the unsteady flowfields, $t = 1000, 2000, 3000$ in Figure 3.63, have been observed at greater Reynolds numbers, $Re = 150, 200$. However, the transition model does not predict stable Taylor vortices in this case, instead predicting stable twist vortices. The model therefore offers an explanation as to why localized twist vortices appear in the simulation, though it is beyond the scope of the transition model to accurately describe the localized behaviour in $\mathbf{D}$ for $t < 3000$. Once again minimization of the saturation time gives the spanwise wavenumber $\beta^{\mathrm{II}} = 1.2$, and the Taylor vortices with this wavenumber lose stability to both wavy twist and twist modes. The wavy twist mode with streamwise wavenumber $\alpha^{\mathrm{III}} = 1.6$ is most unstable, generating the wTWI solution $\boldsymbol{U}^{\mathrm{III}}(1.6, 1.2)$, which in turn loses stability to a harmonic twist mode which initiates a bifurcation to the TWI solution $\boldsymbol{U}^{\mathrm{IV}}(1.6, 1.2)$. $\boldsymbol{U}^{\mathrm{IV}}(1.6, 1.2)$ is stable in $\mathbf{D}$, as is shown in Figure 3.64, and the flowfields of both $\boldsymbol{U}^{\mathrm{III}}(1.6, 1.2)$ and $\boldsymbol{U}^{\mathrm{IV}}(1.6, 1.2)$ are displayed in Figure 3.65.

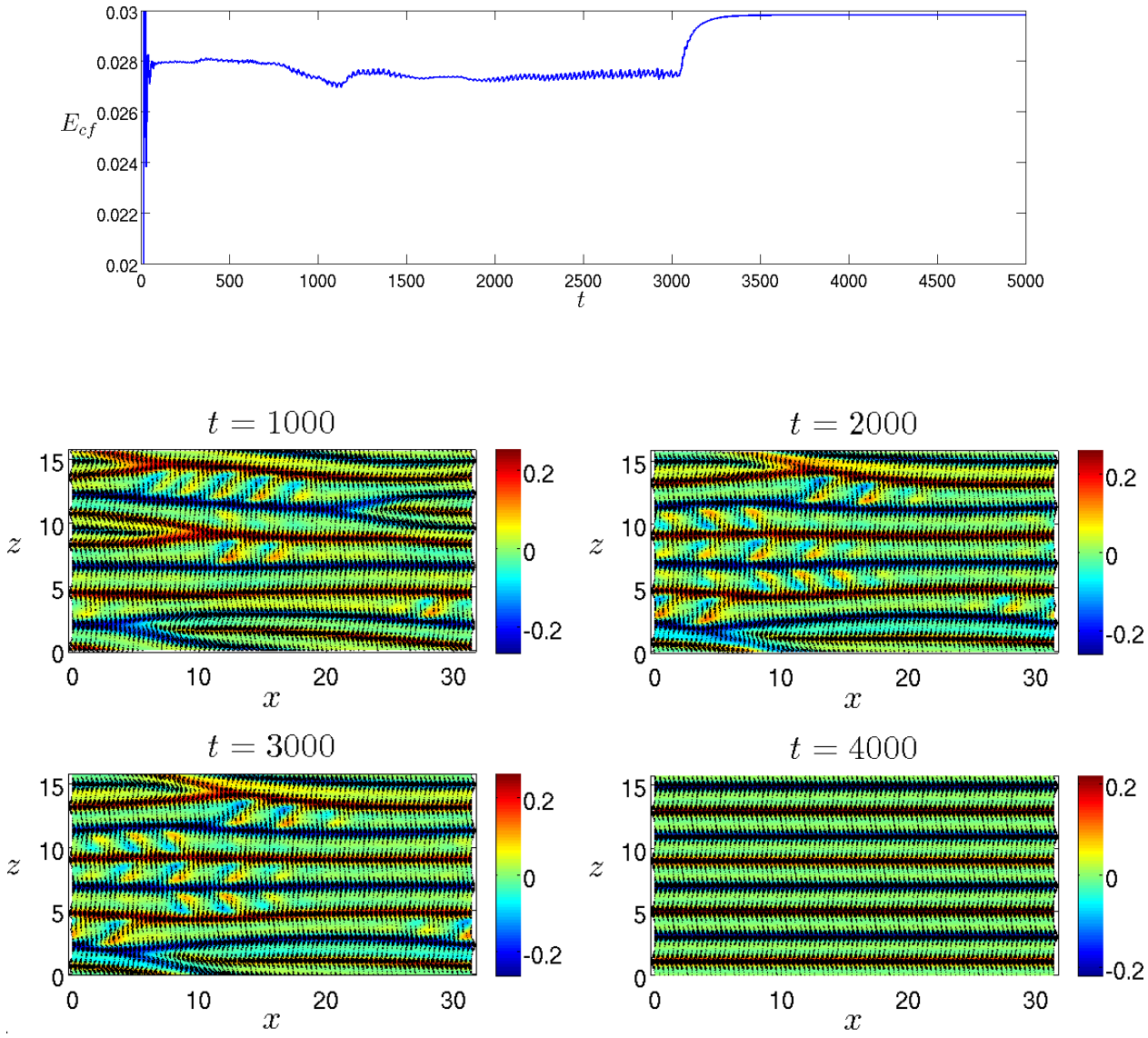

Figure 3.63: Simulation results for $\Omega = 50$. At the top is the E_{cf} evolution. On the bottom is the final flowfield: a stable arrangement of Taylor vortices.

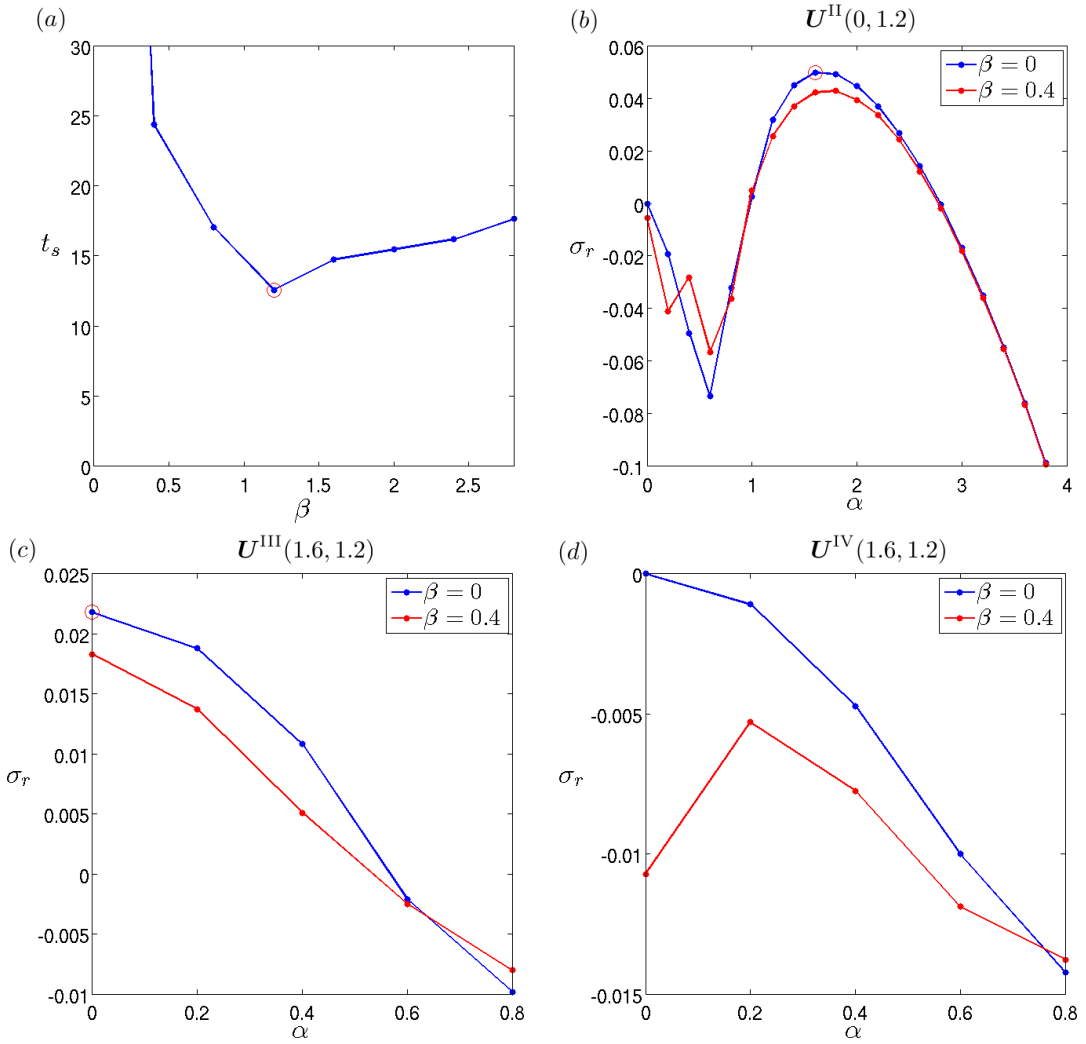

Figure 3.64: Transition model results for $\Omega = 50$. In (a), (b), (c) and (d) we plot the saturation time t_s against spanwise wavenumber β; the stability of $\boldsymbol{U}^{\mathrm{II}}(0, 1.2)$ in $\mathbf{D}$; the stability of $\boldsymbol{U}^{\mathrm{III}}(1.6, 1.2)$; and the stability of $\boldsymbol{U}^{\mathrm{IV}}(1.6, 1.2)$. The red circles in (a), (b) and (c) indicate the wavenumbers selected in each step.

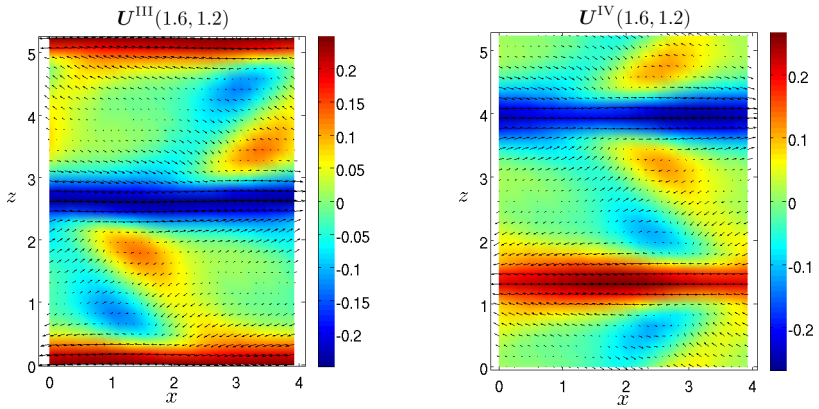

Figure 3.65: Flowfields of $\boldsymbol{U}^{\mathrm{III}}(1.6, 1.2)$ and $\boldsymbol{U}^{\mathrm{IV}}(1.6, 1.2)$ from the transition model for $\Omega = 50$.

3.8.7 Wavy twist vortex flow: $\Omega = 90$

The large simulation and the transition model do not agree in the case $\Omega = 90$, however, the transition model predicts a streamwise periodic wavy twist vortex final state and the simulation finishes on a flowfield with localized folds, which are similar to the experimentally observed structures (A) and (B), respectively, in Figure 3.56. The results of the simulation are displayed in Figure 3.66. After saturation, the flowfield at $t = 500$ contains an upper and lower pair of folds along its centre, with streamwise indepenent streaks of wavenumber $\beta = 1.6$ completing the domain on either side of the folds. The folds resemble the long wavelength wavy twist vortex solution found in §3.7 in Figure 3.44. As the simulation evolves, the upper fold collapses, and a short wavelength wavy twist vortex can be seen at $t = 1500$ before the complete disappearance of the upper fold, leaving only the lower fold surrounded by Taylor vortices. From Floquet theory we fine that the final structure is stable.

The transition model predicts the following transition of states: $\beta^{\mathrm{II}} = 1.2$ initiates TVF $\boldsymbol{U}^{\mathrm{II}}(0, 1.2)$ which loses stability to a wavy twist mode with $\alpha^{\mathrm{III}} = 0.8$; wTWI $\boldsymbol{U}^{\mathrm{III}}(0.8, 1.2)$ loses stability to subharmonic streamwise wavenumber $\alpha^{\mathrm{IV}} = 0.4$ which bifurcates towards a second wTWI $\boldsymbol{U}^{\mathrm{IV}}(0.4, 1.2)$; a further subharmonic streamwise wavenumber $\alpha^{\mathrm{V}} = 0.2$ de-stabilizes $\boldsymbol{U}^{\mathrm{IV}}(0.4, 1.2)$ prompting a bifurcation to a third wTWI $\boldsymbol{U}^{\mathrm{V}}(0.2, 1.2)$ which is stable in $\mathbf{D}$. The stability results are given in Figure 3.67 and the flowfields of the three wTWI solutions are plotted in Figure 3.68.

In Figure 3.69, the final flowfields from the model prediction and the simulation are plotted on a larger domain and placed next to their experimentally observed fields (A) and (B). We find that the model prediction provides a reasonable match for the behaviour seen in flowfield (A), while the simulation captures the folds observed in flowfield (B).

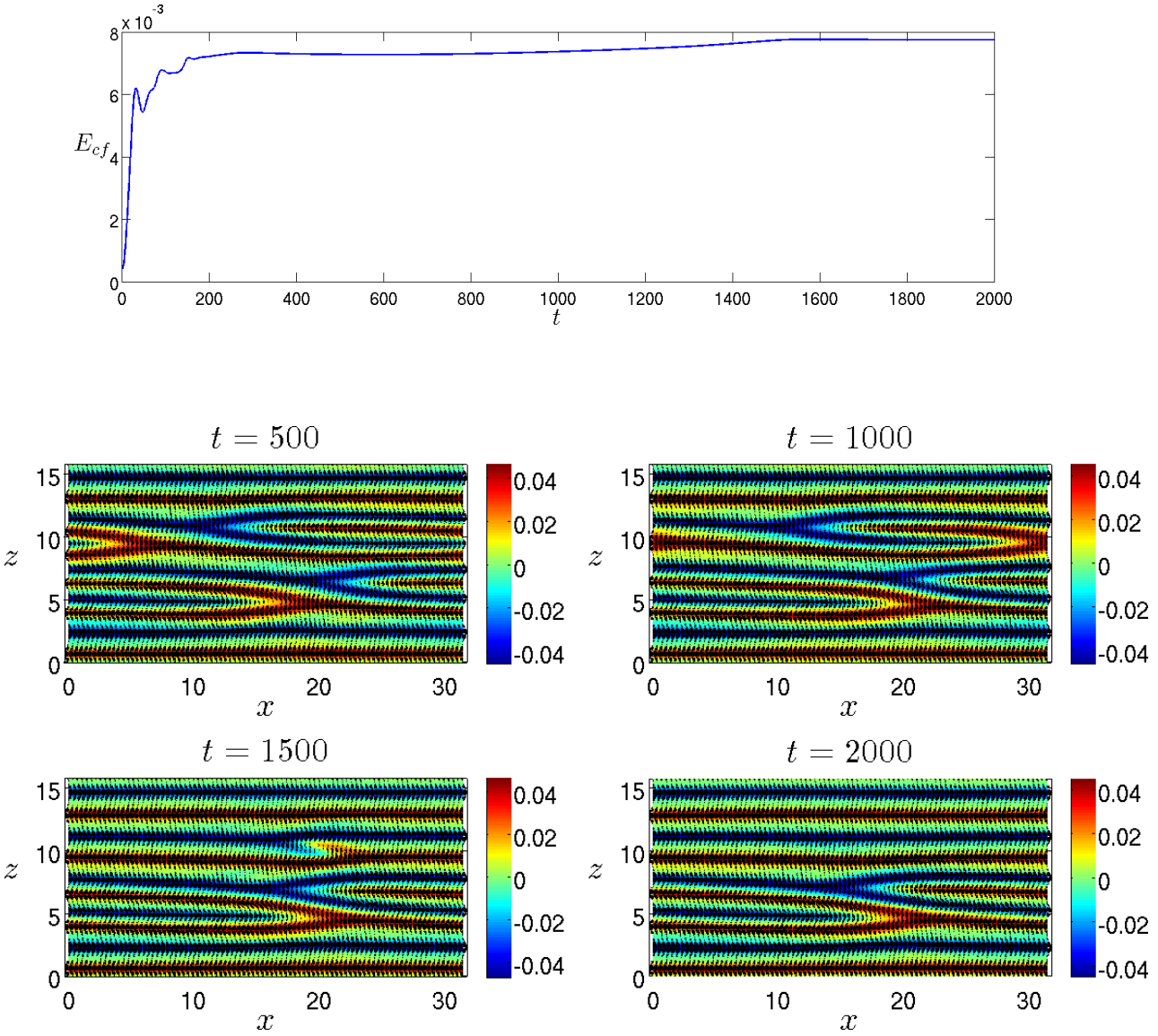

Figure 3.66: Simulation results for $\Omega = 90$. At the top is the E_{cf} evolution. Beneath we plot flowfields for $t = 500, 1000, 1500$ and 2000, showing the decay of the upper fold and persistence of the lower fold.

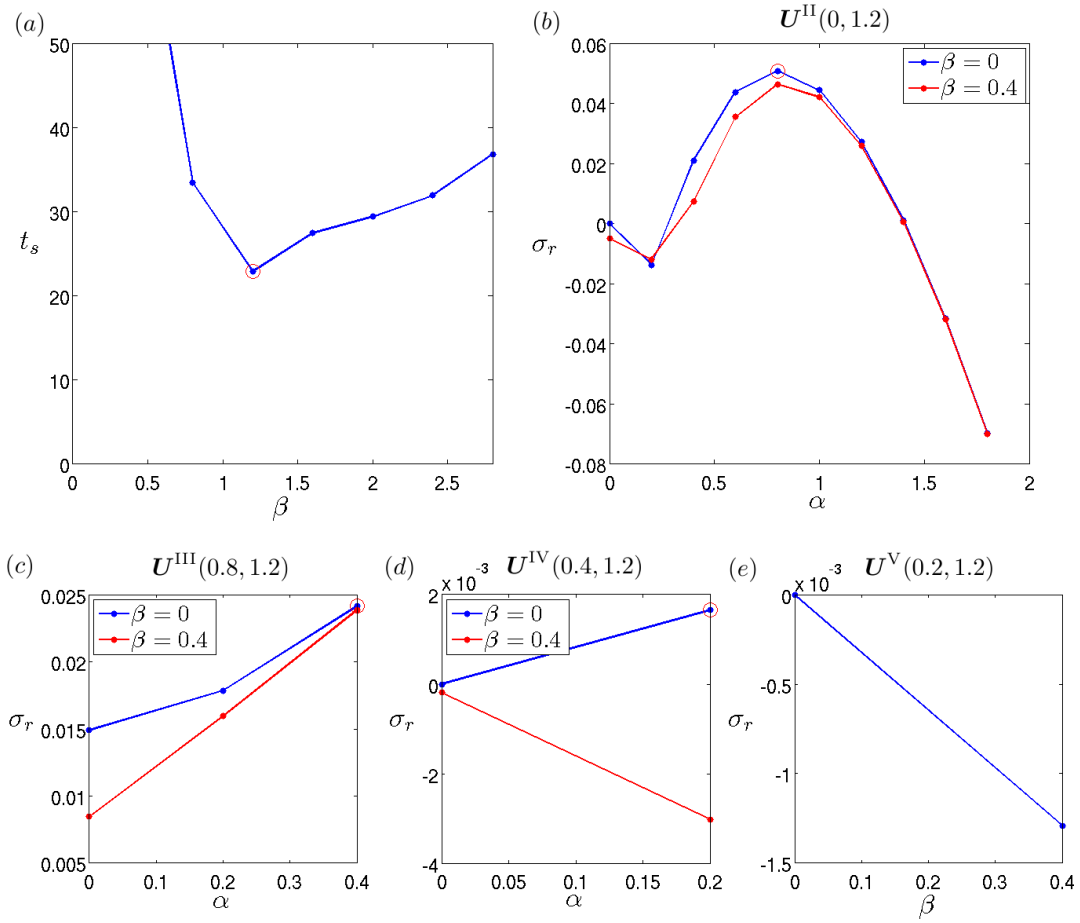

Figure 3.67: Transition model results for $\Omega = 90$. In (a), (b), (c), (d) and (e) we plot the saturation time t_s against spanwise wavenumber β; the stability of $\boldsymbol{U}^{\mathrm{II}}(0, 1.2)$ in $\mathbf{D}$; the stability of $\boldsymbol{U}^{\mathrm{III}}(0.8, 1.2)$; the stability of $\boldsymbol{U}^{\mathrm{IV}}(0.4, 1.2)$; and the stability of $\boldsymbol{U}^{\mathrm{V}}(0.2, 1.2)$. The red circles in (a), (b) and (c) indicate the wavenumbers selected in each step.

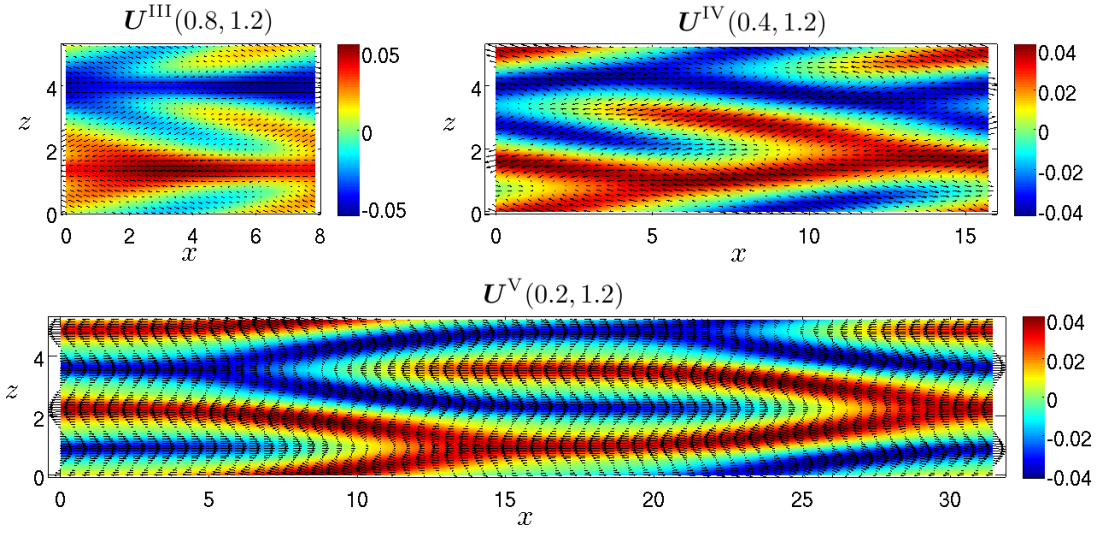

Figure 3.68: Flowfields of the wTWI states $\boldsymbol{U}^{\mathrm{III}}(0.8, 1.2)$, $\boldsymbol{U}^{\mathrm{IV}}(0.4, 1.2)$ and $\boldsymbol{U}^{\mathrm{V}}(0.2, 1.2)$.

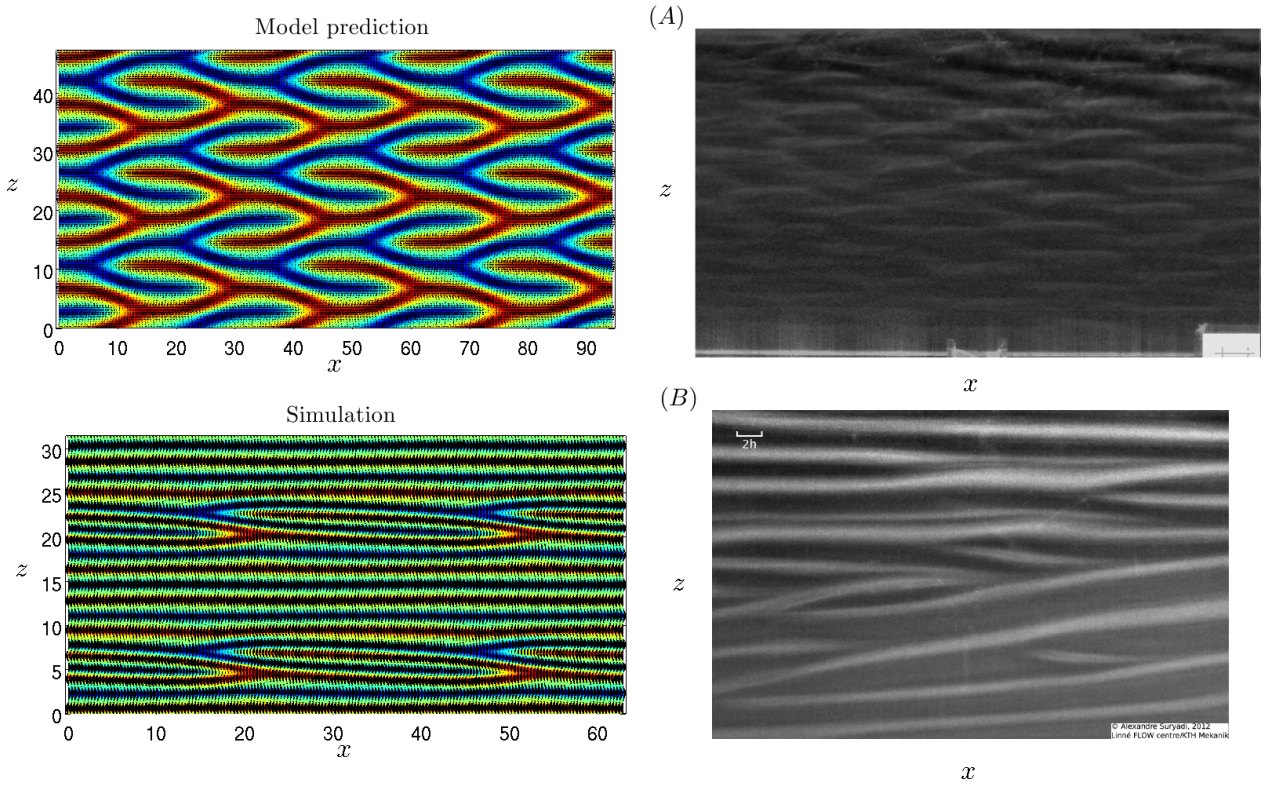

Figure 3.69: Comparison between our model/simulation flowfields and experimentally observed flow structures. The model and simulation flowfields are doubled on to a grid which is roughly comparable to the experimental photograph size as determined by the $2h$ gap given in flowfield (B). The patterns in the model and simulation final flowfields are in reasonable agreement with flowfields (A) and (B), respectively.

3.8.8 Assessment

Our attempts to understand the transition of flow states have had mixed success. The periodic-box simulations have captured the unsteady wavy vortex, steady wavy vortex and Taylor vortex flow regimes at parameter values in agreement with Tsukahara *et al.* (2010) and Suryadi *et al.* (2013), and there is some indication that the simulations reproduce the fold features observed by Suryadi *et al.* (2013) for $\Omega = 90$. However, the unsteady wavy vortices (COU3Ds) are described by Tsukahara *et al.* (2010) as being spatio-temporally intermittent, which was not a feature produced by our simulations. In addition, we did not find any behaviour resembling COU2Dm, described in Tsukahara *et al.* (2010) as a "meandering" two-dimensional roll-cell structure, in our simulations. Discrepancies between simulation and experiment could have come about in three ways. Firstly, the periodic boundary conditions imposed in the simulation may not accurately represent the experimental domain, which would have solid walls at its boundaries. As mentioned previously, Ekman layers are known to form at rotating solid boundaries, and the effect of Ekman layers in the rotating plane Couette experiments has not, to our

knowledge, been investigated. Secondly, the domain size in our simulations was much smaller than that of the experimental test section. A larger domain could introduce instabilities subharmonic to **D**, which affect the dynamics. Furthermore, a larger domain is likely necessary to observe spatio-temporal disruption such as COU3Ds. Thirdly, we chose a randomly generated flowfield as our initial disturbance. Clearly, in a deterministic dynamical system which supports chaotic dynamics, such as the Navier-Stokes equations, the final flowfield may be strongly dependent on the initial state. Even without chaos, the evolution of a system could be highly dependent on the initial energy spectrum, in such a way that wavenumbers with a high initial amplitude may dominate the dynamics. Our initial condition was chosen with a degree of smoothness, which gives the velocity field a physically acceptable appearance but prevents larger wavenumbers from having a high energy excitation. An alternative approach may be to first simulate a turbulent field at a higher Reynolds number and subsequently use this as an inital condition at the lower Reynolds number, since this is exactly what is done in experiments. Simulation a fully turbulent flowfield, however is an expensive task. Hence, a study which can incorporate non-periodic boundary conditions, a larger domain size and a greater range of initial conditions might better replicate some of the flowfields observed experimentally.

The transition model introduced in §3.8.2 has a varied performance when compared both to simulations and experiment. In the cases $\Omega = 2.5, 10, 20$ there is encouraging agreement between all three of experiment, simulation and model. For $\Omega = 50, 90$ the model fails to predict the final flowfield of the simulations, though a structure similar to the predicted state is observed transiently for $\Omega = 50$, and a structure observed in the experiments of Suryadi *et al.* (2013) resembles the model prediction for $\Omega = 90$. Given the simplicity of the model, this could be construed as reasonable success. Furthermore, given the purpose of the model is to provide insight into the complicated dynamics that a fluid experiences on evolution under the Navier-Stokes equations, which solving the equations in a direct numerical simulation does not always offer, we believe it to be adequate. Multiple stable structures can exist as solutions to the equations at given parameters, thus an improvement to the model procedure could be made by choosing not one but a range of wavenumbers which are selected at each stage of transition, and forming a probabilistic model of the emergent states.

We note that the states oWVF and SVF from §3.7 do not appear in any of the simulations, model bifurcation sequences or experimental results. Our model results indicate that, for the chosen initial flowfield, the dominant secondary wavenumber is always $\beta^{\mathrm{II}} = 1.2$. However, from §§3.6 and 3.7 it is clear that $\beta^{\mathrm{II}} > 1.2$ would be required for oWVF or SVF to appear. Hence, to assess the effect of these solutions on large-domain transition,

an initial condition which selected a larger secondary wavenumber in a simulation would be necessary.

3.9 Conclusion

In this chapter we have characterized a range of the secondary and tertiary nonlinear states that emerge in RPCF. In §3.5 we introduced three secondary states, TVF, TVF_2 and OVF. We produced bifurcation diagrams of these states to investigate their behaviour as the rotation parameter Ro is varied, finding that while TVF and TVF_2 undergo relatively straightforward bifurcations in Ro, OVF bifurcates with an upper and lower branch solution which merge as the streamwise wavenumber α_s is increased and leave behind a disconnected low-Ro and high-Ro set of solutions.

The least stable perturbation of the primary, linear Couette profile in RPCF initiates a bifurcation to TVF, meaning TVF is the most likely secondary structure to be observed. Therefore, in §3.6 we performed an extensive Floquet stability analysis on TVF, at three Reynolds numbers identified to be in the transitional flow regime by the experimental study of Tsukahara *et al.* (2010). The stability properties of TVF are shown to be dependent on Re, Ro and the wavenumber of the vortex, and instabilities increase in range and magnitude as Re is increased, giving indication of a wide range of tertiary instabilities possible over the experimentally observed transition region.

Tertiary states which bifurcate from TVF are studied in terms of their bifurcation and stability behaviour in §3.7. With focus on bifurcation in Ro, we see WVF bifurcate at low Ro, oWVF bifurcate for mid-Ro and TWI and wTWI bifurcate at high Ro. We find a streamwise independent structure SVF, which joins TVF and TVF_2 in its bifurcation in rotation number. wTWI is found to emerge in a saddle-node bifurcation at low α, and after a continuation of the solution in α_s the solution branch moves towards the TVF with double the spanwise wavenumber β, suggesting a connection between TVF and wTWI that has not previously been discussed. A regeneration cycle is found to occur for $(\alpha_s, \beta_s, Re, Ro) = (0.8, 3, 100, 0.45)$. After TVF with $\beta = 3$ breaks down, no stable tertiary state exists and the fluid moves between the unstable TVF, an unstable oWVF and a transient state with a slowly varying amplitude. A similar process has been found to occur in Kawahara & Kida (2001) in non-rotating Couette flow at $Re = 400$. Our finding could mean that the process "originates" in RPCF and can be continued over to the non-rotating flow in a manner similar to Nagata (1990, 2013).

Finally in §3.8 we explored the extent to which local stability analysis of the secondary

and tertiary structures from §3.6 and 3.7 can be used to describe the flow regimes observed in a large periodic-box simulation, and the experiments of Tsukahara *et al.* (2010) and Suryadi *et al.* (2013). We performed direct numerical simulation of the Navier-Stokes equations at specific parameter values, finding good agreement between the simulations and experiments. A simple transition model was proposed to predict the form of the final flowfield by assuming a transition between least stable states, with reasonable consistency between experiment and simulation.

Chapter 4

Non-modal growth in rotating plane Couette flow

In this chapter we continue our analysis of stability in rotating plane Couette flow (RPCF) by extending existing non-modal growth analyses across the the entire subcritical parameter space. Our aim is to identify the maximally amplified, *optimal* linear disturbances in subcritical (Re, Ro)-space. There are three known linear energy amplification mechanisms present in RPCF; the lift-up mechanism, the anti lift-up mechanism and the Orr mechanism. In determining the maximally amplified linear disturbances, we can indicate where, in parameter space, each growth mechanism dominates the transient dynamics. We find that for strong rotation, whether cyclonic or anti-cyclonic, the linear optimals two-dimensionalize and grow via the Orr mechanism. The chapter outline is as follows: in §4.1 we introduce the mathematical background for non-modal growth and the computational procedures we used to determine it, in §4.2 we present our findings of the optimal disturbances under both cyclonic and anti-cyclonic rotation and in §4.3 we discuss the relevance of our analysis to the problem of subcritical hydrodynamic transition.

4.1 Non-modal growth

The equations governing RPCF are stated in §3.1, and we do not repeat them here. Consider the linear stability equations (3.8). Fixing $\alpha, \beta, Re, Ro \in \mathbb{R}$ we can solve for $\omega_\ell \in \mathbb{C}$ satisfying

$$A\hat{\boldsymbol{q}}_\ell = \omega_\ell B\hat{\boldsymbol{q}}_\ell, \tag{4.1}$$

with the operators A and B defined as in §3.2 and the vector $\hat{\boldsymbol{q}}_\ell(y)$ defined as $\hat{\boldsymbol{q}}_\ell = (\hat{\boldsymbol{u}}_\ell, p_\ell)$. We can then construct an arbitrary velocity perturbation as an expansion of the first L, say, modes

$$\boldsymbol{u}(x, y, z, t) = \mathrm{e}^{\mathrm{i}(\alpha x+\beta z)} \sum_{\ell=1}^{L} a_\ell \hat{\boldsymbol{u}}_\ell(y)\mathrm{e}^{\omega_\ell t}. \tag{4.2}$$

The physical perturbation kinetic energy $\tilde{E}(t)$ through the streamwise and spanwise periodic domain $[0, \frac{2\pi}{\alpha}] \times [-1, 1] \times [0, \frac{2\pi}{\beta}]$, of a velocity $\boldsymbol{u}$, is given by

$$\tilde{E}(t) = \frac{2\rho\pi^2}{\alpha\beta} \int_{-1}^{1} \boldsymbol{u}^H \boldsymbol{u} \, dy, \tag{4.3}$$

where ρ is the constant density of the fluid and ^{H} denotes the Hermitian transpose. We seek to maximize the gain in kinetic energy at arbitrary time t over all inital velocity profiles. To this end we introduce the kinetic energy-density

$$E(t) = \frac{\alpha\beta\tilde{E}}{2\rho\pi^2} = \int_{-1}^{1} \boldsymbol{u}^H \boldsymbol{u} \, dy = \|\boldsymbol{u}(t)\|^2. \tag{4.4}$$

For $\hat{a} = (a_1, a_2, \ldots, a_L)$ and $\Lambda = \mathrm{diag}(\omega_1, \omega_2, \ldots, \omega_L)$, $E(t)$ can be written

$$E(t) = \hat{a}^H \mathrm{e}^{\Lambda^H t} M \mathrm{e}^{\Lambda t} \hat{a}, \tag{4.5}$$

where $\mathrm{e}^{\Lambda t}$ is the matrix exponential of Λt, and M is the $L \times L$ matrix

$$M_{jk} = \int_{-1}^{1} \hat{\boldsymbol{u}}_k^H \hat{\boldsymbol{u}}_j \, dy. \tag{4.6}$$

M is both Hermitian ($M = M^H$) and positive definite. Since M is Hermitian, its singular value decomposition can be written

$$M = U_M \Sigma_M U_M^H, \tag{4.7}$$

where $\Sigma_M = \mathrm{diag}(\sigma_1, \sigma_2, \ldots, \sigma_L)$ is a diagonal matrix of the singular values of M in descending order $\sigma_1 > \sigma_2 > \ldots > \sigma_L$, and U_M is a unitary matrix. For $\sqrt{\Sigma_M} = \mathrm{diag}(\sqrt{\sigma_1}, \sqrt{\sigma_2}, \ldots, \sqrt{\sigma_L})$ we have

$$F = U_M \sqrt{\Sigma_M}, \tag{4.8}$$

which allows us to factor M into $M = F^H F$. Hence we have

$$\|\boldsymbol{u}(t)\|^2 = \hat{a}^H \mathrm{e}^{\Lambda^H t} F^H F \mathrm{e}^{\Lambda t} \hat{a} = \|F \mathrm{e}^{\Lambda t} \hat{a}\|_2^2, \tag{4.9}$$

where $\|.\|_2$ is the Euclidean 2-norm. The maximum energy amplification G is simply

$$G(t) = \max_{\boldsymbol{u}_0 \neq 0} \frac{E(t)}{E(0)} = \max_{\boldsymbol{u}_0 \neq 0} \frac{\|\boldsymbol{u}(t)\|^2}{\|\boldsymbol{u}_0\|^2}, \tag{4.10}$$

$$= \max_{\hat{a} \neq 0} \frac{\|F\mathrm{e}^{\Lambda t}\hat{a}\|_2^2}{\|F\hat{a}\|_2^2}, \tag{4.11}$$

$$= \max_{\hat{a} \neq 0} \frac{\|F\mathrm{e}^{\Lambda t}F^{-1}F\hat{a}\|_2^2}{\|F\hat{a}\|_2^2}, \tag{4.12}$$

$$= \|F\mathrm{e}^{\Lambda t}F^{-1}\|_2^2. \tag{4.13}$$

$G(0) = 1$ by definition. Linear non-modal energy growth is supported in a flow if $G(t) > 1$ for any t. G represents the maximum possible energy amplification at time t of an initial perturbation, though different initial perturbations may be responsible for maximum growth at distinct times. Suppose, having found the maximum energy amplification achieveable at time t_q, we wish to find the form of the optimal initial perturbation and also its form at t_q. Let $\boldsymbol{q}_0$ denote the optimal perturbation, with

$$\boldsymbol{q}_0 = \mathrm{e}^{\mathrm{i}(\alpha x + \beta z)} \sum_{\ell=1}^{L} a_\ell \hat{\boldsymbol{q}}_\ell, \quad \text{and} \quad \|\boldsymbol{q}_0\| = 1. \tag{4.14}$$

Then since $\boldsymbol{q}_0$ will have energy $\|F\mathrm{e}^{\Lambda t_q}F^{-1}\|_2^2$ at t_q, we have

$$B\hat{a} = \|F\mathrm{e}^{\Lambda t_q}F^{-1}\|_2 \hat{a}\mathrm{e}^{\Lambda t_q} = \mu\hat{a}\mathrm{e}^{\Lambda t_q}, \tag{4.15}$$

where $B = F\mathrm{e}^{\Lambda t_q}F^{-1}$. The constant $\mu = \|F\mathrm{e}^{\Lambda t_q}F^{-1}\|_2$ is simply the principal singular value of B. The singular value decomposition of B lets us write

$$BV_B = U_B\Sigma_B, \tag{4.16}$$

for unitary matrices V_B and U_B, and the matrix of singular values of B, $\Sigma_B = \mathrm{diag}(\sigma_1, \sigma_2, \ldots, \sigma_L)$. If we denote the principal eigenvectors of V_B and U_B as v_1 and u_1 respectively, then since $\mu = \sigma_1$, we have

$$Bv_1 = \sigma_1 u_1, \tag{4.17}$$

from which we can identify $\hat{a} = v_1$. The linear optimal $\boldsymbol{q}_0$ can then be found by expanding $\hat{a}$ over the basis vectors $\hat{\boldsymbol{q}}_1 \ldots \hat{\boldsymbol{q}}_L$.

Our optimal growth formulation follows that of Schmid & Henningson (2001) which utilizes the singular value decomposition. An alternative method exists in the variational Lagrangian formulation, and such an approach allows for a nonlinear or time-dependent

base flow about which optimal growth can be calculated. The variational method has been used to calculate optimal disturbances in complex flows by, for example, Corbett & Bottaro (2001) and Guégan *et al.* (2006) and to calculate nonlinear optimals by Pringle *et al.* (2012), Rabin *et al.* (2012) and Duguet *et al.* (2013). However, since the base flow under consideration in this work is parallel and time-independent, we felt the singular value decomposition approach was appropriate for its ease of implementation.

To compute G, we discretize the linear system (3.8) in the wall-normal direction using an expansion of N Chebyshev polynomials. The resultant finite eigenproblem is solved for eigenvalues ω_ℓ and eigenvectors $\hat{\boldsymbol{q}}_\ell$, for $\ell \in [0, L]$. The eigenvectors are used to compute the matrix M and from the singular value decomposition of M we compute F. Thus we calculate G using the matrix norm in equation (4.13). In Figure 4.1 we plot G as a function of mode truncation L and wall-normal discretization N, with t, α, β, Re and Ro held fixed. The curves for $N = 49$ and $N = 65$ are almost indistinguishable, and there is little change in G for $L > 60$. This is an indication that G is well-converged at these parameters. Accordingly, in our calculations we use discretization/truncation $(N, L) = (49, 60)$.

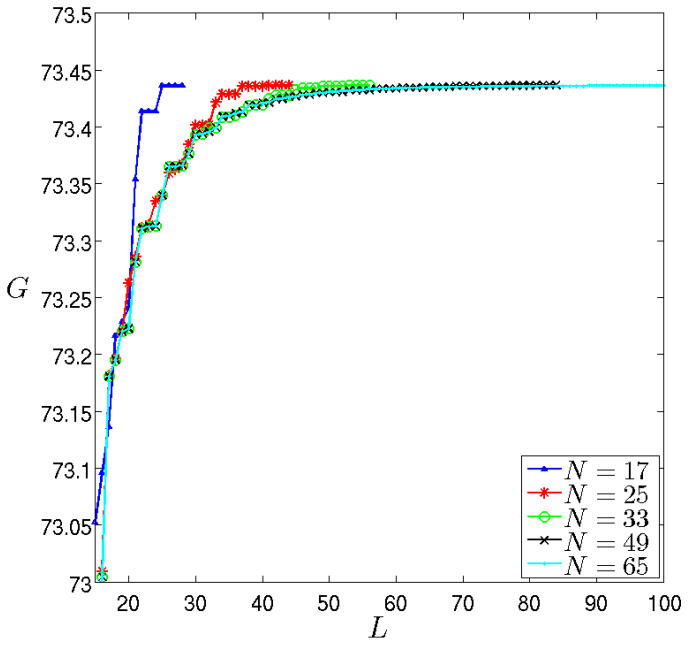

Figure 4.1: Convergence of G at various wall-normal discretizations N. $(t, \alpha, \beta, Re, Ro) = (21.6, 0.1644, 1.6914, 1000, 1.01)$.

4.1.1 Maximum optimal growth

Note that G is a five parameter function, $G = G(t, \alpha, \beta, Re, Ro)$. In recognition of this, G can be maximized over wavenumbers α, β and time t. We define the temporal maxima

G_{max} and t_{max}

$$G_{max}(\alpha, \beta, Re, Ro) = \max_{t} G(t, \alpha, \beta, Re, Ro) = G(t_{max}, \alpha, \beta, Re, Ro) \tag{4.18}$$

and the wavenumber maxima $\mathbb{G}$, α_{max} and β_{max}

$$\mathbb{G}(Re, Ro) = \max_{\alpha,\beta} G_{max}(\alpha, \beta, Re, Ro) = G(T_{max}, \alpha_{max}, \beta_{max}, Re, Ro). \tag{4.19}$$

$\mathbb{G}$ indicates the greatest linear amplification possible at a given Re, Ro combination and we shall refer to the initial condition which reaches this energy amplification as the *linear optimal*. T_{max} is used in (4.19) to denote the time taken to achieve $\mathbb{G}$, and is to be differentiated from t_{max}, which is the time taken to reach the maximum G for an arbitrary wavenumber combination. Optimization routines in MATLAB are used to find both G_{max} and $\mathbb{G}$. Finding G_{max} requires optimization over one variable, so the golden mean search `fminbnd` is used over the time horizon $0 \leq t \leq Re$. In some cases G can have local maxima. By varying the time horizon of the optimization from one iteration to the next, we increase the chances of finding global maxima. Maximizing $\mathbb{G}$ requires optimization over two variables; for this the interior-point algorithm within the function `fmincon` is used, subject to the constraints $\alpha, \beta \geq 0$. In order to lessen the likelihood of finding a local maximum of G_{max}, rather than the global maximum, five random wavenumber pairs are chosen in the domain $0 \leq \alpha \leq 2$, $0 \leq \beta \leq 2$ as initial conditions for the optimization. The algorithm is then applied to each inital condition, with $\mathbb{G}$ presumed to be the maximum of the outcomes of the five iterations. In cases where $\alpha_{max} < 0.1$, we perform golden mean searches over β with $\alpha = 0$ to check for a streamwise independent maximum. A golden mean search over α is similarly performed when $\beta_{max} < 0.1$. In all optimizations, iterations k are continued until $k = K$ satisfying $|f_K - f_{K-1}| < 10^{-10}$, for $f = G_{max}$ or $f = \mathbb{G}$.

4.2 Optimal growth in RPCF

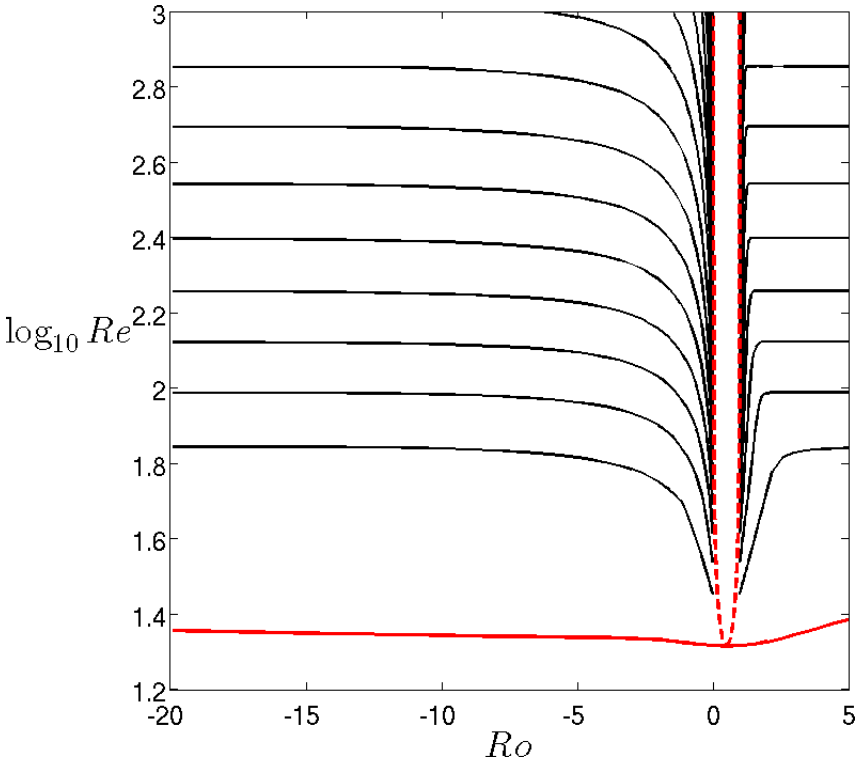

Figure 4.2: Contours of $\mathbb{G}$ in (Ro, Re). The black curves are contours of $\mathbb{G} = 10^{0.125}, 10^{0.25}, 10^{0.375}, \ldots, 10^{4.5}$ The solid red curve represents the energy stability boundary and the dashed red curve is the neutral stability boundary

The central result of this chapter is presented in Figure 4.2, where we plot level curves of $\mathbb{G}$ in the (Ro, Re) parameter space. Contours of $\mathbb{G}$, ranging from $10^{0.125}$ to $10^{4.5}$ in steps of $10^{0.125}$, are computed from a grid of 72×23 points spanning the subcritical (Ro, Re)-space. The neutral curve, which denotes the boundary between linearly stable and unstable modes is plotted as the red dashed line. An unstable perturbation has unbounded maximum growth, $\mathbb{G} = \infty$, since unstable perturbations grow exponentially in time. For this reason we do not include contours in the unstable region. The thick red line in Figure 4.2 corresponds to the energy stability curve, which we define for fixed Ro as the maximum Re for which $\mathbb{G} = 1$. Below the energy stability curve non-modal growth is not supported, thus the energy of any linear disturbance is strictly decaying. The curve is traced via a bisection method, where we fix Ro and calculate the corresponding Re to a tolerance of $\epsilon = 10^{-6}$. The energy stability Reynolds number Re_E, defined here as the minimum Reynolds number on the energy stability curve, is found to be $Re_E \approx 20.67$. By comparison, the critical Reynolds number Re_{cr}, i.e. the minimum Re for which the flow is neutrally stable, is $Re_{cr} \approx 20.69$. Both numbers are plotted in Figure 4.3, which is a blow-up of the $0 < Ro < 1$ region at low Re. Both Re_{cr} and Re_E

are found at $Ro = 0.5$, perhaps because both the neutrally stable and the energy stable perturbations along this section of the curve are streamwise oriented vortices, with $\alpha = 0$ and $\beta \approx 1.55$.

From Figure 4.2 it can be seen that for strong rotation, with $|Ro|$ far from the neutral curve, linear energy amplification is severely weakened and the value of $\mathbb{G}$ becomes independent of rotation. This serves as the main result of this chapter.

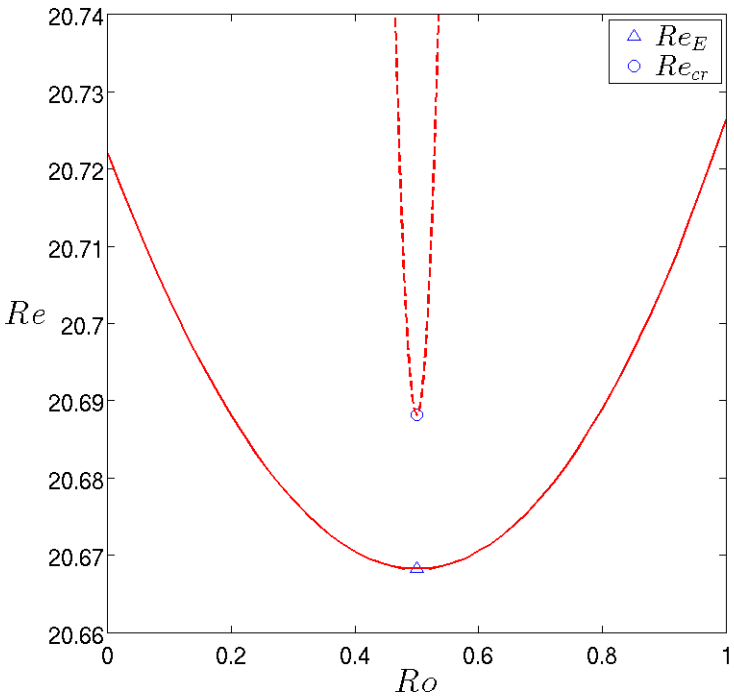

Figure 4.3: The energy stability curve (solid) and the neutral curve (dashed) are plotted with the energy stability Reynolds number Re_E and the critical Reynolds number Re_{cr} indicated.

4.2.1 Cyclonic rotation and the non-rotating case

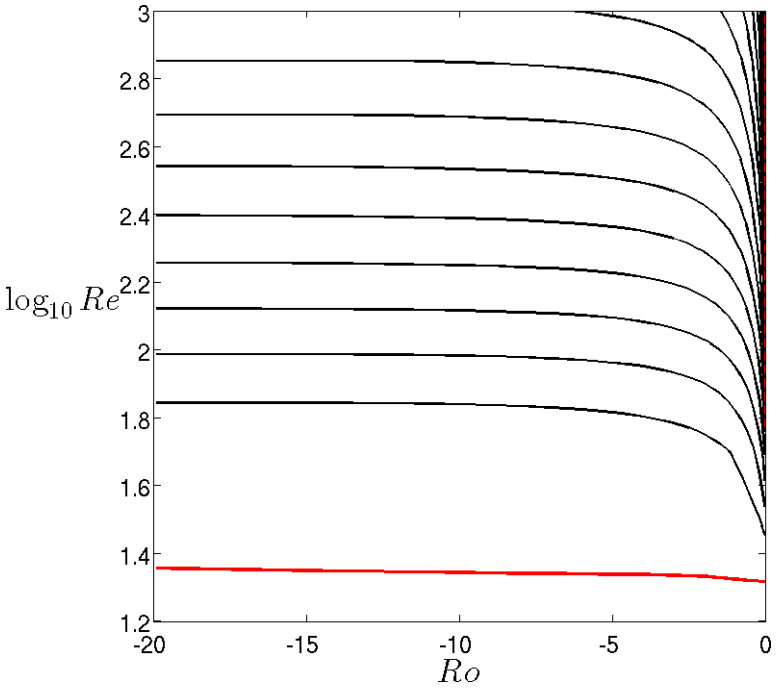

Figure 4.4: Optimal growth in the cyclonic rotation regime. Contours are equivalent to those in Figure 4.2.

Under cyclonic rotation $\mathbb{G}$ decreases sharply for Re held fixed and Ro decreasing from zero. In the absence of rotation we find that $\mathbb{G} \propto Re^2$, and we plot this relationship in Figure 4.5 along with the wavenumbers α_{max} and β_{max}. This scaling is indictative of energy amplification via the lift-up mechanism (see, for example, Landahl (1980), Gustavsson (1991), Schmid & Henningson (2001)), which refers to extraction of energy from the mean shear profile as low-energy streamwise oriented vortices are 'lifted-up' into high-energy streamwise streaks. The mechanism is necessarily three-dimensional. As a representative case, the flowfield of the optimal with $\mathbb{G} = 959.5$ at $(Ro, Re) = (0, 900)$ is depicted in Figure 4.6. Note that $\alpha_{max} = 0.0381$, and from Figure 4.5 that for $Re \geq 100$, $\alpha_{max} \neq 0$, which indictates that the optimal is not streamwise independent but weakly oblique. This trend is in agreement with the observations of Butler & Farrell (1992), who noted that the disturbance achieving the most growth in plane Couette flow used both the lift-up mechanism in addition to the Orr mechanism, Orr (1907). The streamwise wavenumber follows $\alpha_{max} \propto Re^{-1}$, a scaling derived by Chapman (2002). The Orr mechanism is two-dimensional: streamwise periodic rolls (u, v) lean against the mean shear and are amplified as they 'swing' to align with the shear. However, the combined optimal decays faster than the pure streamwise vortex. Using the streamwise, wall-normal

and spanwise energy fractions, defined as

$$E_u = \frac{\int_{-1}^{1} u^* u \, dy}{\int_{-1}^{1} \boldsymbol{u}^H \boldsymbol{u} \, dy}, \qquad E_v = \frac{\int_{-1}^{1} v^* v \, dy}{\int_{-1}^{1} \boldsymbol{u}^H \boldsymbol{u} \, dy}, \qquad E_w = \frac{\int_{-1}^{1} w^* w \, dy}{\int_{-1}^{1} \boldsymbol{u}^H \boldsymbol{u} \, dy}, \tag{4.20}$$

with * denoting the complex conjugate, the optimal at $t = 0$ has $E_v = 0.3282$ and $E_w = 0.6807$ respectively, with a low amount of energy in the streamwise velocity $E_u = 0.0011$. At $t = T_{max}$ however, the energy budget has changed to $E_u = 0.9991$, $E_v = 0.0001$ and $E_w = 0.0008$, which highlights the transition from a streamwise vortex to a high-energy streak.

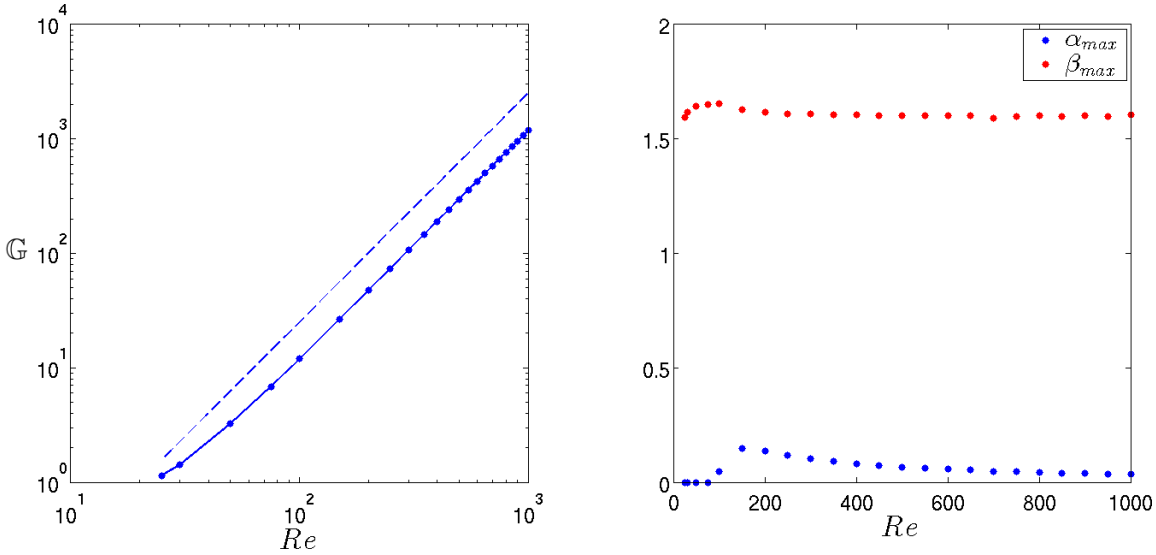

Figure 4.5: Left: $\mathbb{G}$ in Re at $Ro = 0$. The dashed line depicts the scaling $\mathbb{G} \propto Re^2$. Right: wavenumbers α_{max} (blue) and β_{max} (red) for $Ro = 0$.

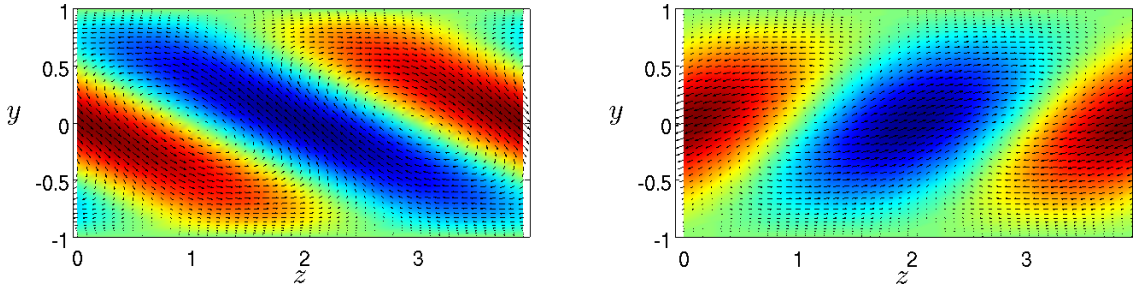

Figure 4.6: (z, y)-profiles of the optimal disturbance at $(Ro, Re) = (0, 900)$ with $(\alpha_{max}, \beta_{max}) = (0.0381, 1.6)$. The velocity at $t = 0$ (top) and $t = T_{max} = 105.7$ (bottom) is shown. Each velocity is represented as a colour-plot of the streamwise velocity u, with red and blue indicating positive and negative, and a vector plot of the wall-normal and spanwise velocities (v, w).

For $Ro \approx -20$ we find $\mathbb{G} \propto Re^{2/3}$, in agreement with the scaling found by Yecko (2004) for two-dimensional disturbances under Keplerian anti-cyclonic rotation $Ro = 4/3$. This scaling is indicative of a disturbance which grows purely under the Orr mechanism, and has been shown to hold for oblique disturbances in planar flows by Chapman (2002) and Heaton & Peake (2007). The Re dependence is shown in Figure 4.7, though larger Re than shown in Figure 4.2 are needed to resolve the scaling. An example of the velocity field is displayed in Figure 4.8 for $\mathbb{G} = 11.96$ at $(Ro, Re) = (-20, 900)$. Since the optimal is two-dimensional, with $w = 0$, a vector plot representation is used in Figure 4.8.

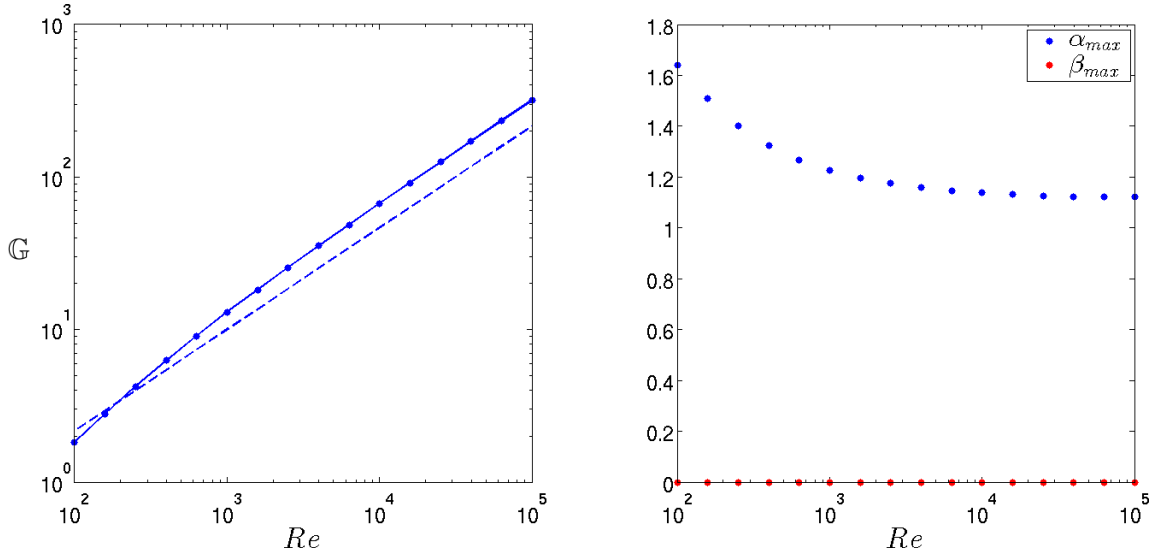

Figure 4.7: Left: $\mathbb{G}$ in Re at $Ro = -20$. The dashed line depicts the scaling $\mathbb{G} \propto Re^{2/3}$. Right: wavenumbers α_{max} (blue) and β_{max} (red) for $Ro = -20$.

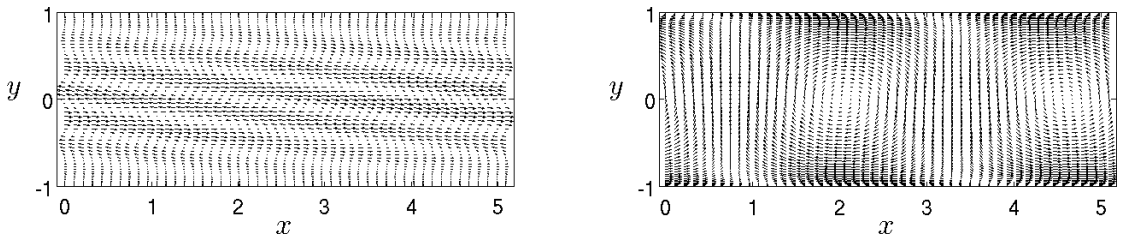

Figure 4.8: (x, y)-profiles of the optimal disturbance at $(Ro, Re) = (-20, 900)$ with $(\alpha_{max}, \beta_{max}) = (1.23, 0)$. The velocity at $t = 0$ (left) and $t = T_{max} = 8.34$ (right) is shown. Each velocity is represented as a vector plot of the streamwise and wall-normal velocities (u, v).

We conclude that for Ro far enough from zero, optimal perturbations can no longer be amplified in an Orr and lift-up mechanism combination and instead rely solely upon the Orr mechanism. As Ro decreases, we find that $\mathbb{G}$ monotonically decreases towards the

two-dimensional optimals of the Orr mechanism. In Figure 4.9 we plot $\mathbb{G}$ and its corresponding optimal wavenumbers over $-20 < Ro < 0$ at $Re = 500$. $\mathbb{G}$ drops sharply from $\mathbb{G} = 296.02$ to $\mathbb{G} = 9.547$ over $-2 < Ro < 0$, beyond which it decreases much more gradually until it reaches a minimum value of $\mathbb{G} = 7.551$ when $Ro \approx -14.46$. To gain insight into the structure of the optimal perturbations as Ro decreases, we plot the energy fractions against Ro of the optimal disturbances at $t = 0$ and $t = T_{max}$ in Figure 4.10. In the Figure it can be seen that non-rotating type optimals, with energy transfer from v and w to u at $t = T_{max}$, survive for only small Ro. The energy fraction E_u for the optimal at T_{max} falls rapidly until $Ro \approx 2$ when it reaches a turning point and begins to steadily increase. Over the same region E_w swiftly grows before beginning a steady decrease at the same turning point. From $-13.82 < Ro < -2$, the optimals transfer energy from an energetically streamwise dominated initial disturbance to an energetically spanwise dominated disturbance. Over $-14.46 < Ro < -13.82$, the greatest energy fraction of the perturbation at T_{max} is in the streamwise velocity, with E_u becoming greater than E_w.

We examine the form of the optimal disturbance at $(Ro, Re) = (-0.2, 500)$ for which there is little streamwise energy transfer as $E_u(0) = 0.416$ and $E_u(T_{max}) = 0.463$. The optimal wavenumbers in this case are $(\alpha_{max}, \beta_{max}) = (0.89, 0.81)$ and their closeness allows for the true aspect ratio of the velocity fields to be accurately depicted and easily viewed. In Figure 4.12 we plot the evolution of $G(t)$ in blue, and in red we plot the evolution of the specific initial condition which maximizes G in time. In Figures 4.13 and 4.14 we plot cross-sections of the perturbation velocities in the (x, y) and (z, y) planes respectively, with each plot at a point in time corresponding to the black dots in Figure 4.12. The counter-rotating vortices in Figures 4.13 and 4.14 are seen to change their orientation in the streamwise and spanwise directions as time evolves. This is indication of a strong dependence on the Orr mechanism for growth at the relatively minor deviation from the non-rotating case, $Ro = -0.2$. For $Ro < -14.46$ our algorithm fails to find a three-dimensional disturbance with greater amplification that the two-dimensional Orr-type optimal, resulting in a discontinuity in the curves of α_{max} and β_{max}. In Figure 4.11, a refined surface plot of G_{max} in the wavenumber domain reveals two peaks, one for $\beta = 0$ and one for β small but non-zero, each at slightly separate α. As rotation is further decreased, the peak with $\beta \neq 0$ decays whilst the $\beta = 0$ is constant. In this way there is a discontinuous transition between three-dimensional and two-dimensional optimals. That large rotation forces the optimal to be two-dimensional can be viewed as a transient version of the Proudman theorem (Proudman (1916)) on the two-dimensionalization of steady, inviscid fluids dominated by Coriolis rotation.

It should be emphasized that since the Orr and lift-up mechanisms are not unique to ro-

tating Couette flow, we find that no new growth mechanisms strong enough to maximize $\mathbb{G}$ emerge under cyclonic rotation. The effect of the introduction of cyclonic rotation on the flow can therefore be viewed as being the reversal of the dominance of the lift-up mechanism.

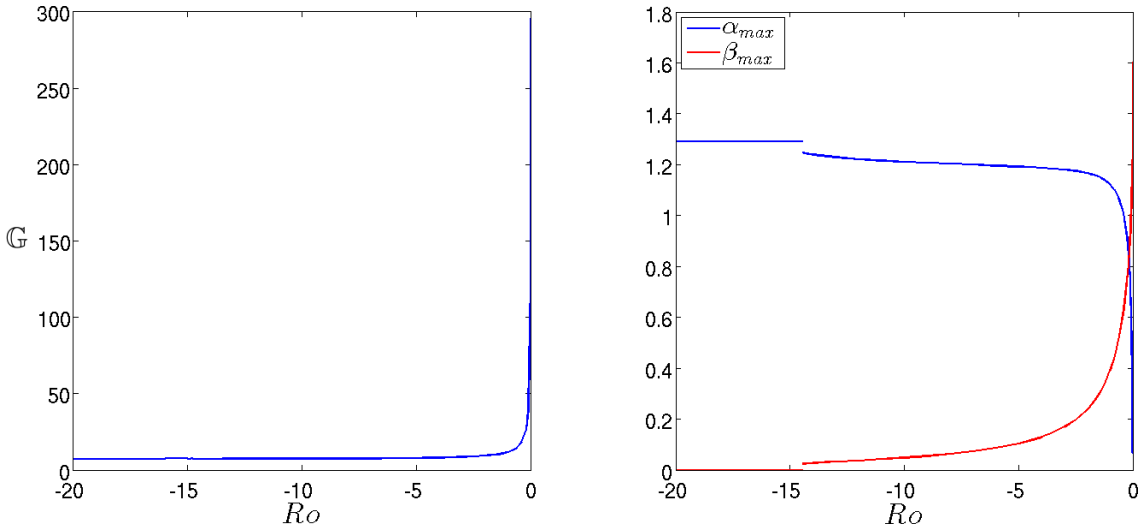

Figure 4.9: $\mathbb{G}$ for $Re = 500$. Left: $\mathbb{G}$ against Ro. Right: Optimal wavenumbers α_{max} and β_{max} against Ro. The transition from lift-up mechanism dominated optimals to Orr mechanism optimals is evident as Ro decreases.

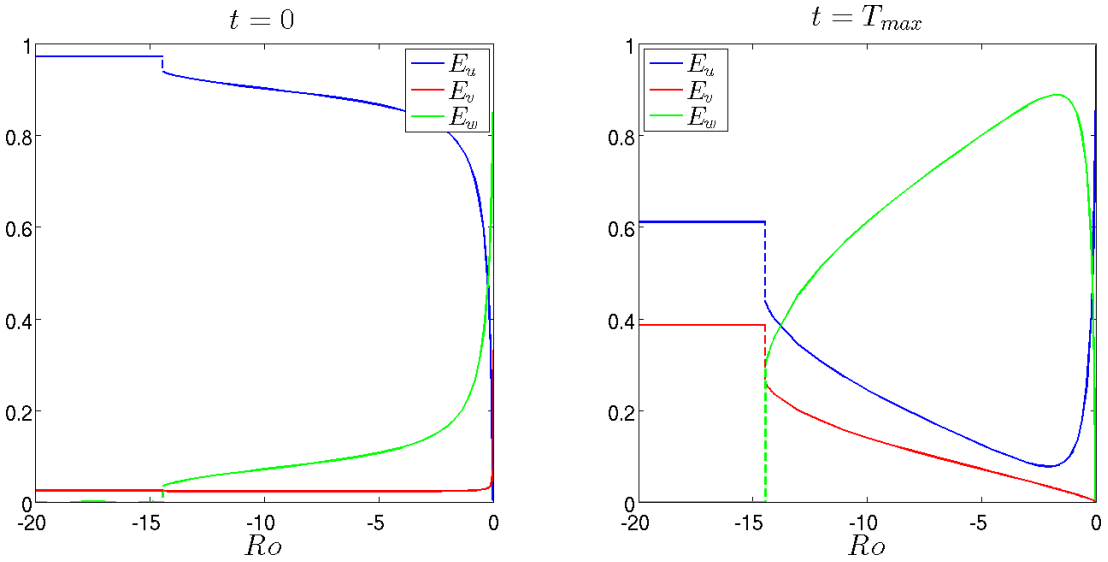

Figure 4.10: Energy fractions of optimal disturbances at $t = 0$ (left) and $t = T_{max}$ (right) for $Re = 500$. E_u, E_v and E_w represent the fraction of total perturbation energy in u, v and w respectively.

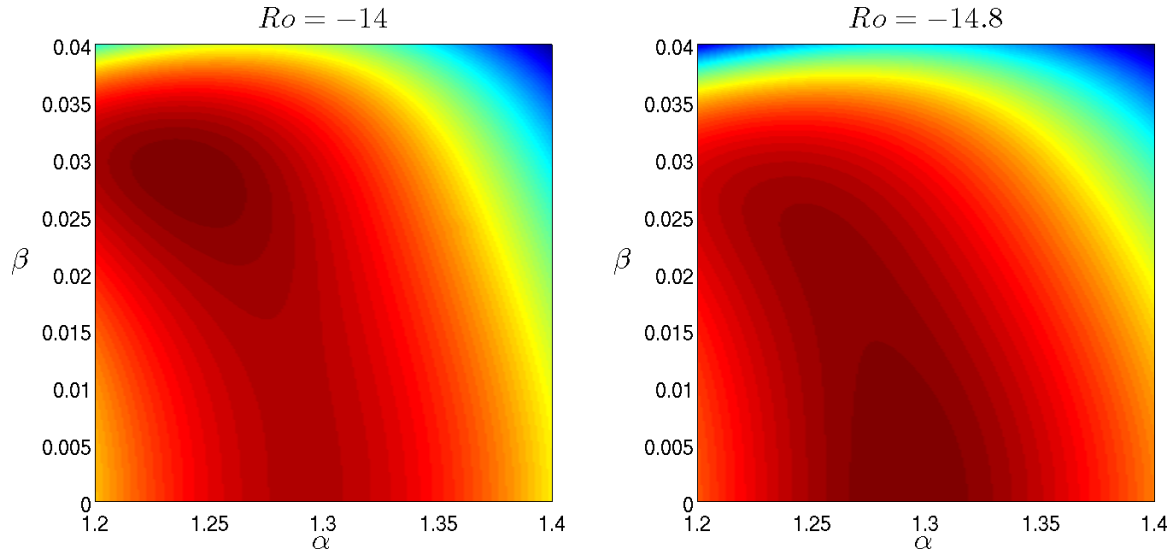

Figure 4.11: Colour-plot of G_{max} in the (α, β)-plane for $Ro = -14$ (left) and $Ro = -14.8$ (right). The switch between $\mathbb{G}$ with $\beta \neq 0$ and $\beta = 0$ can be seen from one panel to the next. The discontinuity in Figures 4.9 and 4.10 is a result when this switch, occuring between $-15 < Ro < -14$.

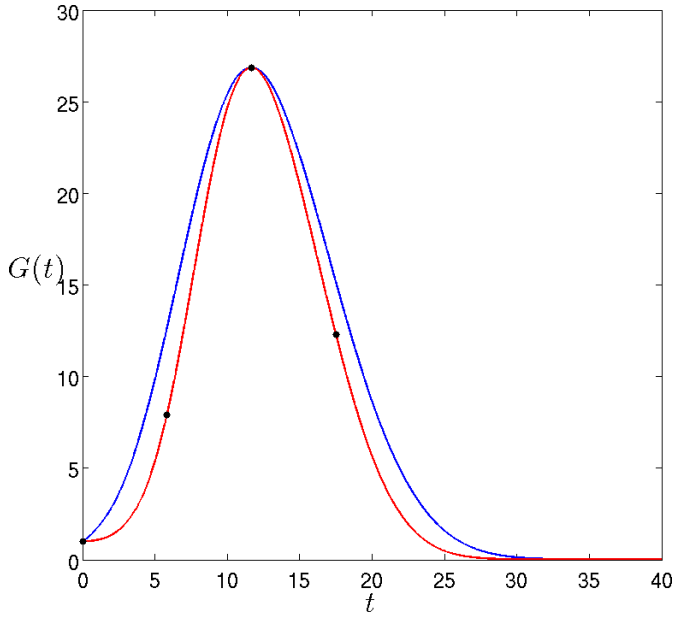

Figure 4.12: Gain curve for $Re = 500$, $Ro = -0.2$, $\alpha = \alpha_{max} = 0.89$, $\beta = \beta_{max} = 0.81$. The blue curve is the gain $G(t)$, which is the maximum growth at time t for an arbitrary initial condition. The red curve is the evolution of the initial condition which maximizes the growth at $t = T_{max} = 11.66$. The black dots indicate the times of the velocity fields shown in Figures 4.13 and 4.14

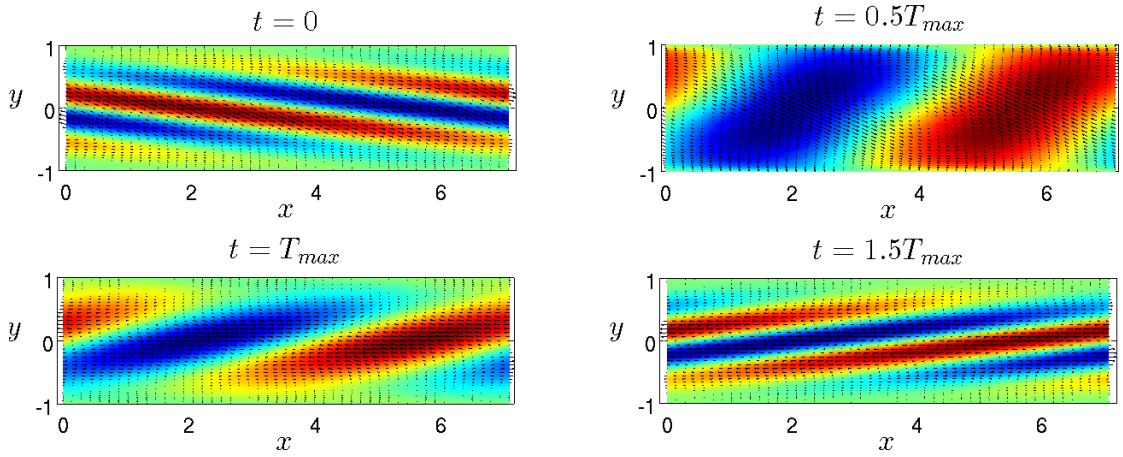

Figure 4.13: Perturbation velocity fields for $Re = 500$, $Ro = -0.2$, $\alpha = \alpha_{max} = 0.89$, $\beta = \beta_{max} = 0.81$. Each image is a vector plot of the streamwise and wall-normal velocities u and v, and a colour-plot of the spanwise velocity w, with red and blue indicating positive and negative, in the (x, y)-plane at $z = 0$. The velocity vectors clearly 'swing' in the x direction as time evolves.

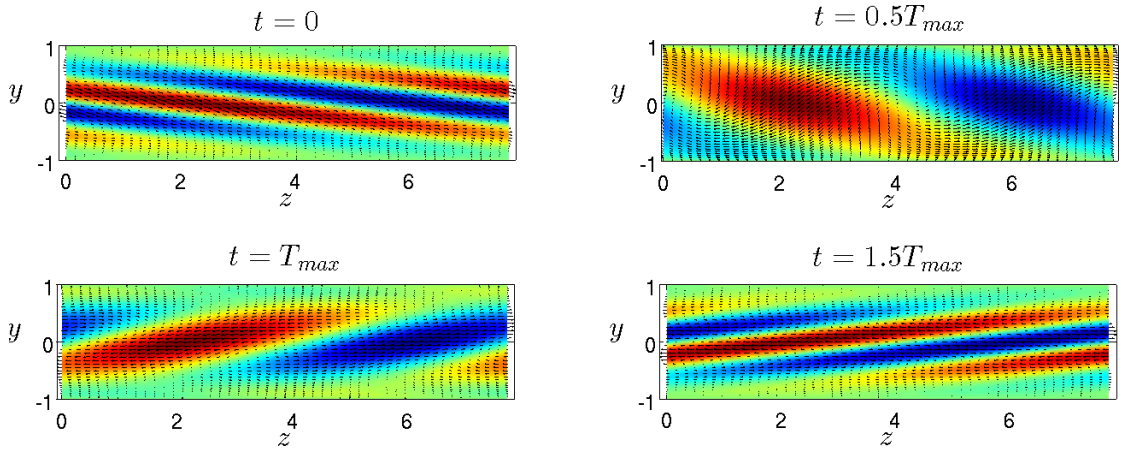

Figure 4.14: Perturbation velocity fields for $Re = 500$, $Ro = -0.2$, $\alpha = \alpha_{max} = 0.89$, $\beta = \beta_{max} = 0.81$. The fields are represented by vector plots of the spanwise and wall-normal velocities w and v, and colour-plots of the streamwise velocity u, with red and blue indicating positive and negative, in the (z, y)-plane at $x = 0$. The velocity vectors 'swing' in the z direction as time evolves.

4.2.2 Subcritical anti-cyclonic rotation

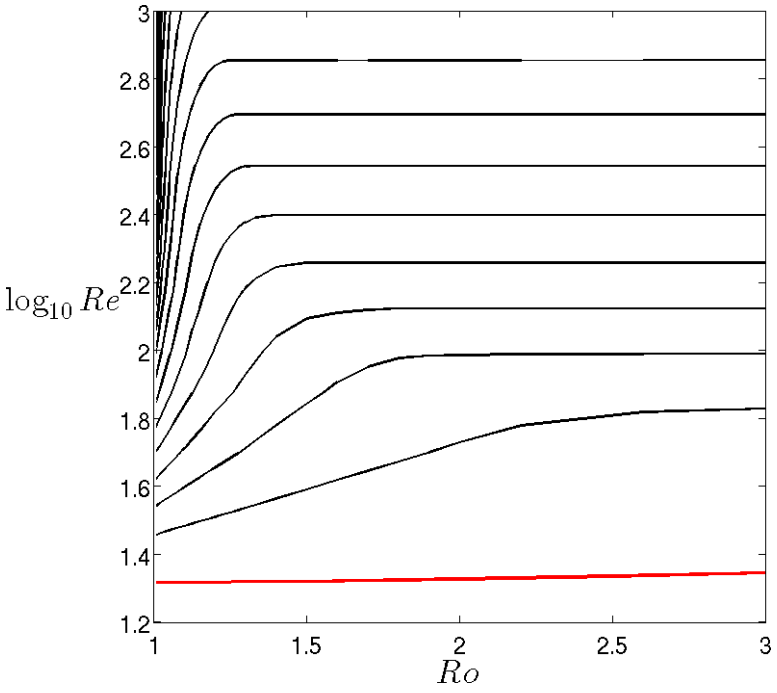

Figure 4.15: Optimal growth in the subcritical anti-cyclonic rotation regime. The black curves are contours of $\mathbb{G} = 10^{0.125}, 10^{0.25}, 10^{0.375}, \ldots, 10^{4.5}$ The solid red curve represents the energy stability boundary.

Our calculations of optimal perturbations in the anti-cyclonic regime repeat the trend of §4.2.1 insofar as $\mathbb{G}$ drops rapidly as Ro is increased from $Ro = 1$. However, unlike cyclonic rotation, the addition of anti-cyclonic rotation introduces a linear growth mechanism not present in the non-rotating flow. Optimals for $Ro = 1$ are amplified by the anti lift-up mechanism identified by Antkowiak & Brancher (2007). The effect is named "anti lift-up" because high energy streamwise vortices are generated from an initial streamwise oriented streak; a process opposite to the lift-up mechanism. Rincon *et al.* (2007) explained the analogy between the two growth mechanisms by analysis of the linearized equations governing the streamwise velocity u and the streamwise vorticity $\xi = \frac{\partial w}{\partial y} - \frac{\partial v}{\partial z}$, under the assumption of streamwise independence,

$$\frac{\partial u}{\partial t} = (Ro - 1)v + \frac{1}{Re}\nabla^2 u, \tag{4.21a}$$

$$\frac{\partial \xi}{\partial t} = -Ro\frac{\partial u}{\partial z} + \frac{1}{Re}\nabla^2 \xi, \tag{4.21b}$$

where we have used that $U' = 1$ for the linear shear profile. For $Ro = 0$ the wall-normal velocity v of the streamwise vorticity field ξ acts as a forcing on the streamwise velocity u, driving a streak. When $Ro = 1$, the $\frac{\partial u}{\partial z}$ term acts as a forcing on ξ, driving a streamwise

vortex field. The scaling $\mathbb{G} \propto Re^2$ holds for anti lift-up optimals, as it did for lift-up optimals, and is shown in Figure 4.16. In optimizing for $\mathbb{G}$, we find that the optimal disturbances for $Ro = 1$ take $\alpha_{max} = 0$, which is consistent with the calculations of Yecko (2004). The $Ro = 1$ case is therefore in contrast to the non-rotating optimals for which α_{max} is small but non-zero. As Ro increases, the anti lift-up effect loses influence on the optimals and beyond a critical Ro, the optimal perturbations have two-dimensionalized and grow via the Orr mechanism. Following our analysis for cyclonic rotation, we fix $Re = 500$ and in Figure 4.17 the evolution of $\mathbb{G}$ and the optimal wavenumbers are plotted as Ro increases. $\mathbb{G}$ decays rapidly from $\mathbb{G} = 291.7$ to $\mathbb{G} = 16.52$ over the range $1 < Ro < 1.05$, whereupon it slowly decays until $Ro = 1.276$ when $\mathbb{G} = 7.55$ and the Ro-independent Orr mechanism dominates. The optimal wavenumbers in the right panel of Figure 4.17 and the energy fractions in Figure 4.18 give a sense of the form of the optimal disturbance at each Ro. The spanwise wavenumber β_{max} increases from $\beta_{max} = 1.658$ to $\beta_{max} = 1.777$ over $1 \leq Ro \leq 1.018$, while α_{max} remains zero, and from Figure 4.18 we see that energy is transfered from u to v and w indicating that the anti lift-up mechanism is preferred over this Ro range. Between $Ro = 1.018$ and $Ro = 1.275$ the optimals are oblique, with α_{max} increasing and β_{max} decreasing for greater rotation. The perturbations behave in the same way as the oblique cyclonic optimal depicted in Figures 4.12, 4.13 and 4.14, though now they are amplified in a mixture of the anti lift-up and the Orr mechanisms. The spanwise energy fraction E_w of the initial disturbance reaches a maximum at $Ro \approx 1.15$, after which it decreases, reaching zero at the onset of two-dimensionalization. The transition from three-dimensional to two-dimensional optimals is noticeably smoother than the transition for cyclonic rotation in Figures 4.9 and 4.10, and occurs over a much shorter range of Ro.

Thus the effect of anti-cyclonic rotation on optimal linear energy growth mechanisms is the introduction and dominance of the anti lift-up mechanism at $Ro = 1$, and the subsequent erosion in strength of three-dimensional growth mechanisms towards dominance of the Orr mechanism as Ro is increased beyond unity.

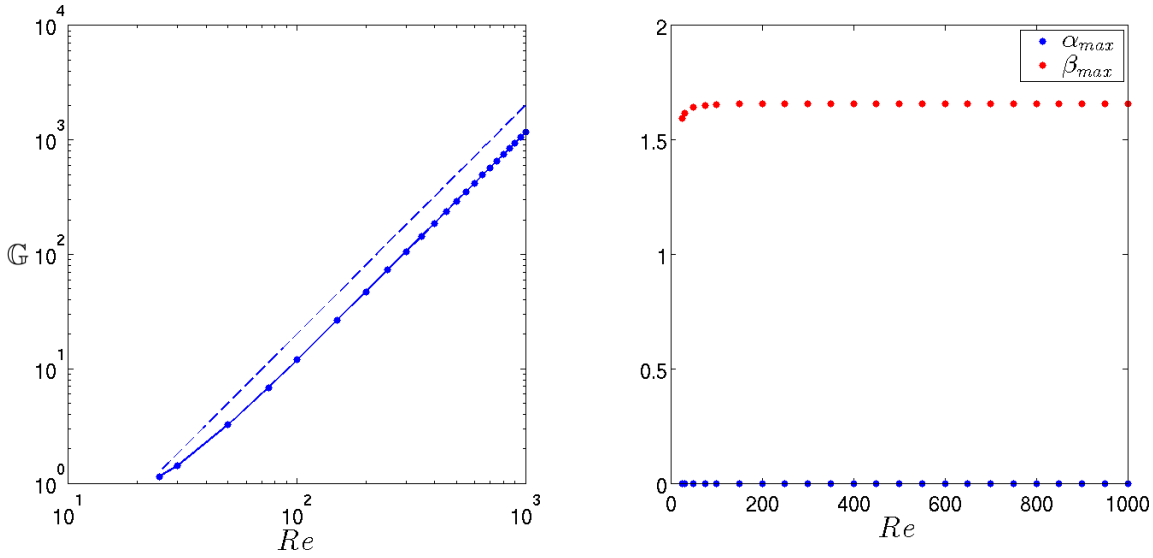

Figure 4.16: Left: Variation of $\mathbb{G}$ with Re for $Ro = 1$. The dashed line depicts the scaling $\mathbb{G} \propto Re^2$. Right: wavenumbers α_{max} (blue) and β_{max} (red) for $Ro = 0$.

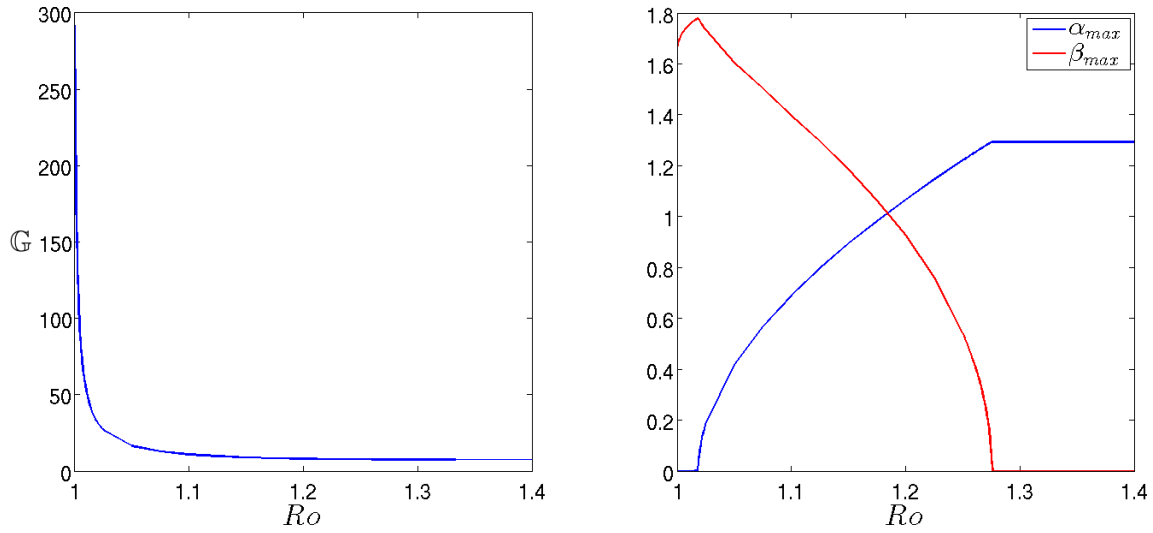

Figure 4.17: Variation of $\mathbb{G}$ for $Re = 500$. Left: $\mathbb{G}$ against Ro. Right: Optimal wavenumbers α_{max} and β_{max} against Ro. The transition from lift-up mechanism dominated optimals to Orr mechanism optimals is evident as Ro decreases.

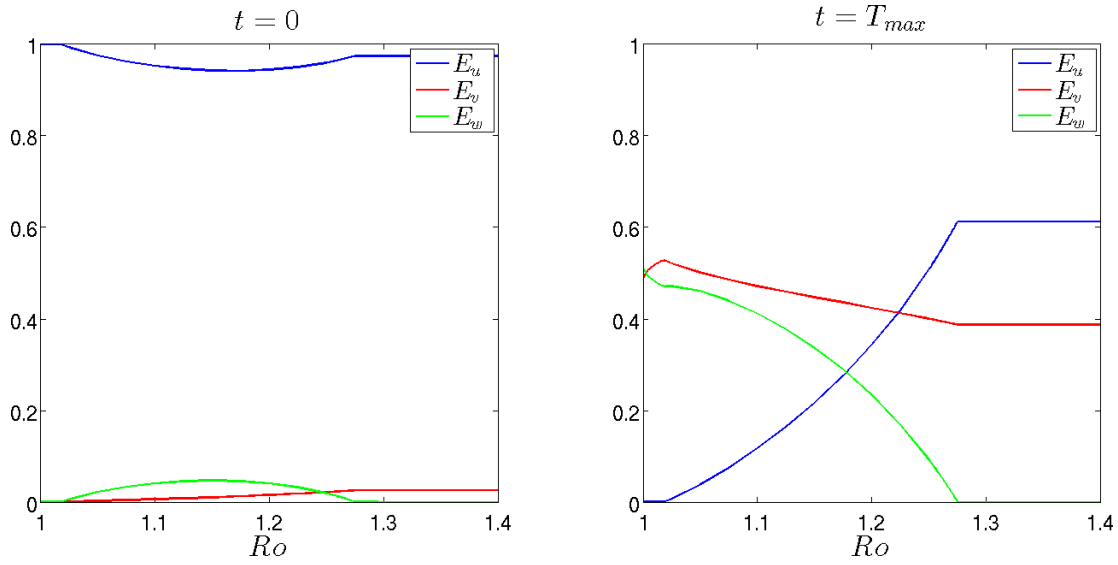

Figure 4.18: Energy fractions of optimal disturbances at $t = 0$ (left) and $t = T_{max}$ (right) for $Re = 500$. E_u, E_v and E_w represent the fraction of total perturbation energy in u, v and w respectively.

4.2.3 Rotational independence of the Orr mechanism

The two-dimensional optimals observed for strong cyclonic and anti-cyclonic rotation in §4.2.1 and §4.2.2 appear to be independent of rotation. We now show that because they are spanwise independent they are therefore necessarily independent of Ro. The spanwise independent perturbation equations reduce to

$$\frac{\partial \tilde{u}}{\partial t} + U\frac{\partial \tilde{u}}{\partial x} + \tilde{v}U' = -\frac{\partial \tilde{p}}{\partial x} + \frac{1}{Re}\nabla^2\tilde{u} + Ro\,\tilde{v}, \tag{4.22a}$$

$$\frac{\partial \tilde{v}}{\partial t} + U\frac{\partial \tilde{v}}{\partial x} = -\frac{\partial \tilde{p}}{\partial y} + \frac{1}{Re}\nabla^2\tilde{v} - Ro\,\tilde{u}, \tag{4.22b}$$

$$\frac{\partial \tilde{w}}{\partial t} + U\frac{\partial \tilde{w}}{\partial x} = \frac{1}{Re}\nabla^2\tilde{w}, \tag{4.22c}$$

$$\frac{\partial \tilde{u}}{\partial x} + \frac{\partial \tilde{v}}{\partial y} = 0, \tag{4.22d}$$

where $' = \frac{d}{dy}$ and $U = y$. Clearly the spanwise velocity $\tilde{w}$ has decoupled from $\tilde{u}$ and $\tilde{v}$; it can therefore play no role in an energy growth mechanism and it is henceforth ignored. Assuming wave-like dependence

$$[\tilde{u}, \tilde{v}, \tilde{p}](x, y) = [u, v, p](y)\mathrm{e}^{\omega t + \mathrm{i}\alpha x}, \tag{4.23}$$

and then using equation (4.22d) to eliminate u, equations (4.22a) and (4.22b) can be combined to eliminate $\tilde{p}$ and to derive a non-constant coefficient fourth order ODE for v

$$v'''' + A(y)v'' + B(y)v = 0, \tag{4.24}$$

where

$$A(y) = Re(\mathrm{i}\alpha y - \omega) - 2\alpha^2, \tag{4.25a}$$
$$B(y) = \alpha^4 - \alpha^2 Re(\mathrm{i}\alpha y - \omega). \tag{4.25b}$$

From the no-slip condition applied to the channel walls, v must satisfy

$$v = v' = 0 \qquad \text{on } y = \pm 1. \tag{4.26}$$

We note in passing that a simpler equation governing the spanwise vorticity could be derived but it is not clear what boundary conditions should be applied to it, since information would be needed concerning $\frac{\partial u}{\partial y}$ on $y = \pm 1$. Equation (4.24) is independent of Ro, hence the evolution of any two-dimensional perturbation (u, v) will not be affected by the introduction of system rotation. To highlight the effect of this on optimal growth, we re-print Figure 4.2 with added contours of G_{max} for the two-dimensional Orr mechanism growth in Figure 4.19. These contours are calculated by constraining the optimization over wavenumbers, described in §4.1.1, such that $\beta = 0$. In the Figure, it can clearly be seen that $\mathbb{G}$ tends towards the Orr mechanism growth for $|Ro|$ large.

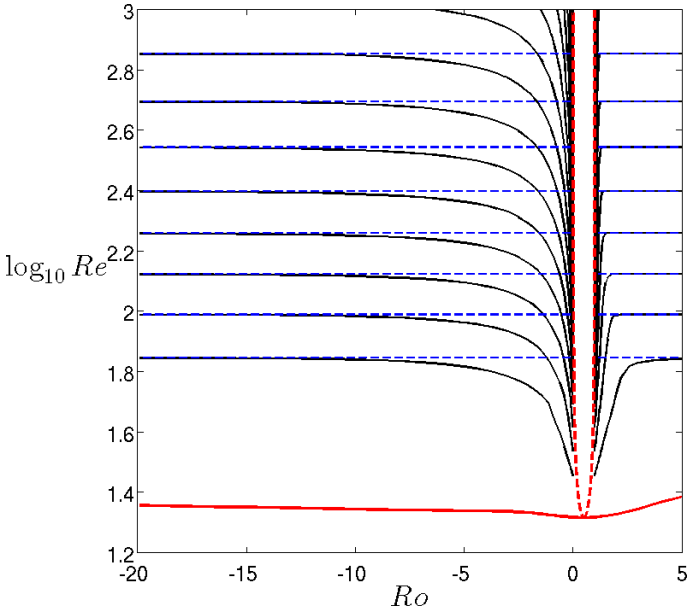

Figure 4.19: Contours of $\mathbb{G}$ in (Ro, Re), as in Figure 4.2 with Ro-independent Orr mechanism growth marked in dashed blue.

4.3 Discussion

Summarizing the results of §4.2, we find that the effect of strong cyclonic or anti-cyclonic rotation is to switch the dominance of the lift-up and anti lift-up energy growth mechanisms to the two-dimensional Orr mechanism. We now discuss what relevance this may have on transition to turbulence in flows with strong rotation. However, we must be careful in drawing conclusions from the behaviour of transients alone. Two recent approaches have been successful in explaining aspects of the transitional process in shear flows: nonlinear optimization over initial conditions, and analysis of finite-amplitude numerical solutions of the Navier-Stokes equations.

It has been shown, using a variational technique over the fully nonlinear Navier-Stokes equations, that transition is not efficiently triggered by finite-amplitude counterparts of the linear transients, but rather by inherently nonlinear states which undergo some localization during their energy growth (Rabin *et al.* (2012), Pringle *et al.* (2012)). These structures have distinct growth phases, using combinations of the lift-up mechanism and the Orr mechanism to drive their energy amplification. Thus we can, tentatively, conjecture that in the absence of one of the linear growth mechanisms the structure of the minimal seed would be much changed, if such a seed were found to exist at all. A new route to transition would be required, one that relies solely on the Orr mechanism. Our results however do not preclude the existence of strong linear growth mechanisms about a modified base flow, though how the base flow would be initially modified would remain in question.

Exact coherent structures, or finite-amplitude solutions to the Navier-Stokes equations, are conjectured to be key components to an understanding of turbulent dynamics in subcritical shear flows. Exact coherent structures are thought to form an invariant set about which chaotic dynamics are supported, and chaotic dynamics are thought to be related to turbulence. There has been recent success in finding exact coherent structures in plane Couette and plane Poiseuille flows (see Nagata (1990, 2013), Waleffe (1998, 2003), Gibson *et al.* (2009), Itano & Generalis (2009)). Furthermore, exact coherent structures are thought to play a role in what is termed a self-sustaining process (Waleffe (1995, 1997, 1998)), which drives and maintains turbulent dynamics in shear flows. The self-sustaining process consists of three phases: weak streamwise vortices re-distribute the streamwise momentum to create spanwise fluctuations in the mean streamwise velocity; spanwise inflections in the streamwise velocity cause a three-dimensional streamwise periodic instability to develop; and nonlinear interaction driven by the three-dimensional instability re-energizes the streamwise vortices such that the process can be repeated.

The lift-up mechanism is thought to be crucial in the first step of the cycle, as energy is transfered from streamwise vortices and amplified into streamwise streaks. Exact coherent structures are thought to result from this action, and then lose stability to streamwise periodic disturbances, as per the second phase of the self-sustaining process. Hence, our results show that in the presence of strong rotation such a cycle would not be possible unless streamwise momentum could be re-distributed, and an exact coherent structure formed, in the absence of the lift-up mechanism. Rincon *et al.* (2007) attempted to continue exact coherent structures from plane Couette flow into the cyclonic and subcritical anti-cyclonic rotation regimes. They found that structures could be continued into the cyclonic regime for very small rotation rates, however they could not find any structures which could be continued into the anti-cyclonic rotation regime for $Re < 500$. If it is the case that the lift-up mechanism is crucial to the generation of exact coherent states, then our results suggest that no such structures would be found for subcritical anti-cyclonic rotation and strong cyclonic rotation. Whether the anti lift-up mechanism could be used to generate an exact coherent structure of another form remains unanswered. We conclude by noting that Lesur & Longaretti (2005) observed transition in numerical simulations for $(Re, Ro) = (3000, 1)$, offering some hope that coherent structures might indeed exist for high Reynolds numbers.

Chapter 5

Nonnormality and optimal growth of the Papkovitch-Fadle operator

In this chapter we address the maximum spatial energy amplification that can be achieved by an arbitrary edge condition expressed as a finite series of Papkovitch-Fadle eigenfunctions. The layout of the chapter is as follows. In §5.1 we state the governing equations and give their formal solution. Our optimal growth framework is defined in §5.2 and we present computations of the optimal disturbances, for both an unconstrained disturbance and a disturbance with constrained corner shear-stress. In §5.3 we conduct an asymptotic analysis of how the energy inner product behaves with respect to the interaction of long and short wavelength modes. In §5.4 we extend our optimal growth analysis to spatially developing, two-dimensional plane Poiseuille flow. Finally in §5.5 we contrast our findings for spatially developing optimal disturbances to temporal optimals through an asymptotic analysis of the energy inner product in temporal plane Couette flow.

5.1 Governing equations and modal solution

We consider the solution of the biharmonic operator problem on a semi-infinite Cartesian domain Ω

$$\Delta^2\Psi = 0, \qquad \Omega = \{x, y : -1 \leq y \leq 1, 0 \leq x \leq \infty\} \tag{5.1a}$$

$$\frac{\partial\Psi}{\partial x}(x, \pm 1) = \frac{\partial\Psi}{\partial y}(x, \pm 1) = 0, \tag{5.1b}$$

$$\frac{\partial\Psi}{\partial x}, \frac{\partial\Psi}{\partial y} \to 0, \text{ as } x \to \infty \tag{5.1c}$$

where Δ is the Laplacian operator $\Delta = \frac{\partial^2}{\partial x^2} + \frac{\partial^2}{\partial y^2}$. This is also known as the Papkovitch-Fadle operator. The boundary conditions (5.1b) and (5.1c) are motivated by conditions of no-slip on the walls in the Stokes edge problem (see Figure 5.1), for which Ψ can be

considered the streamfunction. A formal solution can be written as

$$\Psi(x,y) = \sum_n c_n \psi_n(y) \mathrm{e}^{\mathrm{i}k_n x}, \tag{5.2}$$

for coefficients c_n which specify the conditions at the edge $\Gamma = \{x = 0, -1 \leq y \leq 1\}$. The eigenfunctions $\psi_n(y)$ are the Papkovitch-Fadle eigenfunctions, and they can be even or odd in y. The even eigenfunctions are written as

$$\psi_n(y) = \big(y-1\big)\sinh\big[k_n\big(y+1\big)\big] + \big(y+1\big)\sinh\big[k_n\big(y-1\big)\big], \tag{5.3a}$$

$$k_n + \sinh k_n \cosh k_n = 0, \quad k_n \in \mathbb{C}, \tag{5.3b}$$

and for odd eigenfunctions we have

$$\psi_n(y) = \big(y-1\big)\sinh\big[k_n\big(y+1\big)\big] - \big(y+1\big)\sinh\big[k_n\big(y-1\big)\big], \tag{5.4a}$$

$$k_n - \sinh k_n \cosh k_n = 0, \quad k_n \in \mathbb{C}. \tag{5.4b}$$

The dispersion relations (5.3b) and (5.4b) are transcendental equations which we solve by Newton iteration. The solutions occur as reflections in each quadrant of the complex plane

$$k = \pm k_r + \mathrm{i}k_i, \qquad k = \pm k_r - \mathrm{i}k_i, \tag{5.5}$$

for $k_r, k_i \in \mathbb{R}$. We only include modes for which $\mathrm{Im}\{k\} > 0$ in the solution expansion, to ensure that (5.1c) is satisfied. A selection of the modes are plotted in Figure 5.2. To describe each mode, we use the notation $k_n = k_r + \mathrm{i}k_i$, $k_{-n} = -k_r + \mathrm{i}k_i$ so that we can list the eigenvalues such that

$$\mathrm{Im}\{k_1\} < \mathrm{Im}\{k_2\} < \ldots. \tag{5.6}$$

In addition, neglecting modes with $\mathrm{Im}\{k\} < 0$ renders the system parabolized in x. Therefore we can treat the Papkovitch-Fadle operator (5.1) as an evolution operator.

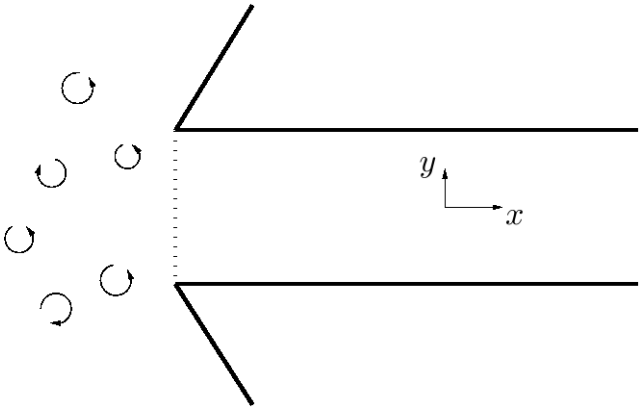

Figure 5.1: Stokes edge problem: The Papkovitch-Fadle operator (5.1) can be thought of as a mathematical description of a spatially developing, two-dimensional, viscous fluid. The fluid is driven by an arbitrary upstream ($x < 0$) stirring, which creates an edge profile at the channel entrance. The Papkovitch-Fadle operator governs the downstream ($x > 0$) development of the fluid along the channel.

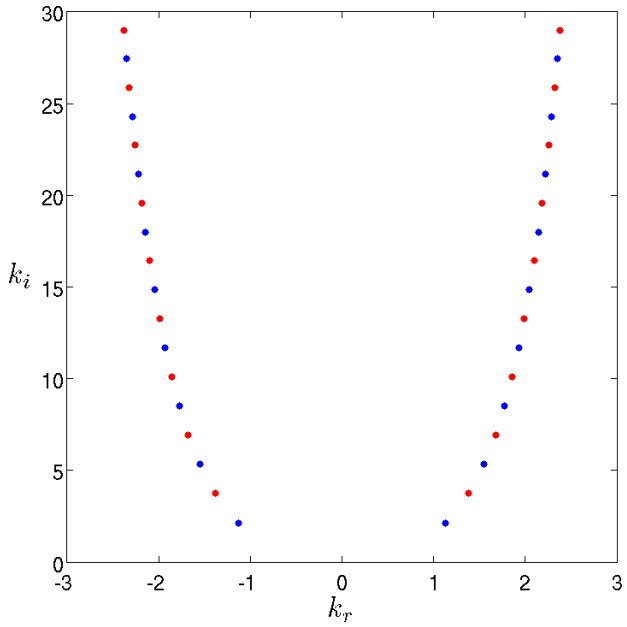

Figure 5.2: Eigenvalue spectrum in the complex k-plane. Blue and red dots denote the even and odd modes respectively.

5.2 Nonnormality and optimal energy growth

The Papkovitch-Fadle eigenfunctions are known to exhibit nonnormal characteristics. We investigate this by first introducing a norm based on the kinetic energy density of a fluid in Stokes flow. Using the expressions for the fluid velocities

$$u = \Psi_y = \sum_n a_n u_n(y) \mathrm{e}^{\mathrm{i}k_n x} = \sum_n c_n \psi_n'(y) \mathrm{e}^{\mathrm{i}k_n x}, \tag{5.7a}$$

$$v = -\Psi_x = \sum_n a_n v_n(y) \mathrm{e}^{\mathrm{i}k_n x} = -\sum_n \mathrm{i}k_n c_n \psi_n(y) \mathrm{e}^{\mathrm{i}k_n x}, \tag{5.7b}$$

and $\boldsymbol{u}_n = (u_n, v_n)$, we define the energy inner product

$$E_{mn} = \langle \boldsymbol{u}_n, \boldsymbol{u}_m \rangle = \frac{1}{2} \int_{-1}^{1} u_m^* u_n + v_m^* v_n \, dy, \tag{5.8}$$

equivalently

$$E_{mn} = \langle \boldsymbol{u}_n, \boldsymbol{u}_m \rangle = \frac{1}{2} \int_{-1}^{1} (\psi_m)^* \psi_n + \frac{1}{k_m^* k_n} (\psi_m')^* \psi_n' \, dy. \tag{5.9}$$

The Papkovitch-Fadle eigenfunctions are non-orthogonal with respect to this inner product. More precisely, odd modes are non-orthogonal to other odd modes, and similarly for even modes. Odd and even modes are orthogonal with respect to each other. If we let $\boldsymbol{p}_n$ and $\boldsymbol{q}_n$ denote odd and even eigenfunctions from (5.4a) and (5.3a) respectively, then we have the following orthogonality relations

$$\begin{aligned} \langle \boldsymbol{p}_n, \boldsymbol{p}_m \rangle = {} & \frac{4 \sinh \alpha}{\alpha^3} \big(\cosh \alpha - \cosh \beta \big) - \frac{4}{\alpha^2} \big(1 - \cosh \alpha \cosh \beta \big) \\ & + \frac{\cosh 2k_n}{k_m^*} \left(\frac{1}{\alpha} - \frac{1}{\beta} \right) + \frac{\cosh 2k_m^*}{k_n} \left(\frac{1}{\alpha} + \frac{1}{\beta} \right), \qquad m \neq -n \end{aligned} \tag{5.10a}$$

$$\begin{aligned} \langle \boldsymbol{q}_n, \boldsymbol{q}_m \rangle = {} & \frac{4 \sinh \alpha}{\alpha^3} \big(\cosh \alpha + \cosh \beta \big) - \frac{4}{\alpha^2} \big(1 + \cosh \alpha \cosh \beta \big) \\ & + \frac{\cosh 2k_m^*}{k_m^*} \left(\frac{1}{\alpha} - \frac{1}{\beta} \right) + \frac{\cosh 2k_n}{k_n} \left(\frac{1}{\alpha} + \frac{1}{\beta} \right), \qquad m \neq -n \end{aligned} \tag{5.10b}$$

$$\langle \boldsymbol{p}_n, \boldsymbol{q}_m \rangle = 0, \qquad \forall m, n \tag{5.10c}$$

where $\alpha = k_n + k_m^*$ and $\beta = k_n - k_m^*$. If $k_m = k_{-n}$ we have $\alpha = 0$, in which case

$$\langle \boldsymbol{p}_n, \boldsymbol{p}_{-n} \rangle = \frac{4}{3} \big(2 + \cosh 2k_n \big) - \frac{2 \sinh 2k_n}{k_n}, \tag{5.11a}$$

$$\langle \boldsymbol{q}_n, \boldsymbol{q}_{-n} \rangle = \frac{4}{3} \big(2 - \cosh 2k_n \big) - \frac{2 \sinh 2k_n}{k_n}. \tag{5.11b}$$

The non-orthogonality of the eigenfunctions is a consequence of the nonnormality of the Papkovitch-Fadle operator. Transient dynamics are an important feature of a nonnormal system and here we investigate the maximum energy amplification that the fluid can experience and the form of the optimal edge condition. A velocity $\boldsymbol{u}$ spanned by the first $2N$ modes is expressed as

$$\boldsymbol{u}(x,y) = \sum_{n\neq 0,\ n=-N}^{N} a_n \tilde{\boldsymbol{u}}_n(y) \mathrm{e}^{\mathrm{i}k_n x}, \tag{5.12}$$

where $\langle \tilde{\boldsymbol{u}}_n, \tilde{\boldsymbol{u}}_n \rangle = 1$. In this notation $\tilde{\boldsymbol{u}}_n$ can be either $\tilde{\boldsymbol{p}}_n$ or $\tilde{\boldsymbol{q}}_n$ depending on whether n corresponds to an odd or even mode.

Using the expressions

$$a = (a_{-N}, \ldots, a_N), \quad a \in \mathbb{C}^{2N} \tag{5.13}$$

$$M_{mn} = \langle \tilde{\boldsymbol{u}}_n, \tilde{\boldsymbol{u}}_m \rangle, \quad M \in \mathbb{C}^{2N\times 2N} \tag{5.14}$$

$$\Lambda = \begin{pmatrix} \mathrm{e}^{\mathrm{i}k_{-N}x} & & \\ & \ddots & \\ & & \mathrm{e}^{\mathrm{i}k_N x} \end{pmatrix}, \quad \Lambda \in \mathbb{C}^{2N\times 2N} \tag{5.15}$$

the energy norm is defined as

$$E(x) = \|\boldsymbol{u}(x)\|_E^2 = \frac{1}{2}\int_{-1}^{1} \boldsymbol{u}^H \boldsymbol{u}\, \mathrm{d}y = a^H \Lambda^H M \Lambda a, \tag{5.16}$$

where ^{H} denotes the Hermitian transpose. The physical, kinetic energy-density $\widetilde{E}$ over the semi-infinite strip is related to the energy norm via the relation

$$\widetilde{E} = \frac{1}{2}\int_0^\infty \int_{-1}^{1} \boldsymbol{u}^H \boldsymbol{u}\, dy\, dx = \int_0^\infty \|\boldsymbol{u}(x)\|_E^2\, dx. \tag{5.17}$$

Thus $\widetilde{E}$ is always constant, as the flow is steady. For a given streamwise location x we compute the maximum energy gain

$$G(x) = \max_{\boldsymbol{u}} \frac{E(x)}{E(0)} = \max_{\boldsymbol{u}_0\neq 0} \frac{\|\boldsymbol{u}(x)\|_E^2}{\|\boldsymbol{u}_0\|_E^2}. \tag{5.18}$$

To determine $G(x)$, we formulate a Lagrangian optimization problem for a. The Lagrangian is

$$\mathcal{L} = a^H P a - \lambda(a^H M a - 1), \tag{5.19}$$

where $P = \Lambda^H M \Lambda$. Taking variations with respect to the Lagrange multipliers, we have

$$\frac{\delta \mathcal{L}}{\delta \lambda} = a^H M a - 1, \tag{5.20}$$

$$\frac{\delta \mathcal{L}}{\delta a^H} = Pa - \lambda M a, \tag{5.21}$$

$$\frac{\delta \mathcal{L}}{\delta a} = a^H P - \lambda a^H M. \tag{5.22}$$

Setting (5.20) to zero fixes $E(0) = 1$. Equating (5.21) or (5.22) to zero gives an eigenvalue problem for right eigenvector a or left eigenvector a^H respectively. We solve

$$Pa = \lambda M a, \tag{5.23}$$

for the largest eigenvalue λ and its eigenvector a. λ corresponds to the maximum, or optimal, gain G achieved at a point x, and a is the coefficient vector which describes the optimal edge velocity.

5.2.1 Optimal growth and convergence

We begin by considering the optimal growth characteristics for a modal truncation with no restrictions on the coefficient vector a. Given that even and odd modes are orthogonal, we restrict our attention to even modes since calculations show them to be responsible for higher gains. For clarity we list the modes from $m = 1 \dots M$ rather than from $n = -N \dots N$ using

$$m(n) = \begin{cases} 2|n| - 1, & n > 0 \\ 2|n|, & n < 0. \end{cases}$$

The absence of conditions on a means that there is no guarantee that any quantities at the edge $\Gamma = \{x = 0, -1 \leq y \leq 1\}$, which are defined by a series in a, will be well-behaved. However, since the computations in this work use a finite expansion of eigenfunctions, we are not concerned with the convergence of an infinite eigenfunction series at the edge or elsewhere. The quantities of interest are the edge velocities and streamfunction

$$u_0 = \sum_{m=1}^{M} \frac{\mathrm{i} a_m}{k_m} \tilde{\psi}'_m(y), \quad v_0 = \sum_{m=1}^{M} a_m \tilde{\psi}_m(y), \quad \Psi_0 = \sum_{m=1}^{M} \frac{\mathrm{i} a_m}{k_m} \tilde{\psi}_m(y), \tag{5.24}$$

where $' = \frac{d}{dy}$ and $\tilde{\psi}_m(y)$ is normalized such that E_{mm}, as defined in equation (5.9), is unity.

We find that the gain $G(x)$ converges slowly as a function of modal truncation M. Results are displayed in Figures 5.3 and 5.4. As M increases, the magnitude of the optimal coefficients, $|a_m|$, become large for $m \approx M$. This suggests that the growth mechanism

is reliant on interactions between high wavenumber modes. We address what drives this effect in §5.3. To quantitatively investigate the rate of convergence of G, we fix x and compute a finite-difference derivative approximation $\frac{\delta G}{\delta M}$, where

$$\frac{\delta G}{\delta M} = \frac{G(M+1) - G(M)}{M+1-M} = G(M+1) - G(M), \quad M \in \mathbb{N}. \tag{5.25}$$

Results are plotted in Figure 5.4. $\frac{\delta G}{\delta M}$ is dependent on x, however for $x > 0.1$ we have the approximate scaling $\frac{\delta G}{\delta M} \propto M^{-2}$. At the trunction $M = 10^4$, G is reasonably well converged for $x \geq 0.1$ and less well converged as x approaches zero. Based on our calculations it is unclear whether G will converge in the limit $x \to 0$. Convergence may require a greater truncation as x approaches zero, or a point may be reached where the gain does not converge at all. Trefethen (1997) stated that the numerical abscissa ω, which can be thought of as the initial gradient of $G(x)$, is unbounded:

$$\omega = \lim_{x \to 0} \frac{dG}{dx} = \infty. \tag{5.26}$$

In Figure 5.6 we show that ω scales with the modal expansion number M, implying an infinite eigenfunction expansion would be required to capture the limit $\omega \to 0$. Nonetheless, the steep inital gradient of $G(x)$ is visible in the right-panel of Figure 5.3 for $M = 10^3$. Trefethen (1997) and Trefethen & Embree (2005) also noted that the repeated oscillations of the gain curve in Figure 5.3 correspond to a sequence of counter-rotating Moffatt vortices in Stokes flow.

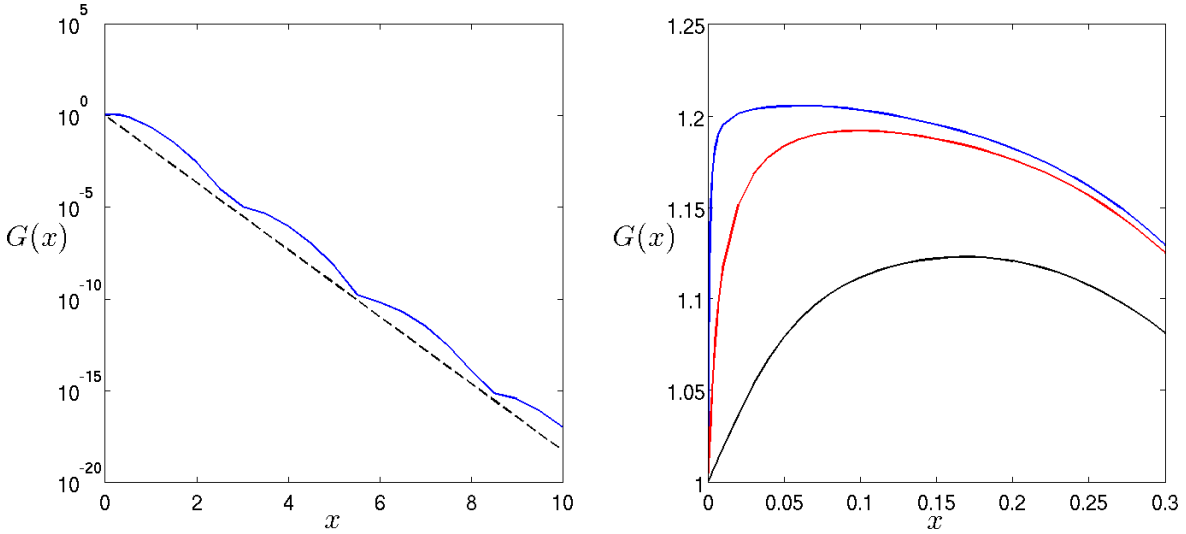

Figure 5.3: On the left we plot $G(x)$ (solid line) for $M = 10^3$. The dashed line is the energy decay rate of the leading mode. On the right is a blow-up for low x with $M = 10, 10^2$ and 10^3 corresponding to the blue, red and black lines respectively.

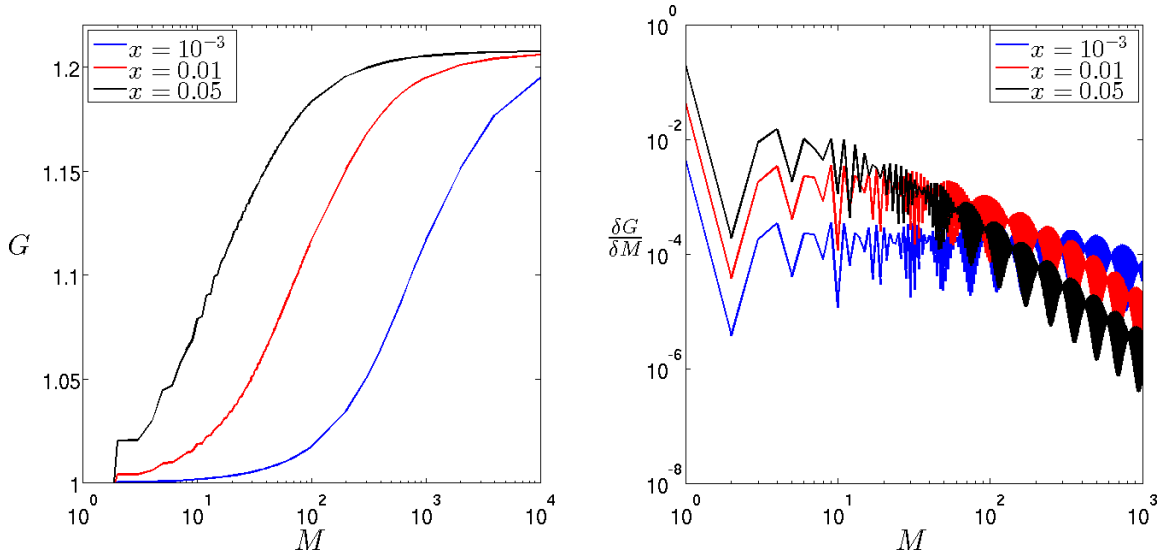

Figure 5.4: G and $\frac{\delta G}{\delta M}$ against M for $x = 10^{-3}, 0.01, 0.05$. G is not well converged for $M \leq 10^4$, for the values of x considered here.

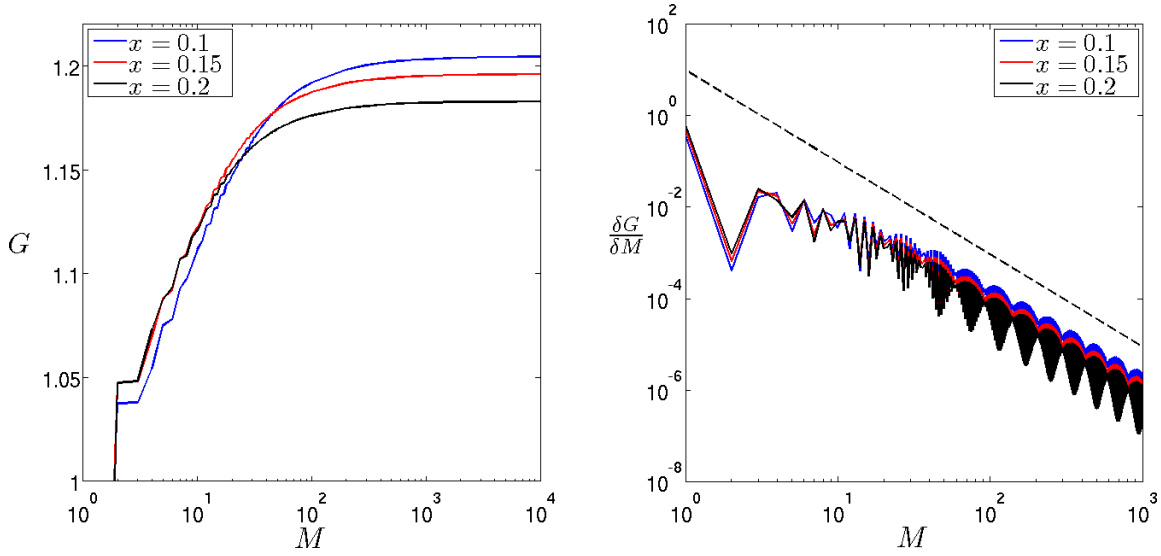

Figure 5.5: G and $\frac{\delta G}{\delta M}$ against M for $x = 0.1, 0.15, 0.2$. The dashed line in the right panel is the slope M^{-2}. G reaches satisfactory convergence for $M = 10^4$.

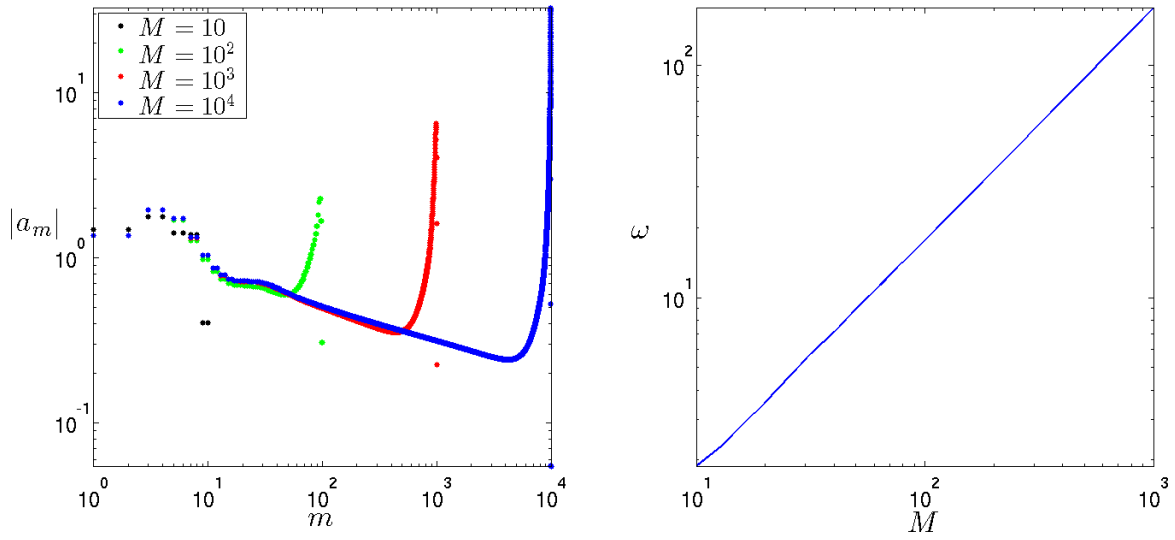

Figure 5.6: On the left we plot $|a_m|$ at four different truncations M for $x = 0.1$. On the right is the numerical abscissa ω against mode truncation M.

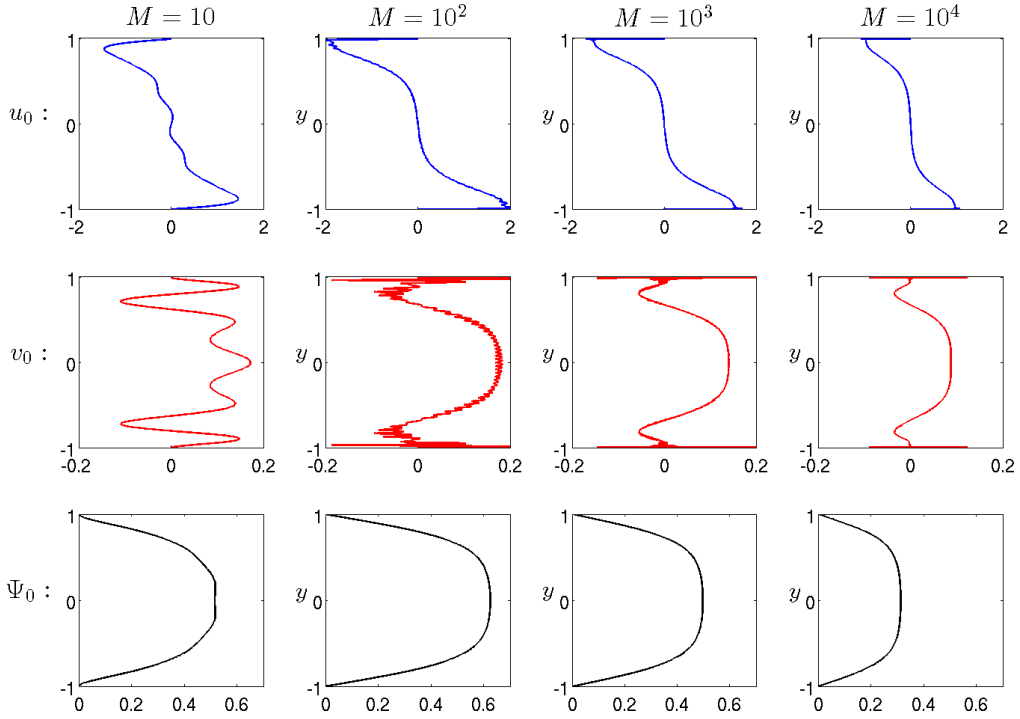

Figure 5.7: Edge profiles in y optimising G at $x = 0.1$. Along each row from the top are u_0, v_0 and Ψ_0 and the columns are the truncations $M = 10, 10^2, 10^3$ and 10^4.

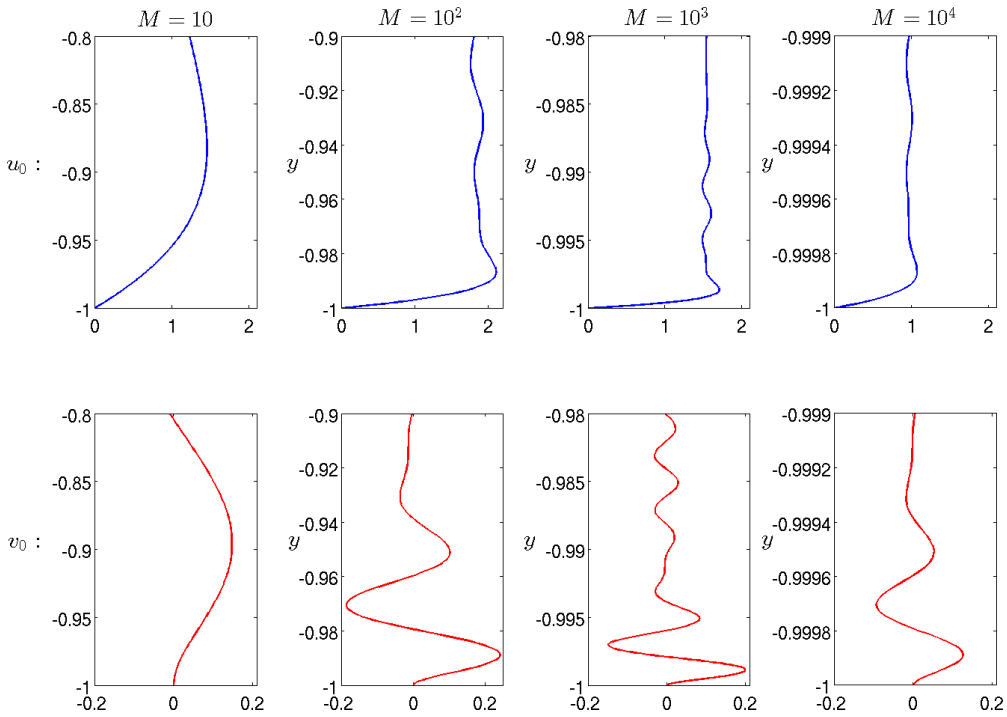

Figure 5.8: Blow-up of the lower wall region of the edge profiles in Figure 5.7. The top and bottom rows are u_0 and v_0, and the columns are the truncations $M = 10, 10^2, 10^3$ and 10^4.

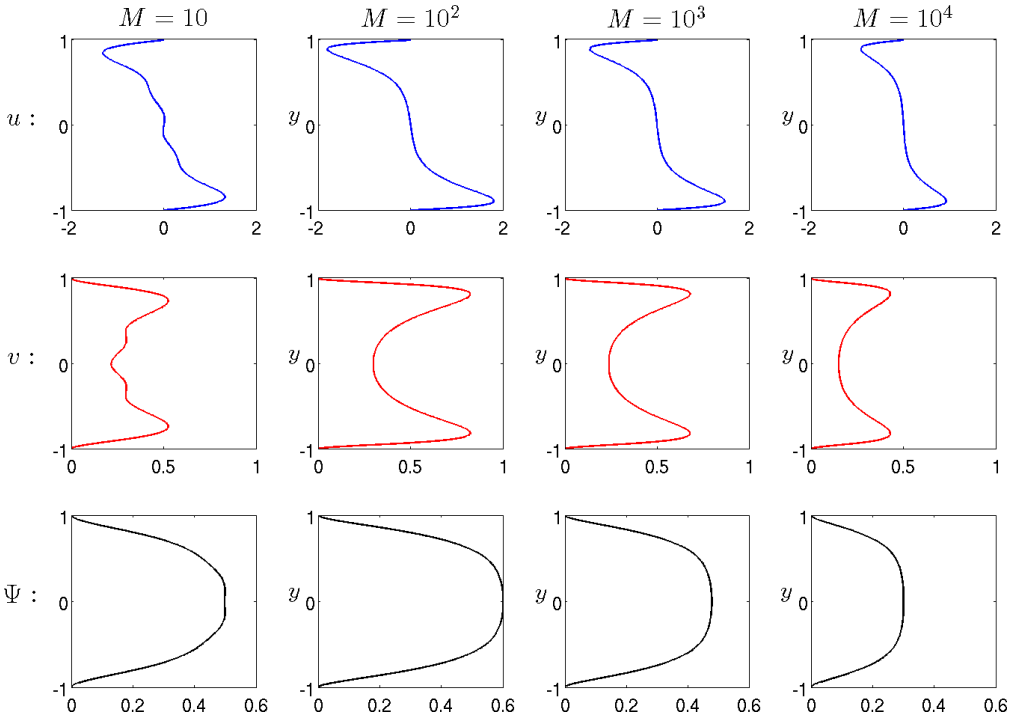

Figure 5.9: Optimal profiles in y at $x = 0.1$. Along each row from the top are $u(0.1, y), v(0.1, y)$ and $\Psi(0.1, y)$ and the columns are the truncations $M = 10, 10^2, 10^3$ and 10^4.

In Figures 5.7 and 5.9 we plot the wall-normal profiles of u, v and Ψ which optimize the energy gain at $x = 0.1$. We plot the profiles both at the edge Γ and their form as they have evolved to $x = 0.1$. While Ψ is well resolved throughout the domain, u_0 and v_0 display sharp oscillatory behaviour near the walls ($y = \pm 1$). This is a consequence of the large amplitude, large wavenumber modes selected by the energy growth mechanism. Increasing the truncation appears to dampen the near-wall oscillations in v_0 but leads to increasingly sharp behaviour in u_0 at the walls, though a blow-up of the lower wall region in Figure 5.8 confirms that the eigenfuctions are always continuous. The sharp near-wall gradient in u_0 suggests that the optimal edge profile tends towards a slip condition in streamwise velocity as the modal resolution is increased. The no-slip condition at the edge, $\Psi_y(0, \pm 1) = 0$, can be relaxed to include a slip profile at the edge, though this has no effect on our findings. Further downstream, the large wavenumber modes become less prominent in the profiles at $x = 0.1$ as they are very highly damped, thus the eigenfunctions have no oscillatory behaviour near the walls.

The optimal velocities and streamfunction are plotted in the (x, y)-plane in Figure 5.10. From the Figure, steady Moffatt vortices are seen to emanate from the corners of the domain. We also plot the streamfunction on a log scale in Figure 5.11, to allow the succession of Moffatt vortices which cause the oscillations in the gain curve of Figure 5.3 to be seen.

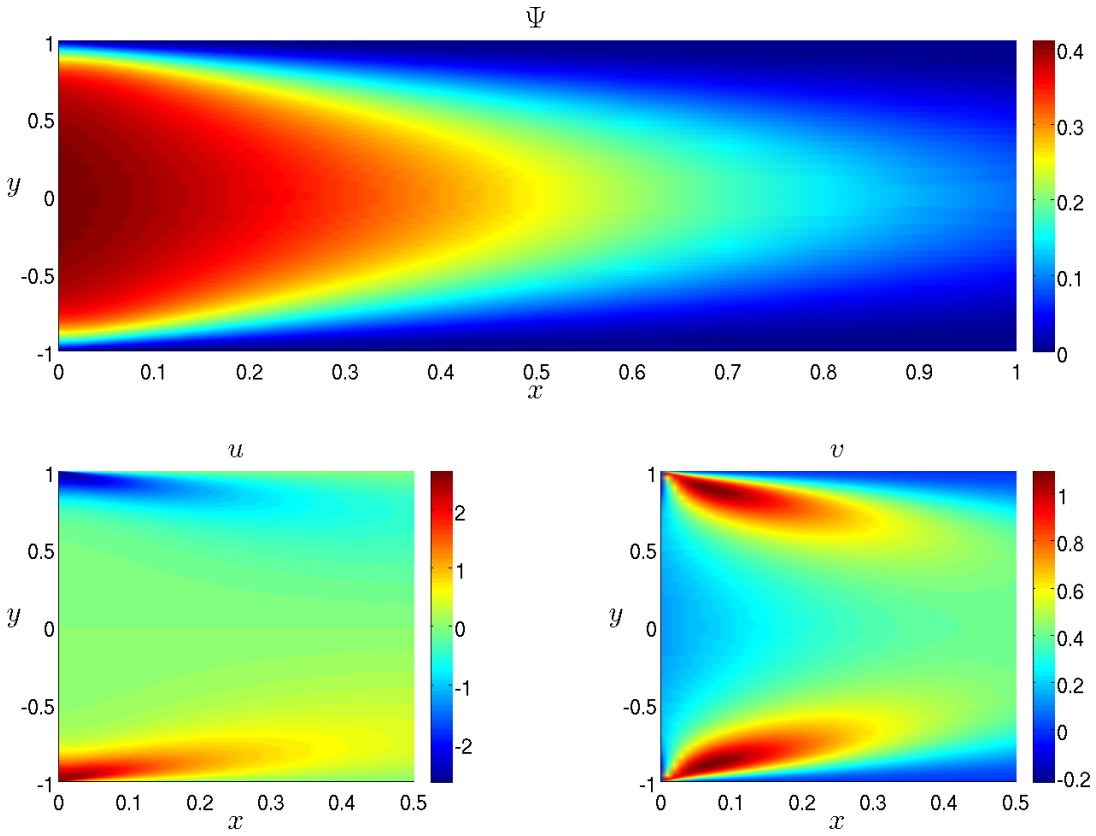

Figure 5.10: Shading plots of Ψ (top), u (bottom-left) and v (bottom-right) for $x = 0.1$. The plots do not have a true aspect ratio, so that the Moffatt vortices can be clearly seen.

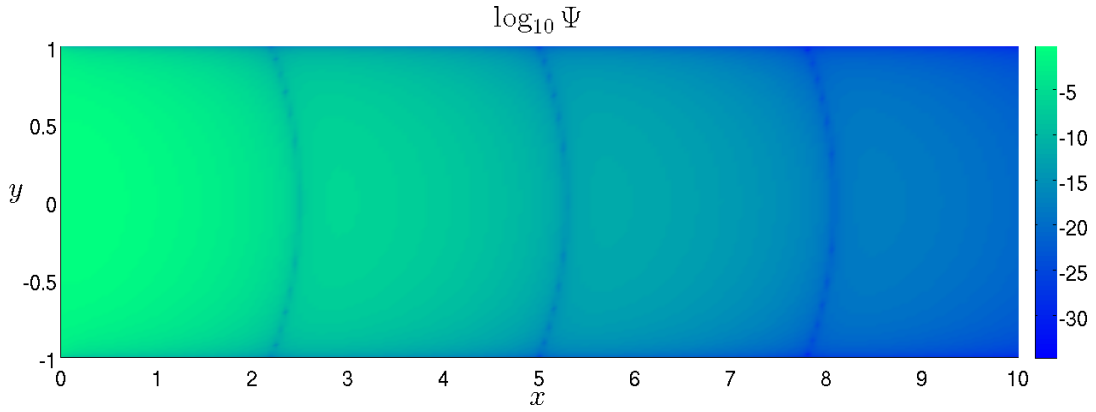

Figure 5.11: Shading plot of $|\log(\Psi)|$. Plotting on the log-scale allows the repeated oscillations of Moffatt eddies to be visualized.

5.2.2 Optimal growth with bounded wall shear

It is found that as the modal resolution of the optimal edge condition found in §5.2.1 is improved, the fluid exerts increasingly high stress on the channel corners. We define τ to be the corner shear stress for normalized viscosity $\mu = 1$

$$\tau = \mu \frac{\partial u}{\partial y}\bigg|_{y=\pm 1, x=0} = \frac{\partial^2 \Psi}{\partial^2 y}\bigg|_{y=\pm 1, x=0}. \tag{5.27}$$

Figure 5.12 suggests that $|\tau|$ scales linearly with the eigenfunction expansion coefficient M, which would imply unbounded stress if an infinite eigenfunction expansion were to be considered. This may be physically questionable, therefore we are motivated to seek a solution Ψ_τ, for which τ is bounded at the corner. The Lagrangian optimization problem in equation (5.19) is re-formulated such that $|\tau|$ is normalized to unity. Writing a_τ for the coefficient vector of the constrained solution, we impose the constraint

$$|\tau|^2 = a_\tau^H B a_\tau = a_\tau^H b^H b a_\tau = 1, \tag{5.28}$$

where

$$b_n = \frac{\mathrm{i}\tilde{\psi}_n''(\pm 1)}{k_n} = \frac{4\mathrm{i}\cosh^2 k_n}{\sqrt{\langle \boldsymbol{q}_n, \boldsymbol{q}_n \rangle}}. \tag{5.29}$$

The Lagrangian now becomes

$$\mathcal{L}_\tau = a_\tau^H P a_\tau - \lambda(a_\tau^H M a_\tau - 1) - \mu(a_\tau^H B a_\tau - 1). \tag{5.30}$$

Setting variations of $\mathcal{L}_\tau$ to zero yields the double-eigenvalue problem

$$P a_\tau = \lambda M a_\tau + \mu B a_\tau. \tag{5.31}$$

Techniques are available for the direct solution of (5.31), such as Blum & Chang (1978) and Ji (1996), however, for its ease of implementation we solve for a_τ and the energy gain $G(x)$ using the active-set constrained nonlinear optimization routine `fmincon` in MATLAB. The routine makes an approximation for the Hessian of the Lagrangian, which is used to define a search direction along which a line search can be conducted. The addition of the new constraint renders the calculations more computationally expensive than in §5.2.1 and owing to this we can calculate a solution as far as truncation number $M = 10^3$. The solutions share qualitiative features with the unconstrained optimals (cf Figures 5.7 and 5.9 with 5.13), suggesting that the growth mechanism is not reliant on large shear stress in the corners of the domain. In Figure 5.12 we note that Ψ_τ experiences less energy amplification than the unconstrained optimal, however the difference narrows as truncation number M is increased.

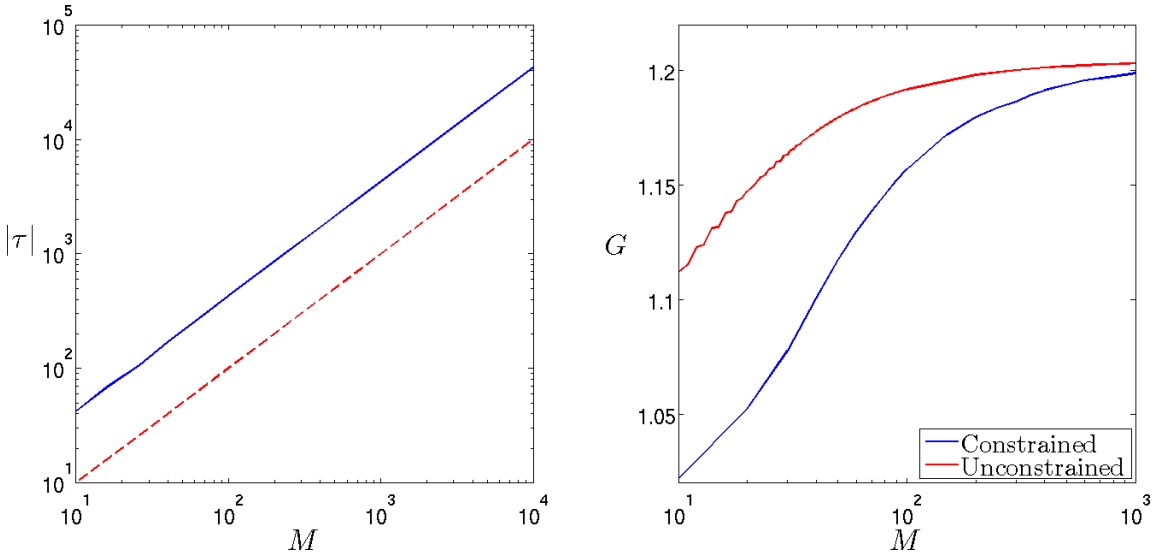

Figure 5.12: On the left: Corner stress $|\tau|$ against expansion number M for optimals at $x = 0.1$. The red dashed curve indicates the slope with gradient one. On the right: G against expansion number M for $x = 0.1$. The blue and red lines are the constrained and unconstrained optimals respectively.

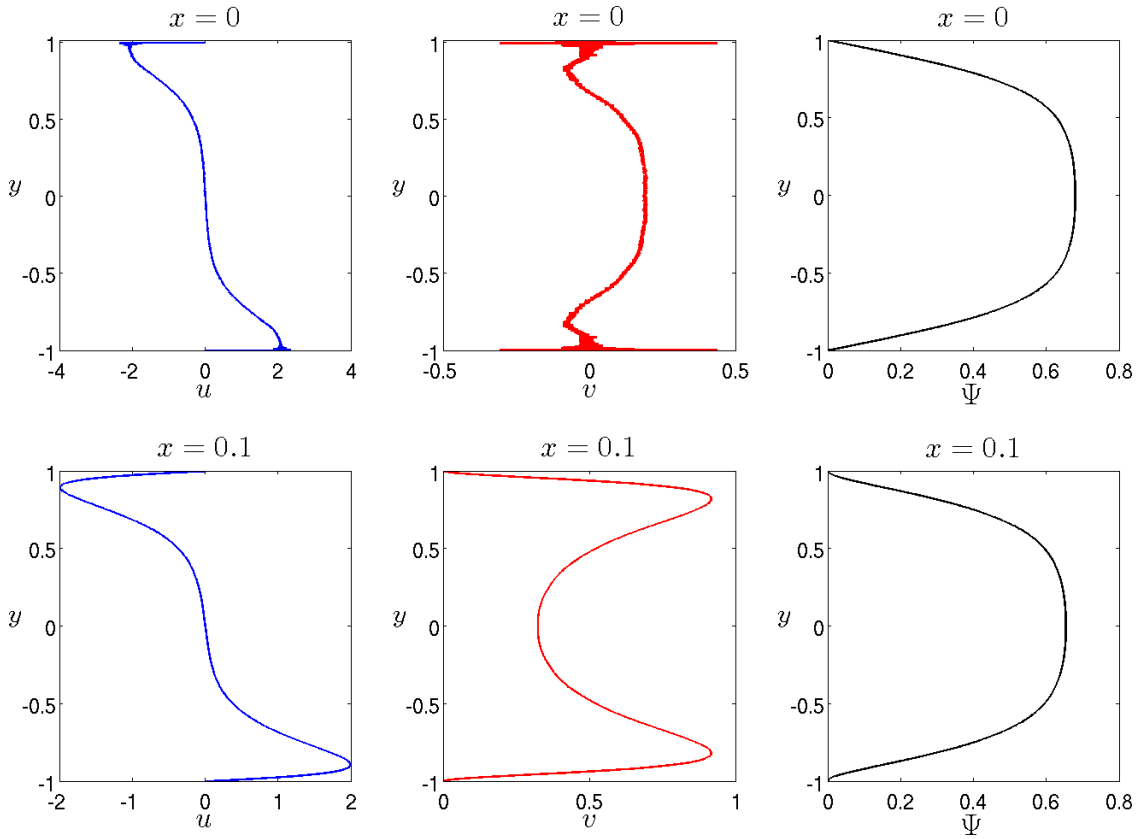

Figure 5.13: Wall-normal profiles of the constrained optimal which maximizes $G(x)$ at $x = 0.1$. The top row has the edge profiles u_0, v_0 and Ψ_0. On the second row we plot $u(0.1, y)$, $v(0.1, y)$ and $\Psi(0.1, y)$.

5.3 Short wavelength asymptotics

In this section we derive asymptotic expressions for short wavelength modes, or equivalently, modes with large wavenumber. Our attention is restriced to even modes since they are found to be responsible for the largest transient growth in §5.2.1. The aim of this analysis is to investigate the energy inner product interactions of modes in the short wavelength limit, in order to provide an insight into why the optimal edge coefficients utilize the non-orthogonality of large wavenumber modes.

We start by splitting the dispersion relation into real and imaginary parts. For a mode k we have

$$k + \sinh k \cosh k = 0. \tag{5.32}$$

Let $\lambda = 2k$. Then

$$\lambda + \sinh \lambda = 0, \tag{5.33}$$

$$\implies (\lambda_r + \sinh \lambda_r \cos \lambda_i) + \mathrm{i}(\lambda_i + \cosh \lambda_r \sin \lambda_i) = 0. \tag{5.34}$$

Hence the following two relations must be satisfied

$$\sinh \lambda_r = -\left(\frac{1}{\cos \lambda_i}\right)\lambda_r, \tag{5.35}$$

$$\sin \lambda_i = -\left(\frac{1}{\cosh \lambda_r}\right)\lambda_i. \tag{5.36}$$

In order for equation (5.35) to be satisfied for large $|\lambda|$, $\cos \lambda_i$ must be small and negative. Therefore we write

$$\lambda_i = \mu + \varepsilon_1 + \varepsilon_2 + \ldots, \qquad \text{for} \quad \mu = \left(2n - \frac{1}{2}\right)\pi, \quad n \in \mathbb{N}, \tag{5.37}$$

for small parameters ε_1 and ε_2 with $\varepsilon_2 < \varepsilon_1$. Equation (5.36) becomes

$$-\sin\Big(\mu + \varepsilon_1 + \varepsilon_2 + \ldots\Big) = -\frac{1}{\cosh \lambda_r}\Big(\mu + \varepsilon_1 + \varepsilon_2 + \ldots\Big). \tag{5.38}$$

Since $\sin \mu = -1$ and $\cos \mu = 0$, we have

$$\cosh \lambda_r\Big(1 - \frac{1}{2}(\varepsilon_1 + \varepsilon_2)^2 + \ldots\Big) = \mu + \varepsilon_1 + \varepsilon_2 + \ldots, \tag{5.39}$$

$$\implies \cosh\lambda_r = \Big(\mu+\varepsilon_1+\varepsilon_2+\dots\Big)\Big(1-\frac{1}{2}\big(\varepsilon_1+\varepsilon_2\big)^2+\dots\Big)^{-1}, \tag{5.40}$$

$$= \Big(\mu+\varepsilon_1+\varepsilon_2+\dots\Big)\Big(1+\frac{1}{2}\big(\varepsilon_1+\varepsilon_2\big)^2+\dots\Big), \tag{5.41}$$

$$= \mu+\varepsilon_1+\varepsilon_2+\frac{\mu\varepsilon_1^2}{2}+2\mu\varepsilon_1\varepsilon_2+\frac{\mu\varepsilon_2^2}{2}+\dots, \tag{5.42}$$

$$= \mu+\delta_r+\dots. \tag{5.43}$$

Let $\varepsilon_1+\varepsilon_2=\delta_i$. From equation (5.35) we get

$$\Big((\mu+\delta_r+\dots)^2-1\Big)^{\frac{1}{2}}\cos\Big(\mu+\delta_i+\dots\Big) = -\cosh^{-1}\Big(\mu+\delta_r+\dots\Big), \tag{5.44}$$

$$\mu\Big(1+\frac{2\delta_r}{\mu}-\frac{1-\delta_r^2}{\mu^2}+\dots\Big)^{\frac{1}{2}}\sin\big(\delta_i+\dots\big) = -\log\Big(\mu+\delta_r+\big((\mu+\delta_r+\dots)^2-1\big)^{\frac{1}{2}}+\dots\Big), \tag{5.45}$$

$$\delta_i+\dots = -\frac{1}{\mu}\Big(\log\big(2\mu+2\delta_r+\dots\big)\Big), \tag{5.46}$$

$$= -\frac{\log 2\mu}{\mu}-\frac{\delta_r}{\mu^2}+\dots, \tag{5.47}$$

$$\implies \varepsilon_1+\varepsilon_2+\dots = -\frac{\log 2\mu}{\mu}-\frac{1}{\mu^2}\Big(\varepsilon_1+\varepsilon_2+\frac{\mu\varepsilon_1^2}{2}+2\mu\varepsilon_1\varepsilon_2+\frac{\mu\varepsilon_2^2}{2}+\dots\Big). \tag{5.48}$$

From this we conclude

$$\varepsilon_1 = -\frac{\log 2\mu}{\mu}, \tag{5.49}$$

$$\varepsilon_2 = -\frac{\varepsilon_1^2}{2\mu} = -\frac{(\log 2\mu)^2}{2\mu^3}. \tag{5.50}$$

Thus we have that

$$\lambda_i = \mu-\frac{\log 2\mu}{\mu}+O\Big(\frac{(\log\mu)^2}{\mu^3}\Big), \tag{5.51}$$

and from equation (5.42)

$$\lambda_r = \log 2\mu+\frac{(\log 2\mu)^2}{2\mu^2}+O\Big(\frac{\log\mu}{\mu^2}\Big). \tag{5.52}$$

Now we can determine how the energy inner product for even modes behaves for $|k| \to \infty$. Recalling equation (5.10b) from §5.1, we have

$$E_{mn} = \frac{4\sinh\alpha}{\alpha^3}\big(\cosh\alpha + \cosh\beta\big) - \frac{4}{\alpha^2}\big(1 + \cosh\alpha\cosh\beta\big) + \frac{\cosh 2k_m^*}{k_m^*}\left(\frac{1}{\alpha} - \frac{1}{\beta}\right) + \frac{\cosh 2k_n}{k_n}\left(\frac{1}{\alpha} + \frac{1}{\beta}\right), \qquad m \neq -n \tag{5.53}$$

where $\alpha = k_n + k_m^*$ and $\beta = k_n - k_m^*$. We investigate modal interactions with respect to the normalized energy inner product.

5.3.1 Normalization factor

First we find an expression for the normalization factor to leading order

$$E_n^2 = E_{nn}, \quad n \to \infty. \tag{5.54}$$

Suppose

$$k_n = \frac{1}{2}\left(\log 2\mu + \frac{(\log 2\mu)^2}{2\mu^2} + O\left(\frac{\log\mu}{\mu^2}\right) + \mathrm{i}\left(\mu - \frac{\log 2\mu}{\mu} + O\left(\frac{(\log\mu)^2}{\mu^3}\right)\right)\right). \tag{5.55}$$

Then $\alpha = 2(k_n)_r = \lambda_r$ and $\beta = \mathrm{i}2(k_n)_i = \mathrm{i}\lambda_i$. Therefore

$$\cosh\alpha = \sinh\alpha = \mu + \frac{(\log 2\mu)^2}{2\mu} + O\left(\frac{\log\mu}{\mu}\right), \tag{5.56}$$

$$\cosh\beta = -\frac{\log 2\mu}{\mu} + O\left(\frac{(\log\mu)^2}{\mu^3}\right). \tag{5.57}$$

So for the energy norm we have

$$E_n^2 = \left(\frac{4\mu^2}{(\log 2\mu)^3} + O\left(\frac{1}{\log\mu}\right)\right) + \left(\frac{4}{\log 2\mu} + O\left(\frac{1}{(\log\mu)^2}\right)\right) + \left(-\frac{2}{\log 2\mu} + O\left(\frac{\log\mu}{\mu^2}\right)\right) + \left(-\frac{2}{\log 2\mu} + O\left(\frac{\log\mu}{\mu^2}\right)\right). \tag{5.58}$$

Hence

$$E_n^2 = \frac{4\mu^2}{(\log 2\mu)^3} + O\left(\frac{1}{\log\mu}\right), \quad n \to \infty \tag{5.59}$$

where $\mu = (2n - \frac{1}{2})\pi$.

5.3.2 Interaction of short wavelength modes

Now consider the leading order behaviour of E_{mn} for two short wavelength modes, i.e. with $|k_n|$ and $|k_m|$ large, but not equal. We investigate the interaction of modes with

$$m = n - a, \text{ with } a \in \mathbb{N}, a = O(1), \quad n \to \infty. \tag{5.60}$$

Expressions for wavenumbers k_n and k_m are

$$k_n = \frac{\log 2\mu}{2} + \frac{a\pi}{\mu} + \frac{(\log 2\mu)^2}{4\mu^2} + O\left(\frac{\log \mu}{\mu^2}\right) + \mathrm{i}\left(\frac{\mu}{2} + a\pi - \frac{\log 2\mu}{2\mu} + O\left(\frac{(\log \mu)^2}{\mu^3}\right)\right), \tag{5.61}$$

$$k_m = \frac{\log 2\mu}{2} + \frac{(\log 2\mu)^2}{4\mu^2} + O\left(\frac{\log \mu}{\mu^2}\right) + \mathrm{i}\left(\frac{\mu}{2} - \frac{\log 2\mu}{2\mu} + O\left(\frac{(\log \mu)^2}{\mu^3}\right)\right). \tag{5.62}$$

Therefore we have

$$\alpha = k_n + k_m^*, \tag{5.63}$$

$$= \log 2\mu + \frac{a\pi}{\mu} + \frac{(\log 2\mu)^2}{2\mu^2} + \mathrm{i}a\pi + O\left(\frac{\log \mu}{\mu^2}\right). \tag{5.64}$$

$$\beta = k_n - k_m^*, \tag{5.65}$$

$$= \frac{a\pi}{\mu} + \mathrm{i}\left(\mu + a\pi - \frac{\log 2\mu}{\mu}\right) + O\left(\frac{(\log \mu)^2}{\mu^3}\right). \tag{5.66}$$

$$\cosh \alpha = (-1)^a \cosh \lambda_r, \tag{5.67}$$

$$= (-1)^a \left(\mu + \frac{(\log 2\mu)^2}{2\mu} + O\left(\frac{\log \mu}{\mu}\right)\right). \tag{5.68}$$

$$\sinh \alpha = (-1)^a \sinh \lambda_r, \tag{5.69}$$

$$= (-1)^a \left(\mu + \frac{(\log 2\mu)^2}{2\mu} + O\left(\frac{\log \mu}{\mu}\right)\right). \tag{5.70}$$

$$\cosh \beta = \cosh\left(\frac{a\pi}{\mu} + \mathrm{i}\left(\mu + a\pi - \frac{\log 2\mu}{\mu} + O\left(\frac{(\log \mu)^2}{\mu^3}\right)\right)\right), \tag{5.71}$$

$$= (-1)^{a+1}\left(\frac{\log 2\mu}{\mu} + \frac{\mathrm{i}a\pi}{\mu}\right) + O\left(\frac{(\log \mu)^2}{\mu^3}\right). \tag{5.72}$$

$$\cosh 2k_m^* = \cosh\left(\lambda_r - \mathrm{i}\lambda_i\right), \tag{5.73}$$

$$= -\log 2\mu + \mathrm{i}\mu + O\left(\frac{(\log \mu)^2}{\mu}\right). \tag{5.74}$$

$$\cosh 2k_n = \cosh\left(\lambda_r + \frac{2a\pi}{\mu} + \mathrm{i}\left(\lambda_i + 2a\pi\right)\right), \tag{5.75}$$

$$= -\log 2\mu + \mathrm{i}\mu + O\left(\frac{(\log \mu)^2}{\mu}\right). \tag{5.76}$$

Using these expressions, the energy inner product E_{mn} becomes

$$E_{mn} = \left(\frac{4\mu^2}{(\log 2\mu)^3} - \mathrm{i}\frac{12a\pi\mu^2}{(\log 2\mu)^4} + O\left(\frac{1}{\log\mu}\right)\right) + \left(\frac{4}{\log 2\mu} + O\left(\frac{1}{(\log\mu)^2}\right)\right) + \left(-\frac{2}{\log 2\mu} + O\left(\frac{1}{(\log\mu)^2}\right)\right) + \left(-\frac{2}{\log 2\mu} + O\left(\frac{1}{(\log\mu)^2}\right)\right). \tag{5.77}$$

Thus to leading order we have

$$E_{mn} = \frac{4\mu^2}{(\log 2\mu)^3} - \mathrm{i}\frac{12a\pi\mu^2}{(\log 2\mu)^4} + O\left(\frac{1}{\log\mu}\right). \tag{5.78}$$

Re-introducting the normalized energy inner product

$$\langle\tilde{\boldsymbol{q}}_{n+a}, \tilde{\boldsymbol{q}}_n\rangle = \frac{E_{mn}}{E_m E_n}, \tag{5.79}$$

we see that

$$\langle\tilde{\boldsymbol{q}}_{n+a}, \tilde{\boldsymbol{q}}_n\rangle = 1 - \mathrm{i}\frac{3a\pi}{\log 2\mu} + O\left(\frac{(\log\mu)^2}{\mu^2}\right), \quad a = O(1), \quad n \to \infty \tag{5.80}$$

where $\mu = (2n - \frac{1}{2})\pi$. Hence in the limit $|k| \to \infty$, modes are non-orthogonal.

5.3.3 Interaction of long and short wavelength modes

We now determine the effect on the energy inner product of the interaction between long and short wavelength modes. We keep one mode fixed, and $O(1)$, and take the limit of the second wavenumber becoming large. In terms of k_n and k_m this means

$$k_n = \frac{\log 2\mu}{2} + \frac{(\log 2\mu)^2}{4\mu^2} + O\left(\frac{\log\mu}{\mu^2}\right) + \mathrm{i}\left(\frac{\mu}{2} - \frac{\log 2\mu}{2\mu} + O\left(\frac{(\log\mu)^2}{\mu^3}\right)\right), \quad k_m = O(1). \tag{5.81}$$

We start by treating

$$\cosh k_n = \cosh\left\{\frac{\log 2\mu}{2} + \frac{(\log 2\mu)^2}{4\mu^2} + O\left(\frac{\log\mu}{\mu^2}\right) + \mathrm{i}\left(\frac{\mu}{2} - \frac{\log 2\mu}{2\mu} + O\left(\frac{(\log\mu)^2}{\mu^3}\right)\right)\right\}, \tag{5.82}$$

$$= \frac{\sqrt{2\mu}}{2}\left(\frac{1}{\sqrt{2}}\right) + \mathrm{i}\frac{\sqrt{2\mu}}{2}\left(-\frac{1}{\sqrt{2}}\right) + O(\mu^{-\frac{1}{2}}), \tag{5.83}$$

$$= \frac{\sqrt{\mu}}{2}(1 - \mathrm{i}) + O(\mu^{-\frac{1}{2}}). \tag{5.84}$$

Therefore we have

$$\cosh\alpha = \cosh(k_n + k_m^*), \tag{5.85}$$
$$= \cosh k_n \cosh k_m^* + \sinh k_n \sinh k_m^*, \tag{5.86}$$
$$= \frac{1}{2}\sqrt{\mu}(1-\mathrm{i})\cosh k_m^* + \frac{1}{2}\sqrt{\mu}(1-\mathrm{i})\sinh k_m^* + O(\mu^{-\frac{1}{2}}), \tag{5.87}$$
$$\implies \cosh\alpha = \frac{\mathrm{e}^{k_m^*}}{2}(1-\mathrm{i})\sqrt{\mu} + O(\mu^{-\frac{1}{2}}). \tag{5.88}$$

Similarly

$$\sinh\alpha = \frac{\mathrm{e}^{k_m^*}}{2}(1-\mathrm{i})\sqrt{\mu} + O(\mu^{-\frac{1}{2}}), \tag{5.89}$$

$$\cosh\beta = \frac{\mathrm{e}^{-k_m^*}}{2}(1-\mathrm{i})\sqrt{\mu} + O(\mu^{-\frac{1}{2}}). \tag{5.90}$$

Using these expressions on the energy inner product (5.10b) we have

$$E_{mn} = \left(\frac{16(\mathrm{e}^{2k_m^*}+1)}{\mu^2} + O\left(\frac{1}{\mu^3}\right)\right) - \left(\frac{8\mathrm{i}}{\mu} + O\left(\frac{1}{\mu^2}\right)\right) + \left(\frac{8\mathrm{i}}{\mu} + O\left(\frac{\log\mu}{\mu^2}\right)\right) + \left(\frac{8\cosh 2k_m^*}{\mu^2} + O\left(\frac{1}{\mu^3}\right)\right). \tag{5.91}$$

The $O(\mu^{-1})$ term cancels, meaning

$$E_{mn} = O\left(\frac{\log\mu}{\mu^2}\right), \quad n \to \infty. \tag{5.92}$$

Hence we have

$$\langle \tilde{\boldsymbol{q}}_n, \tilde{\boldsymbol{q}}_m \rangle = O\left(\frac{(\log\mu)^{\frac{5}{2}}}{\mu^3}\right), \tag{5.93}$$

where $\mu = (2n - \frac{1}{2})\pi$.

5.3.4 Short wavelength growth mechanism

The results of §§5.3.2 and 5.3.3 can be summarized by the following two leading order expressions for the energy norm

$$\text{(i)} \qquad \langle \tilde{\boldsymbol{q}}_n, \tilde{\boldsymbol{q}}_m \rangle \sim 0, \quad m = O(1), \quad n \to \infty \tag{5.94a}$$

$$\text{(ii)} \qquad \langle \tilde{\boldsymbol{q}}_{n+a}, \tilde{\boldsymbol{q}}_n \rangle \sim 1 - \mathrm{i}\frac{3a\pi}{\log 2\mu}, \quad a = O(1), \quad n \to \infty. \quad \mu = \left(2n - \frac{1}{2}\right)\pi \tag{5.94b}$$

From (i) we have that, in the limit of large wavenumber, short wavelength modes are orthogonal to large wavelength modes. (ii) implies that the energy inner product of two short wavelength modes is non-zero, and modes become increasingly parallel on the slow $(\log 2\mu)^{-1}$ scale. We interpret this to mean that short wavelength modes are able to

transfer energy between one another, but they transfer little energy to large wavelength modes. Therefore we believe that the optimal growth calculations in §5.1 exploit this energy transfer by including increasingly short wavelength modes in the expansion for the optimal edge profile. We expect that as the number of modes in the expansion is increased, the $(n+1)^{\text{th}}$ mode, say, becomes almost parallel to the n^{th} mode, and its influence on the optimal edge profile is diminished since its effects are be spanned by the n^{th} mode. Furthermore, since the short wavelength modes are highly damped, as wavelengths are shortened modes are less able to affect the domain far from the edge. This offers an explanation as to why the location of the maximum energy growth, x_{max}, decreases with mode truncation M, as seen in the right panel of Figure 5.3.

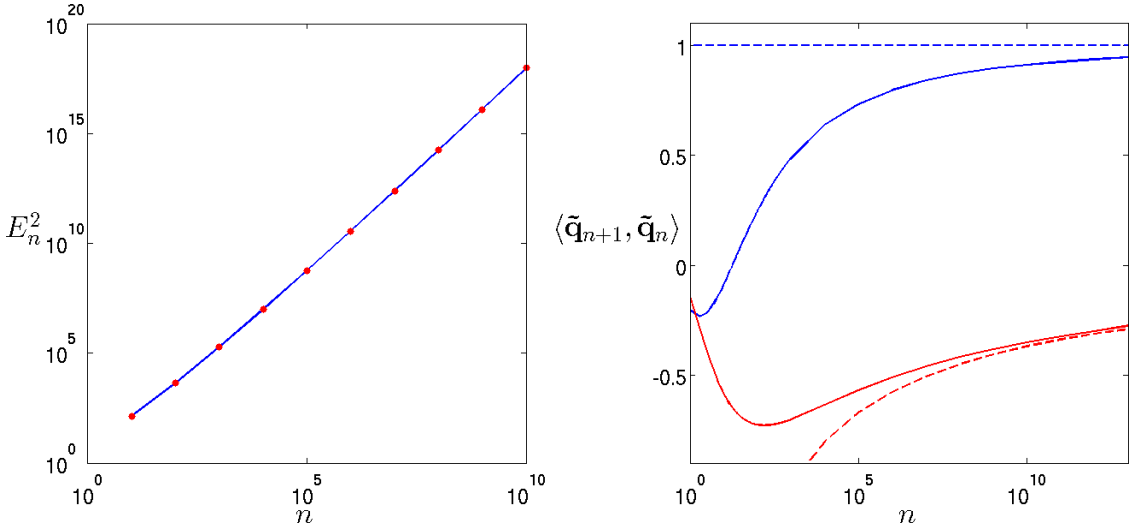

Figure 5.14: On the left panel we plot E_n^2 against n. Red dots represent numerically calculated values and the blue line is our leading order estimate. On the right panel we have the norm $\langle \tilde{\boldsymbol{q}}_{n+1}, \tilde{\boldsymbol{q}}_n \rangle$ against n. The blue and red lines are the real and imaginary parts of the norm, and the blue and red dashed lines are the real and imaginary leading order estimates respectively.

5.4 Spatial Poiseuille flow

To investigate the role that the growth mechanism observed in the previous chapters plays in flows with convection, we address the problem of optimal growth in two-dimensional spatially developing Poiseuille flow of a viscous fluid. For the parabolic Poiseuille base flow $\boldsymbol{U} = U(y)\boldsymbol{e}_x = (1-y^2)\boldsymbol{e}_x$ and velocity and pressure perturbations $(\boldsymbol{u}, p) = [\tilde{u}, \tilde{v}, \tilde{p}](x, y)$, the linearized Navier-Stokes equations for steady fluid motion in a semi-infinite channel are

$$U\frac{\partial \tilde{u}}{\partial x} + \tilde{v}U' = -\frac{\partial \tilde{p}}{\partial x} + \frac{1}{Re}\nabla^2\tilde{u}, \tag{5.95a}$$

$$U\frac{\partial \tilde{v}}{\partial x} = -\frac{\partial \tilde{p}}{\partial y} + \frac{1}{Re}\nabla^2\tilde{v}, \tag{5.95b}$$

$$\frac{\partial \tilde{u}}{\partial x} + \frac{\partial \tilde{v}}{\partial y} = 0, \tag{5.95c}$$

where $'$ denotes differentiation with respect to y and ∇^2 is the Laplacian operator. The Reynolds number $Re = \frac{U_c h}{\nu}$ is based on the centre velocity U_c, the channel half-height h and the kinematic viscosity of the fluid ν. Equations (5.95) are non-dimensionalized in terms of these quantities. We solve on the domain Ω as defined in §5.1 and impose the no-slip boundary conditions on the walls $y = \pm 1$. From this formulation, Stokes flow and the Papkovitch-Fadle operator can be recovered in the limit $Re \to 0$. The linear spatial stability of the system is found by Fourier transforming the perturbations in the streamwise co-ordinate x such that

$$[\tilde{u}, \tilde{v}, \tilde{p}](x, y) = [u, v, p](y)\mathrm{e}^{\mathrm{i}\alpha x}, \tag{5.96}$$

for $\alpha \in \mathbb{C}$. Equations (5.95) now become

$$U\mathrm{i}\alpha u + vU' = -\mathrm{i}\alpha p + \frac{1}{Re}(D^2 - \alpha^2)u, \tag{5.97a}$$

$$U\mathrm{i}\alpha v = -p' + \frac{1}{Re}(D^2 - \alpha^2)v, \tag{5.97b}$$

$$\mathrm{i}\alpha u + v' = 0, \tag{5.97c}$$

where $D = \frac{d}{dy}$. For a given Re, we can determine eigenvalues $\alpha_n \in \mathbb{C}$ which govern the stability of the perturbations. The equations (5.95) are elliptic in space, thus solutions of (5.97) yield upstream and downstream travelling modes. We know from temporal stability theory that Poiseuille flow is linearly stable for $Re < 5772$ (Orszag (1971), Schmid & Henningson (2001)), so we can ignore upstream modes by neglecting eigenvalues with $\mathrm{Im}\{\alpha_n\} < 0$ provided Re is sufficiently small. In this way we can parabolize the system and restrict our attention to disturbances evolving downstream from the edge, $\Gamma = \{x = 0, -1 \leq y \leq 1\}$, of the domain.

A matrix method is used to find the eigenmodes of (5.97). Introducing

$$\bar{u} = \alpha u \quad \text{and} \quad \bar{v} = \alpha v, \tag{5.98}$$

we can recast the system into the linear eigenproblem

$$L\boldsymbol{q} = \alpha M\boldsymbol{q}, \tag{5.99}$$

where the vector $\boldsymbol{q} = [u \;\; v \;\; p \;\; \bar{u} \;\; \bar{v}]^{\mathrm{T}}$ and the operators L and M are

$$L = \begin{pmatrix} \frac{1}{Re}D^2 & -U' & 0 & 0 & 0 \\ 0 & \frac{1}{Re}D^2 & -D & 0 & 0 \\ 0 & -D & 0 & 0 & 0 \\ 0 & 0 & 0 & 1 & 0 \\ 0 & 0 & 0 & 0 & 1 \end{pmatrix}, \tag{5.100}$$

$$M = \begin{pmatrix} \mathrm{i}U & 0 & \mathrm{i} & \frac{1}{Re} & 0 \\ 0 & \mathrm{i}U & 0 & 0 & \frac{1}{Re} \\ \mathrm{i} & 0 & 0 & 0 & 0 \\ 1 & 0 & 0 & 0 & 0 \\ 0 & 1 & 0 & 0 & 0 \end{pmatrix}. \tag{5.101}$$

We then discretize the system in y using Chebyshev polynomials, following the procedure detailed in Schmid & Henningson (2001), and solve the resulting generalized eigenvalue problem for α and $\boldsymbol{q}$.

5.4.1 Spatial spectra

In Figure 5.15 we show that the leading eigenvalue from our calculations at low Re shows good convergence to the leading Papkovitch-Fadle eigenvalue, which we interpret as some validation of the code for arbitrary Re. In Figure 5.16 we plot spatial spectra at various Re. We see that as $Re \to 0$ the spectra are qualitatively similar to the Papkovitch-Fadle operator eigenvalues.

The emergence of stationary downstream propagating modes is investigated in Figure 5.17. We find that for $7 < Re < 8$, a set of upstream propagating stationary modes become increasingly damped as Re is increased. The modes then 'turn around' in space, changing from highly damped upstream to high damped downstream modes. In so doing, the imaginary part of the wavenumber switches from negative to positive infinity, meaning that the stationary upstream modes emerge from infinity.

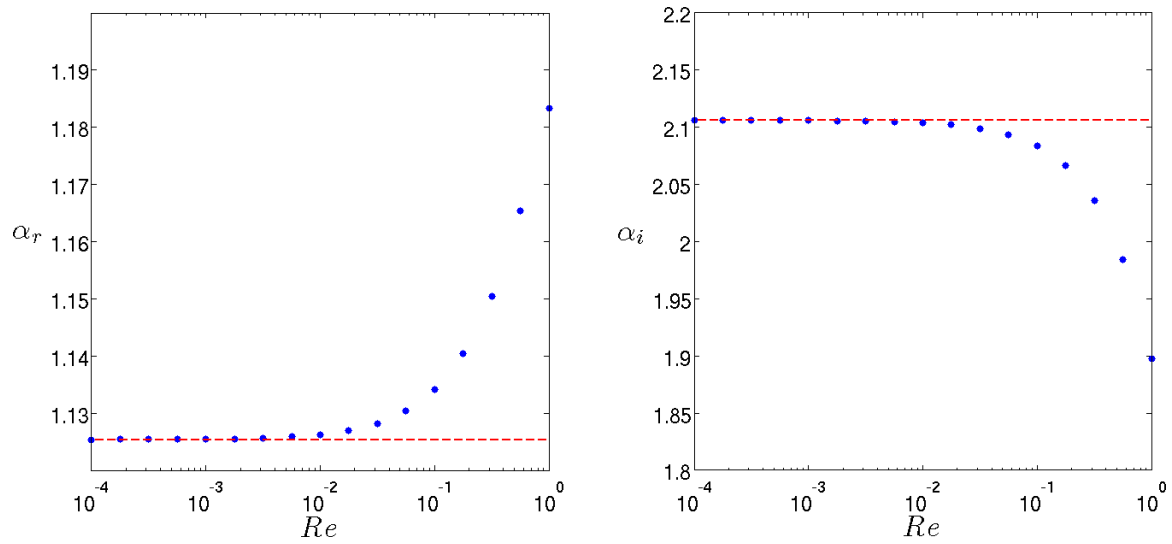

Figure 5.15: Comparison between the leading eigenvalue of our finite Re computations and the Papkovitch-Fadle spectrum. The dots correspond to calculations at the given Re, and the dashed line is the Papkovitch-Fadle mode.

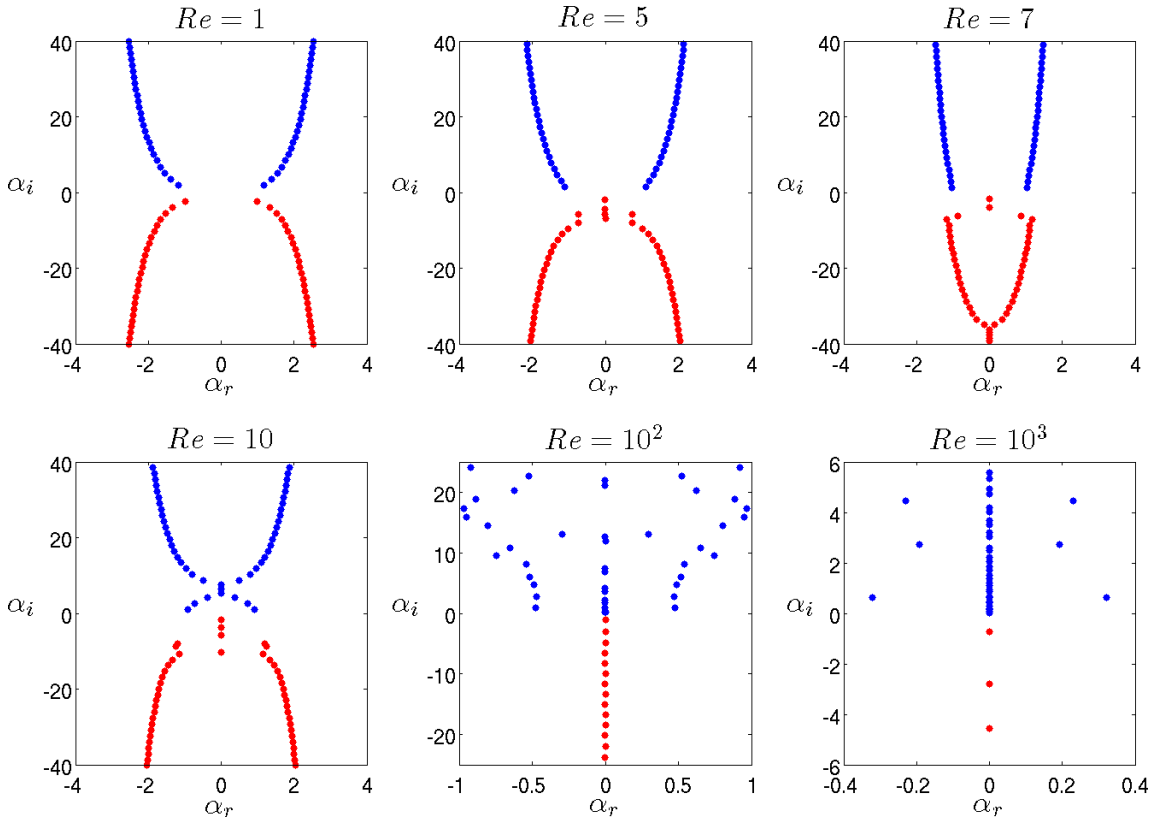

Figure 5.16: Spatial spectra at various Re. Downstream/upstream propagating modes are coloured blue/red. Top row: $Re = 1, 5, 7$. Bottom row: $Re = 10, 100, 1000$.

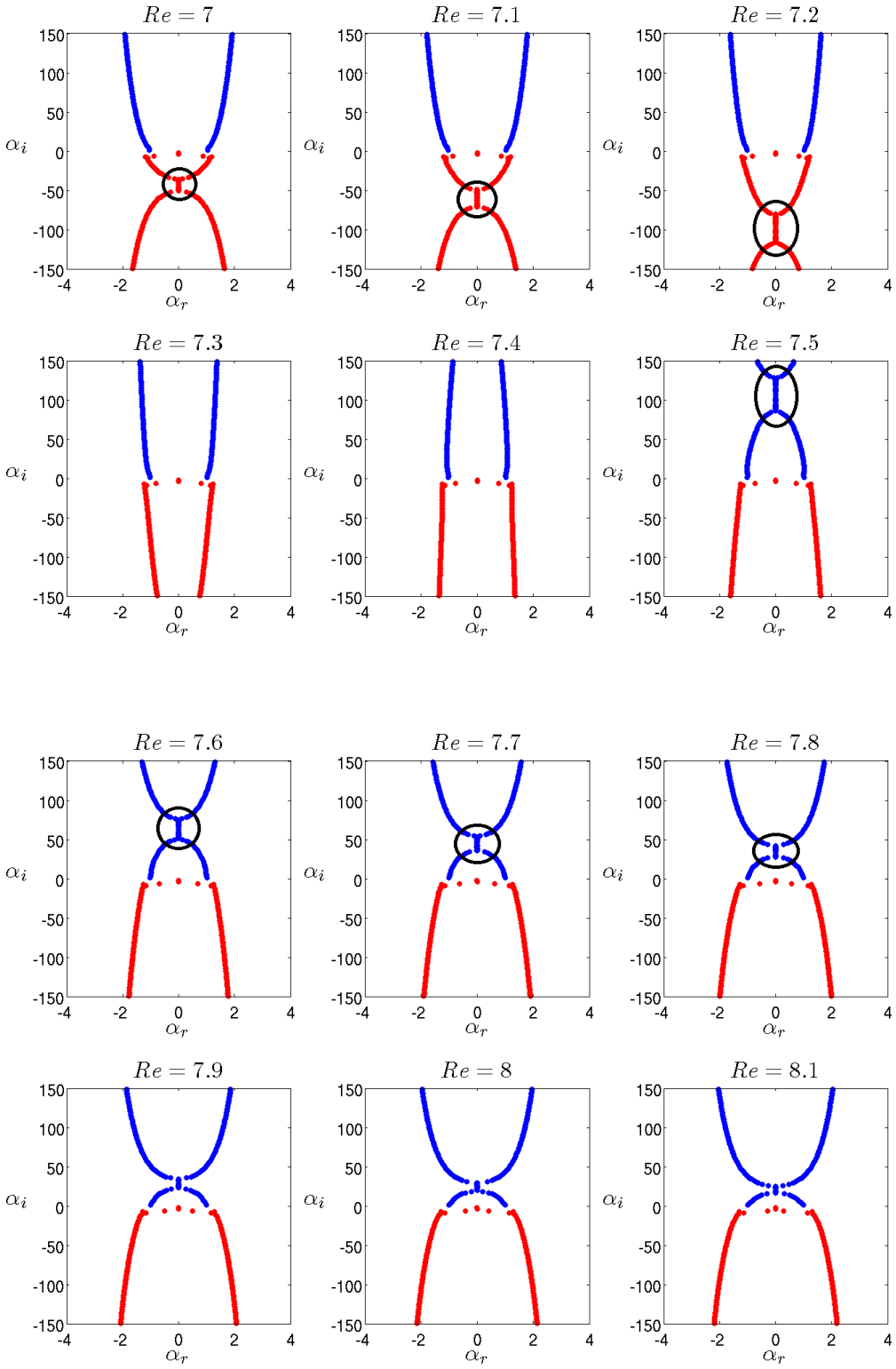

Figure 5.17: Emergence of stationary downstream modes from infinity. Downstream/upstream modes are coloured blue/red. A selection of stationary upstream modes are circled for $Re = 7$. As Re is increased, the upstream modes become more damped before they 'turn around' in space to become highly damped downstream modes. The stationary downstream modes appear in our Figure at $Re = 7.5$. They become less damped as Re is further increased.

5.4.2 Optimal growth and convergence

We now turn our attention to optimal growth. The formulation is the same as in §5.2, but since we no longer have a general analytic solution the energy norm (5.16) is now computed via numerical integration. Having solved (5.97) for u_n and v_n where

$$L\boldsymbol{q}_n = \alpha_n M \boldsymbol{q}_n \text{ and } \boldsymbol{q}_n = [u_n \;\; v_n \;\; p_n \;\; \bar{u}_n \;\; \bar{v}_n]^{\mathrm{T}}, \tag{5.102}$$

the energy inner product

$$E_{mn} = \langle \boldsymbol{u}_n, \boldsymbol{u}_m \rangle = \frac{1}{2}\int_{-1}^{1} u_m^* u_n + v_m^* v_n \,\mathrm{d}y, \tag{5.103}$$

is numerically approximated using Clenshaw-Curtis quadrature (Clenshaw & Curtis (1960); Boyd (2001)), which exploits the choice of Chebyshev polynomials for discretization in y. We then compute the spatial energy gain $G(x)$ as before. Each mode in our calculations has a wall-normal discretization of $N = 601$ Chebyshev polynomials, which ensures that we can include well-resolved highly damped modes.

Figure 5.18 compares curves of the energy amplification $G(x)$ at different Re. Each curve is computed for a perturbation expansion with $M = 500$ modes. We see that for $Re = 1, 10$, $G(x)$ is qualitatively similar to the corresponding curves for the Stokes problem shown in Figure 5.3. At larger Re however, the characteristic oscillations in $G(x)$ are no longer present, since the leading eigenvalue has zero real part. Figure 5.18 also compares the energy growth regions for each flow. A notable feature in common with Stokes flow is that there is a sharp growth gradient near the edge $x = 0$, for every Re considered, suggesting that the unbounded numerical abscissa of the Papkovitch-Fadle operator may extend to flows with Re large.

With respect to our trunction of $M = 500$, we define the quantities G_{max} and x_{max}

$$G_{max} = \max_x G(x) = G(x_{max}). \tag{5.104}$$

However, these maxima may change subject to an increase in the modal truncation.

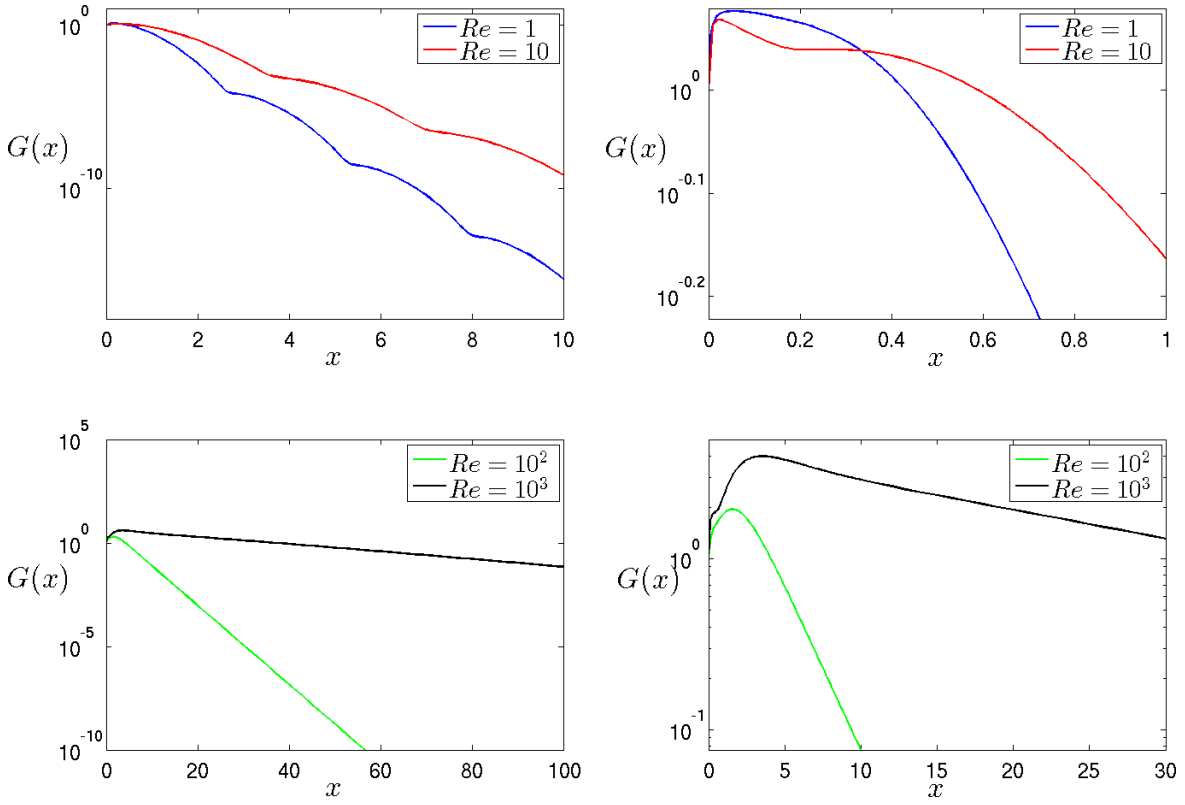

Figure 5.18: Gain curves in x. Top row: $Re = 1, 10$. Bottom row: $Re = 100, 1000$.

To assess the convergence of $G(x)$ four Reynolds numbers, $Re = 1, 10, 100, 1000$, are chosen and in each case x is fixed at a value close to x_{max}. In Figure 5.19 we plot the results. Note that the increases in G are stepped in M. This is because the spatial spectra consist of even and odd modes which are orthogonal, as was the case for the Papkovitch-Fadle operator in §5.2, in equations (5.10). This means if the optimal perturbation is comprised of even modes, say, then odd modes cannot contribute to the energy growth. We compare the magnitude of the optimal perturbation coefficients $|a_m|$ and filter out modes with markedly lower magnitudes (see Figure 5.20), which make no contribution to the optimal growth. On this reduced basis of modes we can consider G at fixed x to be a function of M, and we re-introduce $\frac{\delta G}{\delta M}$ from §5.2.1. $\frac{\delta G}{\delta M}$ can be used as a diagnostic to compare convergence at each Re. $\frac{\delta G}{\delta M}$ is qualitatively similar to the Stokes case for $Re = 1, 10$. The following scalings are computed and plotted in Figure 5.21

$$Re = 0: \quad \frac{\delta G}{\delta M} \propto M^{-2}, \qquad x = 0.1, \tag{5.105a}$$

$$Re = 1: \quad \frac{\delta G}{\delta M} \propto M^{-1.9}, \qquad x = 0.055, \tag{5.105b}$$

$$Re = 10: \quad \frac{\delta G}{\delta M} \propto M^{-1.7}, \qquad x = 0.02. \tag{5.105c}$$

For $Re = 100, 1000$, G grows rapidly in the range $1 \lesssim M \lesssim 100$. For $M \gtrsim 100$ G

increases on a much slower scale; this is shown in on the lower row of Figure 5.19. For these Reynolds numbers we plot $\frac{\delta G}{\delta M}$ in Figure 5.22. We calculate the convergence rates

$$Re = 100: \quad \frac{\delta G}{\delta M} \propto M^{-2}, \quad x = 1.6, \qquad Re = 1000: \quad \frac{\delta G}{\delta M} \propto M^{-2.5}, \quad x = 3.5. \tag{5.106}$$

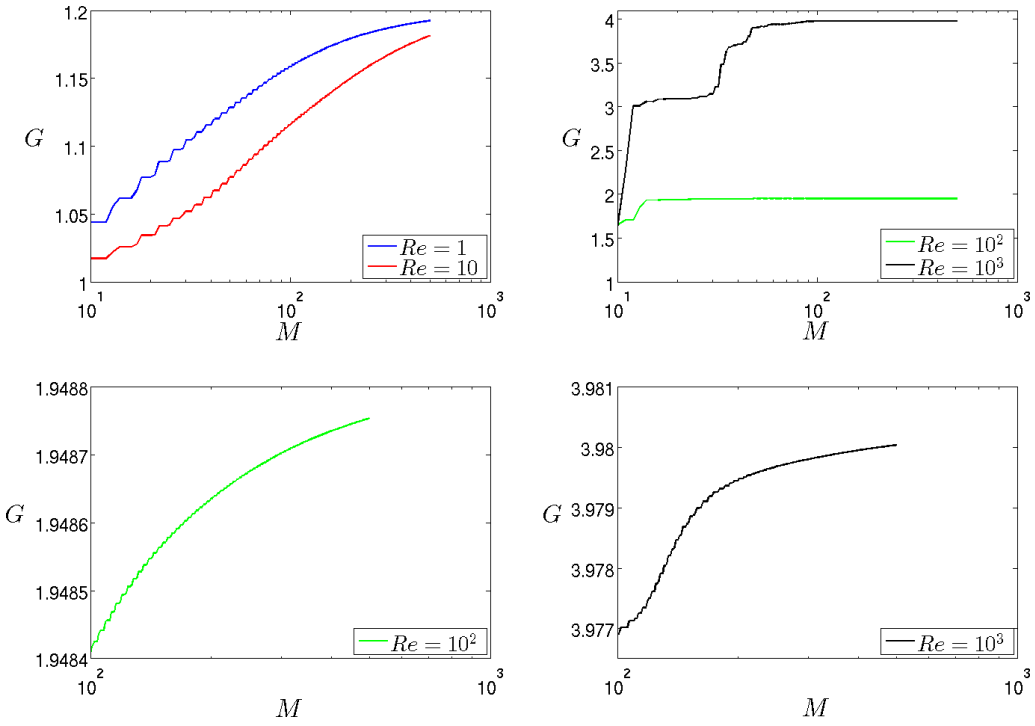

Figure 5.19: Convergence of G in modal truncation M. The streamwise coordinate is fixed at $x = 0.055, 0.02, 1.6$ and 3.5 for $Re = 1, 10, 10^3$ and 10^3 respectively.

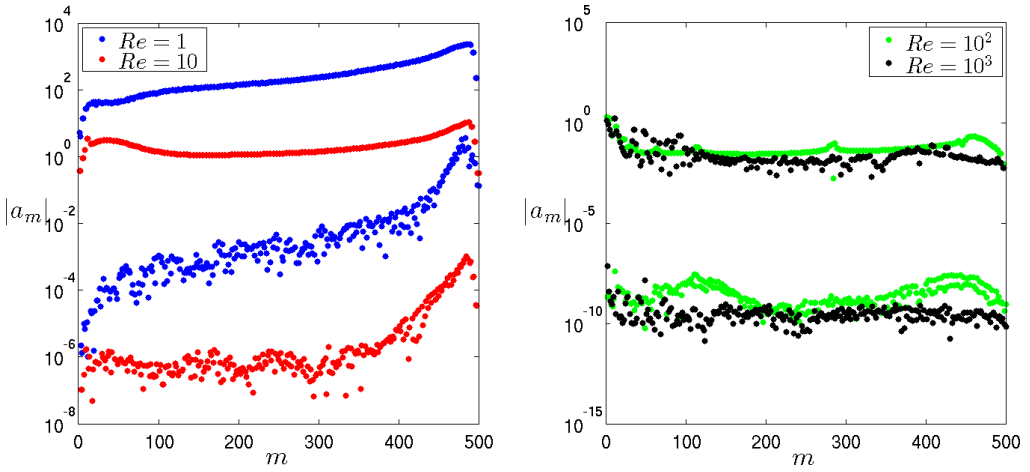

Figure 5.20: Absolute value of the optimal coefficients $|a_m|$ for $Re = 1, 10, 100, 1000$. Modes on the lower order of magnitude are filtered out of the optimal eigenmode expansion to form a reduced basis.

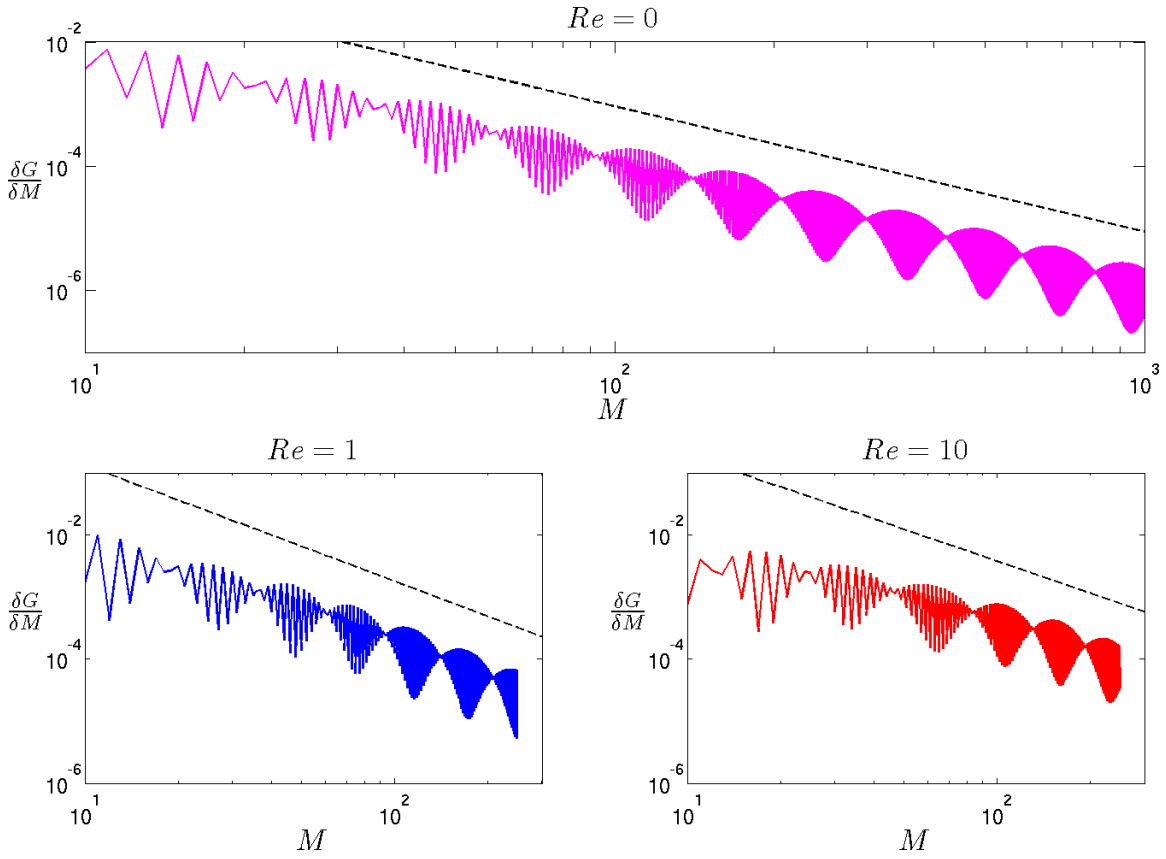

Figure 5.21: Convergence rates $\frac{\delta G}{\delta M}$ for $Re = 0$ (top), $Re = 1$ (bottom-left) and $Re = 10$ (bottom-right). The dashed curves are the numerically calculated exponents in equations (5.105)

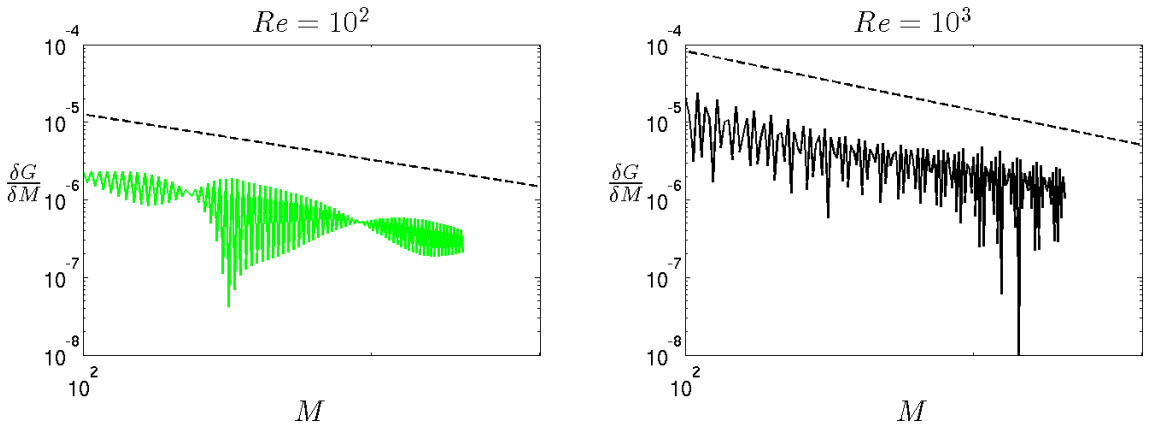

Figure 5.22: Convergence rates $\frac{\delta G}{\delta M}$ for $Re = 100$ (left) and $Re = 1000$ (right). The dashed curves are the numerically calculated exponents in equations (5.106)

5.4.3 Optimal disturbances

In keeping with the trends observed in the previous section, the optimal disturbances at low Re share similar qualitative characteristics with the optimals in the Stokes problem. We plot the modal form of the optimals in Figure 5.23, and their form in the (x, y)-plane in Figure 5.24. For larger Re the optimals still possess oscillatory features at the corners of the domain, however it is less pronounced than for the low Re optimals. At x_{max}, the optimals at large Re have maximum streamwise velocity u away from the wall, suggesting they are extracting energy from the mean shear in a manner similar to the two-dimensional Orr mechanism in temporal flows.

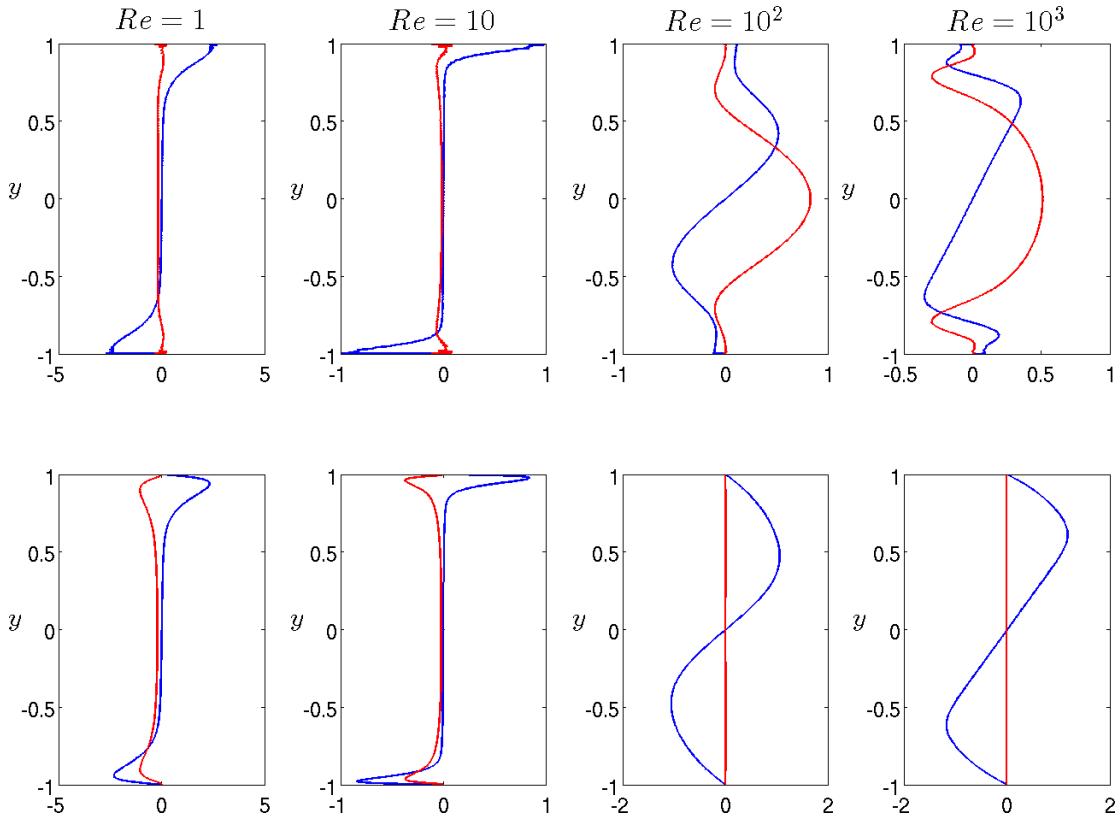

Figure 5.23: Wall normal and optimal profiles with velocities u and v in blue and red, respectively. The top row has the edge optimals, and the bottom row has the optimals near x_{max} for $Re = 1, 10, 100, 1000$.

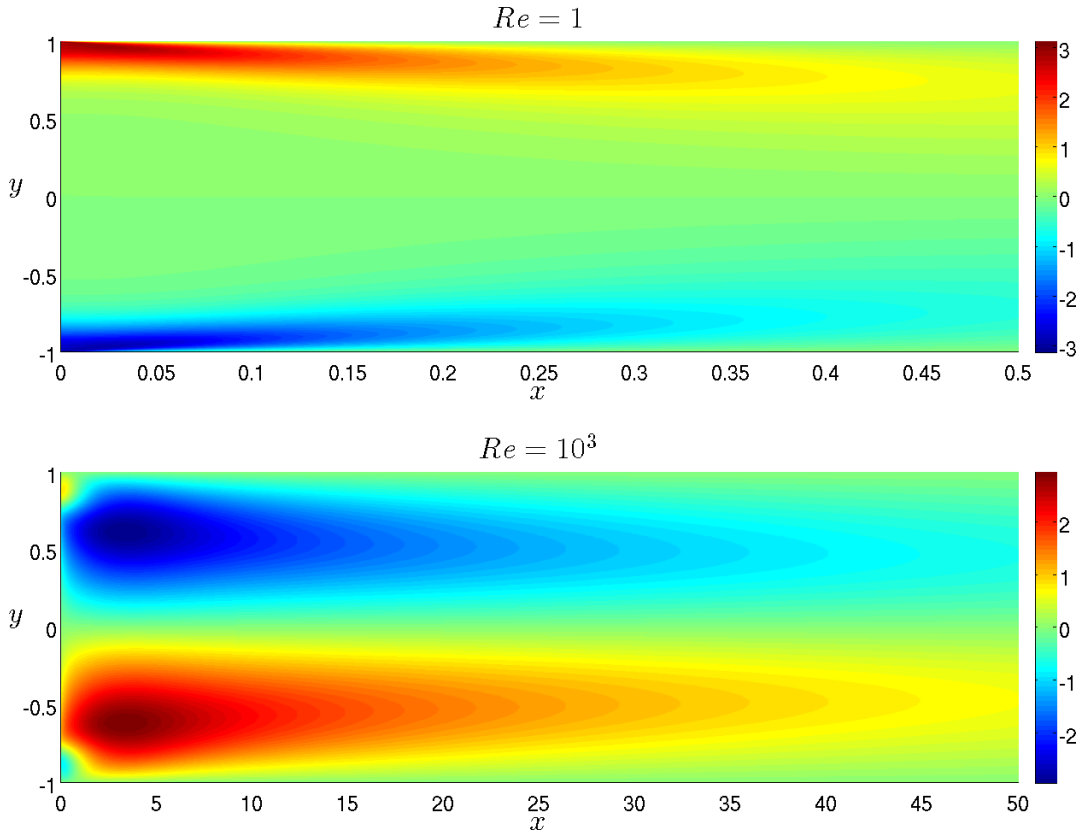

Figure 5.24: Streamwise velocity u for $Re = 1$ (top) and $Re = 1000$ (bottom) in the (x, y)-domain.

5.5 Temporal plane Couette flow

We contrast our findings in the Papkovitch-Fadle problem with an analysis of temporally evolving and streamwise independent plane Couette flow. For this flow we find that numerical computations of the transient perturbation energy density growth converge quickly with respect to the modal truncation of the calculation. An analytic solution is available which allows us to see what is happening to the modes.

We consider the motion of an incompressible, viscous fluid constrained between two infinite plates which move in opposite directions at equal speeds. The no-slip boundary condition is applied on each of the walls. The governing equations are non-dimensionalized with the wall speed $\widetilde{U}$, the channel half-height $\widetilde{h}$ and the kinematic viscosity of the fluid ν. We seek a solution to the linearized perturbation equations with base velocity $\boldsymbol{U} = y\boldsymbol{e}_x$. Furthermore we restrict the solution to streamwise independent and spanwise periodic perturbations such that

$$[u, v, w, p](y, z, t) = [u, v, w, p](y, t)\mathrm{e}^{\mathrm{i}\beta z}. \tag{5.107}$$

If we further assume that the velocity components have exponential dependence in time, $\propto \mathrm{e}^{-\sigma t}$, the linearized Navier-Stokes equations are

$$-\sigma u + v = \frac{1}{Re}(u'' - \beta^2 u), \tag{5.108a}$$

$$-\sigma v = -p' + \frac{1}{Re}(v'' - \beta^2 v), \tag{5.108b}$$

$$-\sigma w = -\mathrm{i}\beta p + \frac{1}{Re}(w'' - \beta^2 w), \tag{5.108c}$$

$$v' + \mathrm{i}\beta w = 0, \tag{5.108d}$$

where D denotes differentiation with respect to y and the Reynolds number is defined as $Re = \frac{\widetilde{U}\widetilde{h}}{\nu}$. The system can be further reduced to

$$v'''' + (\sigma Re - 2\beta^2)v'' - \beta^2(\sigma Re + \beta^2)v = 0, \tag{5.109a}$$

$$u'' + (\sigma Re - \beta^2)u = Re\, v, \tag{5.109b}$$

subject to $v(\pm 1) = v'(\pm 1) = u(\pm 1) = 0$. Using a Green's function approach we derive a general solution for this system with three classes of modes. Writing $\mu^2 = \sigma Re - \beta^2$ we have

$$\text{Class } (a): \quad \mu \tan \mu + \beta \tanh \beta = 0, \quad \text{(even modes)},$$

$$\begin{cases} u &= \frac{Re}{\mu^2+\beta^2}\big(\cosh\beta\cos\mu y - \cos\mu\cosh\beta y\big) + \frac{Re\cosh\beta}{2\mu\cos\mu}\big(y\cos\mu\sin\mu y - \sin\mu\cos\mu y\big), \\ v &= \cosh\beta\cos\mu y - \cos\mu\cosh\beta y, \\ w &= -\frac{\mathrm{i}}{\beta}\big(\mu\cosh\beta\sin\mu y + \beta\cos\mu\sinh\beta y\big). \end{cases}$$

$$\text{Class } (b): \quad \mu\cot\mu - \beta\coth\beta = 0, \quad \text{(odd modes)}$$

$$\begin{cases} u &= \frac{Re}{\mu^2+\beta^2}\big(\sinh\beta\sin\mu y - \sin\mu\sinh\beta y\big) + \frac{Re\sinh\beta}{2\mu\sin\mu}\big(\cos\mu\sin\mu y - y\sin\mu\cos\mu y\big), \\ v &= \sinh\beta\sin\mu y - \sin\mu\sinh\beta y, \\ w &= \frac{\mathrm{i}}{\beta}\big(\mu\sinh\beta\cos\mu y - \beta\sin\mu\cosh\beta y\big). \end{cases}$$

$$\text{Class } (c): \quad \mu = \frac{n\pi}{2} \begin{cases} u &= \sin\mu(y+1), \\ v &= 0, \\ w &= 0. \end{cases} \qquad (u\text{-modes})$$

Given $\beta \in \mathbb{R}$, the transcendental dispersion relations of the even and odd modes can be solved via a Newton iteration algorithm for $\mu \in \mathbb{R}$. The flow is found to be stable ($\sigma > 0$) $\forall\beta$. We will list the modes in terms of increasing μ. For example, μ_n^a denotes the n^{th} a-mode with

$$\sigma_n^a = \frac{(\mu_n^a)^2 + \beta^2}{Re}. \tag{5.110}$$

Similarly, the corresponding eigenfunctions or eigenmodes are denoted $\boldsymbol{u}_n^a$. Note that without loss of generality we can assume $\mu > 0$, since the value of the decay rate depends on the square of μ.

Despite the asymptotic stability of the flow significant transient energy density growth has been shown to exist at moderate Reynolds numbers (Butler & Farrell (1992), Reddy & Henningson (1993)). This growth is a consequence of the nonnormality of the linearized Navier-Stokes operator and the non-orthogonal nature of the eigenmodes of the system with respect to the energy inner product. Writing the kinetic energy through the fluid domain as

$$E = \frac{1}{2}\int_{-1}^{1} u^*u + v^*v + w^*w\,dy, \tag{5.111}$$

we introduce the modal energy inner product

$$\langle \boldsymbol{u}_\lambda, \boldsymbol{u}_\mu \rangle = \frac{1}{2}\int_{-1}^{1} u_\lambda^* u_\mu + v_\lambda^* v_\mu + w_\lambda^* w_\mu\,dy. \tag{5.112}$$

Hence if we have an arbitrary velocity disturbance expanded in terms of the eigenmodes

of the system

$$\boldsymbol{u}(y,z,t)=\sum_{n=1}^{\infty}\kappa_n\boldsymbol{u}_n\mathrm{e}^{\mathrm{i}\beta z-\sigma_n t}=\sum_{j=1}^{\infty}a_j\boldsymbol{u}_j^a\mathrm{e}^{\mathrm{i}\beta z-\sigma_j t}+\sum_{k=1}^{\infty}b_k\boldsymbol{u}_k^b\mathrm{e}^{\mathrm{i}\beta z-\sigma_k t}+\sum_{\ell=1}^{\infty}c_\ell\boldsymbol{u}_\ell^c\mathrm{e}^{\mathrm{i}\beta z-\sigma_\ell t}, \tag{5.113}$$

then the appropriate energy norm is

$$\|\boldsymbol{u}(t)\|^2=\langle\boldsymbol{u},\boldsymbol{u}\rangle. \tag{5.114}$$

In terms of the modal energy we find the following orthogonality relations

$$\langle\boldsymbol{u}_\lambda^a,\boldsymbol{u}_\mu^a\rangle\neq 0, \tag{5.115a}$$
$$\langle\boldsymbol{u}_\lambda^a,\boldsymbol{u}_\mu^b\rangle=0,\quad\forall\mu,\lambda \tag{5.115b}$$
$$\langle\boldsymbol{u}_\lambda^a,\boldsymbol{u}_\mu^c\rangle\neq 0, \tag{5.115c}$$
$$\langle\boldsymbol{u}_\lambda^b,\boldsymbol{u}_\mu^b\rangle\neq 0, \tag{5.115d}$$
$$\langle\boldsymbol{u}_\lambda^b,\boldsymbol{u}_\mu^c\rangle\neq 0, \tag{5.115e}$$
$$\langle\boldsymbol{u}_\lambda^c,\boldsymbol{u}_\mu^c\rangle=0\quad\text{for }\mu\neq\lambda. \tag{5.115f}$$

The energy gain

$$G(t)=\max_{\boldsymbol{u}}\frac{E(t)}{E_0}=\max_{\boldsymbol{u}_0}\frac{\|\boldsymbol{u}(t)\|^2}{\|\boldsymbol{u}_0\|}, \tag{5.116}$$

can be calculated in the same manner as in §5.2, with exact expressions for the energy inner product. The gain, and corresponding optimal disturbance, can also be computed via collocation in y as in Schmid & Henningson (2001). Computations plotted in Figure 5.25, show that the optimal initial condition which reaches G_{max}, where $G_{max}=\max_t G(t)$, is comprised of class (a) and (c) modes. The value of G_{max} is found to be well converged for a modal truncation $N\ll 10^4$, as can be seen in Figure 5.26. Since orthogonal modes can make no contribution to the optimal growth, we assume that in addition to being highly damped, modes with large σ_n orthogonalize so that they make a negligible contribution to the maximum optimal growth. Accordingly, we assess how the relevant modal energy inner products behave in the asymptotic limit of large decay rate.

We begin with exact expressions for the inner products of interest

$$\langle\boldsymbol{u}_\lambda^a,\boldsymbol{u}_\mu^c\rangle=\frac{Re\mu\cos\lambda\cosh\beta}{2}(\cos 2\mu-1)\left(\frac{1}{(\lambda^2-\mu^2)^2}+\frac{1}{\lambda^2+\beta^2}\left(\frac{1}{\lambda^2-\mu^2}+\frac{1}{\mu^2+\beta^2}\right)\right). \tag{5.117}$$

$$\langle \boldsymbol{u}^a_\lambda, \boldsymbol{u}^a_\mu \rangle = \frac{Re^2}{2(\mu^2+\beta^2)(\lambda^2+\beta^2)} \Bigg\{ \cosh^2\beta \bigg(\frac{\sin(\mu-\lambda)}{\mu-\lambda} + \frac{\sin(\mu+\lambda)}{\mu+\lambda} \bigg)$$
$$+ \cos\mu\cos\lambda \bigg(1 + \frac{\sinh 2\beta}{2\beta} \bigg) \Bigg\} + \frac{Re^2\cosh^2\beta}{8\mu\lambda\cos\mu\cos\lambda} \Bigg\{ \frac{\sin^2(\mu-\lambda)}{(\mu-\lambda)^2} - \frac{\sin^2(\mu+\lambda)}{(\mu+\lambda)^2}$$
$$+ 2\cos\mu\cos\lambda \bigg(\frac{\cos(\mu-\lambda)}{(\mu-\lambda)^2} - \frac{\cos(\mu+\lambda)}{(\mu+\lambda)^2} + \frac{\sin(\mu+\lambda)}{(\mu+\lambda)^3} - \frac{\sin(\mu-\lambda)}{(\mu-\lambda)^3} \bigg) \Bigg\}$$
$$+ \frac{Re^2\cosh\beta}{4\mu\cos\mu(\lambda^2+\beta^2)} \Bigg\{ \cos\mu\cosh\beta \bigg(\frac{\sin(\mu+\lambda)}{(\mu+\lambda)^2} + \frac{\sin(\mu-\lambda)}{(\mu-\lambda)^2} - \frac{\cos(\mu+\lambda)}{\mu+\lambda} - \frac{\cos(\mu-\lambda)}{\mu-\lambda} \bigg)$$
$$- \cos\mu\cos\lambda \bigg(\frac{2(\beta\sinh\beta\sin\mu - \mu\cosh\beta\cos\mu - \cosh\beta\sin\mu)}{\mu^2+\beta^2} \bigg)$$
$$- \sin\mu\cosh\beta \bigg(\frac{\sin(\mu+\lambda)}{\mu+\lambda} + \frac{\sin(\mu-\lambda)}{\mu-\lambda} \bigg) \Bigg\}$$
$$+ \frac{Re^2\cosh\beta}{4\lambda\cos\lambda(\mu^2+\beta^2)} \Bigg\{ \cos\lambda\cosh\beta \bigg(\frac{\sin(\mu+\lambda)}{(\mu+\lambda)^2} - \frac{\sin(\mu-\lambda)}{(\mu-\lambda)^2} - \frac{\cos(\mu+\lambda)}{\mu+\lambda} + \frac{\cos(\mu-\lambda)}{\mu-\lambda} \bigg)$$
$$- \cos\mu\cos\lambda \bigg(\frac{2(\beta\sinh\beta\sin\lambda - \lambda\cosh\beta\cos\lambda - \cosh\beta\sin\lambda)}{\lambda^2+\beta^2} \bigg)$$
$$- \sin\lambda\cosh\beta \bigg(\frac{\sin(\mu+\lambda)}{\mu+\lambda} + \frac{\sin(\mu-\lambda)}{\mu-\lambda} \bigg) \Bigg\}, \qquad \text{for } \mu \neq \lambda. \tag{5.118}$$

$$\langle \boldsymbol{u}^a_\mu, \boldsymbol{u}^a_\mu \rangle = \frac{Re^2}{2(\mu^2+\beta^2)^2} \Bigg\{ \cosh^2\beta \bigg(1 + \frac{\sin 2\mu}{2\mu} \bigg) + \cos\mu^2 \bigg(1 + \frac{\sinh 2\beta}{2\beta} \bigg) \Bigg\}$$
$$+ \frac{Re^2\cosh^2\beta}{8\mu^2\cos^2\mu} \Bigg\{ \cos^2\mu \bigg(\frac{1}{3} - \frac{\cos 2\mu}{2\mu^2} + \frac{\sin 2\mu}{4\mu^3} \bigg) - \frac{\sin^2 2\mu}{4\mu^2} + \sin^2\mu \Bigg\}$$
$$+ \frac{Re^2\cosh\beta}{2\mu\cos\mu(\mu^2+\beta^2)} \Bigg\{ \cos\mu\cosh\beta \bigg(\frac{\sin 2\mu}{4\mu^2} - \frac{\cos 2\mu}{2\mu} \bigg) - \sin\mu\cosh\beta \bigg(1 + \frac{\sin 2\mu}{2\mu} \bigg)$$
$$- \cos^2\mu \bigg(\frac{2(\mu\beta\sinh\beta\sin\mu - \mu^2\cosh\beta\cos\mu + \beta\sinh\beta\cos\mu)}{\mu(\mu^2+\beta^2)} \bigg) \Bigg\}$$
$$+ \frac{\sinh 2\beta\cos^2\mu}{2\beta} + \frac{\cosh^2\beta}{2} \bigg(1 + \frac{\sin 2\mu}{2\mu} + \frac{\mu^2}{\beta^2} \bigg(1 - \frac{\sin 2\mu}{2\mu} \bigg) \bigg)$$
$$+ \frac{2\mu\cos\mu\cosh\beta}{\beta(\mu^2+\beta^2)} \bigg(\beta\cosh\beta\sin\mu - \mu\cos\mu\sinh\beta \bigg). \tag{5.119}$$

$$\langle \boldsymbol{u}^c_\mu, \boldsymbol{u}^c_\mu \rangle = \frac{1}{2}. \tag{5.120}$$

Note that the terms appearing in $\langle \boldsymbol{u}^a_\lambda, \boldsymbol{u}^a_\mu \rangle$ are all proportional to Re^2, whereas $\langle \boldsymbol{u}^a_\mu, \boldsymbol{u}^a_\mu \rangle$ contains terms which are not. This indicates that as the Stokes limit, $Re \to 0$, is approached, the inner products orthogonalize, in contrast with the case for spatially evolving

disturbances.

Returning to the problem at hand, we pass to the high decay rate limit and keep Re and β fixed, which gives

$$\mu_n^a \sim n\pi - \varepsilon, \quad n \to \infty. \qquad \varepsilon = \frac{\beta \tanh \beta}{n\pi}. \tag{5.121}$$

Thus

$$\langle \boldsymbol{u}_\mu^a, \boldsymbol{u}_\mu^a \rangle = \frac{\pi^2 \cosh^2 \beta}{2\beta^2} n^2 + O(1), \quad n \to \infty. \tag{5.122}$$

This means that the normalization factor for the a-modes has the asymptotic form

$$N_\mu^a = \frac{\pi \cosh \beta}{\sqrt{2}\beta} n + O(1), \quad n \to \infty \tag{5.123}$$

whilst for the c-modes the normalization factor is simply a constant, $N^c = \sqrt{2}$. Hence we can introduce asymptotically normalized modes

$$\tilde{\boldsymbol{u}}_\mu^a = \frac{\boldsymbol{u}_\mu^a}{N_\mu^a} \text{ and } \tilde{\boldsymbol{u}}_\mu^c = \frac{\boldsymbol{u}_\mu^c}{N^c}, \tag{5.124}$$

such that

$$\langle \tilde{\boldsymbol{u}}_\mu^a, \tilde{\boldsymbol{u}}_\mu^a \rangle \sim 1 \text{ and } \langle \tilde{\boldsymbol{u}}_\mu^c, \tilde{\boldsymbol{u}}_\mu^c \rangle = 1. \tag{5.125}$$

Now we can look at how the modal interactions influence the energy inner product. For the $\langle \tilde{\boldsymbol{u}}_\mu^a, \tilde{\boldsymbol{u}}_\lambda^c \rangle$ inner product we choose three relevant large n limits to investigate

$$\text{(i)} \qquad \mu_n^a = n\pi + O(n^{-1}), \qquad \mu^c = \lambda = O(1), \tag{5.126a}$$

$$\text{(ii)} \qquad \mu^a = \lambda = O(1), \qquad \mu_n^c = \left(n + \frac{1}{2}\right)\pi, \tag{5.126b}$$

$$\text{(iii)} \qquad \mu_n^a = n\pi + O(n^{-1}), \qquad \mu_n^c = \left(n + \frac{1}{2}\right)\pi. \tag{5.126c}$$

For limit (i) we have

$$\langle \tilde{\boldsymbol{u}}_{\mu_n^a}^a, \tilde{\boldsymbol{u}}_\lambda^c \rangle = (-1)^{n+1} \left(\frac{\lambda \beta Re}{\pi^3(\lambda^2 + \beta^2)} \right) n^{-3} + O(n^{-5}), \quad n \to \infty. \tag{5.127}$$

Taking limit (ii) we get

$$\langle \tilde{\boldsymbol{u}}_\lambda^a, \tilde{\boldsymbol{u}}_{\mu_n^c}^c \rangle = \left(\frac{-\sqrt{2}(\lambda^2 + \beta^2) Re \cos \lambda \cosh \beta}{N_\lambda^a \pi^5} \right) n^{-5} + O(n^{-6}), \quad n \to \infty \tag{5.128}$$

where $N_\lambda^a = \sqrt{\langle \boldsymbol{u}_\lambda, \boldsymbol{u}_\lambda \rangle}$. Limit (iii) gives

$$\langle \tilde{\boldsymbol{u}}^a_{\mu_n^a}, \tilde{\boldsymbol{u}}^c_{\mu_n^c} \rangle = (-1)^{n+1} \left(\frac{\beta Re}{\pi^4} \right) n^{-2} + O(n^{-3}), \quad n \to \infty. \tag{5.129}$$

Now considering the $\langle \tilde{\boldsymbol{u}}^a_\mu, \tilde{\boldsymbol{u}}^a_\lambda \rangle$ inner product, we investigate the following limits

$$\text{(iv)} \qquad \mu_n = n\pi + O(n^{-1}), \quad \lambda = O(1), \quad n \to \infty, \tag{5.130a}$$

$$\text{(v)} \qquad \mu_n = n\pi + O(n^{-1}), \quad \mu_{n-p} = (n-p)\pi + O((n-p)^{-1}), \tag{5.130b}$$

$$\text{for } p \in \mathbb{Z} \text{ and } p = O(1),\ n \to \infty.$$

We have dropped the superscripts for μ^a in the above expressions, since both modes are class a in this case. For limit (iv) we have

$$\langle \tilde{\boldsymbol{u}}_{\mu_n}, \tilde{\boldsymbol{u}}_\lambda \rangle = A n^{-3} + O(n^{-5}), \quad n \to \infty \tag{5.131}$$

where

$$A = \frac{\beta Re^2}{\sqrt{2}\pi^3(\lambda^2+\beta^2)N_\lambda^a} \left(\frac{\beta \sinh 2\beta \sin\lambda}{2\lambda} - \cosh^2\beta \left(\cos\lambda + \frac{\sin\lambda}{\lambda} \right) - \cos\lambda \left(1 + \frac{\sinh 2\beta}{2\beta} \right) \right). \tag{5.132}$$

In limit (v) we have, to leading order

$$\langle \tilde{\boldsymbol{u}}_{\mu_n}, \tilde{\boldsymbol{u}}_{\mu_{n-p}} \rangle = (-1)^p \frac{\beta^2 Re^2}{2p^2\pi^6} n^{-4} + O(n^{-5}), \quad n \to \infty. \tag{5.133}$$

Hence it can be seen that in all five limits considered, the asymptotic energy inner products (i), (ii), (iii), (iv) and (v) decay for highly damped modes. Though this is not an exhaustive list of large n limits, we believe that the behaviour shown for the limits considered will extend to others. We posit that this is a key component in the good convergence of optimal disturbances in plane Couette flow.

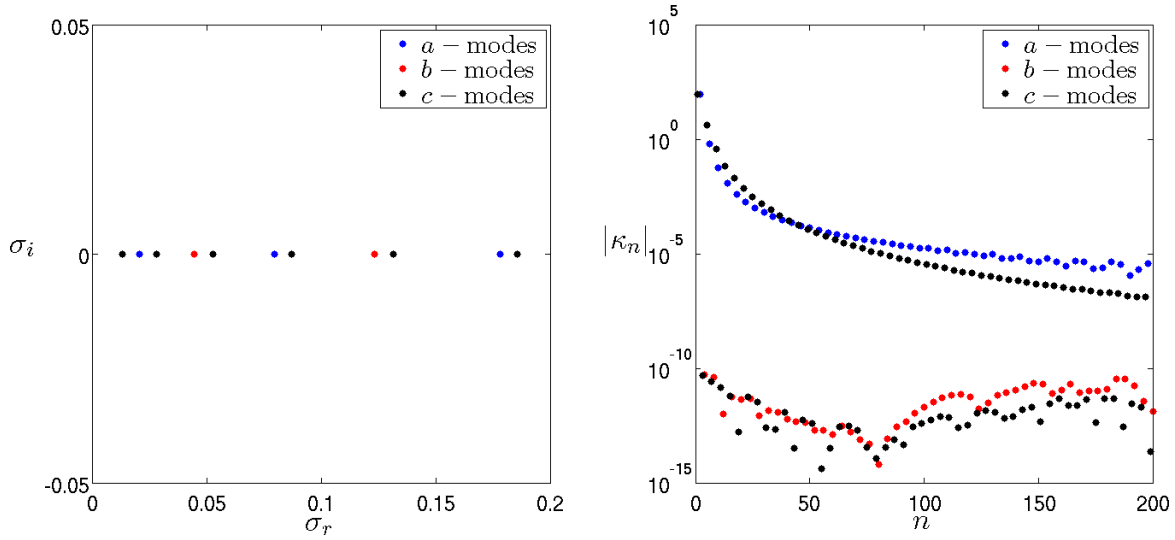

Figure 5.25: On the left is the σ spectrum in the complex plane, with $\beta = 2$ and $Re = 500$. On the right we plot the absolute value of the optimal coefficients $|\kappa_n|$ for the optimal with $\beta = 2$, $Re = 500$ and $t = 100$. $\bullet$, $\circ$ and $*$ are the a, b and c modes respectively.

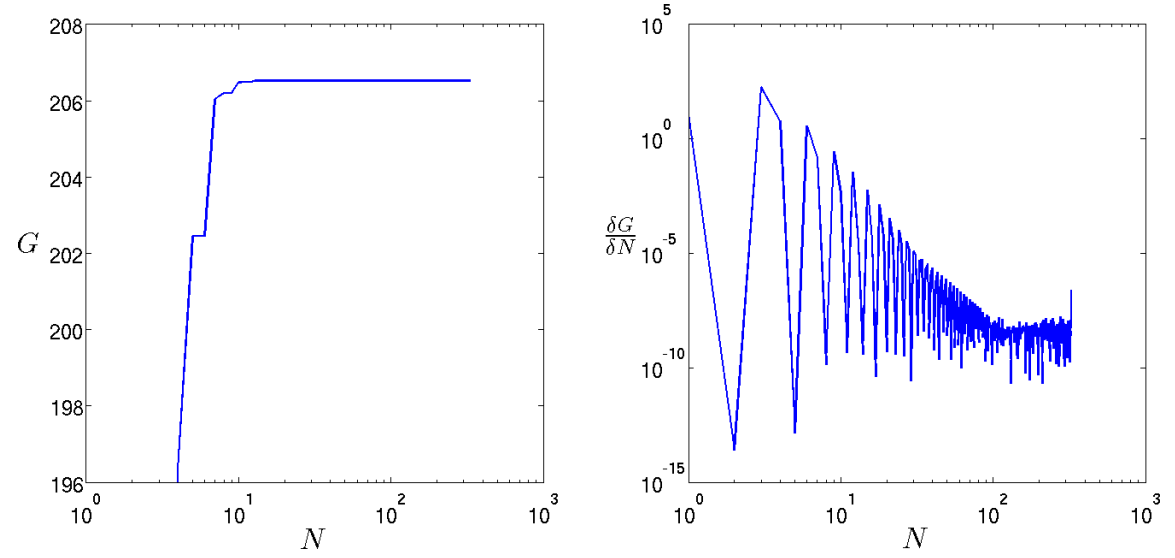

Figure 5.26: We plot G (left) and $\frac{\delta G}{\delta N}$ (right), for $\beta = 2$, $Re = 500$ and $t = 100$, against a modal truncation N comprised of a and c modes.

5.6 Conclusion

Our focus in this chapter has been the spatial optimal growth of an arbitrary, finite expansion of the Papkovitch-Fadle eigenfunctions under boundary conditions motivated by Stokes flow. By analysis of the energy gain $G(x)$ as a function of the number of Papkovitch-Fadle eigenmodes included in the velocity expansion, we have shown that $G(x)$ is not well converged for $x < 0.1$, and that a large number of modes, $M = 10^4$, are required to guarantee convergence for $x > 0.1$. We analyze the form of the optimal edge condition, and find that increasingly large wavenumber modes are selected by the optimization procedure which finds the optimal edge condition for a given downstream location. The large wavenumber modes make a prominent contribution to the optimal edge condition at its corners, inducing highly oscillatory velocity fluctuations, and exerting a large shear stress on the corner walls. In light of this, we solve a constrained optimization problem in which the corner stress is bounded at unity, and we find that though less energy amplification is possible, the optimal edge condition retains the use of large wavenumber modes in its spatial energy growth.

To gain an insight into why the optimal edge velocity is reliant on large wavenumber modes, we undertake an asymptotic analysis of the energy inner product in the large wavenumber limit. We show that the inner product of two large wavenumber modes is O(1), but that the energy inner product interactions of large and low wavenumber modes are asymptotically small. This suggests that there exists a mechanism by which large wavenumber modes instigate energy growth by transferring energy between one another. That such a mechanism exists does not imply that large wavenumber modes definitively *will* contribute to the maximum energy amplification, rather, that they *could* make a contribution. Therefore, our asymptotic results are to be interpreted as some justification for the inclusion of large wavenumber modes in the optimal edge condition, but not an indication that they must be present.

Moving away from Stokes flow, we assess the impact of the large wavenumber growth mechanism on convected flows, choosing two-dimensional spatially developing Poiseuille flow to examine. We find that qualitiative features of the Stokes optimal edge condition are carried over into the finite Re flow; highly oscillatory velocity fluctuations are found near the channel corners, and the energy gain $G(x)$ converges slowly as a function of the modal resolution.

Finally, we analyzed temporal optimal growth in plane streamwise-independent plane Couette flow, for which large optimal energy amplification is well-known and no con-

vergence issues have been reported. We find an analytic solution to the system, which allows us to perform an analogue of the asymptotic analysis of the spatial energy inner product, on the interactions of high and low damped modes. In contrast to our spatial results, we find that the temporal energy inner product invariably decays in the all high damping limits considered, meaning that highly damped modes cannot contribute to non-modal energy growth. This difference highlights the dichotomy between the spatial and temporal frameworks in fluid dynamics.

Chapter 6

Conclusions & further work

By way of concluding this thesis we will re-cap and contextualize the conclusions from the four results chapters §§2, 3, 4 and 5. In addition, with an outlook on potential future work we will discuss the ways in which our results can be developed. Each of the flows considered throughout the thesis will be discussed in turn, in §§6.1, 6.2 and 6.3.

6.1 Annular Poiseuille-Couette flow

In §2 we contribute to existing stability analyses in annular Poiseuille-Couette flow (APCF) with a study of the non-modal linear energy growth. Beginning with a linear stability analysis, we demonstrate that the Rayleigh stability criterion can be used to show that APCF is stable to inviscid perturbations for inner cylinder velocity $V < V^*$. However, the Rayleigh stability criterion is only a necessary condition for instability, and we find no indication that the flow loses stability to inviscid waves for $V \geq V^*$. Viscous waves are known to de-stabilize APCF (Sadeghi & Higgins (1991), Gittler (1993), Walton (2003, 2004, 2005)), and by maximizing over axial and azimuthal wavenumbers we produce neutral curves in (Re, V)-space, for suitably defined Reynolds number Re. Though the neutral curves are not monotonic in (Re, V), the trend is for non-zero V to stabilize the laminar base flow. There appear to be cut-off velocities for positive and negative V, beyond which all perturbations are linearly stable, and our calculations are in agreement with the cut-off velocity for radius ratio $\eta = 0.5$ and $V > 0$ derived by Sadeghi & Higgins (1991). Our non-modal growth analysis focuses on subcritical (Re, V) space, and we find that our conclusion differs from linear stability results: non-zero V has the tendency to de-stabilize the laminar profile, in the sense that the maximum energy gain $\mathbb{G}$ increases with $|V|$, provided $|V|$ is sufficiently large. This is demonstrated in a series of Figures in which contours of $\mathbb{G}$ are plotted in (Re, V) space for a range of η. The level of maximum growth is found to be of a similar order of magnitude regardless of the radius ratio η. Non-axisymmetric modes are found to be amplified by the well-known

lift-up mechanism, while axisymmetric modes are amplified via the Orr mechanism. The presence of both energy growth mechanisms is a strong indication that a subcritical route to transition may be possible in a similar manner to that which is currently understood in the canonical subcritical shear flows: plane Poiseuille flow, plane Couette flow and Hagen-Poiseuille flow. Recent studies such as Pringle *et al.* (2012), Rabin *et al.* (2012) and Duguet *et al.* (2013) indicate, via optimization over the fully nonlinear Navier-Stokes equations, that the minimal amplitude perturbations which instigate transition amplify themselves via combinations of the Orr mechanism and the lift-up mechanism. Additionally, we find that the experimentally observed (Re, V) transition values from Shands *et al.* (1980) lie at similar values of $\mathbb{G}$, which we find to be suggestive of a link between the lift-up mechanism and transition to turbulence.

Further study in APCF might address the existence of exact coherent structures in subcritical (Re, V) space. Wong & Walton (2012) have already found axisymmetric solutions which emerge in a bifurcation from linearly unstable axisymmetric perturbations, and can be continued into the linearly stable regime. This procedure could be extended to non-axisymmetric solutions, whose existence would provide further evidence for the link between exact coherent structures and transition to turbulence in subcritical shear flows. The relationship between the structures and the asymptotic nonlinear solutions of Walton (2003, 2005) could be investigated. An asymptotic analysis in search of linear cut-off velocities for $V < 0$, following the approach of Sadeghi & Higgins (1991) who treated $V > 0$, might prove interesting. Such a study could provide asymptotic confirmation that large magnitude inner cylinder velocities stabilize linear modes for all Re, regardless of whether the inner cylinder motion opposes or aligns with the axial pressure gradient.

6.2 Rotating plane Couette flow

In §3 we study the stability and bifurcation sequences of nonlinear solutions in supercritical rotating plane Couette flow (RPCF). We present bifurcations of steady secondary solutions in rotation number and cross-flow energy space, (Ro, E_{cf}). In addition to well-known Taylor vortex solutions, we discuss steady oblique vortex flows (OVF), finding upper and lower solutions which bifurcate from unstable modes of the primary flow. The steady OVF are related to the travelling wave spiral vortex flows discussed for Taylor-Couette flow (TCF) by, for example, Hoffmann *et al.* (2009), Altmeyer *et al.* (2010) and Deguchi & Altmeyer (2013). Our analysis contributes to the understanding of these oblique flows, and elucidates the differences in bifurcation behaviour between the oblique and streamwise independent flow states.

An extensive stability analysis of Taylor vortex flow (TVF) in §3.6 yields an insight into the bifurcation sequences which develop as Taylor vortices lose stability. Stability calculations across a wide range of TVF allows the characterization of the instabilities affecting TVF and the tertiary flows into which they develop. Alongside the tertiary flows which have already been discovered in RPCF, such as wavy vortex flow (WVF) and twisted vortex flows (TWI and wTWI), in §3.7 we find an oscillating vortex structure (oWVF) and a streamwise indepedent short spanwise wavelength structure which we have named skewed vortex flow (SVF). Bifurcation analyses in Ro and streamwise wavenumber α_s reveal that for small α_s wTWI emerges in a saddle-node bifurcation from TVF. A solution branch of wTWI is found to exist which connects TVF states with $\beta_s = 1.5$ and $\beta_s = 3$, suggesting a more intricate relationship between the two flows than has previously been appreciated. A bifurcation scenario is presented for oWVF where no stable solution exists and flow moves between unstable states in a quasi-chaotic orbit. There is perhaps some novelty that such an orbit can exist in a transitional flow regime, and a related process could form the basis for the turbulent dynamics found at larger Re. In a bifurcation analysis of SVF, we find that it connects the first and second TVF which bifurcate from the primary flow. The stability properties of representative cases for all of these tertiary flows have been analyzed, suggesting the existence of quaternary structures to be investigated in future research. The existence of such a range of tertiary and higher order nonlinear structures could, at larger Reynolds numbers, be important in the understanding of fully turbulent flow.

The relevence of tertiary states to transitional RPCF is assessed in §3.8. Through numerical simulations on a domain which supports a range of wavenumbers and through a model which simplifies the transition process based on bifurcation sequences, we analyze the states observed in the experiments of Tsukahara *et al.* (2010) and Suryadi *et al.* (2013). We find good agreement between model, simulation and experiment in most cases. However, a notable divergence between model and simulation occurs for $Ro = 0.9$, where the model predicts a final flowfield consisting of wTWI and the simulation finishes in a final flowfield with a localized twist vortex amongst streamwise independent TVF. Despite this deviation, the model and simulation flowfields are good approximations for two experimentally observed flowfields at $Ro = 0.9$.

Further studies could include both a Floquet stability analysis of secondary oblique vortices and a study of the bifurcation scenarios which follow when it loses stability. We have some preliminary results in this direction, having found a tertiary oblique wave structure reminiscent of wavy spiral vortex flow of TCF discussed in Hoffmann *et al.* (2009) and Deguchi & Altmeyer (2013), shown in Figure 6.1. We name this structure wavy oblique

vortex flow wOVF.

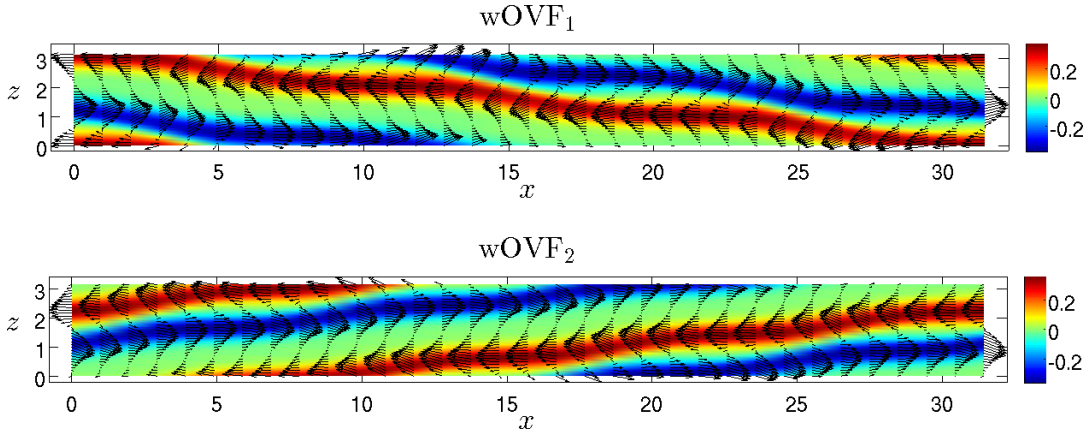

Figure 6.1: Two wOVF flowfields for $(\alpha_s, \beta_s, Re, Ro) = (0.2, 2, 100, 0.1)$ which bifurcate from steady OVF at the same parameters.

It would be interesting to explore the connection between wOVF and the turbulent stripe phenomenon in non-rotating plane Couette flow (PCF). Turbulent stripes are a curious feature known to the fluid dynamics community since they were reported in experiments by Coles (1965), whose images caught the attention of Richard Feynman, and prompted him to coin the phrase "barber-pole turbulence" in description of the stripes (Feynman (1964)). Turbulent stripes are found in experiments and simulations of PCF (see, for example, the recent studies of Prigent *et al.* (2002), Duguet *et al.* (2010), Duguet & Schlatter (2013)), however, the origin of the oblique structure remains an open question. If wOVF or a similar state can be continued from RPCF to PCF, it could serve as a coherent structure from which obliqueness of the stripes could originate, and about which the turbulent dynamics could be organized.

A non-modal growth analysis across subcritical RPCF has been conducted in §4. By optimization over streamwise and spanwise wavenumbers α and β, we compute the maximum linear energy amplification, $\mathbb{G}$, available to perturbations across subcritical (Ro, Re) space. We find that the effect of strong cyclonic $(Ro < 0)$ or anti-cyclonic $(Ro > 0)$ rotation is to hinder the lift-up and anti lift-up mechanisms, such that optimal perturbations rely on the Orr mechanism for energy growth. The restriction of the anti lift-up mechanism in anti-cyclonic RPCF has been noted before by Yecko (2004) and Rincon *et al.* (2007), whose results were interpreted in the context of transition in astrophysical accretion disks. Our contribution is therefore to show that strong cyclonic RPCF behaves comparably to strong anti-cyclonic RPCF, with respect to optimal disturbances. We posit that the absence of the lift-up mechanism in strong cyclonic RPCF will alter the transition scenario as it is currently understood in PCF. The lift-up mechanism is

thought to be relevant in generating the streak component of the self-sustaining process (Waleffe (1995, 1997, 1998)) and vortex-wave interaction theory (Hall & Smith (1991); Hall & Sherwin (2010), Deguchi *et al.* (2013), Blackman *et al.* (2013)), which have been proposed to explain the existence of exact coherent structures in the canonical subcritical shear flows. Furthermore a lift-up mechanism growth phase has been highlighted in the nonlinear optimals found by Pringle *et al.* (2012), Rabin *et al.* (2012) and Duguet *et al.* (2013), for Hagen-Poiseuille flow and PCF. Hence, the absence of the lift-up mechanism would, in theory, prevent these transition scenarios from developing and a new understanding would be required if indeed turbulence was shown to develop in RPCF with strong rotation.

Further study could be made into transition in subcritical RPCF: in the three regimes of large cyclonic rotation, large anti-cyclonic rotation and $Ro = 1$. In the latter case, the anti lift-up mechanism and the Orr mechanism co-exist and Lesur & Longaretti (2005) found that transition occured in numerical simulations. A novel route to transition may then be found for this subcritical shear flow. A search for exact coherent structures, renewing the efforts of Rincon *et al.* (2007), may prove illuminating. Bifurcations from the secondary and tertiary structures of §3 in supercritical RPCF would be the ideal starting point for such a search. Additionally, a study similar to Reddy *et al.* (1998), with an analysis of the secondary stability of transiently amplified structures, could be carried out on the optimal disturbances of subcritical RPCF.

6.3 The Papkovitch-Fadle operator and spatial non-modal growth

In §5 we have studied the non-modal stability properties of the Papkovitch-Fadle operator with application to Stokes flow. We show that convergence of the maximum linear spatial energy amplification in modal truncation is slow, due to reliance of the optimal edge condition on highly damped modes. We demonstrate that the corner shear-stress of the optimal edge condition scales linearly with the number of modes used to expand the optimal disturbance. However, we solve a constrained optimization problem in which the corner stress is fixed at unity, and we show that the constrained optimal edge condition has similar qualitative features to the unconstrained case. An asymptotic analysis of the energy inner product interactions of the Papkovitch-Fadle eigenfunctions reveals that short wavelength modes can transfer energy between one another, but not to a long wavelength mode. This result offers an explanation as to why optimization for the maxmimum energy amplification selects increasingly short wavelength modes. The impli-

cations of our results on convected flows are investigated in an analysis of optimal growth in two-dimensional spatial Poiseuille flow, for which the Papkovitch-Fadle operator can be considered the $Re \to 0$ limit. We find that the optimals in spatial Poiseuille flow share qualitative characteristics with the optimal edge conditions for the Papkovitch-Fadle operator, suggesting that the short wavelength energy growth mechanism is not unique to Stokes flow. Finally, our results are contrasted with a treatment of temporal plane Couette flow, where it is shown that no analogus highly-damped modal coupling does not occurs.

A continuation of our ideas on short wavelength energy transfer in spatially developing flows may serve to complete our understanding of the mechanisms by which fluid structures are energetically amplified. Henningson & Schmid (1994) pointed out that the kinetic energy norm need not behave in the same way with respect to spatially developing disturbances as it does for temporal disturbances. A new approach could be to construct a novel disturbance measure which is not affected by a short wavelength energy transfer, based on the bi-orthogonality properties of the Papkovitch-Fadle eigenfunctions, though the physical interpretation of such a norm would need to be considered. Temporal growth mechanisms are well understood, and have been discussed at length in this thesis. A richer understanding of spatial growth mechanisms, in any norm, would serve to complement our existing knowledge on the important issue of spatio-temporal devlopment in fluid flow.

Bibliography

Alfredsson, P. H. & Tillmark, N. 2005 Instability, transition and turbulence in plane Couette flow with system rotation. In *IUTAM Symposium on Laminar Turbulent Transition and Finite Amplitude Solutions* (ed. T. Mullin & R. R. Kerswell), *Fluid Mechanics and Its Applications*, vol. 77. Springer.

Altmeyer, S., Hoffmann, Ch., Heise, M., Abshagen, J., Pinter, A., Lücke, M. & Pfister, G. 2010 End wall effects on teh transition between Taylor vortices and spiral vortices. *Phys. Rev. E* **81**.

Andereck, C. D., Liu, S. S. & Swinney, H. L. 1986 Flow regimes in a circular Couette system with independently rotating cylinders. *J. Fluid Mech.* **164**, 155–183.

Andersson, P., Berggern, M. & Henningson, D. S. 1999 Optimal disturbances and bypass transition in boundary layers. *Phys. Fluids* **11** (1).

Antkowiak, A. & Brancher, P. 2007 On vortex rings around vortices: an optimal mechanism. *J. Fluid Mech.* **578**, 295–304.

Antonijoan, J. & Sánchez, J. 2000 Transitions from Taylor vortex flow in a co-rotating Taylor-Couette system. *Phys. Fluids* **12**.

Bergström, L. 1993 Optimal growth of small disturbances in pipe Poiseuille flow. *Phys. Fluids A* **5**.

Blackman, H. M., Hall, P. & Sherwin, S. J. 2013 Lower branch equilibria in Couette flow: the emergence of canonical states for arbitrary shear flows. *J. Fluid Mech.* **726**, 35–97.

Blum, E. K. & Chang, A. F. 1978 A numerical method for the solution of the double eigenvalue problem. *IMA J. Appl. Math.* **22**, 29–42.

Boyd, J. P. 2001 *Chebyshev and Fourier Spectral Methods*. Dover, New York.

Butler, K. M. & Farrell, B. F. 1992 Three-dimensional optimal perturbations in viscous shear flow. *Phys. Fluids* **4**.

Chapman, S. J. 2002 Subcritical transition in shear flows. *J. Fluid Mech.* **451**, 35–97.

Chevalier, M., Schlatter, P., Lundbladh, A. & Henningson, D. S. 2007 A pseudo-spectral solver for incompressible boundary layer flows. *Tech. Rep.* TRITA-MEK 2007:07. KTH Mechanics, Stockholm, Sweden.

Clenshaw, C. W. & Curtis, A. R. 1960 A method for numerical integration on an automatic computer. *Numer. Math.* **2** (197).

Coles, D. 1965 Transition in circular Couette flow. *J. Fluid Mech.* **21**, 385–425.

Corbett, P. & Bottaro, A. 2001 Optimal linear growth in swept boundary layers. *J. Fluid Mech.* **435**, 1–23.

Cowley, S. J. & Smith, F. T. 1985 On the stability of Poiseuille-Couette flow: a bifurcation from infinity. *J. Fluid Mech.* **156**, 83–100.

Czarny, O., Serre, E., Bontoux, P. & Lueptow, R. M. 2003 Interaction between Ekman pumping and the centrifugal instability in Taylor-Couette flow. *Phys. Fluids* **15**.

Davey, A., DiPrima, R. C. & Stuart, J. T. 1968 On the instability of Taylor vortices. *J. Fluid Mech.* **31**, 17–52.

Deguchi, K. & Altmeyer, S. 2013 Fully nonlinear mode competitions of nearly bicritical spiral or Taylor vortices in Taylor-Couette flow. *Phs. Rev. E* **87**.

Deguchi, K., Hall, P. & Walton, A. 2013 The emergence of localized vortex-wave interaction states in plane Couette flow. *J. Fluid Mech.* **721**, 58–85.

Duguet, Y., Monokrousos, A., Brandt, L. & Henningson, D. S. 2013 Minimal transition thresholds in plane Couette flow. *Phys. Fluids* **25**.

Duguet, Y. & Schlatter, P. 2013 Oblique laminar-turbulent interfaces in plane shear flows. *Phys. Rev. Lett.* **110**.

Duguet, Y., Schlatter, P. & Henningson, D. S. 2010 Formation of turbulent patterns near the onset of transition in plane Couette flow. *J. Fluid Mech.* **650**, 119–129.

Eagles, P. M. 1971 On stability of Taylor vortices by fifth-order amplitude expansions. *J. Fluid Mech.* **49**, 529–550.

Eckhaus, W. 1965 *Studies in Nonlinear Stability Theory*. Springer.

Ellingsen, T. & Palm, E. 1974 Stability of linear flow. *Phys. Fluids* **18**.

Fadle, J. 1941 Die selbstpannungs-eigenwertfunktionen der quadratischen scheibe. *Ingen. Arch.* **11**, 125–149.

Feynman, R. P. 1964 *Lecture Notes in Physics, Vol. 2*. Addison-Wesley.

Frei, Ch., Lüscher, P. & Wintermantel, E. 2000 Thread-annular flow in vertical pipes. *J. Fluid Mech.* **410**, 185–210.

Gibson, J. F. 2008 Channelflow: a spectral Navier-Stokes simulator in C++. *Tech. Rep.*. Georgia Institute of Technology.

Gibson, J. F., Halcrow, J. & Cvitanović, P. 2009 Equilibrium and travelling-wave solutions of plane Couette flow. *J. Fluid Mech.* **683**, 243–266.

Gittler, Ph. 1993 Stability of axial Poiseuille-Couette flow between concentric cylinders. *Acta Mech.* **101**, 1–13.

Gregory, R. D. 1979 Green's functions, bi-linear forms and the completeness of the eigenfunctions for the elastostatic strip and wedge. *J. Elasticity* **9**, 283–309.

Gregory, R. D. 1980*a* The semi-infinite strip $x \geq 0, -1 \leq y \leq 1$; completeness of the eigenfunctions when $\phi_{xx}(0, y), \phi_{yy}(0, y)$ are prescribed. *J. Elasticity* **10**, 57–80.

Gregory, R. D. 1980*b* The traction boundary value problem for the elastostatic semi-infinite strip; the existence of solutions and completeness of the Papkovitch-Fadle eigenfunctions. *J. Elasticity* **10**, 295–327.

Guégan, A., Schmid, P. J. & Huerre, P. 2006 Optimal energy growth and optimal control in swept Hiemenz flow. *J. Fluid Mech.* **566**, 11–45.

Guo, Y. & Finlay, W. H. 1991 Splitting, merging and wavelength selection of vortices in curved and/or rotating channel flow due to Eckhaus instability. *J. Fluid Mech.* **228**, 661–691.

Gustavsson, L. H. 1991 Energy growth of three-dimensional disturbances in plane Poiseuille flow. *J. Fluid Mech.* **224**, 241–260.

Hall, P. & Sherwin, S. J. 2010 Streamwise vortices in shear flows: harbingers of transition and the skeleton of coherent structures. *J. Fluid Mech.* **661**, 178–205.

Hall, P. & Smith, F. 1991 On strongly nonlinear vortex/wave interactions in boundary-layer transition. *J. Fluid Mech.* **227**, 641–666.

Heaton, C. J. & Peake, N. 2007 Transient growth in vortices with axial flow. *J. Fluid Mech.* **587**, 271–301.

Hegseth, J. J., Baxter, G. W. & Andereck, C. D. 1996 Bifurcations from Taylor vortices between corotating concentric cylinders. *Phys. Rev. E* **53**, 507–521.

Heise, M., Hoffmann, Ch., Will, Ch., Altmeyer, S., Abshagen, J. & Pfister, G. 2013 Co-rotating Taylor-Couette flow enclosed by stationary disks. *J. Fluid Mech.* **716**, 507–521.

Henningson, D. S. & Schmid, P. J. 1994 A note on measures of disturbance size for spatially evolving flows. *Phys. Fluids* **6**, 2862–2864.

Hiwatashi, K., Alfredsson, P. H., Tillmark, N. & Nagata, M. 2007 Experimental observations of instabilities in rotating plane couette flow. *Phys. Fluids* **19**, 48–103.

Hoffmann, Ch., Altmeyer, S., Pinter, A. & Lücke, M. 2009 Transitions between Taylor vortices and Spirals via wavy Taylor vortices and wavy Spirals. *New J. Phys.* **11**.

Hollerbach, R. & Fournier, A. 2004 End-effects in a rapidly rotating cylindrical Taylor-Couette flow. *MHD Couette flows: Experiments and Models* **776**, 114–121.

Itano, T. & Generalis, S. C. 2009 Hairpin vortex solution in planar Couette flow: a tapestry of knotted vortices. *Phys. Rev. Lett.* **102**, 114–501.

Ji, X. 1996 On 2D bisection method for double eigenvalue problems. *J. Comput. Phys.* **126**, 92–96.

Joseph, D. D. 1977 The convergence of biorthogonal series for biharmonic and Stokes flow edge problems. part I. *SIAM J. Appl. Math.* **33**, 337–347.

Joseph, D. D. & Sturges, L. 1978 The convergence of biorthogonal series for biharmonic and Stokes flow edge problems. part II. *SIAM J. Appl. Math.* **34**, 7–26.

Kawahara, G. & Kida, S. 2001 Periodic motion embedded in plane Couette turbulence: regeneration cycle and burst. *J. Fluid Mech.* **449**, 291–300.

Koschmieder, E. L. 1993 *Bénard cells and Taylor vortices*. Cambridge University Press.

Kreilos, T. & Eckhardt, B. 2012 Periodic orbits near the onset of chaos in plane Couette flow. *Chaos* **22**.

Landahl, M. T. 1980 A note on the algebraic instability of inviscid shear flows. *J. Fluid Mech.* **98**, 243–251.

Lesur, G. & Longaretti, P.-Y. 2005 On the relevance of hydrodynamic turbulence to accretion disk transport. *Astron. Astrophys.* **444**, 25–44.

Lezius, D. K. & Johnston, J. P. 1976 Roll-cell instabilities in rotating laminar and turbulent channel flows. *J. Fluid Mech.* **77**, 153–175.

Liu, R. & Liu, Q. S. 2012 Non-modal stability in sliding Couette flow. *J. Fluid Mech.* **484**, 505–544.

Longaretti, P.-Y. 2002 On the phenomenology of hydrodynamic shear turbulence. *Astrophys. J.* **576**, 587–598.

Luchini, P. 2000 Reynolds-number-independent instability of a boundary layer over a flat surface: optimal perturbations. *J. Fluid Mech.* **484**, 289–309.

Moffatt, H. K. 1963 Viscous and resisitive eddies near a sharp corner. *J. Fluid Mech.* **18**.

Nagata, M. 1986 Bifurcations in Couette flow between almost corotating cylinders. *J. Fluid Mech.* **169**, 229–250.

Nagata, M. 1988 On wavy instabilities of the Taylor-vortex flow between corotating cylinders. *J. Fluid Mech.* **188**, 585–598.

Nagata, M. 1990 Three-dimensional finite-amplitude solutions in plane Couette flow: bifurcation from infinity. *J. Fluid Mech.* **217**, 519–527.

Nagata, M. 1998 Tertiary solutions and their stability in rotating plane Couette flow. *J. Fluid Mech.* **358**, 357–378.

Nagata, M. 2013 A note on the mirror-symmetric coherent structure in plane Couette flow. *J. Fluid Mech.* **727**, R1.

Nagata, M. & Kawahara, G. 2004 Three-dimensional periodic solutions in rotating/non-rotating plane Couette flow. In *Advances in Turbulence X, proceedings of the Tenth European Turbulence Conference* (ed. H. I. Andersson & P. Å. Krogstad), *CIMNE*, vol. 77.

Narayan, R., Goldreich, P. & Goodman, J. 1987 Physics of modes in a differentially rotating system - analysis of the shearing sheet. *R. Astron. Soc.* **228**, 1–41.

Navier, C. L. M. H. 1822 Memoire sur les lois du mouvement des fluides. *Mem. Acad. Sci. Inst. France* **6**, 389–440.

Orr, W. M. F. 1907 The stability or instability of the steady motions of a perfect liquid and of a viscous liquid. Part I: A perfect liquid. Part II: A viscous liquid. *Proc. R. Irish Acad. A* **27**, 9–138.

Orszag, S. A. 1971 Accurate solutions of the Orr-Sommerfeld stability equation. *J. Fluid Mech.* **50**, 689–.

Papkovitch, P. F. 1940 Über eine form der lösung des byharmonischen problems für das rechteck. *Russian Acad. Sci. Dokl. Math.* **27**, 334–338.

Prigent, A., Grégoire, G., Chaté, H., Dauchot, O. & van Saarloos, W. 2002 Large-scale finite-wavelength modulation within turbulence shear flows. *Phys. Rev. Lett.* **89**.

Pringle, C. T., Willis, A. P. & Kerswell, R. R. 2012 Minimal seeds for shear flow turbulence: using nonlinear transient growth to touch the edge of chaos. *J. Fluid Mech.* **702**, 415–443.

Proudman, J. 1916 On the motion of solids in a liquid possessing vorticity. *Proc. R. Soc. Lond.* **92**, 408–424.

Rabin, S. M. E., Caulfield, C. P. & Kerswell, R. R. 2012 Triggering turbulence efficiently in plane Couette flow. *J. Fluid Mech.* **712**, 244–272.

Rayleigh, L. 1880 On the stability, or instability, of certain fluid motions. *Proc. Lond. Math. Soc.* **174**, 57–70.

Reddy, S. C. & Henningson, D. S. 1993 Energy growth in viscous channel flows. *J. Fluid Mech.* **252**, 209–283.

Reddy, S. C., Schmid, P. J. & Baggett, J. S. Henningson, D. S. 1998 Stability of streamwise streaks and transition thresholds in plane channel flows. *J. Fluid Mech.* **365**, 269–303.

Reshotko, E. & Tumin, A. 2001 Spatial theory of optimal disturbances in a circular pipe flow. *Phys. Fluids* **13**, 991–996.

Reynolds, O. 1883 An experimental investigation of the circumstances which determine whether the motion of water shall be direct or sinuous, and of the law of resistance in parallel channels. *Phil. Trans. R. Soc. Lond.* **174**, 935–982.

Rincon, F., Ogilvie, G. I. & Cossu, C. 2007 On self-sustaining processes in Rayleigh-stable rotating plane Couette flows and subcritical transition to turbulence in accretion disks. *Astron. Astrophys.* **463**, 817–832.

Romanov, V. A. 1973 Stability of plane-parallel Couette flow. *Funct. Anal. Appl.* **7**, 137–146.

Saad, Y. & Schultz, M. H. 1986 GMRES - A generalized minimal residual algorithm for solving nonsymmetric linear-systems. *SIAM J. Sci. Stat. Comp.* **7**, 856–869.

Sadeghi, V. M. & Higgins, B. C. 1991 Stability of sliding Couette-Poiseuille flow in an annulus subject to axisymmetric and asymmetric disturbances. *Phys. Fluids A* **3**, 2092–2104.

Sánchez, J., Net, M., García-Archilla, B. & Simó, C. 2004 Newton-Krylov continuation of periodic orbits for Navier-Stokes flows. *J. Comput. Phys* **201**, 13–33.

Schmid, P. J. & Henningson, D. S. 1994 Optimal energy density growth in Hagen-Poiseuille flow. *J. Fluid Mech.* **277**, 197–225.

Schmid, P. J. & Henningson, D. S. 2001 *Stability and Transition in Shear Flows*. Springer.

Shands, J., Alfredsson, H. & Lindgren, E. R. 1980 Annular pipe flow subject to axial motion of the inner boundary. *Phys. Fluids* **23**, 2144–2145.

Shartman, E., Hantao, J., Burin, M. J. & Goodman, J. 2012 Stability of quasi-Keplerian shear flow in a laboratory experiment. *Astron. Astrophys.* **543**, 1–13.

Smith, R. C. T. 1952 The bending of a semi-infinite strip. *Aust. J. Scient. Res.* **5**, 227.

Spence, D. A. 1982 A class of biharmonic end-strip problems arising in elasticity and Stokes flow. *IMA J. Appl. Math.* **30**, 107–139.

Stokes, G. G. 1845 On the theories of internal friction of fluids in motion, and of the equilibrium and motion of elastic solids. *Trans. Cam. Phil. Soc.* **8**, 279–319.

Suryadi, A., Tillmark, N. & Alfredsson, P. H. 2013 Rotating plane Couette flow at high rotation number. In *65th Annual Meeting of the APS Division of Fluid Dynamics*, , vol. 57.

Taylor, G. I. 1923 Stability of a viscous liquid contained between two rotating cylinders. *Phil. Trans. R. Soc. Lond.* **223**, 289–343.

Tempelmann, D., Hanifi, A. & Henningson, D. S. 2010 Spatial optimal growth in three dimensional boundary layers. *J. Fluid Mech.* **646**, 5–37.

Tevzadze, A. G., Chagelishvili, G. D., Zahn, J.-P., Chanishvili, R. G. & Lominadze, J. G. 2003 Hydrodynamic shear turbulence in stratified keplerian disks:

transient growth of small-scale 3D vortex mode perturbations. *Astron. Astrophys.* **407**, 779–786.

Trefethen, L. N. 1997 Pseudospectra of linear operators. *SIAM Review* **39**, 383–406.

Trefethen, L. N. & Embree, M. 2005 *Spectra and Pseudospectra*. Princeton University Press.

Trefethen, L. N., Trefethen, A. E., Reddy, S. C. & Driscoll, T. A. 1993 Hydrodynamic stability without eigenvalues. *Science* **261**, 578–584.

Tsukahara, T., Tillmark, N. & Alfredsson, P. H. 2010 Flow regimes in plane Couette flow with system rotation. *J. Fluid Mech.* **648**, 5–33.

Viswanath, D. 2007 Recurrent motions within plane Couette turbulence. *J. Fluid Mech.* **580**, 339–358.

Waleffe, F. 1995 Transition in shear flows. Nonlinear normality versus non-normal linearity. *Phys. Fluids* **7**, 3060–3066.

Waleffe, F. 1997 On a self-sustaining process in shear flows. *Phys. Fluids* **9**, 883–900.

Waleffe, F. 1998 Three-dimensional coherent states in plane shear flows. *Phys. Rev. Lett.* **81**, 4140–4143.

Waleffe, F. 2003 Homotopy of exact coherent structures in plane shear flows. *Phys. Fluids* **15**, 1517–1534.

Walton, A. G. 2003 The nonlinear stability of thread-annular flow at high reynolds number. *J. Fluid Mech.* **477**, 227–257.

Walton, A. G. 2004 Stability of circular Poiseuille-Couette flow to axisymmetric disturbances. *J. Fluid Mech.* **500**, 169–210.

Walton, A. G. 2005 The linear and nonlinear stability of thread-annular flow. *Phil. Trans. R. Soc. A* **363**, 1223–1233.

Weisshaar, E., Busse, F. H. & Nagata, M. 1991 Twist vortices and their instabilities in the Taylor-Couette system. *J. Fluid Mech.* **226**, 549–564.

Wong, A. H. & Walton, A. H. 2012 Axisymmetric travelling waves in annular Couette-Poiseuille flow. *Q. J. Appl. Math.* **65**, 293–311.

Yecko, P. A. 2004 Accretion disk instability revisited: transient dynamics of rotating shear flow. *Astron. Astrophys.* **425**, 383–395.